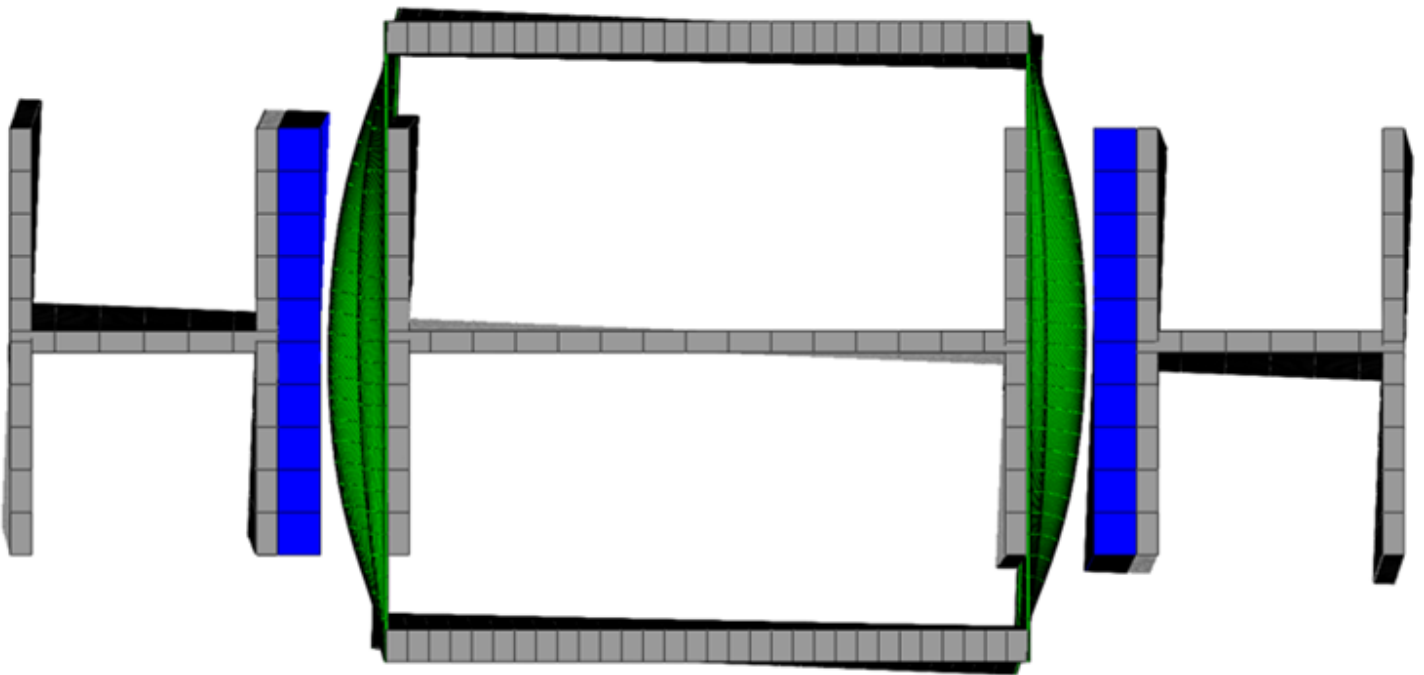# Twist morphing concept based on buckling-driven technologies

A.M. Pereira

TUDelft

Twist morphing concept based on buckling-driven technologies

by

A.M. Pereira

to obtain the degree of Master of Science in Aerospace Engineering
at the Delft University of Technology,
to be defended publicly on Friday January 25, 2022 at 1:00 PM.

Student number: 5148022
Thesis committee: Prof. dr. ir. C. Bisagni,   TU Delft, supervisor
                    Dr. ir. R. De Breuker,   TU Delft
                    Dr. ir. C. Rans,   TU Delft

An electronic version of this thesis is available at `http://repository.tudelft.nl/`.

TUDelft

Abstract

A novel twist morphing concept is explored, that exploits the buckling instabilities of slender spar webs integrated into a wing structure to control the twisting response to external loads. The main novelty of the concept is in controlling the effective shear stiffness of the post-buckled slender spar webs through external variable constraints acting on the out-of-plane buckling deformations. A methodology for the design and analysis of these novel morphing structures is proposed and implemented in the design of a wing box structure of promising twist morphing capabilities. The overall design process is structured into a multilevel process of increased complexity. In the first level, the morphing structure is simplified to a wing box with slender spar webs. With the objective of maximizing the morphing twists that can be achieved under the action of an external quasi-static torque, the wing box design space is explored in terms of its cross-sectional dimensions and the material assigned to the slender spar webs. In the second level, the morphing structure is expanded to include both the wing box and the external devices required to implement the adaptive constraints acting on the slender spar webs' out-of-plane buckling deformations. At this level, the objective is to design adaptive constraining devices that maximize the twist morphing capabilities, for which the influence of the constraining devices over the twisting response and their effectiveness in restraining the slender spar webs' buckling deformations become the main concerns. After an extensive design process, a design solution for the adaptive constraining devices is proposed, for which thorough analyses on the twist morphing capabilities are performed. In addition, the sensitivity of the twist morphing capabilities to the slender spar webs' geometrical imperfections is investigated.

Acknowledgements

Contents

List of Figures

List of Tables

Nomenclature

List of acronyms

3D	Three Dimensional
ATW	Adaptive Torsion Wing
CFD	Computational Fluid Dynamics
CFRP	Carbon Fibre Reinforced Polymer
DLR	German Aerospace Center
FEA	Finite Element Analysis
FEM	Finite Element Model
FishBAC	Fish Bone Active Camber
MALE	Medium Altitude Long Endurance
MPC	Multi-Point Constraint
POLIMI	Polytechnic University of Milan
PVC	Polyvinyl Chloride
PVDF	Polyvinylidene Fluoride
PW	Plain Weave
SMA	Shape Memory Alloy
TRIC	Translation Induced Camber
UAV	Unmanned Aerial Vehicle
UD	Unidirectional
VCCTEF	Variable Camber Continuous Trailing Edge Flap
VSS	Variable Stiffness Spar

List of symbols

Symbol	Definition	Unit
A_m	Cross-sectional enclosed area	[mm^2]
B	Non-dimensional stiffness factor	[-]
G_F	Gap between the front spar web and its external wall	[mm]
G_R	Gap between the rear spar web and its external wall	[mm]
I_f^t	Hashin failure index associated to the fibre tension failure mode	[-]
I_m^t	Hashin failure index associated to the tensile matrix failure mode	[-]
I_{TH}	Tsai-Hill failure index	[-]
K_θ^{FR}	Torsional stiffness in the *full-restraint* condition	[Nm/°]
K_θ^{NR}	Torsional stiffness in the *no-restraint* condition	[Nm/°]
T	External torque	[Nm]
$\overline{T}$	Non-dimensional external torque	[-]
β	Buckling-induced factor	[-]
$\Delta\theta_{FR}$	Twist increment per station in the *full-restraint* condition	[°]
$\Delta\theta_{NR}$	Twist increment per station in the *no-restraint* condition	[°]
θ_{FR}	Tip elastic twist in the *full-restraint* condition	[°]
θ_{NR}	Tip elastic twist in the *no-restraint* condition	[°]
θ_b	Buckling-induced twist	[°]
$\overline{\theta_b}$	Non-dimensional buckling-induced twist	[-]

1

Introduction

Traditional aerodynamic control surfaces and high-lift devices exploited in current commercial aircrafts, such as ailerons and flaps, have proven to be effective in controlling the airflow. However, conventional designs rely on mechanical hinges for rotation, making them aerodynamically inefficient. When deflected, discontinuities along the wing surface due to the discrete changes in wing geometry increase the overall drag.

Alternative solutions to change the aerodynamic shape of the wing in a more aerodynamically efficient way, generally referred to as wing morphing concepts, have been researched in the past. Higher costs, increase of complexity and weight-penalties due to additional actuation systems have historically prevented aircraft manufacturers to adopt these morphing solutions (*Barbarino et al.* [1]). However, in the last decades, researchers have revisited these alternative concepts, as advances in aerospace materials contributed to overcome many of the limitations.

The control of the twist angle along the wingspan is one of these revisited morphing concepts. In the last years, the most studied approach to realize twist morphing has been changing the internal structure of the wing during flight to modify the twisting response to the aerodynamic loads. In particular, by extracting the work required to twist the wing from the aerodynamic flow, the wing aeroelastic twist is to be controlled by adjusting the torsional stiffness and/or the shear centre location along the wing. Multiple solutions have been proposed, ranging from moving structural components, such as translating spar webs ([2, 3]) or rotating spars webs ([3–5]), to integrating components of selective stiffness, for which the use of smart materials ([6, 7]) and the buckling instabilities of slender structural elements ([8–11]) have been explored.

In this thesis, a novel twist morphing concept is explored, that exploits the buckling instabilities of slender spar webs integrated into a wing structure to control the twisting response to external loads. The main novelty of the concept is in controlling the effective shear stiffness of the post-buckled slender spar webs through external variable constraints acting on the out-of-plane buckling deformations. A methodology for the design and analysis of these novel morphing structures is proposed and implemented in the design of a wing box structure of promising twist morphing capabilities.

The chapters of this thesis are structured as follows. First, a literature study on the topic of wing morphing is presented in Chapter 2. In Chapter 3, the scope of the thesis is defined by stating the research questions and the research objective. In Chapter 4, the methodology to analyze the morphing capabilities of a wing box structure embedded with slender spar webs is presented. By implementing this methodology, the wing box design space is then explored in Chapter 5, investigating the effects of different wing box design parameters on the morphing capabilities. In Chapter 6, a design solution for the adaptive constraining devices required to control the slender spar webs' out-of-plane buckling deformations is proposed. Furthermore, the structural FEM developed to analyze the twist morphing capabilities of the overall morphing structure, comprised by the wing box and the adaptive constraining devices, is also presented in this chapter. Then, implementing this structural FEM, the twist morphing capabilities are analyzed in Chapter 7. Finally, the conclusions of this thesis and recommendations for future work are presented in Chapter 8.

1

2

Literature Study

2.1. The shape morphing wing concept

A wing capable of adapting its geometry during flight is referred to as a shape morphing wing. Even though there is no exact definition on the type or extent of geometrical change required for a concept to qualify as a shape morphing solution, it is general agreed on that conventional control surfaces that rely on hinge mechanisms to change the geometry of the wing are not shape morphing solutions.

Wing morphing solutions can be classified in different ways. For example, *Barbarino et al.* [1] propose a classification based on the geometrical parameter being affected. In Figure 2.1, their classification scheme is illustrated, from which three main categories can be identified.
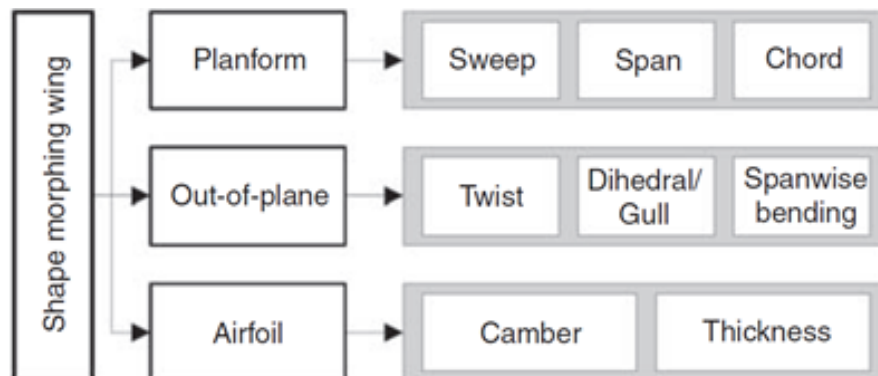
Figure 2.1: Classification of wing shape morphing solutions based on the geometrical parameter being affected. Adapted from *Barbarino et al.* [1].

The first group is referred to as planform morphing solutions. As can be inferred from the name, these concepts change the planform of the wing, either by affecting the span dimension, chord length or sweep angle of the wings. Techniques that have been investigated include telescopic wings to affect the wingspan length (e.g., *Samuel and Pines* [12]) and pivoting the wing at the wing root to change the sweep angle (exploited in many military aircrafts, such as the MiG-23 and the F-14).

The second group comprises the out-of-plane morphing solutions, which adapt the wing geometry either by twisting the wing, bending the wing or adjusting the dihedral angle of the wing. Within this group, morphing concepts that twist the wing have been studied the most.

The last group comprises the airfoil adjustment solutions, which are morphing concepts that change the wing airfoil, either by affecting its camber and/or thickness. Traditional control surfaces, such as elevators, ailerons and flaps, aim to control the camber (i.e., the curvature) of the airfoil. However, it should be highlighted that while modern commercial aircrafts rely on hinge mechanisms to deflect these control surfaces, creating gaps and surface discontinuities over the wing, camber morphing concepts aim to create continuous and smooth changes of camber along the wingspan.

2.2. Motivations for wing morphing

Wing morphing solutions can be divided into two groups based on the motivation behind the morphing concept. On one hand are the planform morphing solutions. These concepts introduce large shape changes during flight, allowing the aircraft to fulfill diverse requirements of altitude, speed, take-off and landing, radically expanding the aircraft flight envelope. However, as heavy actuation systems are usually required to realize the associated large geometrical changes, planform morphing solutions tend to be restricted to military aircrafts, for whom the necessity for versatility and mission flexibility may overcome the higher weights and costs.

On the other hand, the out-of-plane and airfoil adjustment concepts can be included in a broader category, referred to as *performance morphing* (*Cooper* [13]). Instead of affecting the planform of the wing, these morphing concepts only affect the wing aerodynamic shape, with the main objective of improving the wing aerodynamic performance. As an improvement of wing performance can lead to lower fuel consumption, lighter wings and an increase in aircraft range, *performance morphing* solutions are of great interest for the civil aircraft industry.

Four main drivers can be identified for introducing continuous and smooth changes to the wing aerodynamic shape: drag reduction, lift enhancement, roll control and load control. These drivers are analyzed in the following sub-sections.

2.2.1. Drag reduction

Modern commercial aircrafts are designed to perform at the wing maximum lift-to-drag ratio during the cruise segment of the flight, at a specific cruising altitude, speed and aircraft weight. However, for any other point of the flight envelope, aircraft wings perform sub-optimally, with a lower lift-to-drag ratio. Adapting the aerodynamic shape of the wing during flight makes possible to maintain the maximum lift-to-drag ratio at different flight conditions. Thus, the overall drag can be reduced when the aircraft operates at non-optimal flying conditions, e.g., due to air traffic control restrictions, environmental conditions or changes in fuel loading throughout the flight.

On the other hand, the replacement of hinged control surfaces and high-lift devices by shape morphing concepts that introduce continuous and smooth changes into the wing geometry contributes to decreasing the overall aerodynamic drag. Ultimately, these reductions in aerodynamic drag contribute to increasing the aircraft range and reducing the fuel consumption.

2.2.2. Lift enhancement

High-lift devices, like flaps, change the aerodynamic shape of the wing to increase the generated lift during take-off and landing, which contributes to reducing take-off and landing distances and speeds. Replacing conventional high-lift devices used in modern commercial aircrafts by morphing high-lift devices that introduce continuous and gapless changes to the wing geometry can reduce drag and airframe noise associated to conventional high-lift devices.

2.2.3. Load control

Since the 1970s, systems have been developed to actively control the structural loading of the wing by deflecting control surfaces, such as ailerons, elevators and rudders. This technology, referred to as active load alleviation, reduces critical loading for design, created by gusts or demanding maneuvers, leading to lighter wing designs. In addition, reducing the structural loading of the wing contributes to increasing passenger comfort.

Shape morphing solutions have the potential to replace the use of the more aerodynamically inefficient hinged control surfaces for controlling the wing structural load. However, due to the high frequency of gusts loads, the active changes in wing geometry need to be very fast to successfully control the structural loading of the wing. For this reason, wing morphing concepts for load control purposes require high actuation bandwidth.

2.2.4. Roll control

Shape morphing of the wing can also be exploited to enhance the roll performance of discrete control surfaces (i.e., ailerons) or even replace their use. Camber morphing and twist morphing concepts have been investigated for these purposes.

Three drivers can be identified for the replacement of the traditional hinged ailerons by camber or twist morphing concepts. Firstly, to reduce drag by introducing continuous and smooth changes to the wing geometry. Secondly, to increase the stealth of the aircraft by reducing the radar signature of deflected surfaces and sharp edges, of interest for military aircrafts. Lastly, morphing concepts that rely on smart materials for actuation or that exploit the aerodynamic forces to deform the wing can lead to significant weight-savings in comparison to hinged control surfaces.

On the other hand, when exploiting morphing solutions to enhance the roll performance of discrete control surfaces, the morphing can contribute to increasing the dynamic pressure at which aileron reversal occurs (*Pendleton et al.* [14]), to increasing the rolling rate (*Chen et al.* [4]) and to providing sufficient roll authority using smaller control surfaces (*Cooper* [13]), which can increase stealth, of interest for military aircrafts, and reduce drag, of great importance for civil aviation.

2.3. Actuation strategies for wing morphing

The two performance morphing solutions that have been researched the most are camber control and wing twisting, and the motivations for their development have already being discussed in Section 2.2. In this section, the different actuation strategies that have been investigated for their implementation will be addressed. Based on the actuation strategy, two groups can be identified: Active Adaptive Concepts and Aeroelastic Adaptive Concepts.

2.3.1. Active Adaptive Concepts

Active Adaptive Concepts achieve morphing by using a system of actuators to deform a flexible wing to a desired shape. Most camber control concepts exploit this actuation strategy, applying actuation methods that rely either on conventional actuators or smart materials. On the other hand, this actuation strategy has been exploited for twist morphing concepts to a much lesser extent, as most of these concepts rely on the aerodynamic forces to twist the wing.

Active Adaptive Concepts' main limitation is the need for actuators capable of providing enough force and stroke to deform the structure. For conventional actuators, which include electromagnetic motors and hydraulic or pneumatic actuators, the size and weight of the actuators increase with the actuation forces and strains that need to be supplied. For this reason, the weight penalty has historically been the main challenge for morphing the wing in a continuous fashion using conventional actuators.

To reduce the weight penalty associated to conventional actuators, new actuation mechanisms based on solid-state smart materials have been considered for shape morphing application. Smart materials, specifically shape memory alloys and piezoelectric materials, allow for the integration of the actuation capability within the structure of the wing, making possible to change the wing geometry in a continuous manner, while reducing weight and maintenance costs by avoiding the use of conventional actuators.

The two smart materials most studied for actuation, for both camber and twisting morphing concepts, are the shape memory alloys (e.g., *Nam et al.*[15], *Leal et al.*[16] and *Bishay et al.*[17]) and the piezoelectric materials (e.g., *Molinari et al.*[18], *Vos et al.*[19], *Bilgen et al.*[20]). In the case of shape memory alloys, large strains can be applied, but they have the drawbacks of a relatively low load output and slow frequency response. In the case of piezoelectric materials, even though they can apply very low strains, they are very attractive due to their high load output and their fast frequency response.

2.3.2. Aeroelastic Adaptive Concepts

On the other hand, Aeroelastic Adaptive Concepts extract the mechanical work required to deform the wing from the aerodynamic forces acting upon the lifting surface. In this way, the changes of wing geometry consist solely of aeroelastic deformations, and, accordingly, the design of these aeroelastic concepts require a multidisciplinary approach between Structures and Aerodynamics.

In order to have authority over the aeroelastic deformations, the most studied approach consists in adapting the internal structure of the wing during flight, which in turn modifies the wing structural response to the aerodynamic loads. A distinction can be made depending on whether the concept requires any sort of actuation to adapt the wing internal structure: concepts that require actuation are referred to as Active Aeroelastic Adaptive Concepts, while those that do not require actuation are referred to as Passive Aeroelastic Adaptive Concepts.

Most twist morphing concepts rely on the aerodynamic forces to twist the wing, qualifying as Aeroelastic Adaptive Concepts. On the other hand, even though most investigated camber morphing solutions qualify as Active Adaptive Concepts, some researchers have proposed camber morphing concepts that exploit the aerodynamic forces to control the wing camber (e.g., *Kuder et al.* [21]).

2.4. Active Adaptive Concepts for camber morphing

As mentioned before, Active Adaptive Concepts have been mostly developed for camber control purposes. In this section, different morphing leading and trailing edge devices developed for camber control will be presented.

2.4.1. The Fish Bone Active Camber (FishBAC) concept

A state-of-the-art concept for camber morphing is the Fish Bone Active Camber concept, referred to as the FishBAC concept. First introduced by *Woods and Friswell* [22], it is a morphing trailing edge device capable of creating large, smooth and continuous changes in camber. As illustrated in Figure 2.2 (on the left side), it consists of a central bending beam, referred to as the spine, with stringers branching off to support a flexible skin. The structure has a high spanwise bending stiffness due to the stringers stiffening effect, but a low chordwise bending stiffness that is exploited for camber morphing. This low chordwise bending stiffness allows creating large changes in camber with low actuation energy requirements.
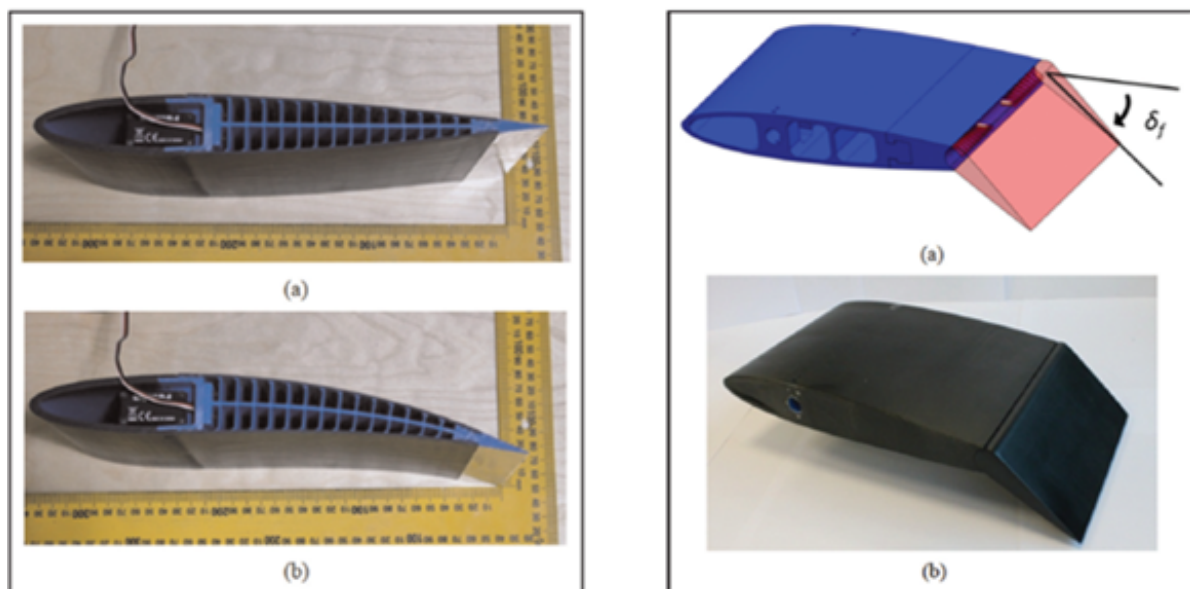
Figure 2.2: Illustration of the FishBAC wind tunnel model (left) and the flapped airfoil wind tunnel model (right) used for wind tunnel tests. Adapted from *Woods et at.* [23].

Woods et at. [23] performed wind tunnel tests on two similar 3D printed models, illustrated in Figure 2.2, one exploiting the FishBAC concept and the other a conventional hinged flap. The FishBAC model achieved drag reductions of 25% with respect to the hinged flap model, as it changes the airfoil camber without creating gaps and surface discontinuities.

Rivero et al. [24] developed a second-generation wind tunnel FishBAC model with a composite spine made of a carbon fibre reinforced polymer, illustrated in Figure 2.3. A composite spine can further amplify the anisotropic nature of the device (higher spanwise bending stiffness than chordwise bending stiffness) and allows tailoring the structural stiffnesses. The capability to tailor the chordwise bending stiffness of the structure is very important in order to satisfy the trade-off between compliance and rigidity. The structure has to be compliant enough for the actuation forces to create sufficient camber deformations, while it also needs to be stiff enough to withstand the external aerodynamic forces.
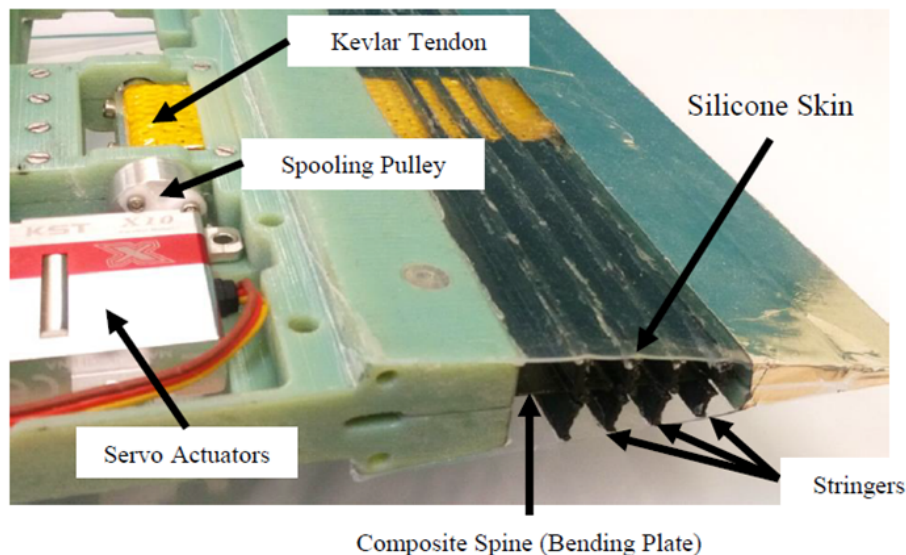
Figure 2.3: Structure and actuation mechanism of a FishBAC-based trailing edge device with a composite spine. Adapted from *Rivero et al.* [24].

With regard to the actuation, all FishBAC prototypes have relied on a tendon-pulley system driven by an electric servo-actuator. Figure 2.3 provides a clear illustration of the actuation method. A Kevlar tendon tape travels from the trailing edge, where it is joined to the spine, to the front of the FishBAC section, passing through slots in the stringers. At the front of the FishBAC section, the Kevlar tendon is spooled around a pulley that is driven by a servo-actuator. Then, as the servo-actuator inputs a torque and rotation to the spooling pulley, the Kevlar tendon introduces a chordwise bending moment to the spine, creating the desired camber deformation due to the low chordwise bending stiffness of the structure.

As a state-of-the-art morphing concept for camber control, the structural modeling of the concept and its aerodynamic performance have been investigated during the last few year. *Rivero et al.* [24] developed an analytical structural model based on Kirchhoff-Love plate theory, later extended to a Mindlin-Reissner plate theory (taking into consideration shear deformations through the thickness of the plate) in *Rivero et al.* [25]. These analytical predictions were in very good agreement with finite element analyses, while requiring much lower computational time. Subsequently, *Rivero et al.* [26] performed a preliminary static aeroelastic analysis, coupling this Mindlin-Reissner plate model to an aerodynamic model, to study how the FishBAC concept can be used to control the lift distribution along the wingspan.

2.4.2. The Variable Camber Continuous Trailing Edge Flap (VCCTEF)

The Variable Camber Continuous Trailing Edge Flap (VCCTEF) is a morphing trailing edge flap concept initially developed by NASA in 2010 (*Nguyen* [27]), and further developed by a collaboration between NASA and Boeing between 2012 and 2014 (*Urnes et al.* [28], *Lebofsky et al.* [29]). The VCCTEF consists of individual active sections, referred to as "flap sections", distributed along the wingspan. For the wind tunnel model tested at the University of Washington Aeronautical Laboratory (UWAL), five flap sections were considered, as illustrated in Figure 2.4. As each flap section can be independently deflected to a specific camber configuration, adjacent flap sections are inter-connected through a flexible transition material in order to ensure a continuous trailing edge. For example, for the wind tunnel model illustrated in Figure 2.4, a silicone elastomeric material was used as transition material.
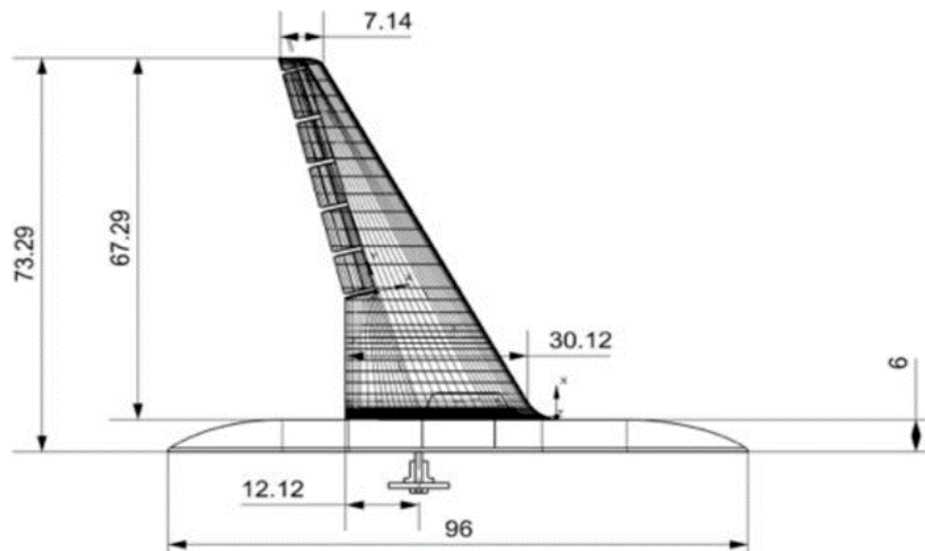
Figure 2.4: UWAL wind tunnel model exploiting the VCCTEF developed by NASA and Boeing. Adapted from *Lebofsky et al.* [29].

Each flap section consists of 3 segments that can be individually commanded, as illustrated in Figure 2.5, leading to a variable camber flap that produces higher lift-to-drag ratios than a straight simple flap. The target camber deflections are created by rotating each of the three rigid segments around hinge lines, which in turn deform the flexible skin covering the flap section. The three hinged segments of the flap sections manufactured for the UWAL wind tunnel model are illustrated in Figure 2.6.
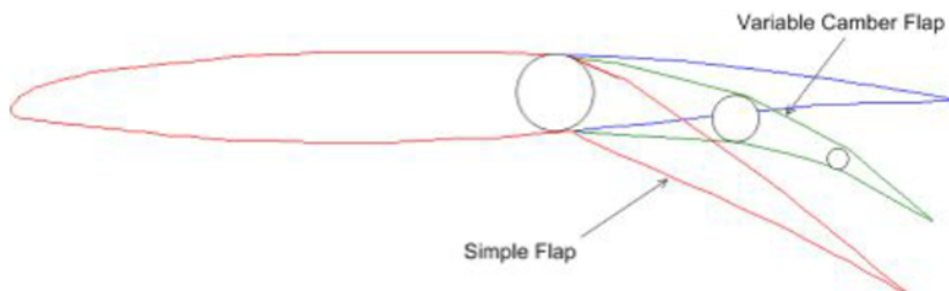
Figure 2.5: The Variable Camber Flap of the VCCTEF concept. Adapted from *Lebofsky et al.* [29].
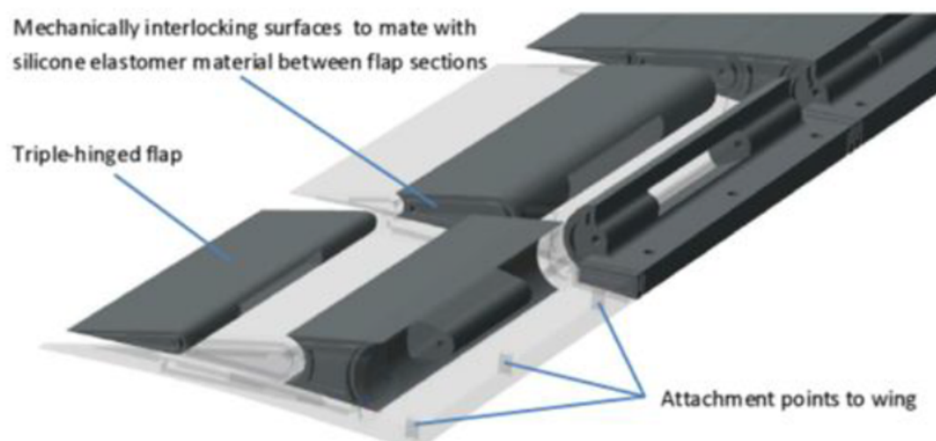
Figure 2.6: CAD model of the flap sections manufactured for the UWAL wind tunnel model. Adapted from *Lebofsky et al.* [29].

With regard to the actuation, the first and second segments are rotated by SMA rods placed along the hinge lines. However, due to the low actuation bandwidth characteristic of SMA-based actuators, the last segment is actuated by a fast electrical actuator. In this way, the third segment of the morphing flap can be used for roll control and for suppressing aeroelastic dynamic modes.

2.4.3. The SmartX wing

At the Delft University of Technology, an autonomous morphing wing concept referred to as the SmartX wing has been developed (*Mkhoyan et al.* [30, 31]). The SmartX wing, illustrated in Figure 2.7, includes six individual trailing edge morphing modules distributed along the wingspan. As each morphing module can be actuated independently, allowing for local camber control across the span, adjacent modules are interconnected by an elastomeric skin material to ensure a continuous trailing edge. In addition, fast piezoelectric bi-morph actuators are placed at the tip of the morphing trailing edge for aeroelastic control.
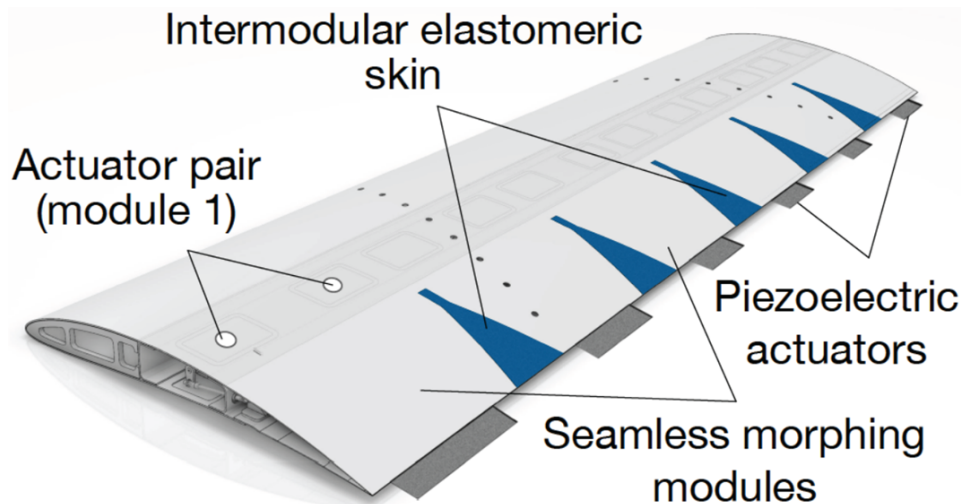
Figure 2.7: Detailed view of the SmartX wing. Adapted from *Mkhoyan et al.* [31].

The trailing edge morphing modules are based on the Translation Induced Camber (TRIC) morphing concept introduced by *Werter et al.* [32]. As illustrated in Figure 2.8, the trailing edge bottom skin is translated in chord-wise direction and partially in spanwise direction to match the target morphing shapes. The actuation system relies on two pairs of high performance servo actuators per module, and has a very compact design that allows reserving considerable space inside the wing for the installment of additional auxiliary systems.
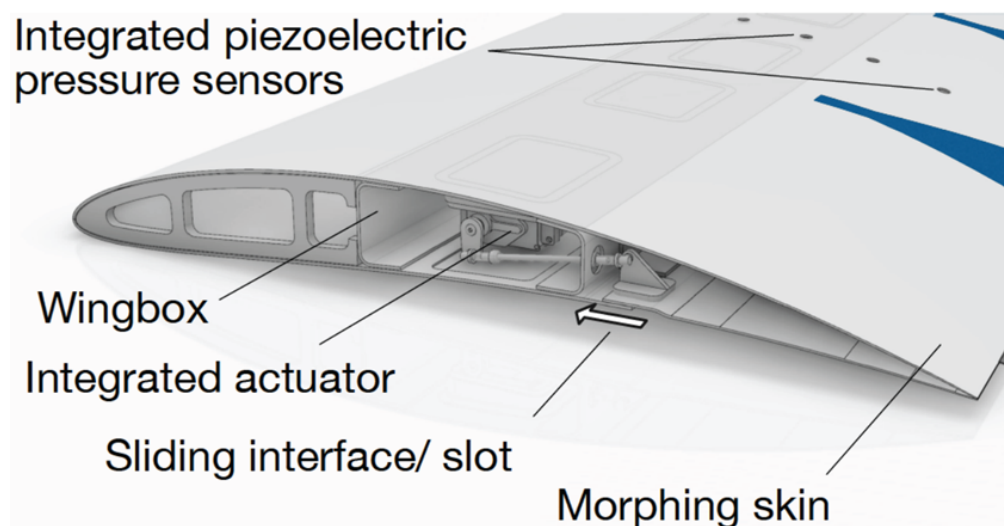
Figure 2.8: TRIC morphing module. Adapted from *Mkhoyan et al.* [31].

A wing demonstrator has been manufactured, and static and dynamic wind-tunnel tests have been conducted at the Open Jet Facility (OJF) at the Delft University of Technology.

2.4.4. The morphing droop nose

The development of morphing droop noses has received much attention during the past years. The German Aerospace Center (DLR) started investigating smart leading-edge devices in cooperation with Airbus in 2009. Since then, research on morphing droop nose devices has been performed under several European research projects, such as SADE (*Pantelakis et al.* [33]), SARITSU (*Kintscher et al.* [34]) and NOVEMOR (*Vasista et al.* [35]).

During the last years, DLR has been investigating a novel high-lift system (*Rudenko et al.* [36], *Vasista et al.* [37], *Vasista et al.* [38]), illustrated in Figure 2.9, for which a gapless morphing nose droop is fundamental to reach very high lift coefficients, in the range of 5-6. It comprises a trailing edge flap that deflects to 65°, air blown from a compressor, regulated by an active lip, and a large displacement morphing droop nose device capable of reaching 90° deflections.
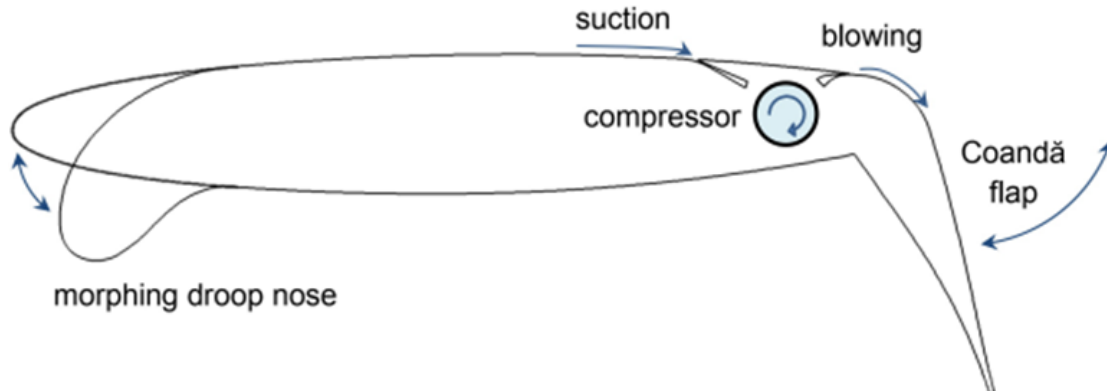
Figure 2.9: Novel high-lift device investigated by DLR with a large deflection morphing droop nose. Adapted from *Vasista et al.* [38].

A brief review on the workflow applied by researchers for the design of morphing droop nose devices is presented below. This workflow is divided into two general steps: (i) the definition of the target droop shapes as the result of a shape optimization process, and (ii) the design of a morphing structure that can match the target droop shapes.

Step 1: Shape optimization process

The first step consists in defining the morphed droop shapes that provide optimal aerodynamic performance at different flight conditions. These optimum shapes are defined through optimization processes based on aerodynamic CFD analyses.

At DLR, the droop target shapes for the morphing droop nose devices developed by *Vasista et al.* [39] and *Vasista et al.* [35] were solely determined based on aerodynamic performance, leading to the subsequent structural challenge of designing a morphing structure capable of adapting to such target shapes. On the other hand, at POLIMI, *De Gaspari et al.* [40] developed a morphing droop nose device whose target droop shapes were also optimized based on aerodynamic efficiency parameters, but, under structural skin constraints. A zero axial strain constraint is generally imposed to prevent the stretching or contraction of the skin material, leading to a bending-dominant response that can be further constrained by imposing a maximum bending stress or strain (*De Gaspari et al.* [41]). Including skin structural constraints in the shape optimization process simplifies the design of a morphing skin capable of adjusting to the target shapes, and, at the same time, contributes to limiting the actuation power required to deform the skin (*De Gaspari and Ricci* [42]).

Step 2: Design of the morphing structure

The subsequent step consists of designing a morphing structure capable of adapting to the target droop shapes. As active adaptive concepts, linear or torsional actuation inputs have been used in the past to deform the flexible skin of the leading-edge device, and two general approaches have been investigated for transferring these actuation inputs to the morphing skin: conventional kinematic mechanisms and compliant mechanisms.

Morphing droop nose devices based on conventional kinematic mechanisms have been developed at DLR (*Kintscher et al.* [34], *Rudenko et al.* [36], *Vasista et al.* [37]) and at the Delft University of Technology (*Sodja et al.* [43]). Figure 2.10 illustrates the morphing droop nose concept reported by DLR (*Vasista et al.* [37]) for the novel high-lift device presented in Figure 2.9. Kinematic ribs are placed along the wingspan at a given distance from each other and fulfil the function of supporting the skin under the external loads and drive the skin to the target droop position in response to a torsional actuation input.
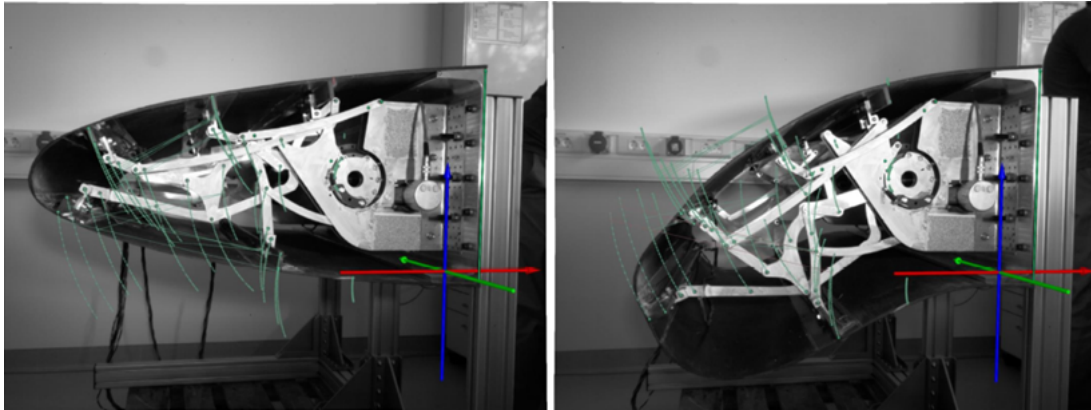
Figure 2.10: Photographs of the morphing droop nose demonstrator developed for DLR novel high-lift device. Adapted from *Vasista et al.* [38]

Morphing droop nose devices based on compliant mechanisms have been developed at DLR (*Vasista et al.* [39], *Vasista et al.* [35]) and POLIMI (*De Gaspari et al.* [42]) during the European research project NOVEMOR. The motivations for replacing conventional kinematic ribs by compliant mechanisms include the potential reduction of weight and the reduction of assembly complexities, time and costs (*Vasista et al.* [35]).

The morphing droop nose device designed at POLIMI by *De Gaspari et al.* [40] exploits compliant ribs to transfer the actuation forces to the flexible skin, and its design is based on a two-level optimization approach introduced by *De Gaspari and Ricci* [42]. In the first level, the target droop shapes are optimized under structural skin constraints. In the second level, the compliant mechanism is designed by using a topological optimization tool based on the Load Path Representation method and solved by a genetic algorithm.

The topological optimization tool provides a two-dimensional solution that includes the stiffness contribution of the skin. In Figure 2.11a, the two-dimensional topological solution obtained by *De Gaspari et al.* [40] for the morphing leading edge of a wind tunnel model is illustrated. Subsequently, this topological solution was post-processed to a three-dimensional final design, illustrated in Figure 2.11b, defining a 10mm thickness for the compliant ribs, adding stringers at the locations where the compliant ribs attach to the skin, and distributing 9 equally spaced compliant ribs along the 0.93 m length of the device. The compliant ribs are driven by linear displacements introduced through rods connected to a rotating shaft, as illustrated in Figure 2.12.

(a)   (b)
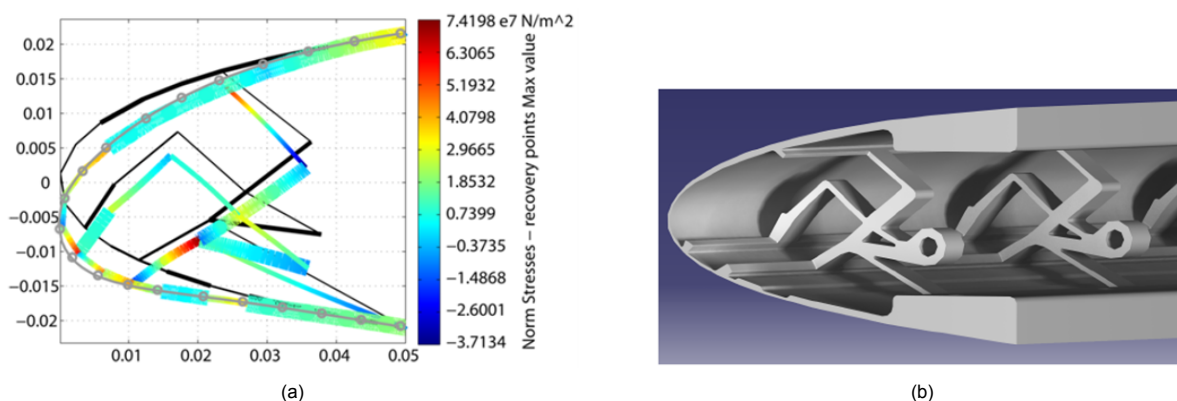
Figure 2.11: (a) Two-dimensional topological solution for the compliant mechanism. (b) CAD model of the leading-edge morphing device. Adapted from *De Gaspari et al.* [40].
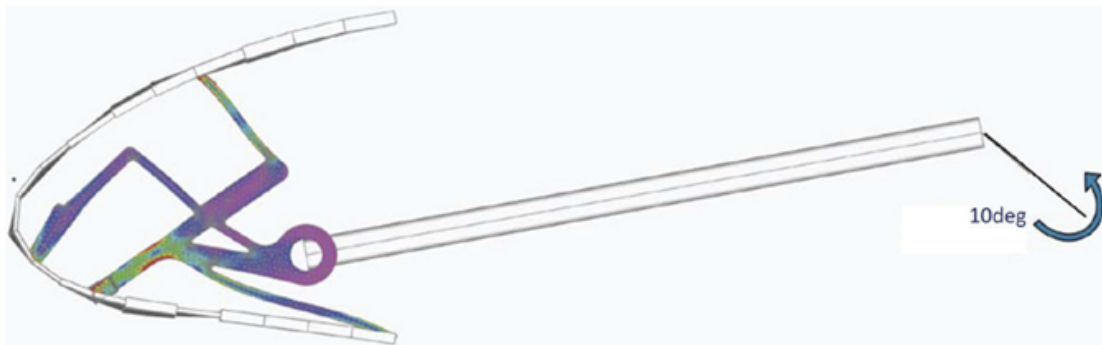
Figure 2.12: FEA result of the morphing leading edge device. Adapted from *Vasista et al.* [35].

Throughout the years, the design procedure based on the two-level approach (*De Gaspari and Ricci* [42]) has been further developed at POLIMI. In *De Gaspari* [44], the state-of-the-art design procedure consisting of a four-level optimization procedure is explained and applied to the design of a morphing droop nose.

2.5. Aeroelastic Adaptive Concepts for twist morphing

Even though wing twisting was applied by the Wright Brothers to enable roll control of their aircraft, this shape morphing solution was discarded for almost 80 years in favor of the traditional ailerons, as the required wing flexibility to twist the wing would lead to a weak structure not capable of withstanding high aircraft weights, and would cause aeroelastic instabilities at high flying-speeds (*Barbarino et al.* [1]). However, since the 1980s, there has been a growing interest in twist morphing solutions as advances in composite materials allowed many of the limitations to be overcome.

The twist morphing concept developed during the pioneer Active Flexible Wing (AFW) program in the 1980s relied on a flexible composite wing twisted by the external aerodynamic forces created by traditional leading and trailing edge control surfaces. Thus, the rolling moment to control the aircraft was created by the aeroelastic twist of the wing, but conventional control surfaces were needed to control this aeroelastic twist. Even though the aerodynamic inefficiency associated to discrete control surfaces was still present, the wing flexibility contributed to reducing the wing structural weight. Moreover, a rolling moment based on the twisting of the wing allowed the aircraft to operate at higher dynamic pressures without aileron reversal problems. This technology was later tested on a F/A-18 fighter aircraft during the Active Aeroelastic Wing (AAW) research program (*Pendleton et al.* [14]), proving the feasibility of the concept.

Later on, a new approach was developed, which became the most studied approach in the research to come. To control the aeroelastic twist, the internal structure of the wing is changed during flight, modifying its structural response to the aerodynamic loads. The objective is to affect two structural properties of great influence on the wing aeroelastic twist: the torsional stiffness and the shear centre location.

The torsional stiffness defines how much elastic twist a wing experiments in response to an applied torque. Thus, for a given torsional moment acting along the wing, adapting the torsional stiffness allows either amplifying (when decreased) or reducing (when increased) the elastic twists.

On the other hand, the cross-sectional shear centre location has a great influence on the torque acting at a wing cross-section. A main contributor to this torque is the torsional moment created by the offset between the lift force application point (aerodynamic centre) and the shear centre. This moment is usually nose-up, as the shear centre is usually located behind the aerodynamic centre. Therefore, when relocating the shear centre, the moment arm is affected, changing the magnitude of this moment contribution. When the shear centre is shifted forward during flight, the nose-up moment reduces causing an aeroelastic nose-down twist, while when the shear centre is shifted back, the moment increases causing an aeroelastic nose-up twist.

Twist morphing concepts that adapt the wing internal structure to control the aeroelastic twist will be classified into two groups, based on their strategy to change the wing internal structure. Concepts that rely on the movement of internal components are addressed in Section 2.5.1, while concepts that integrate components with selective stiffness are addressed in Section 2.5.2.

2.5.1. Strategy 1: Movable internal components

Many well-established approaches rely on the movement of internal components of the wing to change the structural response to the aerodynamic loads. Rotative spars and spars able to translate in chord-wise direction have been intensely studied due to their capability to change the torsional stiffness, bending stiffness (in case of rotative spars) and shear centre location along the wingspan.

Chen et al. [4] developed the variable stiffness spar (VSS) concept, which relies on the rotation of a spar to change the cross-sectional torsional stiffness, bending stiffness and shear centre location throughout the wingspan. Designed for the purpose of enhancing roll performance, leading and/or trailing edge control surfaces are still required to control the aeroelastic twist, but the aeroelastic twist can be further amplified by changing the torsional stiffness and the shear centre location. Moreover, the aeroelastic bending deflections can also be controlled, as the rotation of the spar also affects the bending stiffness of the wing.

To demonstrate the potential of the VSS, *Chen et al.* [4] applied the concept to a F/A-18 fighter air-craft, predicting via numerical analysis a roll rate increase of 6% - 22% depending on the flight condition. *Florance et al.* [5] also applied a morphing concept based on the VSS solution (i.e., with a rotative spar) to a F/A-18 fighter aircraft, but, in this case, wind tunnel tests were performed. Figure 2.13a illustrates the location of the steel VSS inside the wing (starting from the root, close to the trailing edge) and the leading and trailing edge control surfaces required to control the aeroelastic twist. Figure 2.13b shows the wind tunnel model used for the experiments. Measured changes in stiffnesses (bending and torsional) and in aeroelastic deformations (bending deflections and twist angles) when varying the orientation of the VSS proved the feasibility of the concept.

(a)   (b)
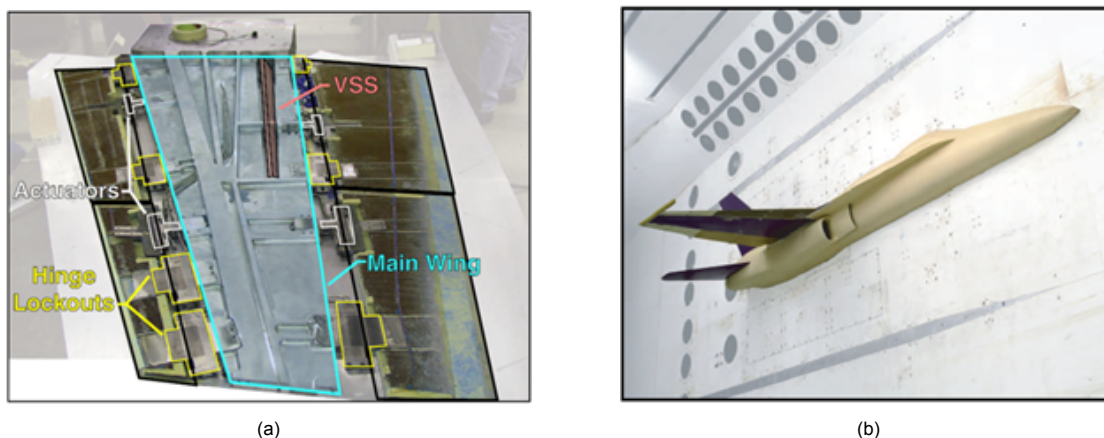
Figure 2.13: (a) Photo of the wing lower surface. (b) Photo of the wind tunnel model inside the wind tunnel. Adapted from *Florance et al.* [5].

Ajaj et al. [2] investigated the Adaptive Torsion Wing (ATW) concept, which involves the translation of the front and rear spar webs of a two-spar wingbox. Unlike the VSS solution, the translation of the spar webs does not affect the spanwise bending stiffness, so the concept does not allow for the control of the aeroelastic bending deformations.

As illustrated in Figure 2.14, the highest and lowest torsional stiffness configurations are those with the largest and smallest enclosed area, respectively. However, as both spar webs translate the same distances between these two configurations, the shear centre location does not change. To affect the shear centre location, the translation of the spar webs must not be symmetrical respect to a vertical axis passing through the initial shear centre.

Ajaj et al. [2] studied the capability of the morphing concept to replace conventional ailerons. To demonstrate the potential of the ATW for roll control, the concept was applied to a MALE UAV, and it was analyzed if the same rolling moment created by an aileron deflection of 5° at cruising flight conditions could be generated by adjusting the spar webs locations. Moreover, to compare the roll performance to that of conventional ailerons, the rolling efficiency factor (ratio of rolling moment to yawing moment) was analyzed. Based on numerical calculations, *Ajaj et al.* [2] concluded that "the ATW provides a more useful rolling device as it can minimize the associated adverse yawing moment by up to 35%, which would result in much lower drag overall". It should be noted that the analysis of the concept was entirely theoretical, as no prototype was manufactured and tested.
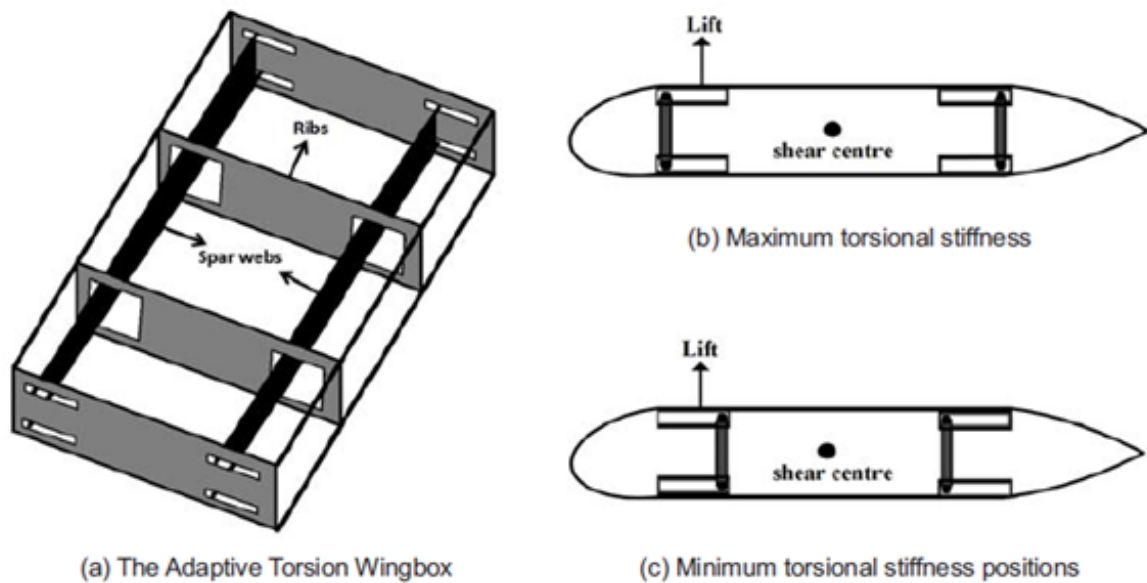
Figure 2.14: Conceptual sketch of the Adaptive Torsion Wing concept. Adapted from *Ajaj et al.* [2]

To conclude this section, some remarks are given with respect to the actuation systems considered for moving the internal structural components of the wing. Specifically, the actuation systems need to either rotate spars through a 90° angle or translate spars in chord-wise direction, for which all twist morphing concepts developed along this line of research have relied on conventional actuators. For rotative spars, electric servo-actuators have been used (*Chen et al.* [4], *Cooper* [13]), while for the translation of a spar in horizontal direction, hydraulic actuators (*Ajaj et al.* [2]), pneumatic actuators (*Cooper* [13]) and worm-drives driven by electric motors (*Cooper* [13]) have been proposed. In terms of actuation, the rotation of spars has shown more promise for roll control than the translation of spars, due to the higher actuation bandwidth of electric servo-actuators. *Cooper* [3] achieved the rotation of a spar from the minimum to maximum stiffness configuration in 0.5 seconds using electric servo-actuators, while it took 10 seconds to translate a spar from the minimum to maximum stiffness configuration using a worm-drive driven by an electric motor.

The main challenges identified for the implementation of morphing concepts that move internal structural components to control the aeroelastic twist are: the weight of the actuation systems, the actuation bandwidth, the transfer of the aerodynamic loads to the moving spars, and, for those aircrafts that carry fuel inside the wingbox (like commercial aircrafts), the containment of the fuel inside a wingbox with moving spars.

2.5.2. Strategy 2: Selective stiffness components

During the last years, instead of moving structural components, researchers have focused on the integration of structural components with selective stiffness to change the overall structural response of the wing. The main advantage of this approach, relative to the previous one, is that it does not need the heavy mechanisms required to move structural components, which also suffer from wear and need to be assembled and lubricated (*Raither et al.* [6]). However, it also creates the structural challenge of designing components with selective stiffness. In *Kuder et al.* [45], the authors provide a review of the existing approaches to achieve stiffness variability, from which, the use of smart materials and the buckling instabilities of slender structural elements have been explored in different twist morphing concepts. .

Selective stiffness by exploiting smart materials:

One strategy to design components with selective stiffness relies on the use of smart materials capable of changing their elastic properties in a control fashion when excited under an external stimulus.

Along this line of research, *Raither et al.* [6] introduced the concept of a thin-walled rectangular cross-section beam capable of adapting its torsional stiffness and shear centre location. This beam has a web made of a smart material capable of varying its shear modulus, for which thermo-responsive polymers and electro-bonded laminates are proposed. When applying this adaptive-stiffness capability to the rear web of the beam, as illustrated in Figure 2.15, the shear centre shifts forward when reducing the web shear stiffness, and shifts back when increasing the web shear stiffness. As was explained before, when applying a bending load at an offset from the shear centre, a torsional moment is created, inducing a twist on the beam. Therefore, this bending-twisting coupling can be varied by the relocation of the shear centre, providing authority over the twist angle of the beam. Moreover, affecting the web shear stiffness also provides control over the torsional stiffness of the beam, which can also be exploited to control the twisting response.
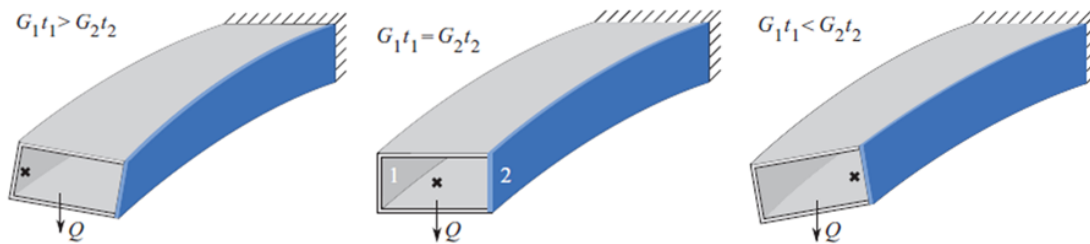
Figure 2.15: Beam with a smart web capable of adapting its torsional stiffness and shear centre location. Adapted from *Raither et al.* [6].

The values of torsional stiffness and shear centre location that can be selected depend on the cross-sectional geometry and the properties of the materials involved. In *Raither et al.* [6], the concept is applied to an experimental beam with the geometrical dimensions specified in Figure 2.16, a base aluminum structure and a variable-stiffness web made of hard polyvinyl chloride (PVC). The shear modulus of this thermoplastic polymer can be varied within a two orders of magnitude range, $10^9 - 10^7$ GPa , when affecting the material temperature in the range of its glass-transition temperature, between 60-100°C.
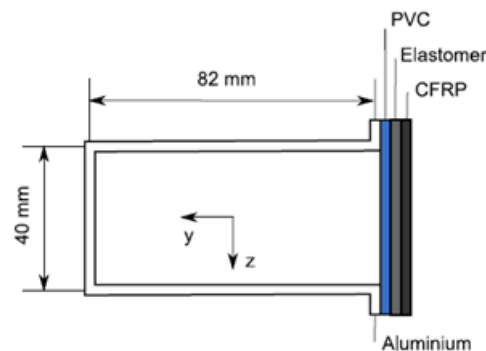
Figure 2.16: Cross-section of experimental beam with a thermo-responsive active rear web. Adapted from *Raither et al.* [6].

As can be observed in Figure 2.16, the PVC web temperature is controlled by heating a carbon fibre reinforced polymer (CFRP) bonded to the PVC with a very compliant elastomeric adhesive. This elastomeric thermal interface conducts the thermal energy to the PVC while preventing the transfer of structural loads to the CFRP. The CFRP is heated by running an electrical current through its conductive carbon fibres (Joule heating) and the temperature of the CFRP is monitored with thermocouples.

Raither et al. [7] implemented this concept to control the aeroelastic twist of a composite wing, whose cross-section is illustrated in Figure 2.17. Three adaptive interfaces made of PVC material are introduced in the structure to affect the torsional stiffness and shear centre location. One of these PVC interfaces is located between overlaps of the front spar plates, with the objective of reducing the wingbox torsional stiffness and shift the shear centre backward (inducing a nose-up twist). However, even when "deactivating" the transfer of shear load through the front spar, the wing cross-section would still remain close, with a relatively high torsional stiffness. For this reason, two additional adaptive interfaces are introduced, at the leading and trailing edge sections, to be able to "open" the wing cross-section and maximize the reduction of torsional stiffness. A close-up on the front spar adaptive interface of the manufactured demonstrator is presented in Figure 2.18.
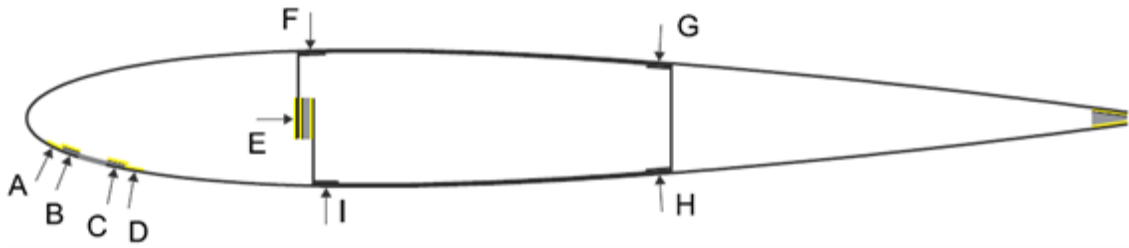
Figure 2.17: Wing cross-section illustrating the three adaptive interfaces. Adapted from *Raither et al.* [7].

Figure 2.18: Adaptive interface in the front spar of the experimental wing. Adapted from *Raither et al.* [7].

Raither et al. [7] developed a finite element model of the entire wing to predict the changes in shear centre location and torsional stiffness that could be created by activating different combinations of adaptive interfaces. Furthermore, this structural model was then coupled to an aerodynamic model to predict the aeroelastic deformations at different flight conditions and actuation conditions. Based on these aeroelastic predictions, roll moment coefficients were on the same order as those of conventional ailerons.

Even though *Raither et al.* [7] did not calculate the overall drag, lower drags than conventional ailerons are to be expected due to the continuous changes of wing geometry. In addition, potential weight-savings could be achieved by replacing an aileron system with these adaptive interfaces. On the other hand, in terms of the actuation bandwidth, *Raither et al.* [7] recognize that a thermal solution has an inherent low response that might not fulfill the activation speed requirements for roll control, so electro—bonded laminates (of higher activation speed and lower energy consumption) are suggested as a more promising solution for future research.

Selective stiffness by exploiting buckling instabilities:

Another strategy to design components with selective stiffness is more recent and relies on the elastic buckling of slender structural elements. Research devoted to the study of wing twisting by exploiting buckling instabilities is very limited. The most relevant work comprises a Passive Aeroelastic Morphing Concept (*Runkel et al.* [8], *Runkel* [9] and *Runkel et al.* [10]), and an investigation conducted by *Zhang and Bisagni* [11] on different buckling-driven mechanisms with potential for wing twisting.

The approach was first introduced by *Runkel et al.* [8], and it is based on the concept developed by *Raither et al.*[6] of a thin-walled rectangular cross-section beam capable of adjusting its torsional stiffness and shear centre location by controlling the shear stiffness of the rear web (illustrated in Figure 2.16). However, instead of using a smart material capable of varying its shear modulus, *Runkel et al.* [8] propose to exploit the reduction in effective shear stiffness cause by the shear buckling of a slender web, as illustrated in Figure 2.19. The reduction in the rear web's effective shear stiffness shifts the shear centre forward and reduces the torsional stiffness. Then, for a downward transverse force applied at the initial shear centre location ($S.C^0$ in Figure 2.19), the shifting forward of the shear centre induces a clock-wise buckling-induced twist.
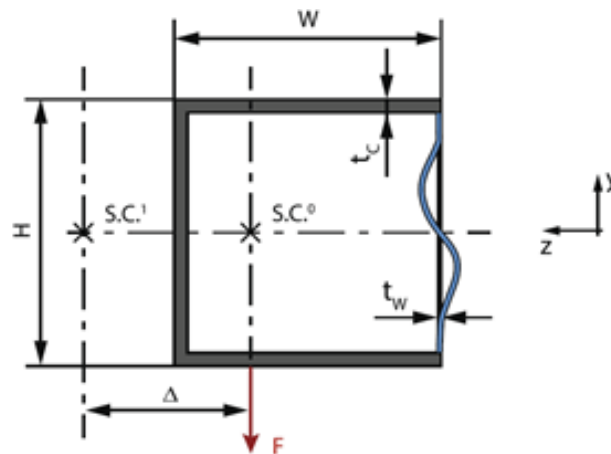
Figure 2.19: Shear centre for the unbuckled configuration $S.C^0$ shifts forward to $S.C^1$ after the shear buckling of the rear web. Adapted from *Runkel et al.* [8].

Runkel et al. [8] applied the concept to a composite thin-walled rectangular beam with a 50x50 mm cross-section. A unidirectional slender rear web made from unidirectional carbon plies was integrated into the structure. Based on FEA, the buckling-induced twists created by a bending load applied at the initial shear centre location ($S.C^0$ in Figure 2.19) were calculated considering different fibre angles for the unidirectional slender rear web. The maximum specific buckling-induced twists (i.e., [°/m]) before the material failure of the slender web were predicted to be within the range of $1.2°/m \leq \theta \leq 2.1°/m$ depending on the web's fibre orientation, proving the potential of the concept for wing twisting applications. Moreover, an experimental demonstrator was manufactured and tested, allowing for the validation of the FEA results.

Later on, *Runkel et al.* [10] applied the approach to induce an aeroelastic twist in a composite wing, as a Passive Aeroelastic Adaptive Concept. Illustrated in Figure 2.20, the wing has a two-spar wingbox with a slender rear spar web designed to buckle at a specific level of aerodynamic load. Once the rear spar web buckles, its effective shear stiffness reduces, shifting the shear centre forward and decreasing the torsional stiffness. As the shear centre is located behind the aerodynamic centre, shifting forward the shear centre reduces the nose-up torsional moment created by the offset between the lift force and the shear centre, inducing a nose-down aeroelastic twist. Therefore, the effect of shifting forward the shear centre can also be represented as the introduction of a nose-down buckling-induced moment M_{BIM} that creates a nose-down aeroelastic twist, as illustrated in Figure 2.20.
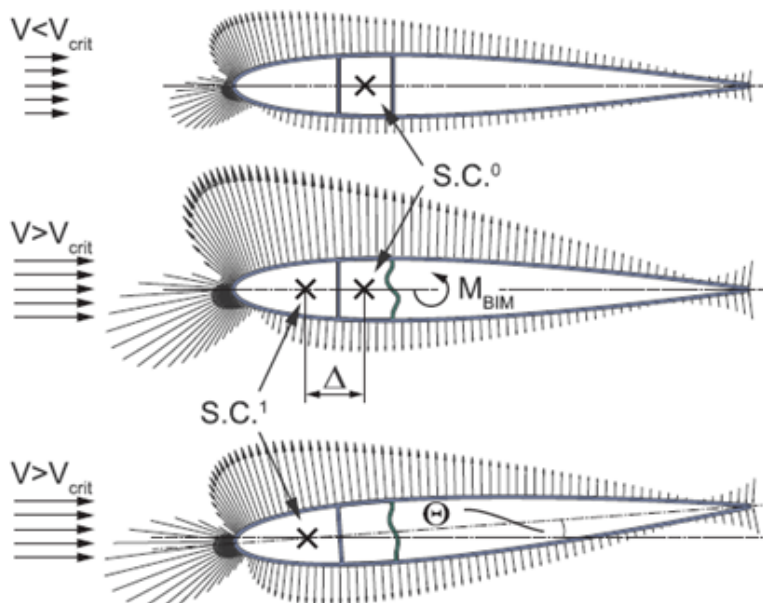
Figure 2.20: Buckling-induced aeroelastic twist caused by the shear centre relocation. Adapted from *Runkel et al.* [10].

To create a wing whose torsional stiffness is dominated by the adaptive wingbox, the leading and trailing edge sections of the wing are physically opened. Such openings are made in the lower surface of the wing and extend over the entire wingspan, through wing skin and ribs, as illustrated in Figure 2.21. However, as closed airfoils might be required to increase aerodynamic efficiency, *Runkel et al.* [10] envision closing these gaps with electro-bonded laminates (of variable-stiffness capability) to selectively control the torsional compliance of the front and rear cells.
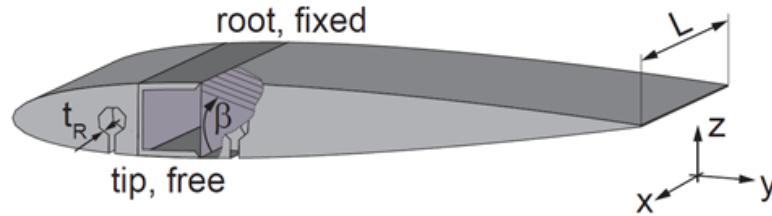
Figure 2.21: Wing structure with a slender rear spar web designed to buckle. An internal cut illustrates the fiber angle β of the unidirectional rear spar web. Adapted from *Runkel et al.* [10].

Runkel et al. [10] coupled a structural finite element model of the wing with an aerodynamic model to predict the buckling-induced aeroelastic twists created at different flight conditions. In Figure 2.22, the buckling-induced twist at the tip of the wing $\Delta\theta$ is represented as a function of the airflow velocity and the slender spar web's fibre angle β and thickness t_G. Firstly, it can be observed that as the morphing twist is created by the external aerodynamic loads, it increases with the airflow velocity. Secondly, for a web thickness of 0.15mm, a maximum buckling-induced twist of $\Delta\theta=2.5°$ is predicted at an airflow velocity of 60 m/s, while for a web thickness of 0.35 mm, the maximum buckling-induced twist at an airflow velocity of 60 m/s reduces to $\Delta\theta=0.5°$, showing that the morphing capabilities reduce with the slender spar web's thickness.
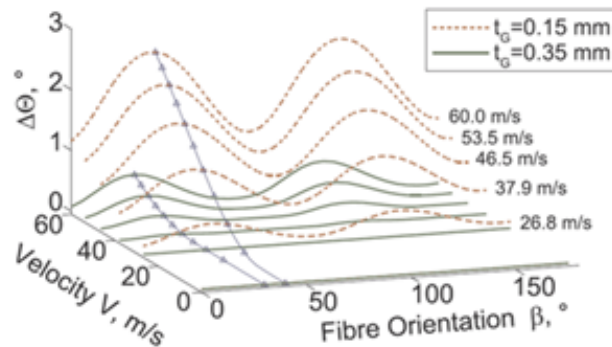
Figure 2.22: Buckling-induced twist $\Delta\theta$ at the tip of the wing, as a function of airflow velocity and the slender spar web fiber angle β and thickness t_G. Adapted from *Runkel et al.* [10].

Runkel et al. [10] designed the concept for load alleviation purposes. The passive nose-down aeroelastic twist triggered at a specific level of aerodynamic load is exploited to diminish the critical lifting forces, generated by gusts or demanding maneuvers, that cause the buckling of the rear spar web. Consequently, critical loading for design can be reduced, leading to lighter wing structures.

On the other hand, *Zhang and Bisagni* [11] also exploited the buckling of a slender rear spar web integrated into a two-spar wingbox to realize twist morphing. However, the novelty of their work is that they propose to actively control variable constraints acting on the spar web's buckling deformations, allowing the selection of multiple stable states for the same external loading.

In particular, *Zhang and Bisagni* [11] analyzed the effects that different types of buckling-driven constraints have on the buckling load and post-buckling stiffness of a representative composite wingbox station (i.e., between two ribs) when loaded axially, in shear or in torsion. To limit the research space, three buckling-driven constraints, illustrated in Figure 2.23, were investigated, referred to as the point constraint (a point of the slender spar web is restricted for transverse displacement), the area constraint (an area of the slender spar web is restricted for transverse displacement) and the maximum displacement constraint. In the case of the maximum displacement constraint, the slender spar web is located between two parallel rigid surfaces. Then, by modifying the gaps between the spar web and these confining rigid surfaces, referred to as confining gaps, the slender spar web's maximum out-of-plane buckling deformations can be adjusted.

(a)   (b)

(c)
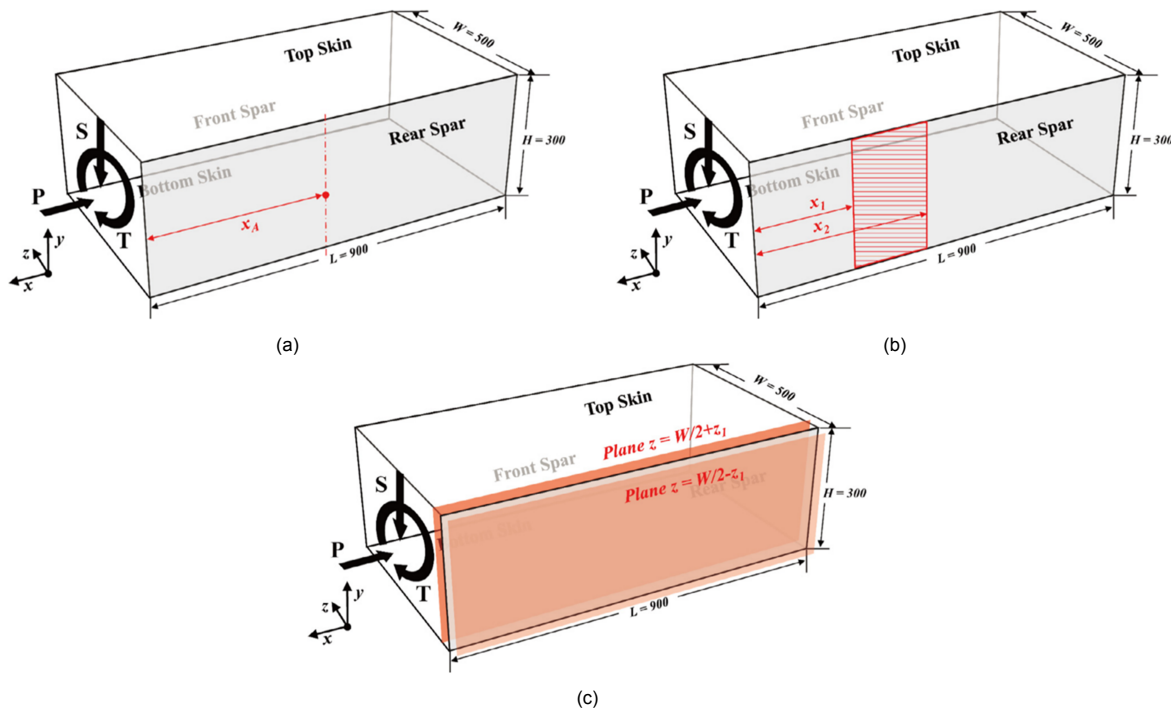
Figure 2.23: Illustrations of the buckling-driven constraints investigated by *Zhang and Bisagni* [11]: (a) point constraint, (b) area constraint and (c) maximum displacement constraint. Adapted from *Zhang and Bisagni* [11].

For the maximum displacement constraint, two different constraining conditions were studied, corresponding to the symmetric confining gaps of ± 1.5 mm and ± 2 mm. The numerical predictions for the tip twist responses to an external torque are presented in Figure 2.24. Once the slender spar web's buckling deformations come into contact with the confining rigid surfaces (condition denoted with horizontal dash-dotted lines in Figure 2.24), the torsional stiffness increases relative to that of a wingbox with an unconstrained rear spar web (baseline configuration), computing an increase of 18.4% for a gap of ± 1.5mm and an increase of 9.6% for a gap of ± 2 mm.
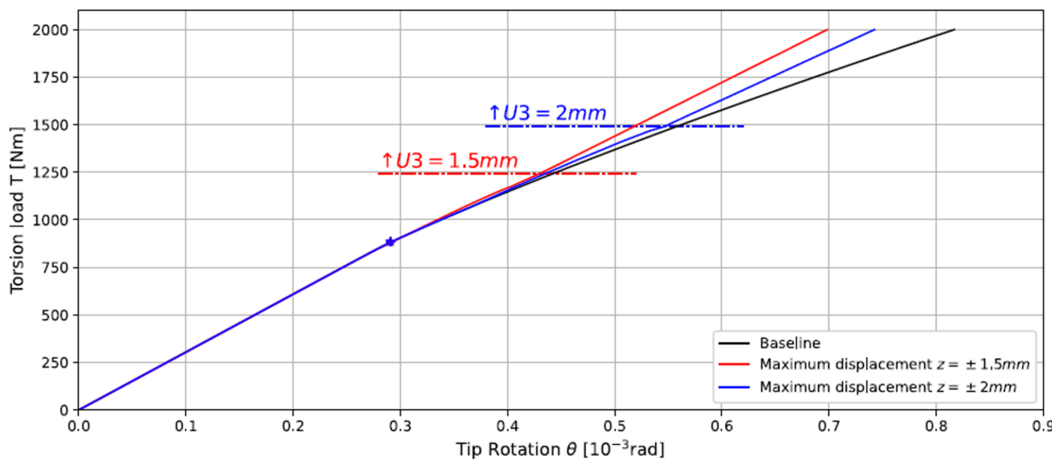
Figure 2.24: Tip twist response to an external torsional load for different maximum displacement constraints. Adapted from *Zhang* [46].

In order to develop a twist morphing concept based on these buckling-driven constraints, further investigation is required. Due to the novelty of the approach (the pioneering and only work corresponds to *Zhang and Bisagni* [11]), many research gaps still remain to properly understand its capabilities and limitations. Furthermore, a morphing wing concept based on these buckling-driven mechanisms has yet to be defined. Besides an application for load alleviation purposes, as investigated by *Runkel et al.* [10], the buckling mechanisms proposed by *Zhang and Bisagni* [11] could potentially be integrated into a morphing wing to provide roll control, as different controllable aeroelastic twists could be induced for the same aerodynamic load by adjusting the positions of the buckling-driven constraints.

2.6. Post-buckled elements under bilateral constraints

As previously mentioned, a state-of-the-art strategy for wing twisting consists in adjusting the torsional stiffness and shear center location of a wing by controlling variable constraints acting on the buckling deformations of a slender spar web integrated into the wing structure (*Zhang and Bisagni* [11]). Therefore, for the development of a wing twist morphing concept that exploits this strategy, research devoted to the study of post-buckled slender elements under bilateral constraints becomes relevant. This section presents a review on the research devoted to the study of this topic.

The post-buckling of plates under bilateral constraints has not been an active research topic during the last years. The most relevant work corresponds to *Roman et al.* [47] and *Chai* [48], and both studies analyze post-buckled isotropic plates under pure compressive displacements and bilaterally constrained by rigid walls. Therefore, there is a research gap in the study of bilaterally constrained post-buckled composite plates under shear loading, which represents the expected loading condition in a wing spar web. *Zhang and Bisagni* [11] performed a numerical investigation on how the structural response of a wingbox station is affected when constraining a post-buckled composite spar web by different configurations of bilateral constraints (illustrated in Figure 2.23). However, these predictions still need experimental validation, and the influence of other design parameters on the post-buckling response (e.g., plate aspect ratio, thickness, lay-up and deformability of the constraints) still need to be investigated.

On the other hand, the structural response of bilaterally constrained post-buckled beam elements under axial loading has been a very active research topic during the last years. The problem statement usually corresponds to a clamped-clamped beam, laterally constrained by a wall placed adjacent to the beam and a second wall placed at a prescribed distance from the beam, as illustrated in Figure 2.25a. Bilaterally constrained post-buckled beams are investigated due to the possibility to trigger snap-through transitions between different buckling modes in response to quasi-static changes in loading. For example, a snap-through transition from the 1st buckling mode to the third buckling mode is illustrated in Figure 2.25b.

(a)   (b)
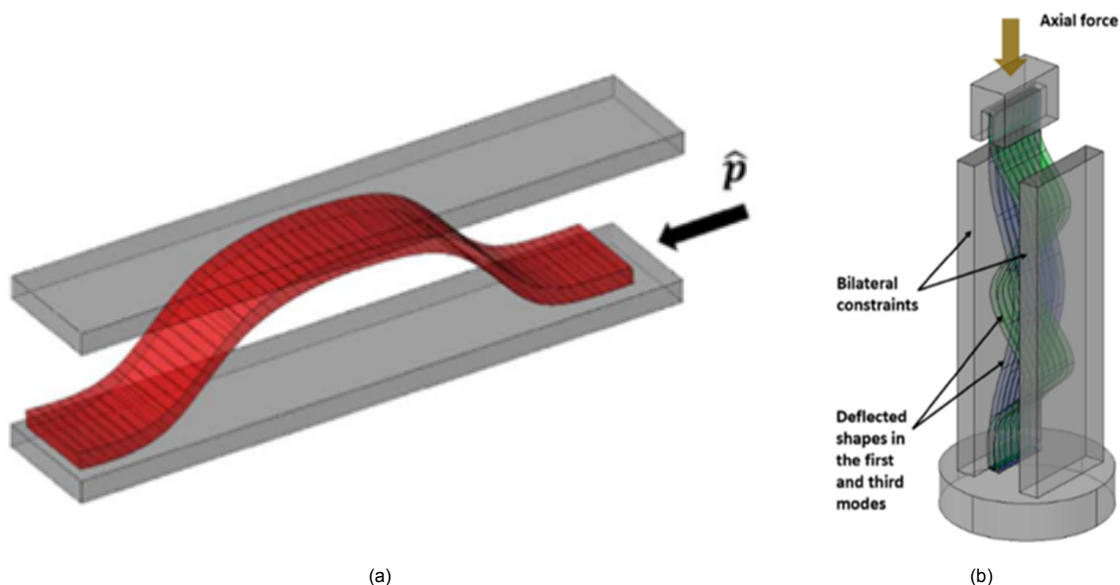
Figure 2.25: (a) Schematic representation of the bilaterally constrained beam. Adapted from *Jiao et al.* [49]. (b) Representation of the snap-through transition between the first and third buckling mode. Adapted from *Jiao et al.* [50].

During these snap-through events between different buckling modes, part of the accumulated strain energy stored in the deflected beam is released as kinetic energy, leading to localized high-acceleration motions along the beam. In 2014, *Lajnef et al.* [51] introduced a new energy harvesting concept that exploits these high-rate motions to excite a piezoelectric vibrator, converting part of the released kinetic energy in electrical power. Most research on the post-buckling behavior of bilaterally constrained beams has been devoted to the development of this energy harvesting concept. However, other authors have also motivated their research based on medical procedures, such as endoscopic examinations, or on the effect of delamination in composite laminates (e.g., *Katz et al.* [52] and *Chai* [53]).

2.6.1. The energy harvest solution

The energy harvest solution proposed by *Lajnef et al.* [51] consists in attaching a piezoelectric vibrator to the location along a beam that experiments the largest displacement during a snap-through event. In Figure 2.26a, the installation of a piezoelectric energy harvester in a cantilever configuration is illustrated (*Jiao et al.* [54]). Made from a piezoelectric polyvinylidene fluoride (PVDF) element with a mass at the tip, a snap-through excitation causes the system to oscillate. Then, the high deformations of the vibrating piezoelectric cantilever beam are converted to electric power and stored in a capacitor bank. This concept has been envisioned to power wireless sensors used for structural health monitoring, without the limitations of a battery lifetime. The potential implementation of the concept is illustrated in Figure 2.26b, for which the bilaterally constrained beam is enclosed in a capsule embedded in a structural component. Then, the snap-through events between buckling modes are triggered by the quasi-static changes in axial loading induced by the service deformations of the structural component.
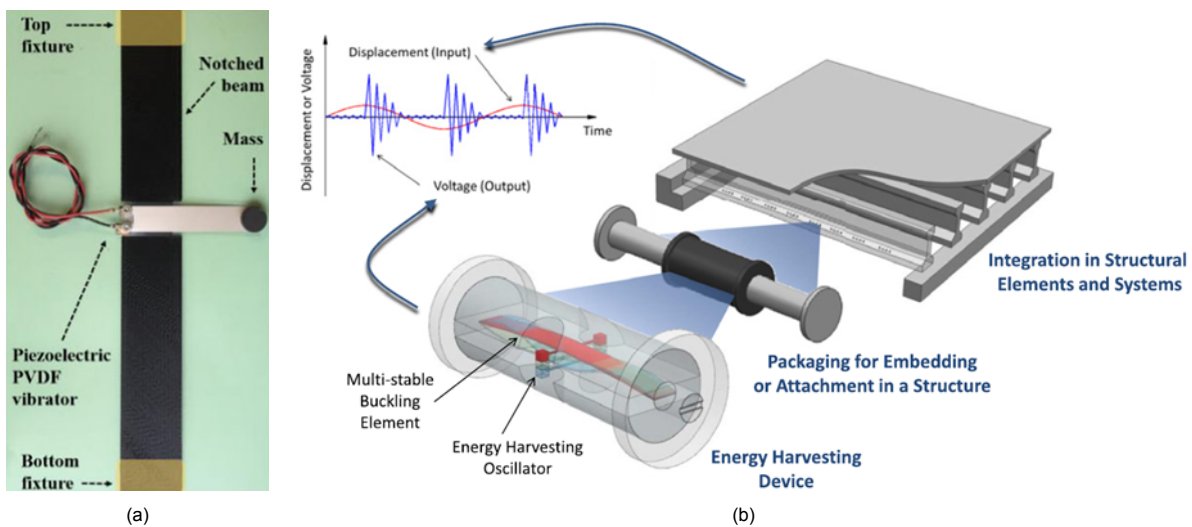
Figure 2.26: (a) Piezoelectric energy harvester attached to the slender beam. Adapted from *Jiao et al.* [54]. (b) Potential implementation of the energy harvesting concept for structural health monitoring. Adapted from *Lajnef et al.* [51].

In 2020, *Jiao et al.* [55] proposed a new concept, illustrated in Figure 2.27, that implements a similar energy harvesting strategy but at a nanoscale. Envisioned to harvest the electrical energy required to power nano-electrical-devices used in nanocrafts, the changes in axial load required to trigger the snapping events would originate from inertial forces, induced by accelerations or decelerations (e.g., due to changes in gravity while approaching other planets).
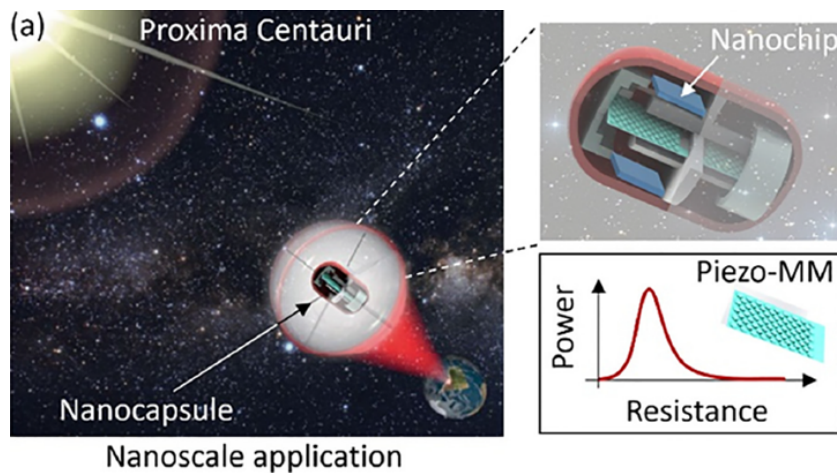
Figure 2.27: Potential nanoscale application of the energy harvesting concept. Adapted from *Jiao et al.* [55].

2.6.2. Tailoring of the post-buckling response

Two aspects are of great importance to maximize the levels of electrical energy that can be harvested by implementing this energy harvest solution. Firstly, the piezoelectric beam must be attached to the point of the beam that travels the most during each snap-through event, referred to in literature as the snap-through location. This represents a challenge, as the snap-through location may not occur at the same location for different buckling modes transitions. Secondly, the spacing between the critical loads at which the buckling mode transitions occur has to be tailored to an optimal spacing condition to maximize the harvested electric power.

Since *Lajnef et al.* [51] introduced the new energy harvesting strategy, much research has been done on the tailoring of the beam post-buckling response, in particular with regard to the snap-through location and the spacing between critical loads. Three different strategies have been investigated: (i) assembling multiple uniform beams in parallel configuration, (ii) affecting the geometry of non-uniform cross-section beams, i.e., non-prismatic beams, and (iii) affecting the deformability of the bilateral walls.

Approach 1: Assembling multiple uniform beams in parallel configuration

Borchani et al. [56] proposed to assemble multiple bilaterally constrained uniform beams of different dimensions and/or materials in parallel configuration, as illustrated in Figure 2.28a. This allows increasing the number of critical snap-through events, but, more importantly, the spacing between them can be tailored as they correspond to the buckling mode transition of different beams. For example, Figure 2.28b illustrates the force-displacement response of an assembly of 3 uniform beams, whose geometries were tailored to achieve equally spaced mode transitions every 0.25 mm axial displacements.

(a)	(b)
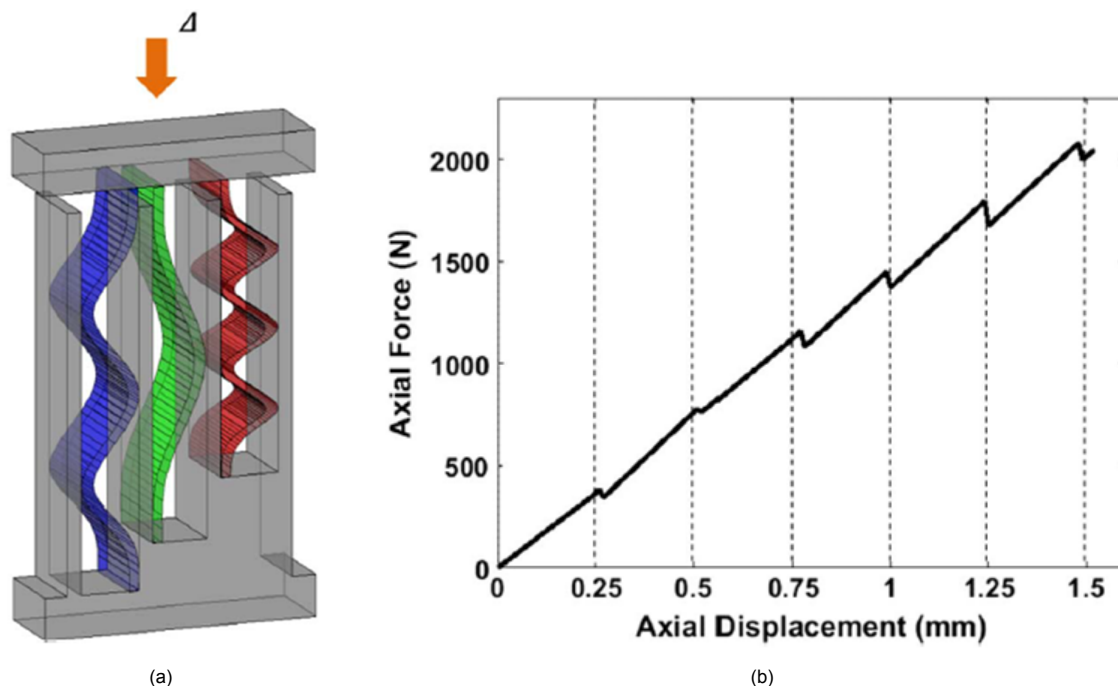
Figure 2.28: (a) Assembly of multiple bilaterally constrained uniform beams in parallel configuration. (b) Force-displacement response of an assembly of 3 uniform beams tailored to achieve snap-through events every 0.25 mm axial displacements. Adapted from *Borchani et al.* [56].

Approach 2: : Affecting the geometry of non-prismatic beams

An alternative method for tailoring the spacing between snap-through events consists in adjusting the geometry of a non-prismatic beams, i.e., of non-uniform cross-section, which was investigated by *Jiao et al.* [57] and *Jiao et al.* [54]. Through this method, voluminous devices such as the one illustrated in Figure 2.28a can be avoided. Figure 2.29b illustrates the spacing between snap-through events for a notched beam geometry similar to that represented in Figure 2.29a, which was tailored by *Jiao et al.* [54] to have the same spacing between different snap-through events.

<div align="center">(a)   (b)</div>
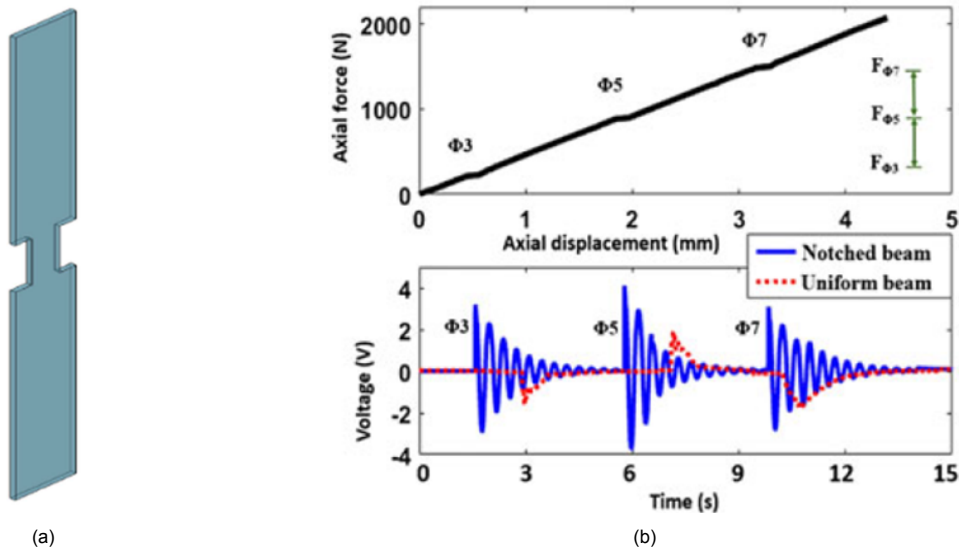
Figure 2.29: (a) Representation of a notched beam geometry. Adapted from *Jiao et al.* [50]. (b) Force-displacement response of a tailored beam with a notched geometry. Adapted from *Jiao et al.* [54].

Furthermore, *Jiao et al.* [50] proved that affecting the geometry of a non-prismatic beam also allows tailoring the snap-through locations. Figure 2.30 illustrates the buckling mode transitions of a tailored notched beam for which the snap-through locations are approximately at the same position for different buckling mode transitions.
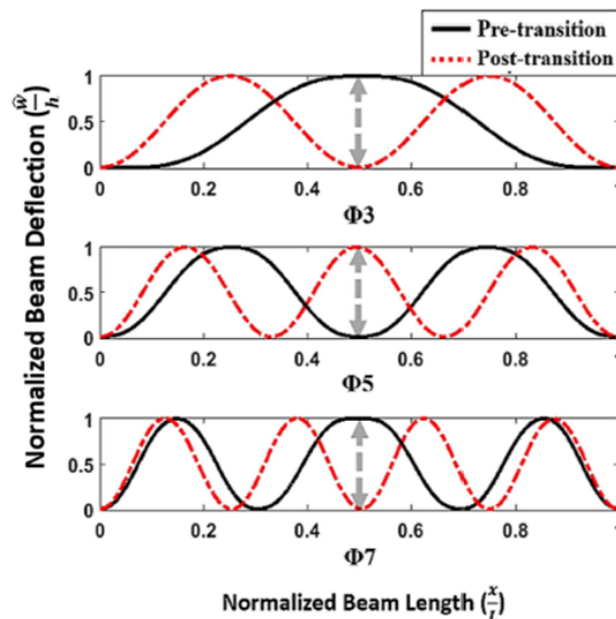
Figure 2.30: Snap-through locations for a tailored beam with a notched geometry. Adapted from *Jiao et al.* [50].

Approach 3: Affecting the deformability of the bilateral walls

Even though most studies on the post-buckling response of bilaterally constrained post-buckled beams consider rigid walls, deformable walls have also been investigated by *Jiao et al.* [58], *Jiao et al.* [59] and *Katz and Givli* [52]. When accounting for the deformability of the confining walls, three general types of constraints have been studied: rigid and fixed walls, referred to as regular constraints, rigid walls capable of moving against a linear spring, referred to as movably constraints or springy walls, and flexible and fixed walls, referred to as flexible constraints. When studying the effects that these constraints have on the response, the wall adjacent to the beam is always considered regular (rigid and fixed), while the wall that is apart from the beam is changed between a regular, movably or flexible condition, as illustrated in Figure 2.31.
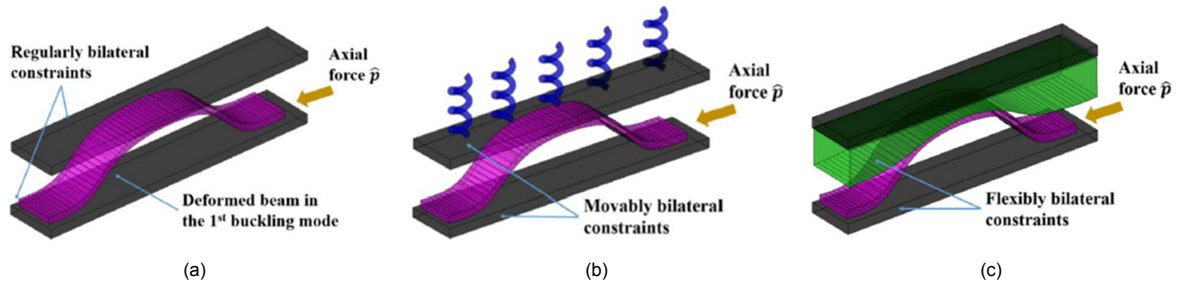
Figure 2.31: Type of lateral constraints investigated in literature: (a) regular constraints, (b) movably constraints and (c) flexible constraints. Adapted from *Jiao et al.* [59].

The implementation of a springy or flexible wall causes a "softening" of the force-displacement response in comparison to a regular wall. This is illustrated in Figure 2.32, where the predictions obtained by *Jiao et al.* [59] for the force-displacement response of a microscopic beam under regular and flexible constraints are compared to each other. The "softening" effect of the flexible walls is illustrated by a reduction in the beam's stiffness with the axial displacement, while the stiffness of the beam bilaterally constrained by regular walls stays practically unchanged.
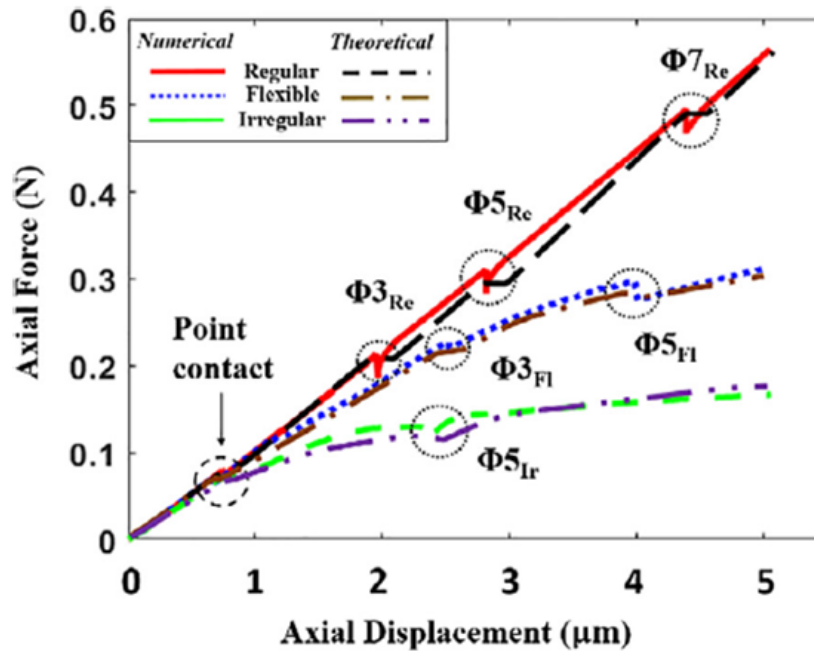
Figure 2.32: Comparison of theoretical and numerical predictions for the force-displacement response of a beam under regular constraints and flexible constraints. Adapted from *Jiao et al.* [59].

<div align="right">

3

</div>

Research Questions and Objective

3.1. Research Questions

In recent years, different wing morphing concepts have been investigated that employ the buckling instability of a slender spar web to realize twist morphing. The general objective is to exploit the buckling-induced reductions in the spar web's effective shear stiffness to adjust the torsional stiffness and/or the shear centre location along the wing. In this way, the twisting response of the wing to the aerodynamic loads can be changed.

Even though the strategy has already been explored in different twist morphing concepts, many research gaps still remain due to the novelty of the approach. Based on the analysis of the literature presented in the previous chapter, the research question that will be explored throughout this thesis is established:

"How does the structural design of a representative wing structure influence the morphing twists that can be created under the action of an external quasi-static torque by controlling the out-of-plane buckling deformations of slender spar webs integrated into the structure?"

The research question is then split into the following research sub-questions:

- Are the twist morphing capabilities dependent on the cross-sectional size of the wing?

- Are the twist morphing capabilities affected by the geometrical imperfections of the slender spar webs?

- How are the twist morphing capabilities affected by the material assigned to the slender spar webs?

- What type of adaptive constraints acting on the spar webs' out-of-plane buckling deformations allow for an effective control over the spar webs' effective shear stiffness?

- How does the integration into the wing structure of the external devices required to implement the adaptive constraints acting on the slender spar webs' out-of-plane buckling deformations affect the twist morphing capabilities?

3.2. Research Objective

The research objective of this thesis is to design a representative wing structure whose twisting response to an external quasi-static torque can be selectively adjusted by controlling the out-of-plane buckling deformations of slender spar webs integrated into the structure.

Due to the complexity of the design problem, the overall design process is structured into a multi-level process of increased complexity. In the first level, the morphing structure is simplified to a wing box with slender spar webs. With the objective of maximizing the morphing twists that can be achieved under the action of an external quasi-static torque, the wing box design space is explored in terms of its cross-sectional dimensions and the material assigned to the slender spar webs. In the second level, the morphing structure is expanded to include both the wing box and the external devices required to implement the adaptive constraints acting on the slender spar webs' out-of-plane buckling deformations. At this level, the objective is to design adaptive constraining devices that maximize the twist morphing capabilities, for which the influence of the constraining devices over the twisting response and their effectiveness in restraining the slender spar webs' buckling deformations become the main concerns.

<div style="text-align: right; font-size: 3em;">4</div>

Wing box under torsion

In this chapter, the morphing structure is simplified to a wing box with slender spar webs, assuming that the torsional stiffness of the morphing wing is dominated by the wing box. The wing box structural response to an external quasi-static torque is investigated under different buckling constraints, and the methodology for evaluating the twist morphing capabilities is presented.

4.1. Wing box structural model

The wing box under investigation has a uniform rectangular cross-section consisting of four panels: the front and rear spar webs and the top and bottom skins. As illustrated in Figure 4.1, both the front and rear spar webs are slender panels designed to reach a post-buckled state under the investigated loads. Furthermore, it is assumed that the slender spar webs' out-of-plane buckling deformations can be adjusted between two conditions: a *full-restraint* condition, in which the spar webs are ideally prevented from buckling, and a *no-restraint* condition, in which the spar webs are free to buckle.
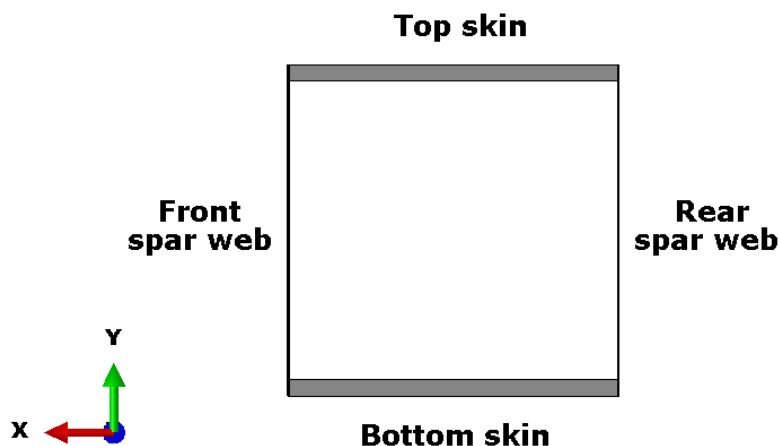
Figure 4.1: Cross-section of the wing box under investigation.

In Chapter 5, multiple wing box configurations with varying cross-sectional dimensions and slender spar webs made from different materials will be investigated. However, in this chapter, the methodology developed for evaluating the twist morphing capabilities is explained for a baseline configuration, defined as configuration A-1.

The wing box configuration A-1 has a height of 60 mm, measured as the distance between the skins' outer surfaces, a width of 60 mm, measured as the distance between the midlines of the slender spar webs, and a spanwise length of 900mm. Furthermore, as illustrated in Figure 4.2, the wing box is divided into 3 stations of 300mm by positioning 4 equally-spaced ideal rigid ribs, with one rib located at the wing box tip and another at the root.
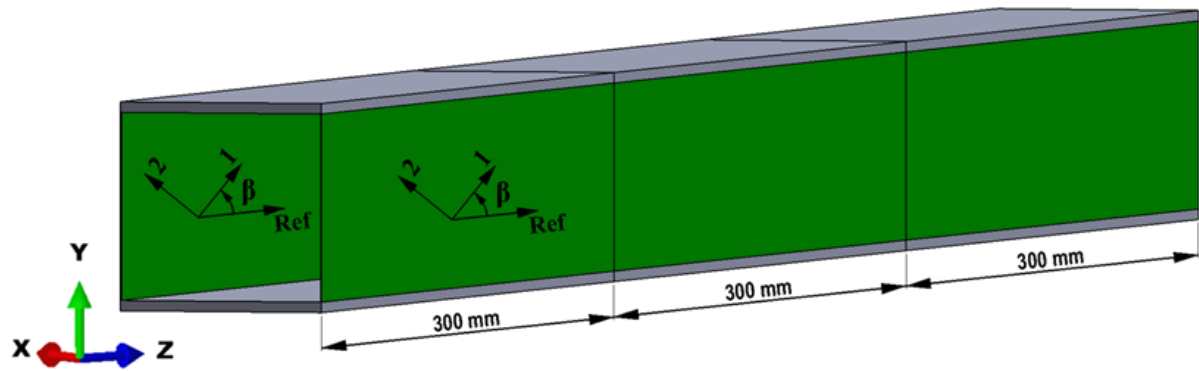
Figure 4.2: Configuration A-1 — Principal axes orientation β of the front and rear spar webs' plies.

The top and bottom skins consist of 3 mm thickness aluminum alloy panels, whose material properties are presented in Table 4.1. On the other hand, the front and rear spar webs are unidirectional composite laminates made from unidirectional carbon plies IM7/8552, whose material properties are presented in Table 4.2. Both unidirectional composite spar webs are made of two plies and have opposite layups, assigning a $[+45°/+45°]$ layup to the front spar web and a $[-45°/-45°]$ layup to the rear spar web, both measured counter-clockwise relative to the spanwise axis when seen from the rear side of the wing box, as illustrated in Figure 4.2.

Table 4.1: Material properties of the aluminum alloy.

Property	Symbol	Value
Young's modulus	E	70 GPa
Poisson's ratio	ν	0.33

Table 4.2: Material properties of unidirectional carbon plies IM7/8552 ([60, 61]).

Property	Symbol	Value
Longitudinal Young's modulus	E_{11}	146 GPa
Transverse Young's modulus	E_{22}	8.22 GPa
Major Poisson's ratio	ν_{12}	0.34
In-plane Shear modulus	G_{12}	4.5 GPa
Ply thickness	t_{ply}	0.125 mm
Longitudinal tensile strength	X^t	2768 MPa
Longitudinal compressive strength	X^c	1690 MPa
Transverse tensile strength	Y^t	55 MPa
Transverse compressive strength	Y^c	285 MPa
Shear strength	S	90 MPa

The structural response of the wing box to an external quasi-static torque, and under the two buckling constraints of interest, ie. the *no-restraint* and *full-restraint* conditions, is predicted by finite element analysis conducted with the commercial finite element software ABAQUS. It should be highlighted that the external devices required to apply the *full-restraint* and *no-restraint* constraints to the slender spar webs' buckling deformations are not modeled at this stage, neglecting their influence over the structural response. However, the structural design of these external devices, taking into account their influence over the structural response and their capability to restrain the buckling deformations, will be addressed in Chapter 6.

The wing box is modeled by linear shell elements S4R uniformly distributed across the wing box with a mesh seed size of 2 mm, resulting in a total of 54,000 elements and 54,120 nodes. Although coarser meshes can provide converged solutions with regard to the wing box tip elastic twist, the mesh is refined to a mesh seed size of 2 mm to properly capture the failure indexes along the buckling spar webs for a material failure assessment.

On the other hand, the ideal rigid ribs are modelled by beam type Multi-Point Constraints (MPC). At each rib location, a beam type MPC constraint is defined, selecting the nodes along the wing box cross-section as slave nodes, and a reference point placed at the cross-section's centroid as the control point. In this way, the nodes of the wing box are constrained to have equal displacement and rotation, as would be the case for an ideal rigid rib. In Figure 4.3, the beam type MPC constraints simulating the ribs are illustrated.
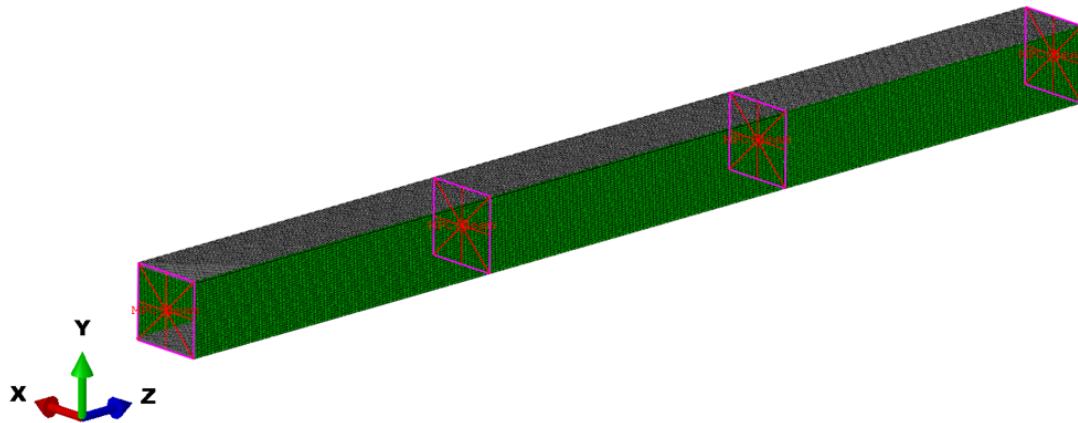
Figure 4.3: Beam type Multi-Point Constraints simulating the ideal rigid ribs of the wing box.

The boundary and loading conditions are defined in Table 4.3, and their application to the FEM is illustrated in Figure 4.4. The wing box is fixed at the root by imposing an encastre boundary condition to the control point of the MPC constraint simulating the rib at the root. On the other hand, a positive concentrated torsional moment T is applied to the control point of the MPC constraint simulating the rib at the tip of the wing box. This positive torque corresponds to a clockwise moment when seen from the wing box root, also referred to as nose-up, which in turn creates a positive nose-up elastic twist.

Table 4.3: Boundary and loading conditions applied to the finite element model of the wing box under torsion.

Location	Boundary Condition	Loading Condition
Root ($Z = 0$)	$U_x = 0,\ U_y = 0,\ U_z = 0,$ $UR_x = 0,\ UR_y = 0,\ UR_z = 0$	—
Tip ($Z = 900$ mm)	—	Torque: CM3 $= T$
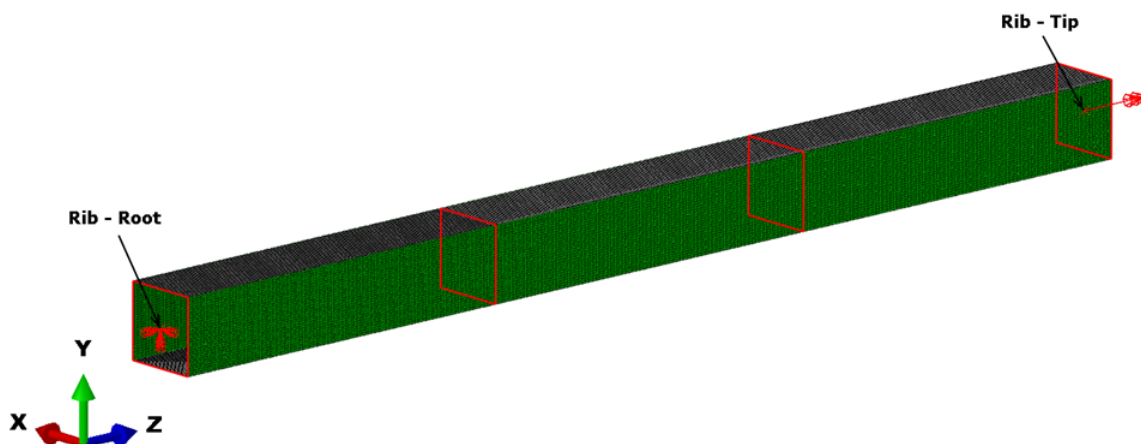
Figure 4.4: Boundary and loading conditions applied to the wing box finite element model.

When considering a *full-restraint* buckling condition, i.e., with ideally non-buckling spar webs, the structural response to a quasi-static external torque is calculated by a linear static general analysis using the Abaqus/Standard solver, assuming that the slender spar webs have no geometrical imperfection. As this type of analysis cannot capture the slender spar webs' non-linear buckling instabilities, the spar webs' out-of-plane (buckling) deformations remain zero under the action of the external torque.

On the other hand, when considering a *no-restraint* buckling condition, in which the slender spar webs are free to buckle, the structural response to an external quasi-static torque is calculated by a dynamic implicit analysis of quasi-static application using the Abaqus/Standard solver, accounting for geometric nonlinearities. For this analysis, an initial geometrical imperfection is introduced into the spar webs by superposing the shape function of their first buckling mode, scaled to a maximum deflection of 10% the spar web thickness. This means that for the baseline wing box configuration A-1, in which the spar webs have a thickness of 0.25 mm, maximum out-of-plane deflections of 0.025 mm are introduced into the front and rear spar webs of each wing box station.

Calculated with the Lanczos eigensolver, the shape functions of the wing box first three buckling modes for a positive external torque are superposed as geometrical imperfection, as each buckling mode represents the spar webs' first buckling mode at a different station.[1] For the baseline wing box configuration A-1, the three buckling modes occur for the same buckling torque of 8.2 Nm, and, as illustrated in Figure 4.5 and Figure 4.6, the first buckling mode is associated to the tip station, the second buckling mode to the middle station and the third buckling mode to the root station. On the other hand, as the external torque creates shear flows of equal magnitude but opposite direction along the front and rear spar webs, both spar webs buckle with opposite buckling patterns and for the same external torque due to their opposite layups. Furthermore, the diagonal buckling patterns are due to the internal diagonal compressive stresses created by the shear flows acting on the spar webs.

(a)

(b)

(c)
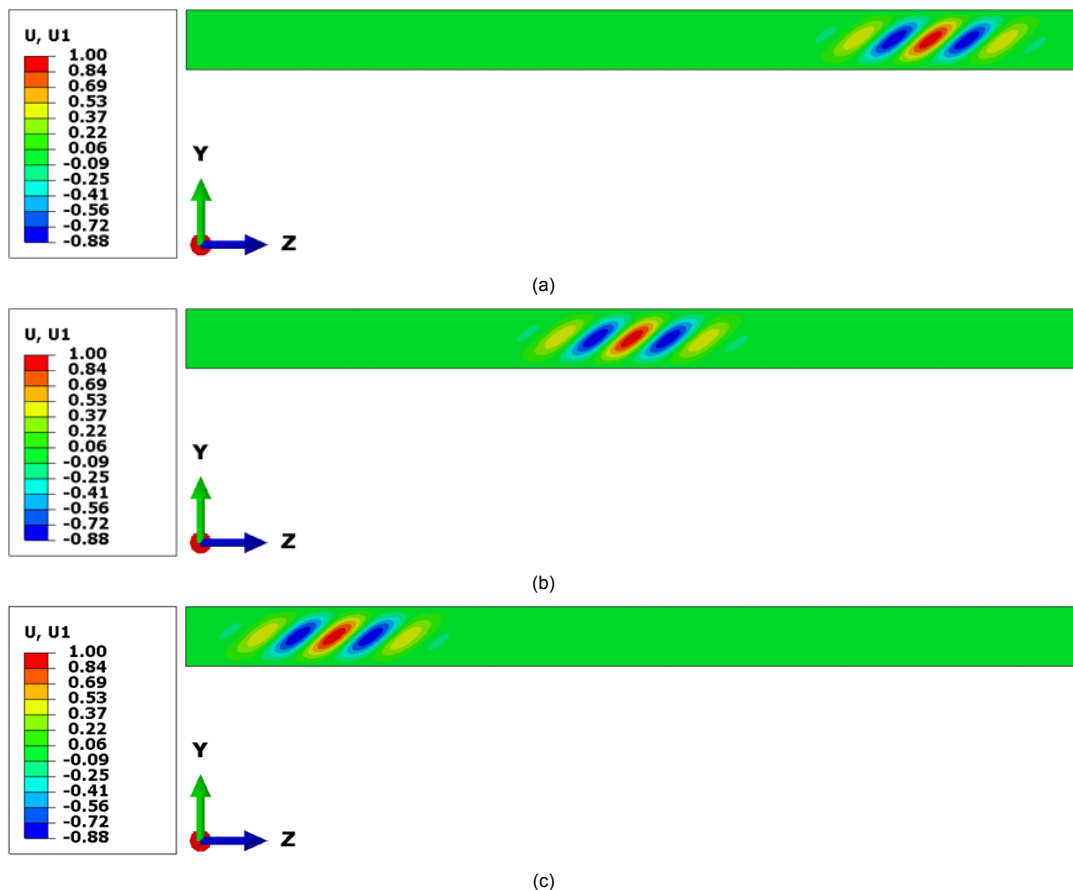
Figure 4.5: Configuration A-1 — Front spar web buckling mode shape for: (a) first buckling mode, (b) second buckling mode, (c) third buckling mode.

---

[1] Due to the orthotropic elastic properties of the spar webs' composite material, different buckling loads and buckling shapes are obtained for a positive and a negative external torque. As the wing box is investigated under a positive torque, the first 3 buckling modes for a positive external torque are introduced as geometrical imperfection.

(a)

(b)

(c)
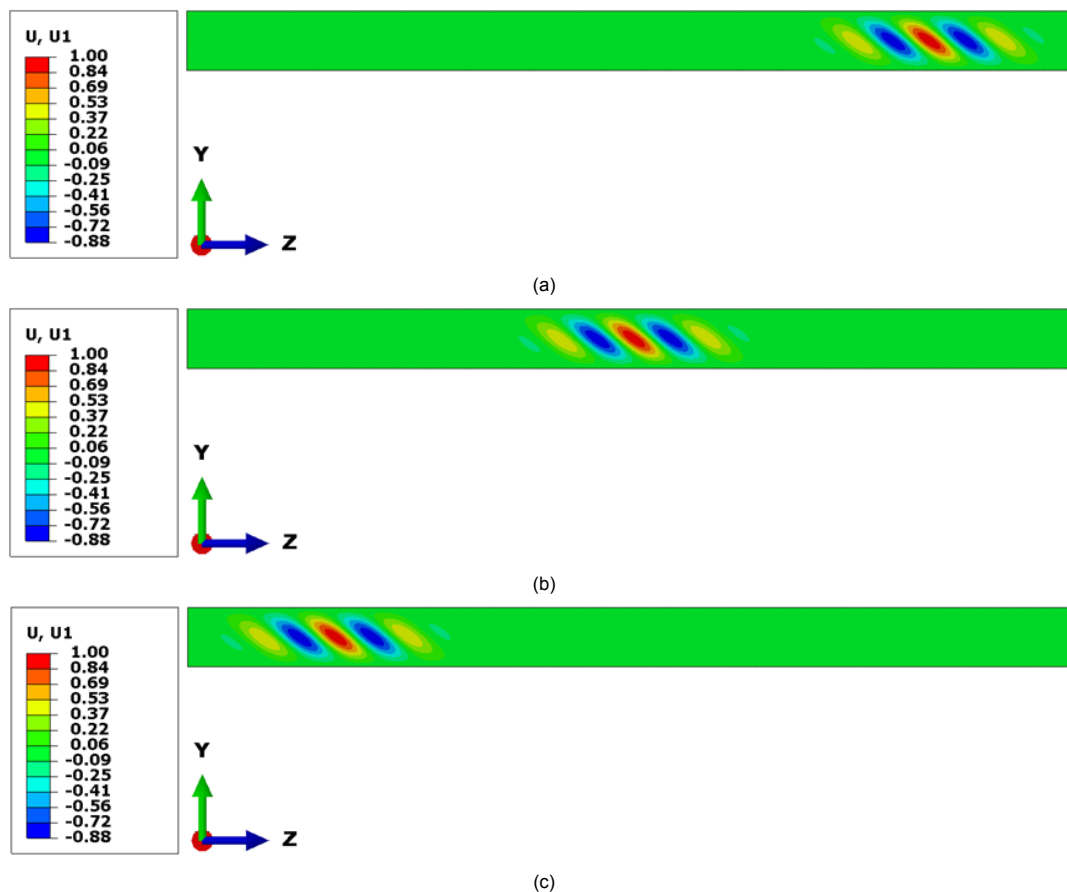
Figure 4.6: Configuration A-1 — Rear spar web buckling mode shape for: (a) first buckling mode, (b) second buckling mode, (c) third buckling mode.

Therefore, when analyzing the twisting response of the wing box A-1 in the *no-restraint* condition, the front and rear spar webs of each wing box station present a maximum initial out-of-plane deflection of 0.025 mm, introduced by scaling each buckling mode shape function to a maximum deflection of 0.025 mm.

4.2. Failure assessment

To assess the wing box morphing capabilities, it is important to predict the maximum external torque T_{max} that the wing box can sustain previous the material failure of the buckling spar webs. To assess the material failure of spar webs made from unidirectional composite plies, the Hashin failure criterion (*Hashin* [62]) is applied, as it accounts for the fiber and matrix individual failure modes of fiber tension, fiber compression, matrix tension and matrix compression. However, when assessing the material failure of spar webs made from non-unidirectional plies, the Tsai-Hill failure criterion (*Tsai* [63]) is applied instead, as the Hashin criterion is developed for unidirectional composite materials. Unlike the Hashin failure criterion, the Tsai-Hill criterion does not allow for the prediction of the composite material failure mode.

On the other hand, the material failure of the aluminum alloy top and bottom skins is neglected, as it could be prevented by either increasing the skin thickness or changing the skin material (e.g., to a carbon fibre reinforced polymer composite material) without affecting the spar webs' effective shear stiffness adaptation capabilities. However, it is important to prevent the buckling of the skins for the investigated external torque magnitudes; otherwise, the changes in torsional stiffness created by the application of an external torque cannot be attributed solely to the buckling of the slender spar webs, hindering the evaluation of the morphing twists that could be created by the shear stiffness adaptation of the slender spar webs. For this reason, a 3 mm thickness is assigned to the aluminum alloy skin panels, ensuring that their buckling instabilities occur for high external torques (relative to the torque that causes the buckling of the slender spar webs).

4.3. Twisting response: *No-restraint* condition

Based on the FEA results for the twisting response of the wing box A-1 in the *no-restraint* condition, a positive nose-up elastic twist is created along the span of the wing box, that increases from a zero twist at the root to a maximum twist at the tip, with each wing box station providing the same elastic twist increment. This is illustrated in Figure 4.7, where the elastic twist registered at each rib location is presented as a function of the external torque, up to the maximum external torque of 82.5 Nm, for which the front spar web experiments material failure.
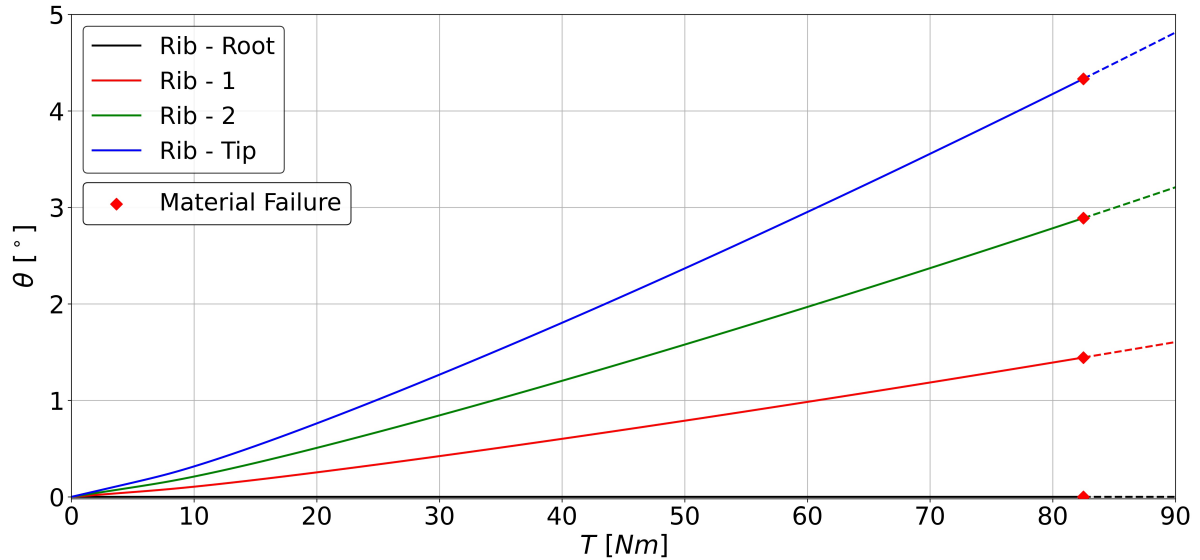
Figure 4.7: Configuration A-1 in the *no-restraint* condition — Elastic twist at each rib location as a function of the external quasi-static torque.

To reduce the number of variables, the twisting response to the external quasi-static torque is analyzed throughout this chapter in terms of the elastic twist registered at the tip of the wing box. However, it should be highlighted that results could be easily extrapolated to the twist increment per station $\Delta\theta_{NR}$ by dividing the tip twist by three, or to the twist of any rib by adding the corresponding number of increments $\Delta\theta_{NR}$. Hence, the elastic twist at the tip of the wing box in the *no-restraint* condition, defined as θ_{NR}, is presented in Figure 4.8 as a function of the external quasi-static torque T.
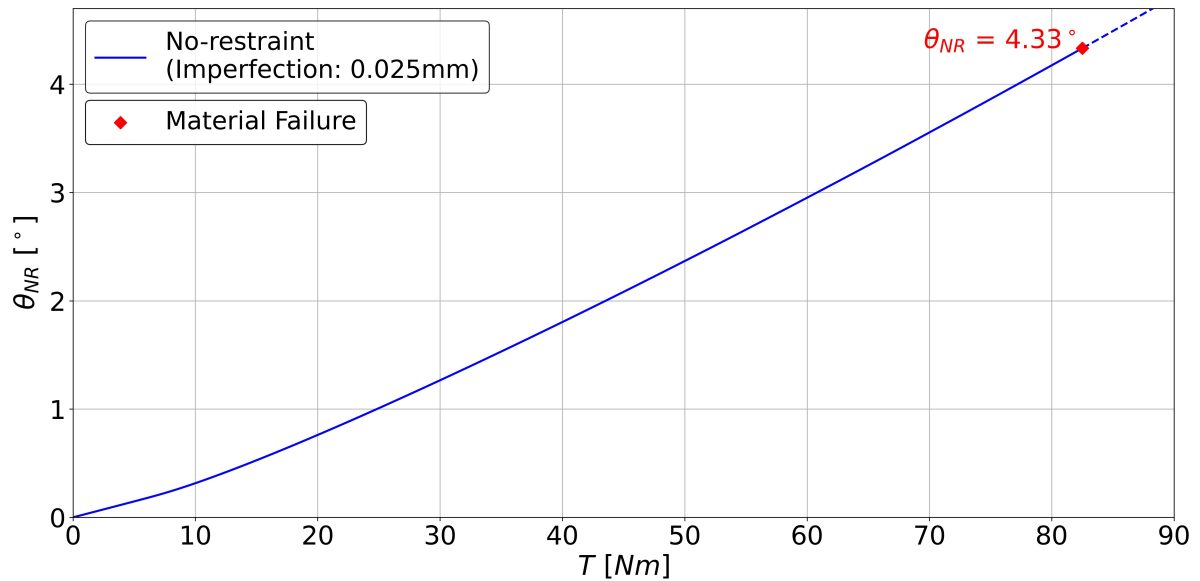
Figure 4.8: Configuration A-1 in the *no-restraint* condition — Evolution of the tip elastic twist with the external quasi-static torque.

On the other hand, taking into account that the torsional stiffness is the reciprocal of the rate of tip twist per unit torque, the torsional stiffness as a function of the external torque can be described as

$$K_\theta^{NR}(T) = \left[\frac{d\theta_{NR}(T)}{dT} \right]^{-1} \tag{4.1}$$

where K_θ^{NR} represents the wing box torsional stiffness and θ_{NR} the elastic tip twist. Approximating the derivative of the tip twist with respect to the external torque $d\theta_{NR}(T)/dT$ by a forward finite difference, the torsional stiffness for each computed torque increment T_i can be approximated by the equation

$$K_\theta^{NR}(T_i) \approx \left[\frac{\theta^{NR}(T_{i+1}) - \theta^{NR}(T_i)}{T_{i+1} - T_i} \right]^{-1} = \frac{T_{i+1} - T_i}{\theta^{NR}(T_{i+1}) - \theta^{NR}(T_i)} \tag{4.2}$$

Then, applying Eq.(4.2) to the torque-twist data illustrated in Figure 4.8, the evolution of the torsional stiffness with the external torque is presented in Figure 4.9.[2]
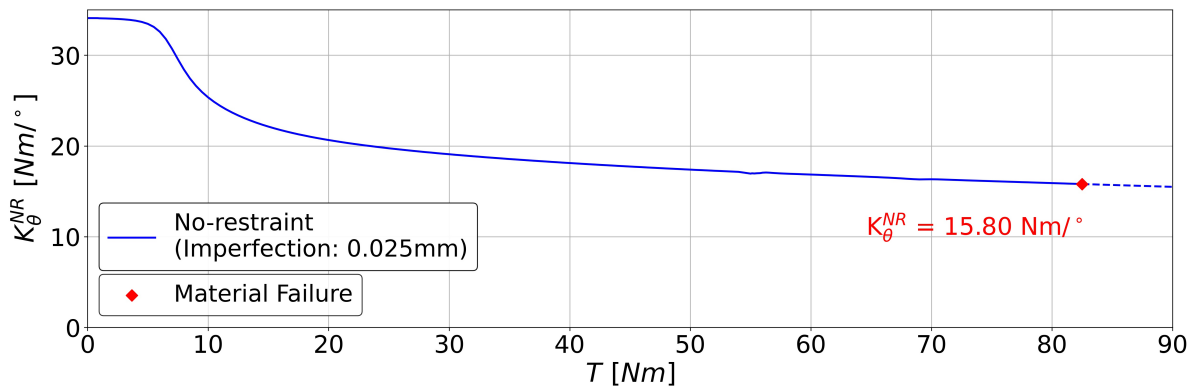
Figure 4.9: Configuration A-1 in the *no-restraint* condition — Evolution of the torsional stiffness with the external quasi-static torque.

When the slender spar webs buckle under the shear loads created by the external torque, diagonal buckling patterns as to those illustrated in Figure 4.5 and Figure 4.6 develop throughout the spar webs, causing the shear load acting on a spar web to be supported by diagonal tension in the direction perpendicular to the buckle. Even though the buckled spar webs can continue taking load, these diagonal tension fields reduce the spar webs' effective shear stiffnesses, ultimately causing a reduction in the wing box torsional stiffness.

From Figure 4.9, the buckling-induced reductions in torsional stiffness start manifesting for torques slightly lower than the linear buckling torque of 8.2 Nm (determined in Section 4.1) due to the spar webs' geometrical imperfections. The torsional stiffness reduction rate is the highest at the onset of buckling, rapidly flattening off for higher torques as the spar webs progress into their post-buckling regimes. On the other hand, the small local disturbances in torsional stiffness registered in Figure 4.9 for the external torques of 55 Nm and 69 Nm are induced by small sudden changes in the rear spar web buckling shape.

Applying the Tsai-Hill failure criterion to assess the material failure of the unidirectional composite spar webs, the front spar web is predicted to fail first, and for the external torque of 82.5 Nm. Hence, for this external torque, the associated failure index I_{TH}, also referred to as output variable $TSAIH$ in ABAQUS, surpasses a value of 1. In Figure 4.10a, the envelope plot of the failure index I_{TH} across the middle station front spar web is displayed for the external torque of 82.5 Nm.[3] On the other hand, the rear spar web does not fail for an external torque of 82.5 Nm, as it experiments a slightly different buckling shape evolution than the front spar web. The envelope plot of the failure index I_{TH} across the middle station rear spar web is displayed for the external torque of 82.5 Nm in Figure 4.10b, showing a different pattern than the front spar web and lower I_{TH} values.

---

[2]The torsional stiffness is relatively small for the very first computed torque increment, increasing and settling at a slightly higher value in the subsequent increment. This initial small nonphysical oscillation in torsional stiffness is filtered out of the response.
[3]The front spar web of all stations have practically the same plot. However, the envelope plot is reduced to the middle station of the wing box to improve the clarity of the results.

(a)

(b)
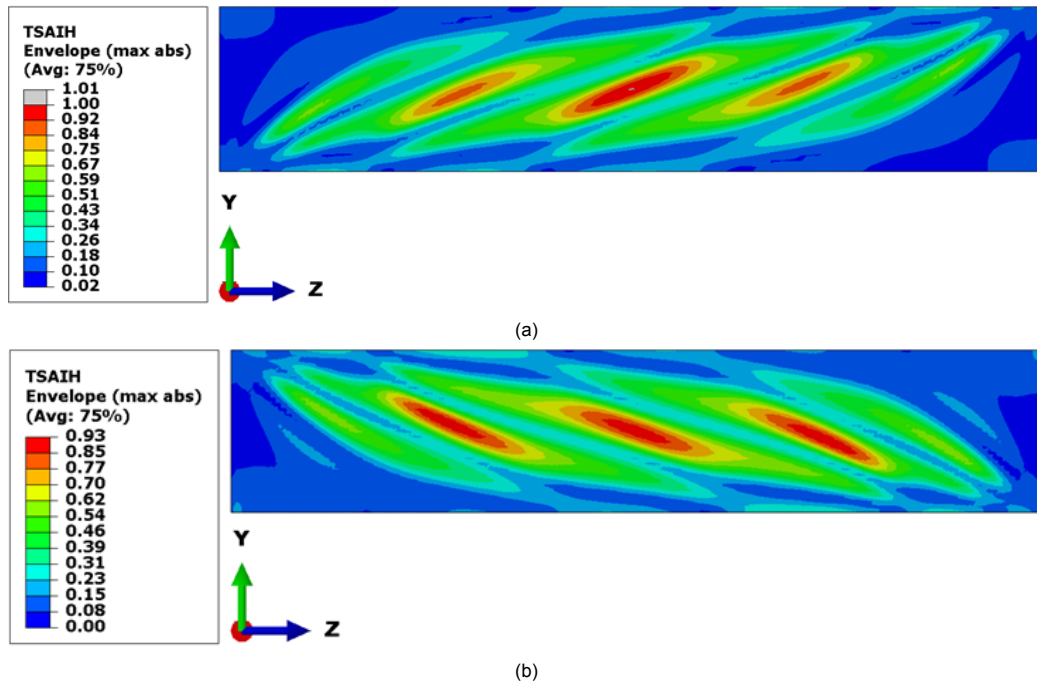
Figure 4.10: Configuration A-1 in the *no-restraint* condition for an external torque of 82.5 Nm — Envelope plot of failure index I_{TH} across the middle station (a) front spar web and (b) rear spar web.

Even though the Tsai-Hill failure criterion allows for the prediction of the spar webs' material failure, the criterion does not provide any information regarding the failure mode of the composite plies. On the other hand, when applying the Hashin failure criterion to assess the material failure of the unidirectional composite spar webs, the front spar web is also predicted to fail first, and for the same external torque of 82.5 Nm, but the criterion also identifies that the critical lamina fails in a tensile matrix failure mode.

For the external torque of 82.5 Nm, the failure index associated to the tensile matrix failure mode I_m^t, also referred to as output variable $HSNMTCRT$ in ABAQUS, becomes the first failure index to surpass a value of 1, among the four different failure indexes (associated to four different failure modes) considered in the Hashin failure criterion. In Figure 4.10, the envelope plots of the failure index I_m^t across the middle station front and rear spar webs are displayed for the external torque of 82.5 Nm.

(a)

(b)
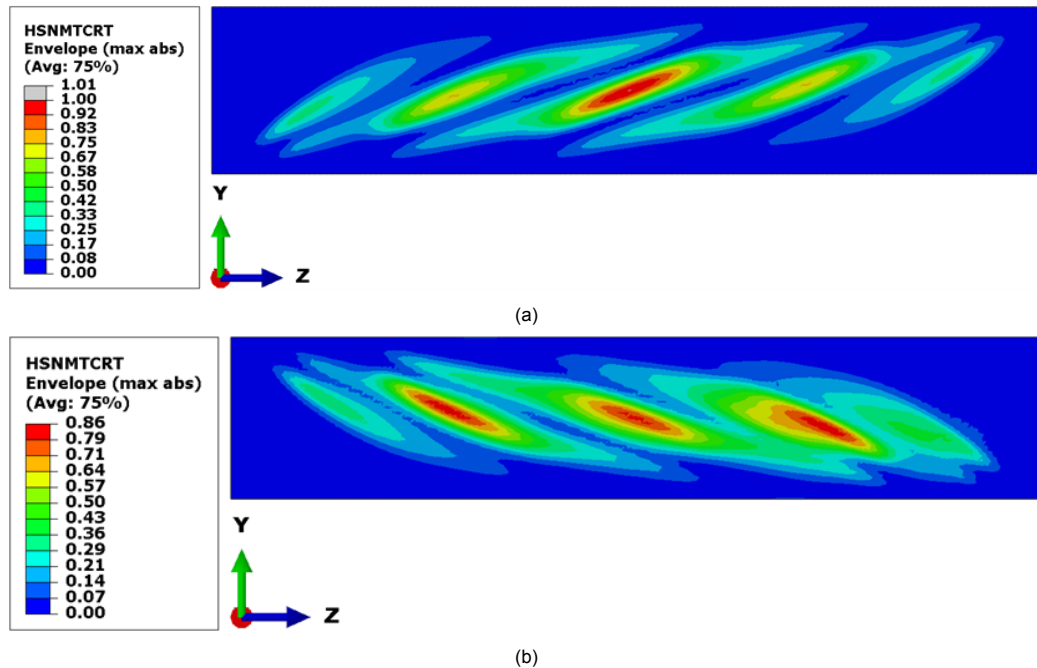
Figure 4.11: Configuration A-1 in the *no-restraint* condition for an external torque of 82.5 Nm — Envelope plot of failure index I_m^t across the middle station (a) front spar web and (b) rear spar web.

From Figure 4.11a, material failure initiates at the laminate location experiencing the greatest out-of-plane buckling deformation. To determine why failure initiates at this location and in a tensile matrix mode, the tensile matrix damage initiation criterion applied to calculate I_m^t along each ply is analyzed. This criterion is given by

$$I_m^t = \left(\frac{\hat{\sigma}_{22}}{Y^t}\right)^2 + \left(\frac{\hat{\tau}_{12}}{S}\right)^2 \qquad if \quad \hat{\sigma}_{22} > 0 \tag{4.3}$$

where $\hat{\sigma}_{22}$ is the (tensile) effective normal stress in transverse fibre direction and $\hat{\tau}_{12}$ represents the effective in-plane shear stress. On the other hand, as previously introduced in Table 4.2, the symbols Y^t and S represent the transverse tensile strength and the shear strength of the material, respectively.

Due to the characteristic low tensile transverse strength Y^t of unidirectional composite plies (as a material property dominated by the matrix), transverse tensile stresses represent the most critical type of loading. Taking this into account, failure initiates at the location experiencing the greatest out-of-plane buckling deformation due to the bending-induced tensile stresses in transverse fibre direction.

4.4. Twisting response: *Full-restraint* condition

The elastic twist at the tip of the wing box in the *full-restraint* condition, defined as θ_{FR}, is presented in Figure 4.12 as a function of the external quasi-static torque T. As in the *no-restraint* condition, these results could be easily extrapolated to the twist increment per station $\Delta\theta_{FR}$ by dividing the tip twist by three, or to the twist of any rib by adding the corresponding number of increments $\Delta\theta_{FR}$.
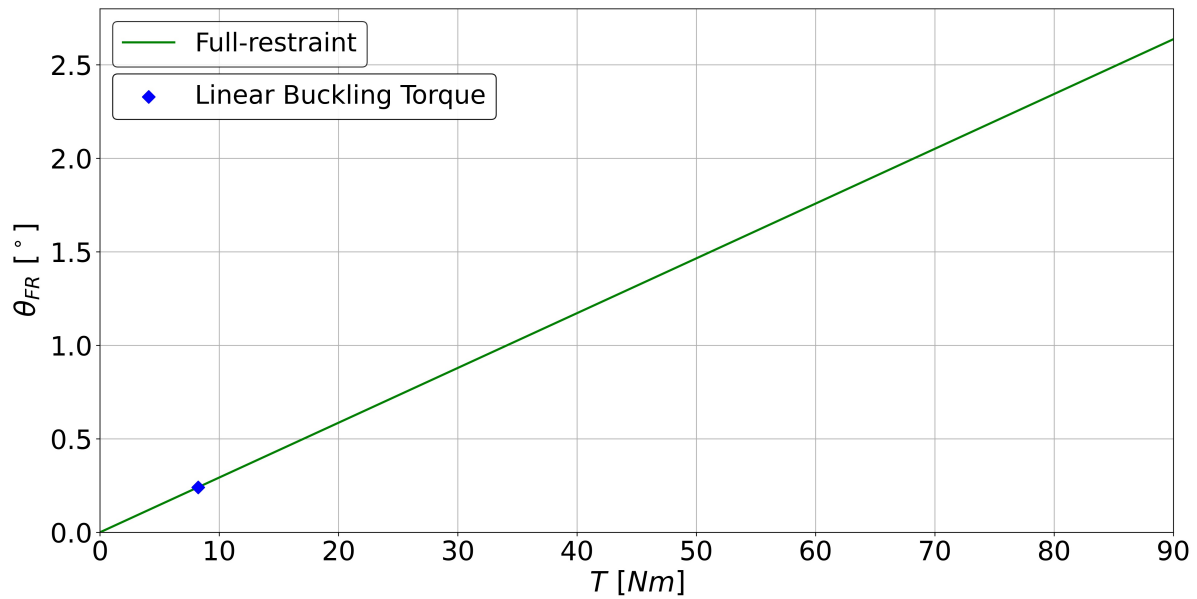
Figure 4.12: Configuration A-1 in the *full-restraint* condition — Evolution of the tip elastic twist with the external quasi-static torque.

From Figure 4.12, the tip twist increases linearly with the external torque. As the slender spar webs are prevented from buckling, the wing box torsional stiffness remains unchanged past the linear buckling torque of 8.2 Nm, leading to a constant rate of twist per unit torque. Applying Eq. (4.2) to the torque-twist data, the evolution of the wing box torsional stiffness with the external torque is presented in Figure 4.13, where, as expected, the torsional stiffness of $K_\theta^{FR} = 34.14\,Nm/°$ remains unchanged after the linear buckling torque of 8.2 Nm is surpassed.

Applying the Hashin damage initiation criteria to assess the material failure of the unidirectional composite spar webs, material failure does not occur for the investigated torque magnitudes. In particular, for the external torque of 82.5 Nm, at which the front spar web fails in the *no-restraint* condition, the spar webs are far from failing, as the restraint of the out-of-plane buckling deformations prevents the creation of bending-induced tensile stresses in transverse fibre direction.
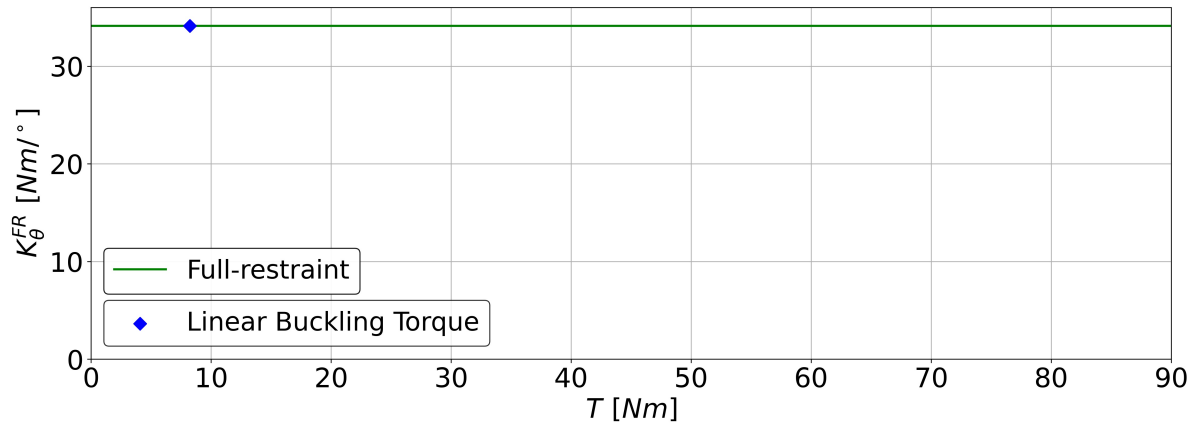
Figure 4.13: Configuration A-1 in the *full-restraint* condition — Evolution of the torsional stiffness with the external quasi-static torque.

4.5. Active Region & Buckling-induced twist

Summarizing and comparing the findings presented so far for the twisting response of the wing box configuration A-1, Figure 4.14 presents the wing box tip twist and torsional stiffness as a function of the external quasi-static torque in the *no-restraint* and *full-restraint* conditions. From Figure 4.14, the reader can observe that higher twists are created in the *no-restraint* condition due to the buckling-induced reductions in torsional stiffness.
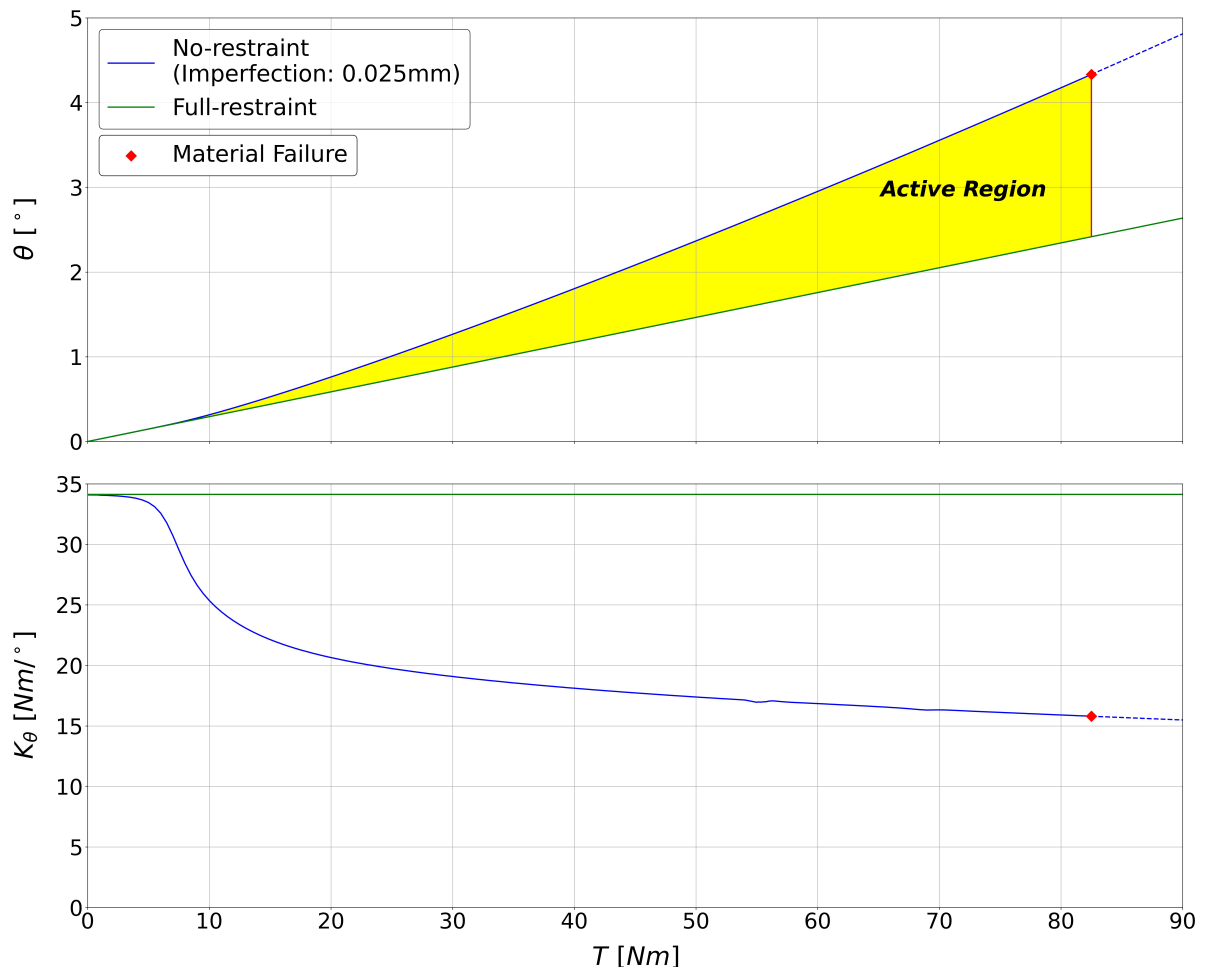
Figure 4.14: Configuration A-1 in the *no-restraint* and *full-restraint* conditions — Evolution of the tip elastic twist and torsional stiffness with the external quasi-static torque.

The yellow region comprised between the two curves, referred to as the *Active Region*, encloses the different controllable elastic tip twists that could be selected by actively adjusting the buckling constraints acting on the slender spar webs. In this way, the twisting responses predicted for the two extreme buckling constraints, i.e., the *no-restraint* and *full-restraint* conditions, can be used to delimit the twisting response associated to a *partial-restraint* condition, defined as any type of buckling constraint between a *full-restraint* and a *no-restraint* condition.

Even though the twisting response associated to a *partial-restraint* buckling constraint cannot be predicted without defining how the slender spar webs' buckling deformations are to be partially restrained, i.e., the constraint-strategy, the morphing capabilities can still be evaluated by predicting the twisting responses in the *no-restraint* and *full-restraint* conditions.

In this way, the maximum active tip twist that could be introduced by adjusting the spar webs' buckling deformations, referred to as the buckling-induced twist θ_b, can be calculated by subtracting the elastic tip twists predicted in the *no-restraint* and *full-restraint* conditions; that is,

$$\theta_b(T) = \theta_{NR}(T) - \theta_{FR}(T) \tag{4.4}$$

where θ_{NR} is the elastic tip twist in the *no-restraint* condition and θ_{FR} is the elastic tip twist in the *full-restraint* condition. Applying Eq. (4.4), the evolution of θ_b with the external torque is presented in Figure 4.15, registering a maximum buckling-induced twist of $\theta_b^{max} = 1.92°$ for the maximum external torque of 82.5 Nm, at which the front spar web experiments material failure in the *no-restraint* condition.
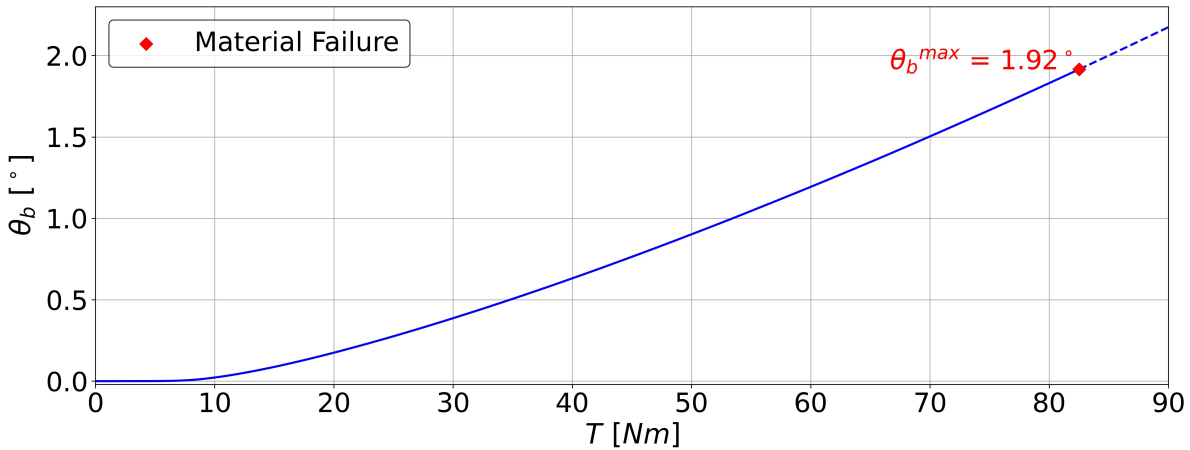
Figure 4.15: Configuration A-1 — Evolution of the buckling-induced twist at the tip of the wing box with the quasi-static external torque.

4.6. Buckling-induced twist: Analytical Description

In the previous section, the buckling-induced twist θ_b was defined as the morphing twist created by an external torque when adjusting the buckling constraints from the *full-restraint* condition to the *no-restraint* condition. Then, as defined by Eq. (4.4), the buckling-induced twist can be calculated as

$$\theta_b(T) = \theta_{NR}(T) - \theta_{FR}(T)$$

where θ_{NR} is the elastic tip twist in the *no-restraint* condition and θ_{FR} is the elastic tip twist in the *full-restraint* condition.

Taking into account that the elastic tip twist created by an external quasi-static torque T can be calculated by integrating the rate of tip twist per unit torque from zero to T, the tip twists θ_{NR} and θ_{FR} can be described as

$$\theta_{NR}(T) = \int_0^T \frac{d\theta_{NR}(T)}{dT} * dT \tag{4.5}$$

$$\theta_{FR}(T) = \int_0^T \frac{d\theta_{FR}(T)}{dT} * dT \tag{4.6}$$

Considering that the rate of tip twist per unit torque is the reciprocal of the wing box torsional stiffness, the tip twists θ_{NR} and θ_{FR} can be expressed in terms of their corresponding torsional stiffnesses as

$$\theta_{NR}(T) = \int_0^T \frac{dT}{K_\theta^{NR}(T)} \tag{4.7}$$

$$\theta_{FR}(T) = \int_0^T \frac{dT}{K_\theta^{FR}(T)} \tag{4.8}$$

where K_θ^{NR} is the torsional stiffness in the *no-restraint* condition and K_θ^{FR} is the torsional stiffness in the *full-restraint* condition. Taking into account that the torsional stiffness K_θ^{FR} is independent of the external torque T (as illustrated in Figure 4.13 for wing box A-1), Eq. (4.8) becomes

$$\theta_{FR}(T) = \frac{T}{K_\theta^{FR}} \tag{4.9}$$

Then, substituting in Eq. (4.4) for θ_{NR} and θ_{FR} from Eq. (4.7) and Eq. (4.9), respectively, the buckling-induced twist θ_b becomes

$$\theta_b(T) = \int_0^T \frac{dT}{K_\theta^{NR}(T)} - \frac{T}{K_\theta^{FR}} \tag{4.10}$$

As the maximum buckling-induced twist $\theta_b{}^{max}$ takes place for the maximum external torque T_{max}, at which the spar webs experiment material failure, by evaluating Eq. (4.10) at T_{max}, the maximum buckling-induced twist $\theta_b{}^{max}$ becomes

$$\theta_b{}^{max} = \int_0^{T_{max}} \frac{dT}{K_\theta^{NR}(T)} - \frac{T_{max}}{K_\theta^{FR}} \tag{4.11}$$

Then, changing the external torque variable T by a non-dimensional torque $\overline{T}$ results in:

$$\theta_b{}^{max} = T_{max} * \left[\int_0^1 \frac{d\overline{T}}{K_\theta^{NR}\left(\overline{T}\right)} - \frac{1}{K_\theta^{FR}} \right] \tag{4.12}$$

where

$$\overline{T} = \frac{T}{T_{max}} \tag{4.13}$$

and rearranging Eq. (4.12) in terms of a non-dimensional stiffness factor B, yields

$$\theta_b{}^{max} = \frac{T_{max}}{K_\theta^{FR}} * \left[\int_0^1 \frac{d\overline{T}}{B\left(\overline{T}\right)} - 1 \right] \tag{4.14}$$

where

$$B\left(\overline{T}\right) = \frac{K_\theta^{NR}\left(\overline{T}\right)}{K_\theta^{FR}} \tag{4.15}$$

Finally, rearranging Eq. (4.14) in terms of the maximum twist in the *full-restraint* condition $\theta_{FR}{}^{max}$ and a buckling-induced factor β, the maximum buckling-induced twist $\theta_b{}^{max}$ can be expressed as

$$\theta_b{}^{max} = \beta * \theta_{FR}{}^{max} \tag{4.16}$$

where

$$\beta = \int_0^1 \frac{d\overline{T}}{B\left(\overline{T}\right)} - 1 \tag{4.17}$$

$$\theta_{FR}{}^{max} = \frac{T_{max}}{K_\theta^{FR}} \tag{4.18}$$

The Eq. (4.16) becomes useful for the exploration of the wing box design space as it decouples the buckling-induced twist $\theta_b{}^{max}$ into two separate parameters. In this way, Eq. (4.16) can be used to understand the reasons why certain design changes may influence the twist morphing capabilities in the way they do, but, in addition, the objective of maximizing the buckling-induced twist $\theta_b{}^{max}$ can be addressed by finding structural solutions that contribute to increasing the buckling-induced factor β and/or the twist $\theta_{FR}{}^{max}$.

To validate Eq. (4.16), the wing box A-1 buckling-induced twist $\theta_b{}^{max}$ is first computed in terms of the buckling-induced factor β and the twist $\theta_{FR}{}^{max}$, and then compared to the twist calculated in Section 4.5 by subtracting the elastic tip twists predicted in the *no-restraint* and *full-restraint* conditions.

The first step to calculate the buckling-induced factor β is to find the evolution of the stiffness factor B with the non-dimensional torque. Applying Eq. (4.15) to the torsional stiffness data presented in Figure 4.14 for the wing box A-1, the evolution of the stiffness factor B with the non-dimensional torque is illustrated in Figure 4.16.
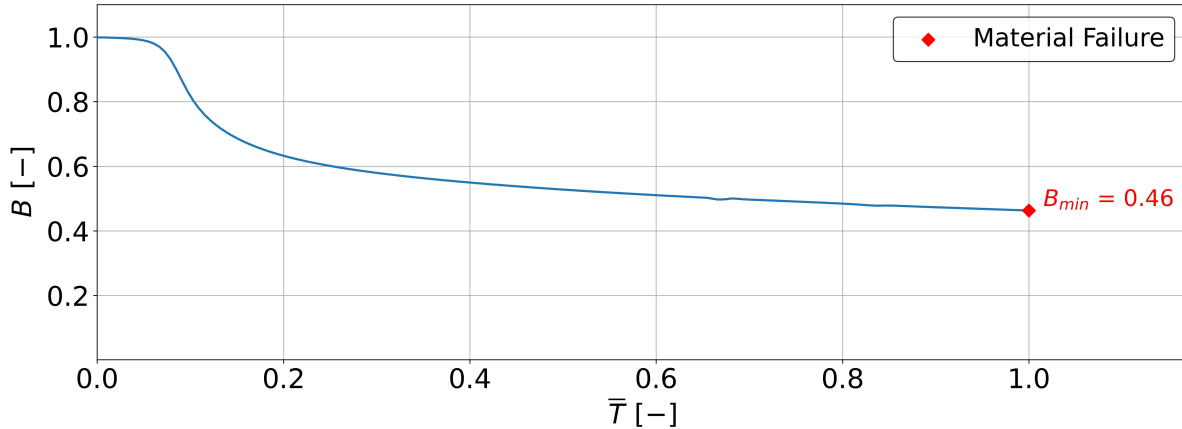
Figure 4.16: Configuration A-1 — Evolution of the stiffness factor B with the non-dimensional torque $\overline{T}$.

From Figure 4.16, the stiffness factor B presents a value of 1 in the unloaded state (i.e., $\overline{T} = 0$), showing that the spar webs' small geometrical imperfections of 0.025 mm do not affect the wing box pre-buckling torsional stiffness, which coincides with the torsional stiffness computed for spar webs with no geometrical imperfection. On the other hand, the evolution of the stiffness factor B with the external torque is similar to the evolution of the torsional stiffness in the *no-restraint* condition (presented in Figure 4.9), registering the greatest buckling-induced reduction in B at the onset of buckling, rapidly flattening off for greater torques. Ultimately, the lowest stiffness factor of $B_{min} = 0.46$ is achieved for the maximum external torque (i.e., $\overline{T} = 1$), showing that the torsional stiffness in the *no-restraint* condition reduces up to a value that is 54% lower than the pre-buckling torsional stiffness.

The next step is to compute the definite integral present in Eq. (4.17), which is numerically approximated by a trapezoidal rule, leading to the following expression for the buckling-induced factor β

$$\beta \approx \sum_{i=1}^{N} \frac{\left[B\left(\overline{T}_i\right) + B\left(\overline{T}_{i-1}\right)\right] * \left(\overline{T}_i - \overline{T}_{i-1}\right)}{2 * B\left(\overline{T}_i\right) * B\left(\overline{T}_{i-1}\right)} - 1 \tag{4.19}$$

where $\overline{T}_0 = 0$ and $\overline{T}_N = 1$. Then, applying Eq. (4.19) to the data presented in Figure 4.16, the buckling-induced factor β for wing box A-1 becomes

$$\beta \approx 0.796$$

On the other hand, the maximum twist in the *full-restraint* condition $\theta_{FR}{}^{max}$ for wing box A-1 can be easily calculated by applying Eq. (4.18), that is,

$$\theta_{FR}{}^{max} = \frac{T_{max}}{K_\theta^{FR}} = \frac{82.5\,Nm}{34.14\,Nm/°} = 2.4°$$

Finally, substituting these values of β and $\theta_{FR}{}^{max}$ in Eq. (4.16), the maximum buckling-induced twist $\theta_b{}^{max}$ for wing box A-1 becomes

$$\theta_b{}^{max} \approx \beta * \theta_{FR}{}^{max} = 1.9°$$

which is practically the same value as the one calculated in Section 4.5 by subtracting the elastic tip twists predicted in the *no-restraint* and *full-restraint* conditions, as illustrated in Figure 4.15.

5

Exploration of the Design Space

With the objective of maximizing the twist morphing capabilities, the wing box design space is explored in terms of its cross-sectional dimensions and the material assigned to the slender spar webs. Furthermore, the sensitivity of the twist morphing capabilities to the slender spar webs' geometrical imperfections is investigated.

5.1. Dimensional Study

In this section, the wing box design space is explored in terms of the wing box cross-sectional dimensions, evaluating their influence on the maximum buckling-induced twist $\theta_b{}^{max}$. Three different wing box configurations are investigated, referred to as configurations A-1, B-1 and C-1. Their general dimensions are presented in Table 5.1, while the components' materials, layups and thicknesses are displayed in Table 5.2. Different cross-sectional dimensions, consisting of the width and height, are assigned to each wing box, keeping the same ratio height/width for all wing boxes. Based on the cross-sectional dimensions displayed in Table 5.1, wing box A-1 has the smallest cross-section, respectively followed by wing boxes B-1 and C-1. On the other hand, all other design parameters, such as the spanwise length, station length, materials, layups and thicknesses, are kept the same as those assigned to wing box A-1, whose structural model was thoroughly explained in Section 4.1.

Table 5.1: General dimensions for wing boxes A-1, B-1 and C-1.

Dimension	A-1	B-1	C-1
Width	60 mm	100 mm	150 mm
Height	60 mm	100 mm	150 mm
Spanwise length	900 mm	900 mm	900 mm
Station length	300 mm	300 mm	300 mm

Table 5.2: Materials, layups and thicknesses for wing boxes A-1, B-1 and C-1.

Component	Material	Layup	Thickness
Top & bottom skin	Aluminum Alloy	-	3 mm
Front spar web	IM7/8552	$[+45°/+45°]$	0.25 mm
Rear spar web	IM7/8552	$[-45°/-45°]$	0.25 mm

The structural response of wing box A-1 to an external quasi-static torque in the *no-restraint* and *full-restraint* conditions has already been addressed in Sections 4.3 - 4.5. On the other hand, the structural responses of wing boxes B-1 and C-1 are presented below.

For wing box configuration B-1, Figure 5.1 illustrates the evolution of the tip twist and torsional stiffness with the external quasi-static torque in the *no-restraint* and *full-restraint* conditions.
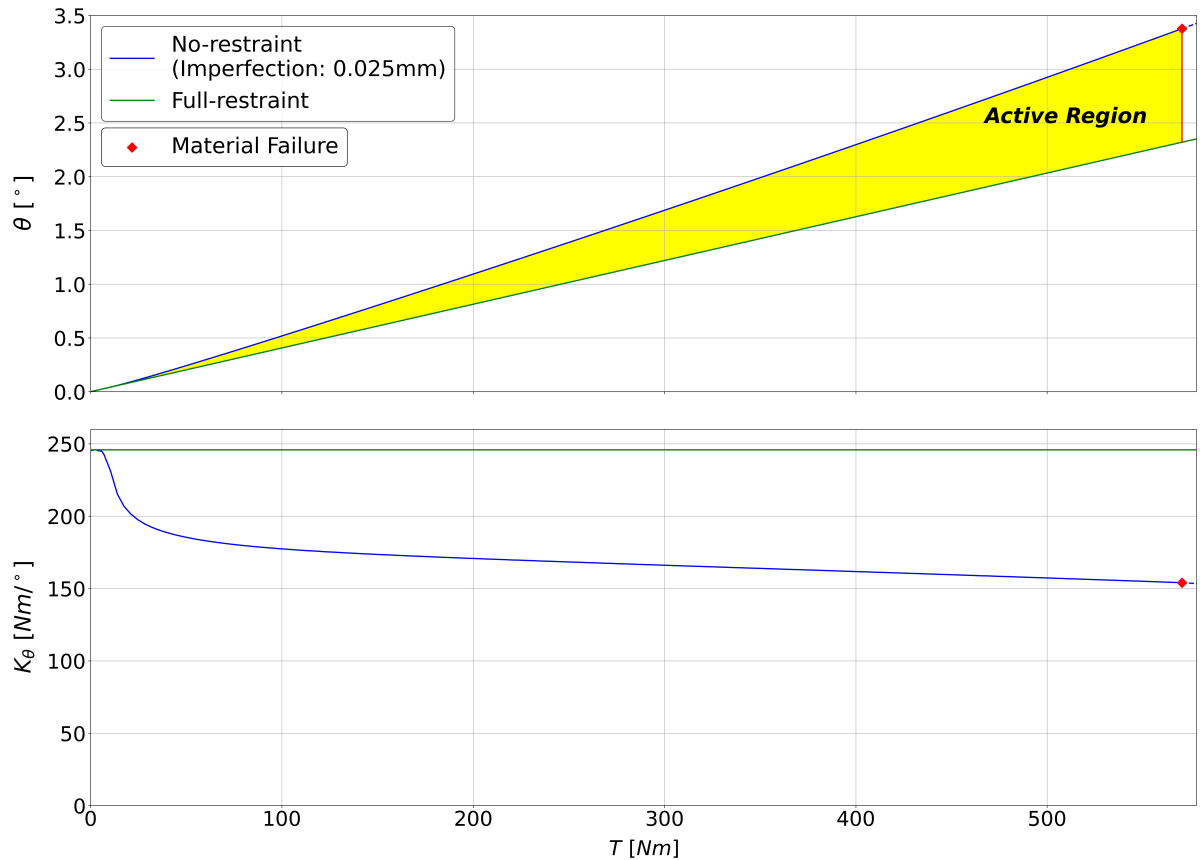
Figure 5.1: Configuration B-1 in the *no-restraint* and *full-restraint* conditions — Evolution of the tip elastic twist and torsional stiffness with the external quasi-static torque.

Applying the Hashin damage initiation criteria to assess the material failure of the unidirectional composite spar webs, the front spar web is predicted to fail first, in a tensile matrix failure mode for an external torque of 570.5 Nm. For this external torque, the failure index associated to the tensile matrix failure mode I_m^t becomes the first failure index to surpass a value of 1. In Figure 5.2, the envelope plot of the failure index I_m^t across the middle station front spar web is displayed for the external torque of 570.5 Nm.[1]
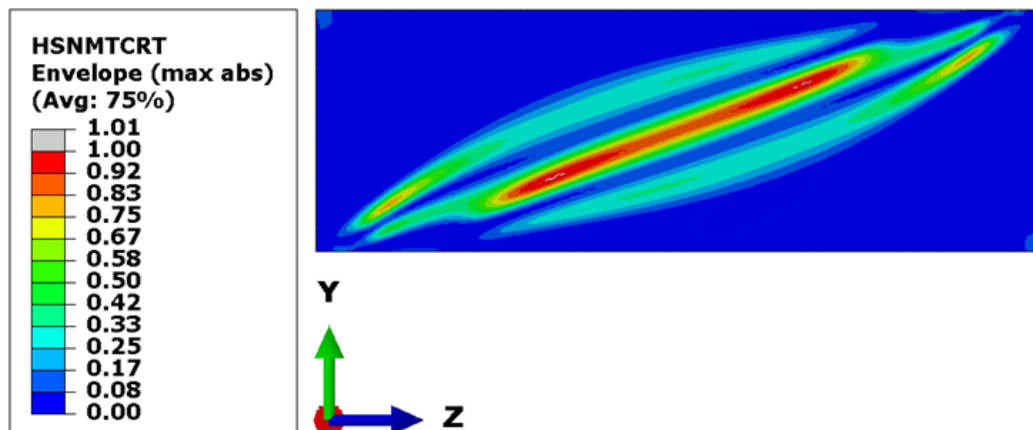
Figure 5.2: Configuration B-1 in the *no-restraint* condition — Envelope plot of the failure index I_m^t across the middle station front spar web for an external torque of 570.5 Nm.

---

[1] The front spar web of all stations have practically the same plot. The envelope plot is reduced to the middle station of the wing box to improve the clarity of the results.

On the other hand, Figure 5.3 presents the tip twist and torsional stiffness of wing box C-1 in the *no-restraint* and *full-restraint* conditions, as a function of the external quasi-static torque.
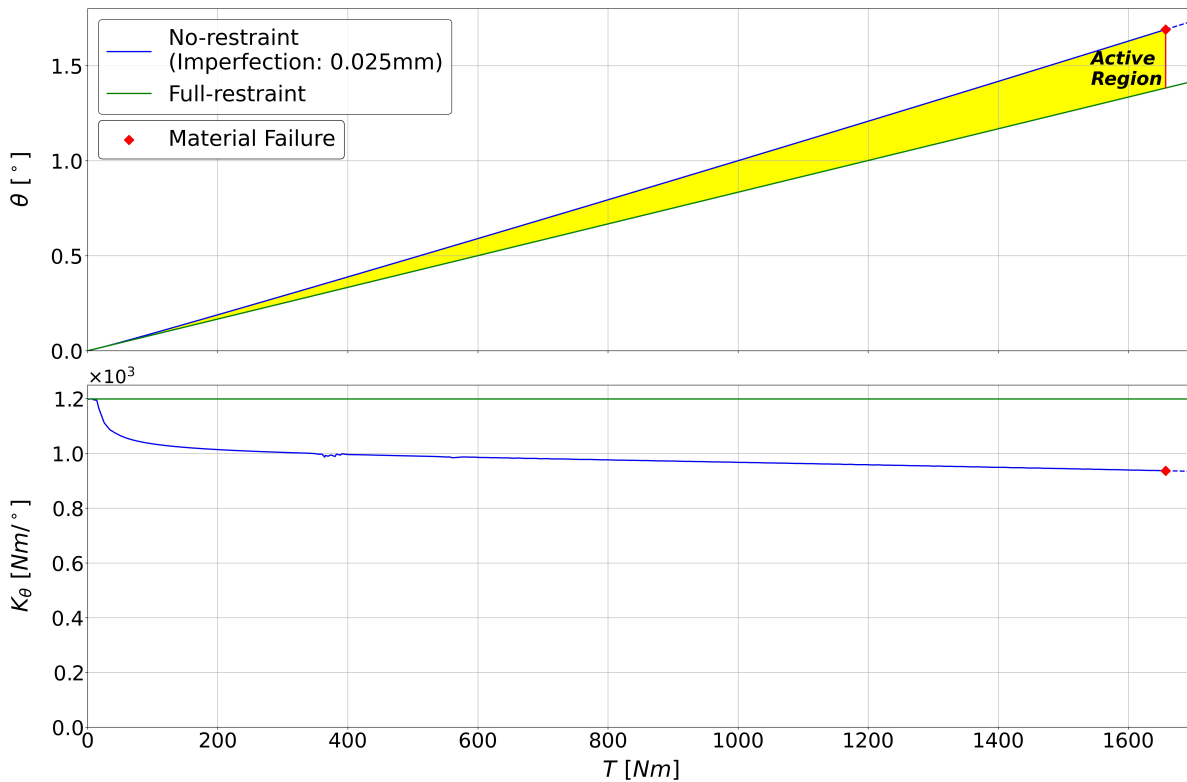
Figure 5.3: Configuration C-1 in the *no-restraint* and *full-restraint* conditions — Evolution of the tip elastic twist and torsional stiffness with the external quasi-static torque.

Applying the Hashin damage initiation criteria to assess the material failure of the unidirectional composite spar webs, the front spar web is predicted to fail first, in a tensile matrix failure mode for an external torque of 1657.5 Nm. For this external torque, the failure index associated to the tensile matrix failure mode I_m^t becomes the first failure index to surpass a value of 1. In Figure 5.4, the envelope plot of the failure index I_m^t across the middle station front spar web is displayed for the external torque of 1657.5 Nm.[2]
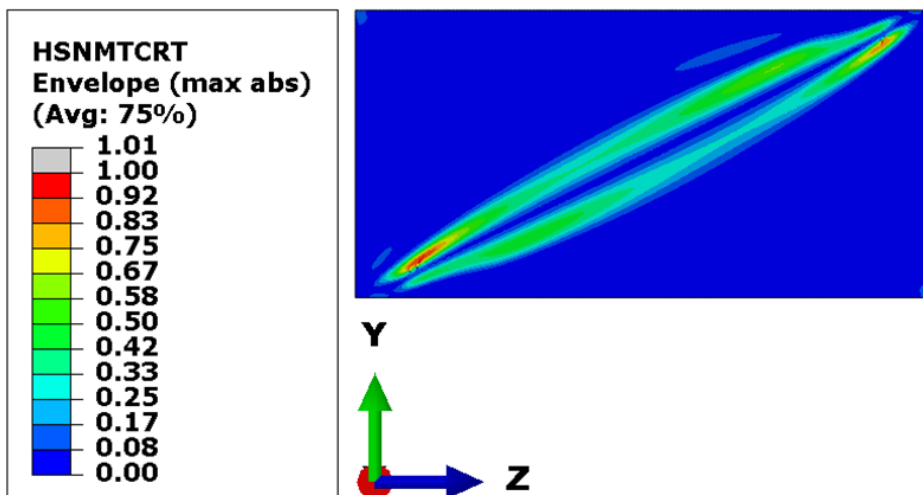
Figure 5.4: Configuration C-1 in a *no-restraint* condition — Envelope plot of the failure index I_m^t across the middle station front spar web for an external torque of 1657.5 Nm.

---

[2]The front spar web of all stations have practically the same plot. The envelope plot is reduced to the middle station of the wing box to improve the clarity of the results.

Taking into account that each wing box configuration has a different maximum external torque T_{max} (for which the spar webs experiment material failure in the *no-restraint* condition), the wing boxes' morphing capabilities are compared to each other as a function of the non-dimensional torque $\overline{T}$, which, according to Eq. (4.13), is defined as

$$\overline{T} = \frac{T}{T_{max}}$$

Therefore, the *Active Regions* of wing box configurations A-1, B-1 and C-1 are compared to each other in Figure 5.5, as a function of the non-dimensional torque $\overline{T}$.
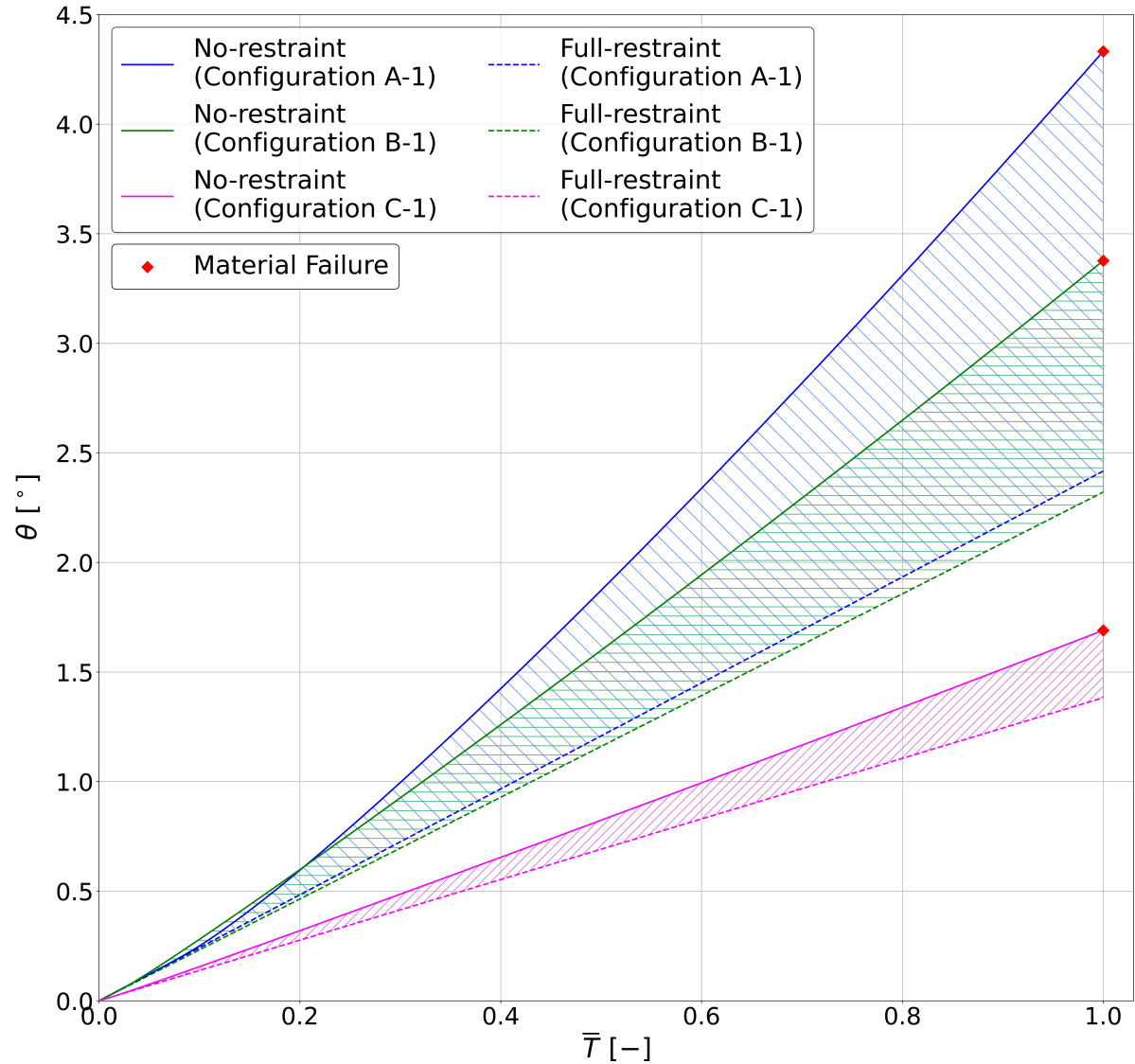
Figure 5.5: Active regions of wing box configurations A-1, B-1 and C-1 as a function of the non-dimensional torque $\overline{T}$.

Each *Active Region* encloses the different elastic tip twists that could be selected by actively adjusting the buckling constraints acting on the slender spar webs. In this way, the maximum active tip twist that could be introduced for a given external torque, referred to as the buckling-induced twist θ_b, is given by

$$\theta_b\left(\overline{T}\right) = \theta_{NR}\left(\overline{T}\right) - \theta_{FR}\left(\overline{T}\right) \tag{5.1}$$

where θ_{NR} is the elastic tip twist in the *no-restraint* condition and θ_{FR} is the elastic tip twist in the *full-restraint* condition. The evolution of the buckling-induced twist θ_b with the non-dimensional torque $\overline{T}$ is presented in Figure 5.6 for the three investigated wing box configurations.
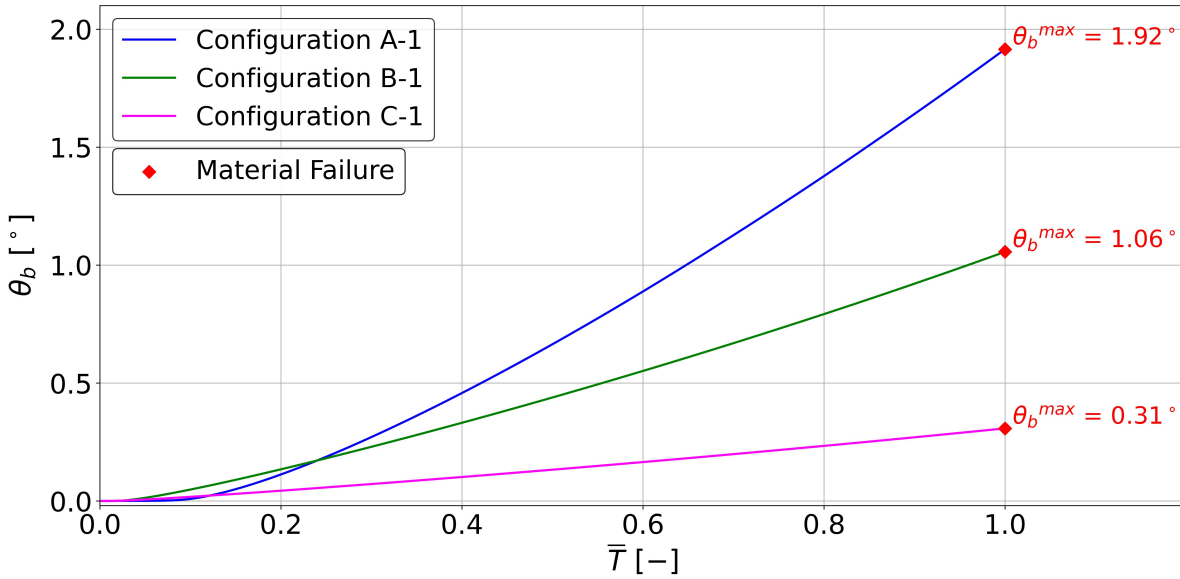
Figure 5.6: Evolution of the buckling-induced twist θ_b with the non-dimensional torque $\overline{T}$ for wing box configurations A-1, B-1 and C-1.

Figure 5.6 clearly illustrates that the buckling-induced twist θ_b for a given non-dimensional torque reduces as the cross-section size is increased.[3] Consequently, the maximum buckling-induced twist $\theta_b{}^{max}$ registers the greatest value of $1.92°$ for wing box A-1 and the lowest value of $0.31°$ for wing box C-1. The reasons why the maximum buckling-induced twist $\theta_b{}^{max}$ reduces for larger cross-sections are investigated through Eq. (4.16), namely,

$$\theta_b{}^{max} = \beta * \theta_{FR}{}^{max}$$

where $\theta_{FR}{}^{max}$ is the maximum twist in the *full-restraint* condition and β is the buckling-induced factor. These parameters are calculated for wing box configurations B-1 and C-1 by following the same procedure illustrated in Section 4.6 for wing box A-1. The values of these parameters are presented in Table 5.3 for wing box configurations A-1, B-1 and C-1, together with the buckling-induced twists $\theta_b{}^{max}$ calculated by substituting these parameters in Eq. (4.16). From Table 5.3, the maximum buckling-induced twist $\theta_b{}^{max}$ reduces as the cross-section size is increased due to a reduction in the twist $\theta_{FR}{}^{max}$ and a reduction in the buckling-induced factor β.

Table 5.3: Twist $\theta_{FR}{}^{max}$, buckling-induced factor β and maximum buckling-induced twist $\theta_b{}^{max}$ for wing box configurations A-1, B-1 and C-1.

Configuration	$\theta_{FR}{}^{max}$ [°]	β [−]	$\theta_b{}^{max}$ [°]
A-1 (60x60mm)	2.42	0.80	1.92
B-1 (100x100mm)	2.32	0.46	1.06
C-1 (150x150mm)	1.38	0.22	0.31

To understand why the twist $\theta_{FR}{}^{max}$ reduces for larger cross-sections, Table 5.4 presents the parameters used to calculate $\theta_{FR}{}^{max}$ according to Eq.(4.18), namely,

$$\theta_{FR}{}^{max} = \frac{T_{max}}{K_\theta^{FR}}$$

where T_{max} is the maximum external torque and K_θ^{FR} is the torsional stiffness in the *full-restraint* condition.

---

[3]Disregarding the behaviour registered for the buckling-induced twists created by non-dimensional torques $\overline{T} < 0.25$, which lack of practical application due to their low magnitudes.

Table 5.4: Maximum external torque T_{max}, torsional stiffness K_θ^{FR} and twist $\theta_{FR}{}^{max}$ for wing box configurations A-1, B-1 and C-1.

Configuration	T_{max} [Nm]	K_θ^{FR} [Nm/°]	$\theta_{FR}{}^{max}$ [°]
A-1 (60x60mm)	82.5	34.14	2.42
B-1 (100x100mm)	570.5	245.81	2.32
C-1 (150x150mm)	1657.5	1198.85	1.38

From Table 5.4, the torsional stiffness K_θ^{FR} becomes larger as the cross-section size is increased, which has the effect of reducing $\theta_{FR}{}^{max}$. This behaviour can be explained in terms of the influence that the area enclosed by the wing box cross-section has on the torsional stiffness. Based on the Bredt-Batho theory for the torsion of closed section beams ([64]), the torsional stiffness K_θ^{BB} of a beam with a uniform thin-walled closed section, subjected to a pure torque and free to warp, is given by:

$$K_\theta^{BB} = \frac{4}{L * \oint \frac{ds}{G*t}} * A_m{}^2 \tag{5.2}$$

where L is the beam length, ds is an infinitesimal segment along the cross-section, G is the material shear modulus, t is the wall thickness and A_m is the cross-sectional enclosed area, defined as the area enclosed by the midline of the cross-section's wall. For the wing box configurations A-1, B-1 and C-1, the cross-sectional enclosed areas can be calculated as:

$$A_m{}^A = (60mm - 3mm) * 60mm = 3420 \, mm^2$$
$$A_m{}^B = (100mm - 3mm) * 100mm = 9700 \, mm^2$$
$$A_m{}^C = (150mm - 3mm) * 150mm = 22050 \, mm^2$$

As the warping deformations are restrained at the ribs (which are modelled as ideally rigid through beam type MPC constraints), Eq. (5.2) underestimates the value for the torsional stiffness K_θ^{FR}. Nevertheless, Eq. (5.2) shows that the torsional stiffness has a quadratic dependency on the cross-sectional enclosed area A_m, which coincides with the relation registered between the torsional stiffnesses K_θ^{FR} of the wing boxes A-1, B-1 and C-1 and the cross-sectional enclosed areas A_m, as illustrated in Figure 5.7. The best-fit curve for a second degree monomial of the form $f(A_m) = a * A_m^2$, obtained by the method of least squares, is included in the plot, showing a very good fit to the data.
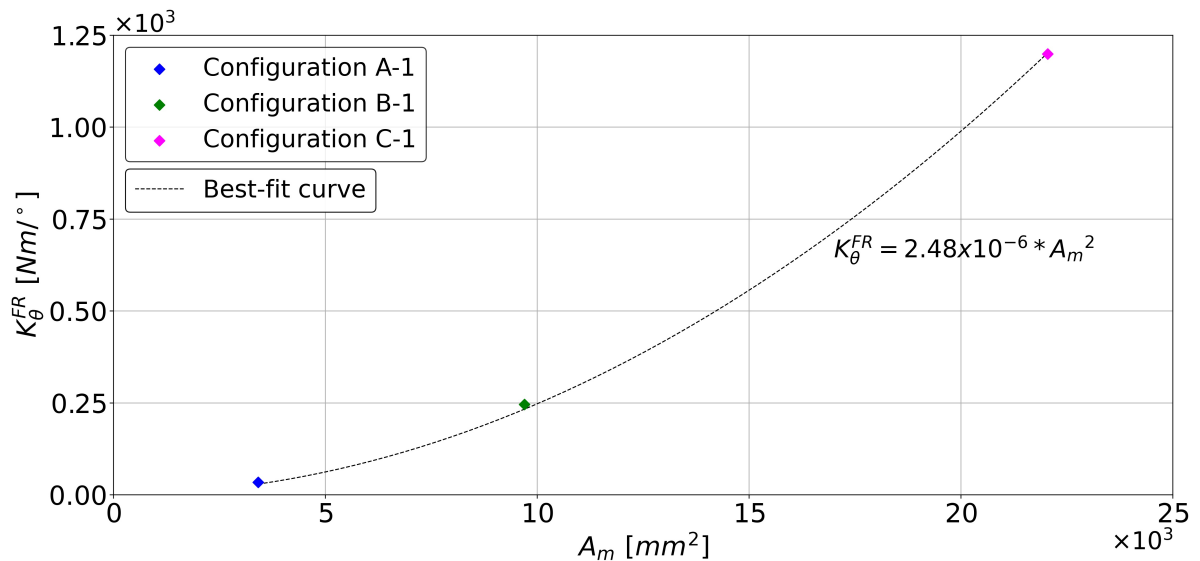
Figure 5.7: Wing box configurations A-1, B-1 and C-1 torsional stiffnesses in the *full-restraint* condition $K_\theta{}^{FR}$ as a function of the cross-sectional enclosed areas A_m.

On the other hand, from Table 5.4, the external torque T_{max} becomes larger as the cross-section size is increased, which has the effect of increasing θ_{FR}^{max}. Furthermore, for the investigated cross-sections, the external torque T_{max} shows a linear dependency on the cross-sectional enclosed area A_m, as illustrated in Figure 5.8. The best-fit line, obtained by the method of least squares, is included in the plot, showing a very good fit to the data.
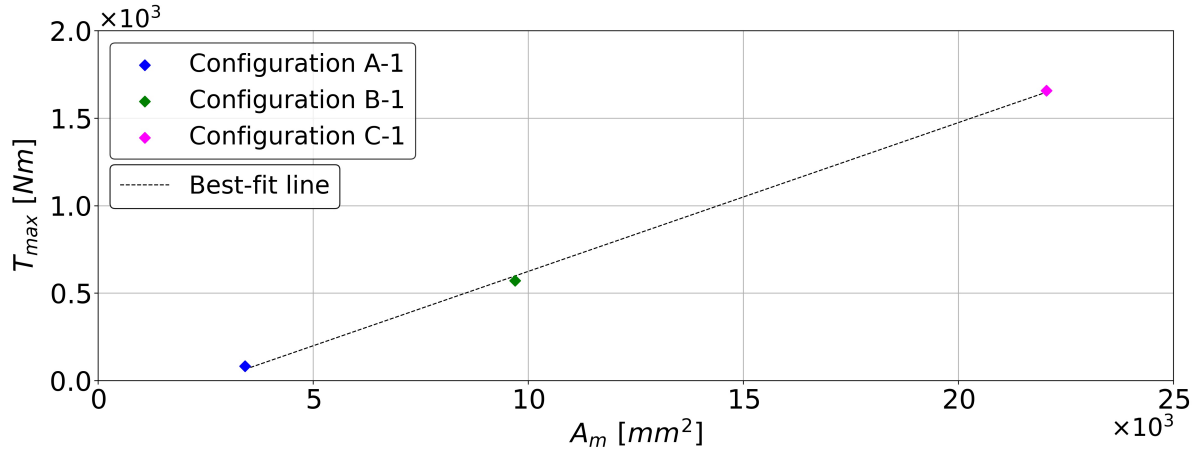
Figure 5.8: Wing box configurations A-1, B-1 and C-1 maximum external torques T_{max} as a function of the cross-sectional enclosed areas A_m.

This linear dependency of T_{max} on the cross-sectional enclosed area A_m can be explained in terms of the influence that the cross-sectional enclosed area A_m has on the shear flow acting on the spar webs. Based on the Bredt-Batho theory for the torsion of closed section beams ([64]), the constant shear flow q acting on a section of a thin-walled closed section beam subjected to a pure torque T and free to warp is related to the applied torque T by the following equation, often referred to as the Bredt-Batho formula:

$$T = 2 * q * A_m \tag{5.3}$$

Taking into account that the spar webs of wing boxes A-1, B-1 and C-1 have the same layups and unidirectional composite plies, one may assume that the post-buckled spar webs in the *no-restraint* condition fail for the same critical shear flow q_f. Under this hypothesis, Eq. (5.3) defines a linear relation between the enclosed area A_m and the maximum external torque T_{max}, given by

$$T_{max} = 2 * q_f * A_m \tag{5.4}$$

Overall, increasing the cross-sectional enclosed area A_m increases both the torsional stiffness K_θ^{FR} and the external torque T_{max}, which in turn have the opposite effects of reducing and increasing the twist θ_{FR}^{max}, respectively. For the 184% increase of A_m measured for wing box B-1 relative to wing box A-1, both effects tend to cancel each other, registering a 589% increase in T_{max} and a 620% increase in K_θ^{FR}, leading to a small 4% decrease of θ_{FR}^{max}.

However, due to the quadratic dependency of the torsional stiffness K_θ^{FR} on the enclosed area A_m, in contrast to the torque T_{max} linear dependency, the (percentage) increase of K_θ^{FR} becomes larger than the (percentage) increase of T_{max} as the enclosed area A_m is further increased. Consequently, for the 546% increase of A_m measured for wing box C-1 relative to wing box A-1, the twist θ_{FR}^{max} now experiments a large 43% reduction, due to a 3412% increase in torsional stiffness K_θ^{FR} and only a 1905% increase in T_{max}. Therefore, the twist θ_{FR}^{max} is expected to keep reducing (at a quadratic rate) as the cross-sectional enclosed area A_m is further increased.

On the other hand, it can be observed from Table 5.3 that the buckling-induced factor β also reduces for larger cross-sections, contributing to the reduction of the maximum buckling-induced twist θ_b^{max}. A lower buckling-induced factor β indicates smaller buckling-induced reductions in the effective shear stiffness of the spar webs, which in turn leads to lower buckling-induced reductions in the torsional stiffness of the wing box. The fact that lower buckling-induced reductions in torsional stiffness are achieved for larger cross-sections is illustrated in Figure 5.16 in terms of the evolution of the stiffness factor B with the non-dimensional torque $\overline{T}$.
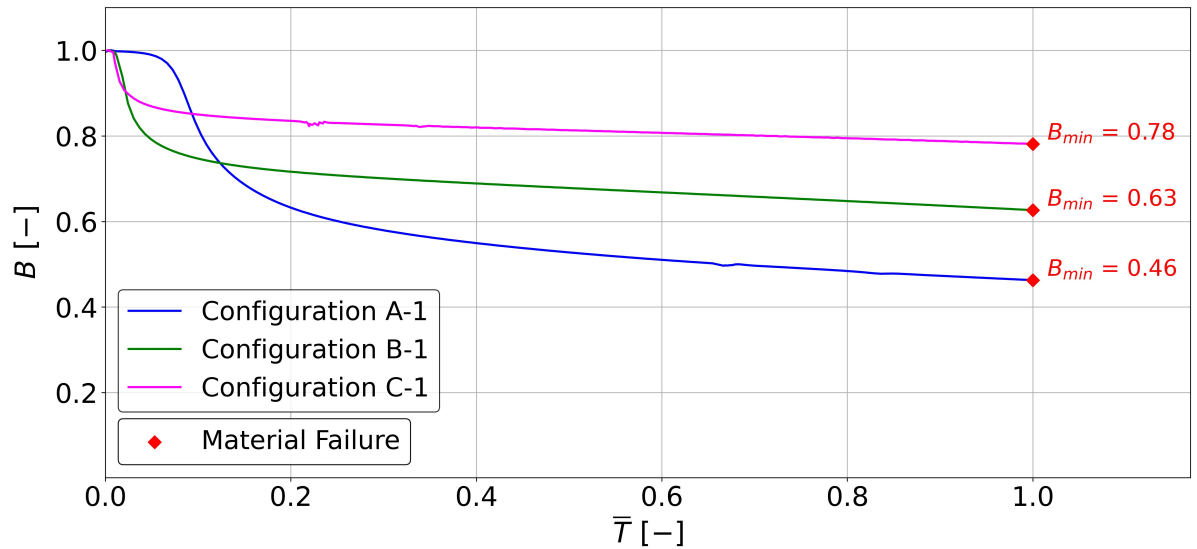
Figure 5.9: Evolution of the stiffness factor B with the non-dimensional torque $\overline{T}$ for wing box configurations A-1, B-1 and C-1.

As defined by Eq. (4.15), the stiffness factor B measures the ratio between the torsional stiffness provided by post-buckled spar webs in the *no-restraint* condition K_θ^{NR} and the torsional stiffness provided by non-buckling spar webs in the *full-restraint* condition K_θ^{FR}; namely,

$$B(\overline{T}) = \frac{K_\theta^{NR}\left(\overline{T}\right)}{K_\theta^{FR}}$$

From Figure 5.9, the higher stiffness factors B obtained for greater cross-sections indicate that the buckling-induced reductions in torsional stiffness are smaller for larger cross-sections, causing the wing box torsional stiffness in the *no-restraint* condition to be closer to that in the *full-restraint* condition. Ultimately, taking into account that the buckling-induced twist θ_b is defined as the difference in tip twist between the *no-restraint* and *full-restraint* conditions, this has the effect of reducing the buckling-induced twist θ_b.

Such differences in the evolution of the stiffness factor B are captured by the buckling-induced factor β, which Eq. (4.17) defines as:

$$\beta = \int_0^1 \frac{d\overline{T}}{B\left(\overline{T}\right)} - 1$$

Based on Eq. (4.17), smaller buckling-induced reductions in stiffness factor B lead to lower buckling-induced factors β, which in turn, according to Eq. (4.16), has the effect of reducing the maximum buckling-induced twist θ_b^{max}.

The reasons why smaller buckling-induced reductions in torsional stiffness are registered for larger cross-sections need to be further investigated. These reasons may be related to the fact that, in this dimensional study, the cross-sectional dimensions are affected without changing the distance between ribs, i.e. the wing box stations' lengths. Thus, the buckling-induced reductions in the spar webs' effective shear stiffnesses may be sensitive to the spar webs' aspect ratios, ultimately leading to different buckling-induced reductions in torsional stiffness. Secondly, based on the *St. Venant* principle ([65]), if the cross-section size is increased without affecting the distance between ribs, the constrained warping conditions imposed at the ribs' locations start having a greater influence over the structural response, which may have an effect on the buckling-induced reductions in torsional stiffness.

In conclusion, this dimensional study has shed light on the fact that greater buckling-induced twists θ_b^{max} can be created for wing boxes of smaller cross-section, due to their lower pre-buckling torsional stiffness and greater buckling-induced reductions in torsional stiffness. In this way, the morphing concept capability to actively twist the wing increases as the size of the wing box is reduced. On the other hand, the fact that a maximum buckling-induced twist of only 0.31° is predicted for a 150x150mm cross-section (Configuration C-1), illustrates that the morphing concept becomes difficult to realize for relatively large size wing boxes.

5.2. Material Study

Taking into account that greater buckling-induced twists can be created for higher external torques, the maximum external torque T_{max} that the wing box can support in the *no-restraint* condition limits the maximum buckling-induced twist $\theta_b{}^{max}$. Based on the material failure assessment performed in Section 4.3 for wing box A-1, the buckled spar webs fail in the *no-restraint* condition due to the low transverse tensile strength Y^t of the UD carbon plies IM7/8552. For this reason, it is of interest to investigate if the buckling-induced twists can be increased by substituting the spar webs' UD carbon plies for woven carbon fabric plies, of higher transverse tensile strength Y^t due to their additional fibre direction.

For this purpose, a new wing box configuration referred to as configuration A-2 is investigated, for which the spar webs are made of plain weave carbon fabric plies, instead of UD carbon plies. In particular, the prepreg TC250 reinforced by a HTS 12K PW carbon fabric is selected as representative material, whose material properties are presented in Table 5.5. These carbon fabric plies have a transverse tensile strength of $Y^t = 803\,MPa$, which is almost 14 times higher than the transverse tensile strength of the UD carbon plies IM7/8552, of $Y^t = 55\,MPa$.

Table 5.5: Material properties of carbon fabric plies HTS 12K PW/TC250 ([66]).

Property	Symbol	Value
Longitudinal Young's modulus	E_{11}	69.6 GPa
Transverse Young's modulus	E_{22}	68 GPa
Major Poisson's ratio	ν_{12}	0.045
In-plane shear modulus	G_{12}	4.5 GPa
Ply thickness	t_{ply}	0.27 mm
Longitudinal tensile strength	X^t	888 MPa
Longitudinal compressive strength	X^c	898 MPa
Transverse tensile strength	Y^t	803 MPa
Transverse compressive strength	Y^c	818 MPa
Shear strength	S	91.7 MPa

On the other hand, due to the undulation of the fibres (crimped fibres), the carbon fabric plies HTS 12K PW/TC250 have a longitudinal tensile strength of $X^t = 888\,MPa$, which is approximately a third of the UD carbon plies IM7/8552 longitudinal tensile strength, of $X^t = 2768\,MPa$. Nevertheless, this imposes no limitation on the maximum external torque T_{max}, as the post-buckled spar webs are far from failing in a fibre tension failure mode. For wing box A-1 under its failure torque of 82.5 Nm, the failure index associated to the fibre tension failure mode I_f^t reaches a maximum value across the spar webs lower than 0.02.

The ply thickness is another important difference between woven carbon fabric plies and UD plies. The woven carbon fibre tows lead to higher ply thicknesses than UD plies. Thus, an HTS 12K PW/TC250 carbon fabric ply presents a consolidated ply thickness of 0.27 mm, which is more than 2 times the ply thickness of an IM7/8552 UD carbon ply, of 0.125 mm. As the thickness of the spar webs influence the structural response, the spar webs of the wing box configuration A-2 are made of a single HTS 12K PW/TC250 carbon fabric ply, assigning a $+45°$ orientation to the front spar web ply and a $-45°$ orientation to the rear spar web ply. In this way, the spar webs present a thickness of 0.27 mm, which is very close to the thickness of the spar webs of wing box A-1, of 0.25 mm.

All other design parameters of wing box A-2, such as the wing box spanwise length, station length, cross-sectional dimensions and skins' materials and thicknesses, are kept the same as those assigned to wing box A-1. For clarity, Table 5.6 compares the general dimensions assigned to wing boxes A-1 and A-2, while the components' materials, layups and thicknesses are displayed in Table 5.7 for wing box A-1, and in Table 5.8 for wing box A-2.

Table 5.6: General dimensions of wing boxes A-1 and A-2.

Dimension	A-1	A-2
Width	60 mm	60 mm
Height	60 mm	60 mm
Spanwise length	900 mm	900 mm
Station length	300 mm	300 mm

Table 5.7: Materials, layups and thicknesses of wing box A-1.

Component	Material	Layup	Thickness
Skins	Aluminum Alloy	-	3 mm
Front spar web	IM7/8552	$[+45°/+45°]$	0.25 mm
Rear spar web	IM7/8552	$[-45°/-45°]$	0.25 mm

Table 5.8: Materials, layups and thicknesses of wing box A-2.

Component	Material	Layup	Thickness
Skins	Aluminum Alloy	-	3 mm
Front spar web	HTS 12K PW/TC250	$[+45°]$	0.27 mm
Rear spar web	HTS 12K PW/TC250	$[-45°]$	0.27 mm

The structural response of wing box A-1 to an external quasi-static torque in the *no-restraint* and *full-restraint* conditions has already been addressed in Sections 4.3 - 4.5. On the other hand, for the wing box configuration A-2, Figure 5.10 illustrates the evolution of its tip twist and torsional stiffness with the external quasi-static torque in the *no-restraint* and *full-restraint* conditions.
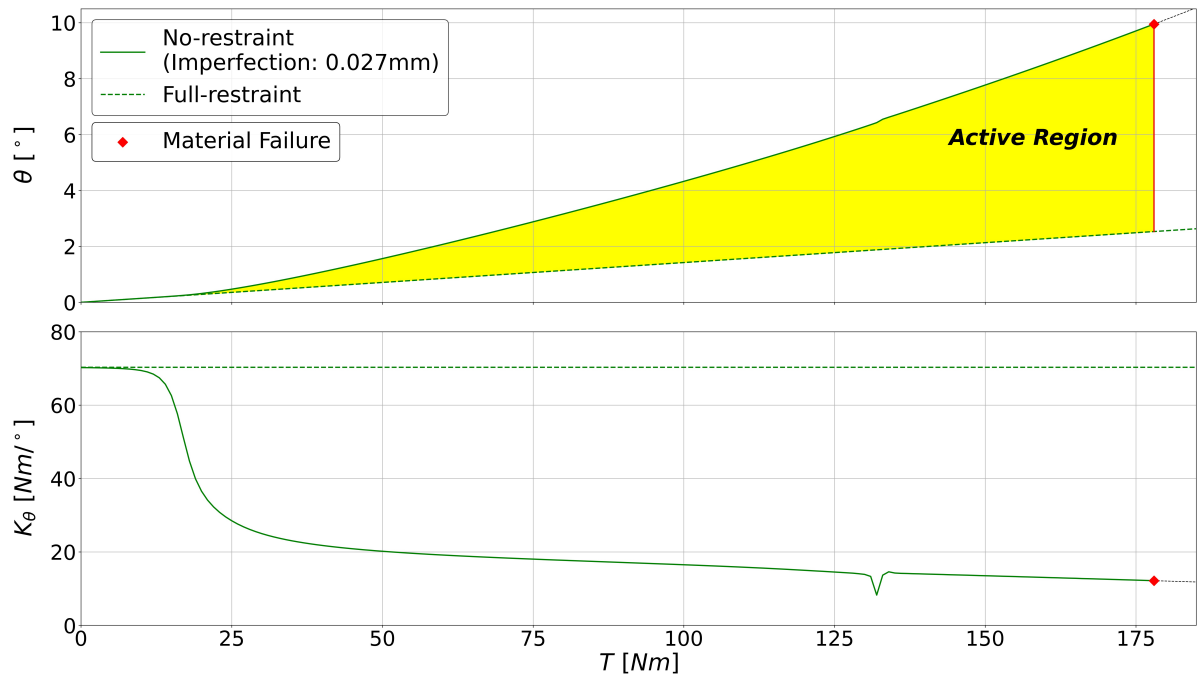
Figure 5.10: Configuration A-2 in the *no-restraint* and *full-restraint* conditions — Evolution of the tip elastic twist and torsional stiffness with the external quasi-static torque.

From Figure 5.10, the buckling of the spar webs in the *no-restraint* condition induces a reduction in torsional stiffness. The greatest reduction rate occurs at the onset of buckling, rapidly flattening off for higher torques as the spar webs progress into their post-buckling regimes. However, for the external torque of 133.0 Nm, the torsional stiffness experiments a sudden drop in value, in what is referred to as a *snapping event*. This drop in torsional stiffness is caused by a sudden change in the spar webs' buckling shape. However, as the new buckling shape stabilizes, the torsional stiffness increases again, returning to its original response (i.e., the response prior the snapping event).

On the other hand, with regard to the evolution of the elastic tip twist, the drop in torsional stiffness created by a snapping event induces a jump in twist angle (that can be identified in Figure 5.10). However, once the torsional stiffness settles again around its original response, the elastic tip twist continues increasing with the external torque at its original rate.

At the snapping event, the buckling shape of a spar web panel (i.e., between two adjacent ribs) snaps from a configuration constituted by 4 half-waves to a new configuration constituted by 3 half-waves. This buckling shape transition is illustrated in Figure 5.11 for the rear spar web panel of the root station, from which it can be observed that the half-wave closest to the root (i.e., closest to $Z = 0$) disappears, causing the three remaining half-waves to snap into new positions, filling up the space left by the dissipated half-wave. It should be highlighted that the evolution of the buckling shapes with the external torque will be analyzed in much more detail in Chapter 6.

(a)

(b)
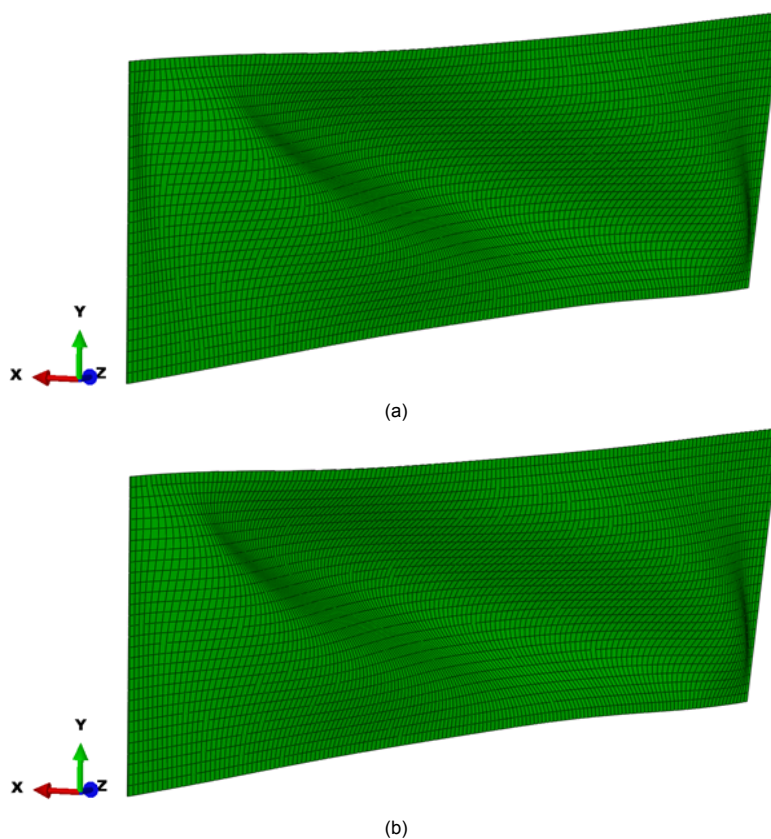
Figure 5.11: Configuration A-2 in the *no-restraint* condition — Deformed shape of the root station rear spar web at two different torque levels: (a) 132.0 Nm, (b) 133.0 Nm. Deformation scale factor: 3.

Taking into account that the Hashin failure criterion is developed for unidirectional composite materials, the Tsai-Hill failure criterion is applied to assess the material failure of wing box A-2 composite spar webs, which are made from plain weave carbon fabric plies. Applying the Tsai-Hill failure criterion, the front and rear spar webs are predicted to fail for the same external torque of 178.0 Nm. For this external torque, the associated failure index I_{TH} surpasses a value of 1. In Figure 5.12, the envelope plots of failure index I_{TH} across the middle station front and rear spar webs are displayed for the external torque of 178.0 Nm.[4]

---

[4] The spar webs of all stations have practically the same plot. The envelope plot is reduced to the middle station of the wing box to improve the clarity of the results.
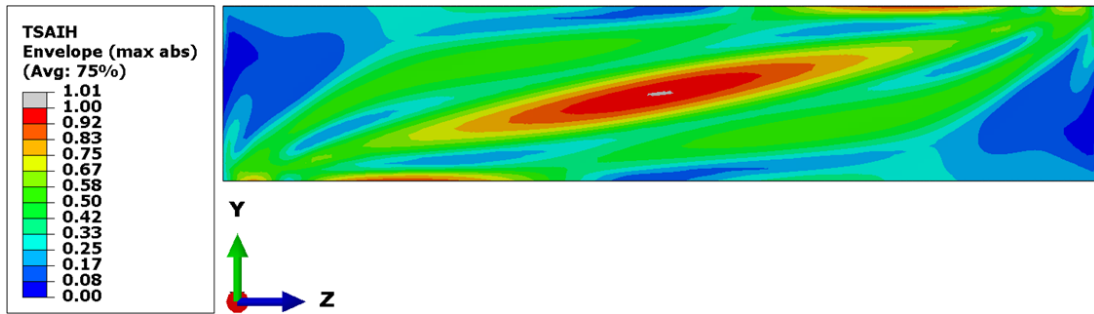
(a)
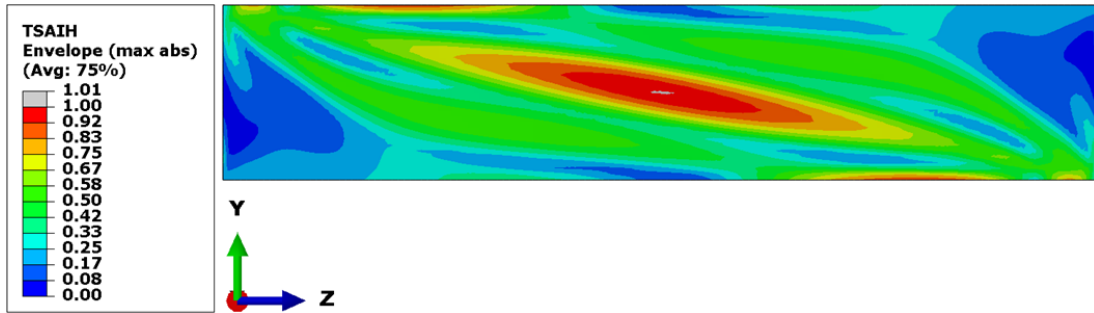
(b)

Figure 5.12: Configuration A-2 in the *no-restraint* condition for an external torque of 178.0 Nm — Envelope plot of failure index I_{TH} across the middle station (a) front spar web and (b) rear spar web.

As the Hashin failure criterion is developed for unidirectional composite plies, it overestimates the maximum external torque that the spar webs can sustain previous material failure. Illustrating this, Figure 5.13 presents the envelope plot of the the failure index I_m^t (Hashin failure index associated to a tensile matrix failure mode) across the middle station front and rear spar webs for the external torque of 178.0 Nm. It should be highlighted that the failure index associated to the tensile matrix failure mode I_m^t registers the greatest values among the four different failure indexes considered in the Hashin failure criterion.

(a)

(b)

Figure 5.13: Configuration A-2 in the *no-restraint* condition for an external torque of 178.0 Nm — Envelope plot of failure index I_m^t across the middle station (a) front spar web and (b) rear spar web.

From Figure 5.13, it can be observed that the failure index I_m^t only reaches a maximum value of 0.79, meaning that the spar webs could support greater torques than 178.0 Nm. Furthermore, the maximum values are not registered at the locations experimenting the greatest out-of-plane buckling deformations, but, they locate at the interfaces between the spar webs and the skins. At the spar webs' locations experimenting the greatest out-of-plane buckling deformations, the failure index values are lower than 0.5. Overall, the Hashin failure criterion provides inaccurate predictions when assessing the material failure of spar webs made from carbon fabric plies HTS 12K PW/TC250.

On the other hand, to analyze how the morphing capabilities are affected by the change in the spar webs' material, the *Active Regions* of wing boxes A-1 and A-2 are compared to each other in Figure 5.14, as a function of the non-dimensional torque $\overline{T}$.
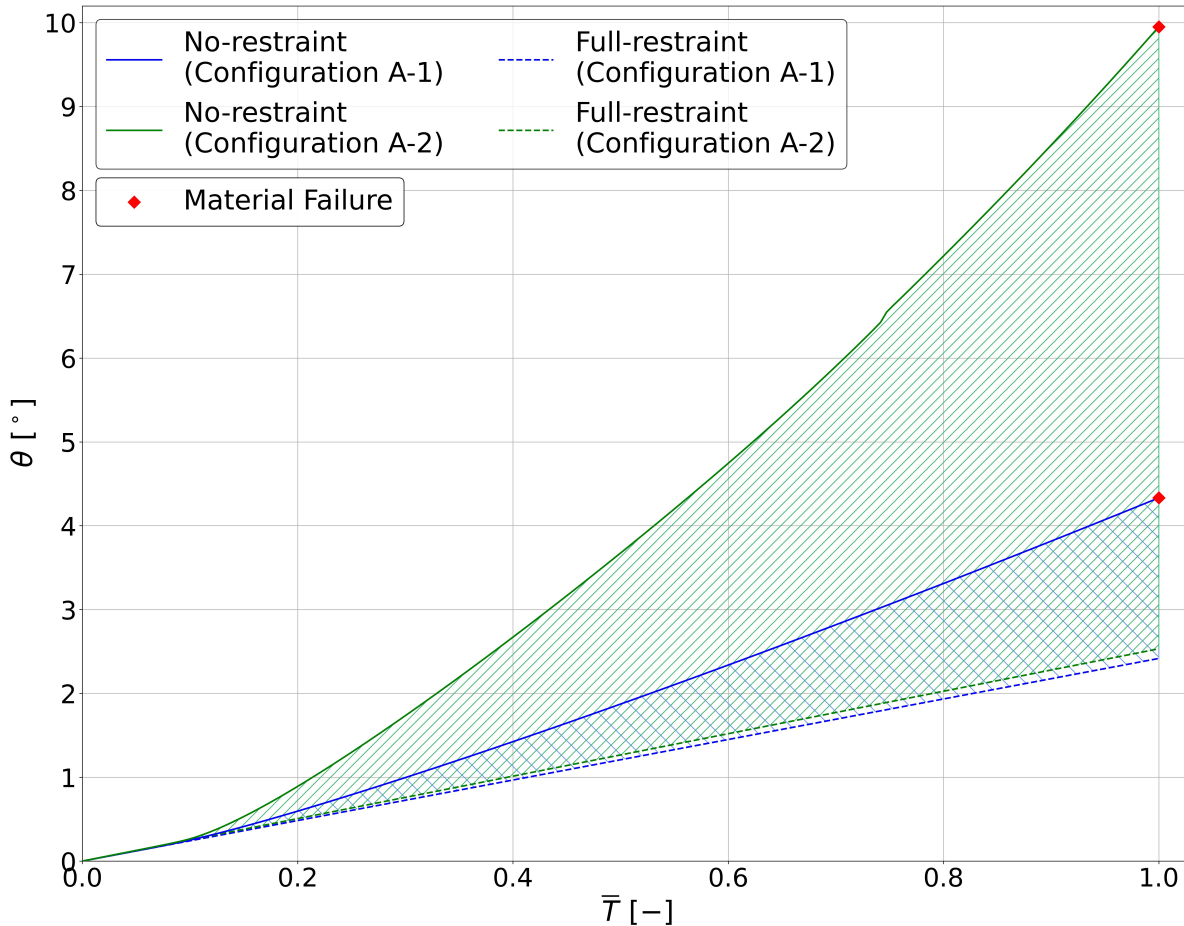
Figure 5.14: Active regions of wing box configurations A-1 and A-2 as a function of the non-dimensional torque $\overline{T}$.

Each *Active Region* encloses the different elastic tip twists that could be selected by actively adjusting the buckling constraints acting on the slender spar webs. In this way, the maximum active tip twist that could be introduced for a given external torque, referred to as the buckling-induced twist θ_b, is given by Eq. (5.1), namely,

$$\theta_b\left(\overline{T}\right) = \theta_{NR}\left(\overline{T}\right) - \theta_{FR}\left(\overline{T}\right)$$

where θ_{NR} is the elastic tip twist in the *no-restraint* condition and θ_{FR} is the elastic tip twist in the *full-restraint* condition. The evolution of the buckling-induced twist θ_b with the non-dimensional torque $\overline{T}$ is presented in Figure 5.15 for wing boxes A-1 and A-2.

From Figure 5.15, higher buckling-induced twists θ_b are obtained for spar webs made from plain weave carbon fabric plies than for spar webs made from UD carbon plies. In particular, the wing box A-2 reaches a maximum buckling-induced twist of $\theta_b{}^{max} = 7.42°$, which is almost 4 times the maximum buckling-induced twist of wing box A-1, of $\theta_b{}^{max} = 1.92°$.
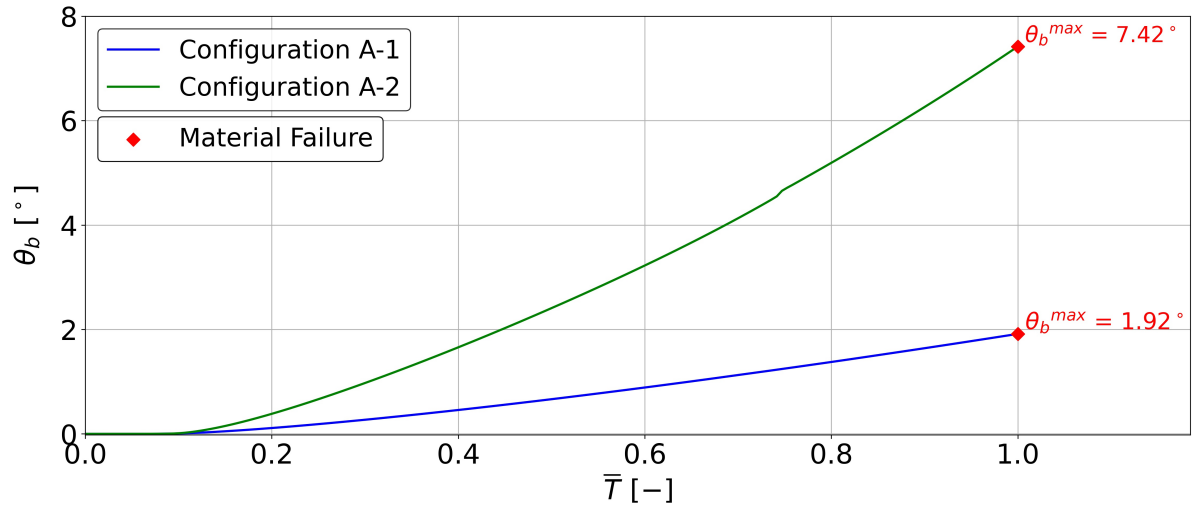
Figure 5.15: Evolution of the buckling-induced twist θ_b with the non-dimensional torque $\overline{T}$ for wing box configurations A-1 and A-2.

The reasons why a greater maximum buckling-induced twist $\theta_b{}^{max}$ is predicted for wing box A-2 can be investigated through Eq. (4.16), namely,

$$\theta_b{}^{max} = \beta * \theta_{FR}{}^{max}$$

where $\theta_{FR}{}^{max}$ is the maximum twist in the *full-restraint* condition and β is the buckling-induced factor. These parameters are calculated for wing box A-2 by following the same procedure illustrated in Section 4.6 for wing box A-1. The values of these parameters are presented in Table 5.9 for wing box configurations A-1 and A-2, together with the buckling-induced twists $\theta_b{}^{max}$ calculated by substituting these parameters in Eq. (4.16).

Table 5.9: Twist $\theta_{FR}{}^{max}$, buckling-induced factor β and maximum buckling-induced twist $\theta_b{}^{max}$ for wing box configurations A-1 and A-2.

Configuration	$\theta_{FR}{}^{max}$ [°]	β [−]	$\theta_b{}^{max}$ [°]
A-1	2.42	0.80	1.92
A-2	2.53	2.94	7.42

From Table 5.9, the wing box A-2 reaches a higher maximum buckling-induced twist $\theta_b{}^{max}$ than wing box A-1 because it has a higher twist $\theta_{FR}{}^{max}$ and a greater buckling-induced factor β than wing box A-1. In particular, the greatest contribution is provided by the buckling-induced factor β, which is 267% higher than that of wing box A-1. On the other hand, the twist $\theta_{FR}{}^{max}$ is only 4.5% greater than that of wing box A-1.

First, to understand why wing box A-2 presents a twist $\theta_{FR}{}^{max}$ that is 4.5% greater than that of wing box A-1, Table 5.4 presents the parameters used to calculate $\theta_{FR}{}^{max}$ according to Eq. (4.18), namely, the maximum external torque T_{max} and the torsional stiffness in the *full-restraint* condition K_θ^{FR}.

Table 5.10: Maximum external torque T_{max}, torsional stiffness K_θ^{FR} and twist $\theta_{FR}{}^{max}$ for wing box configurations A-1 and A-2.

Configuration	T_{max} [Nm]	K_θ^{FR} [Nm/°]	$\theta_{FR}{}^{max}$ [°]
A-1	82.5	34.14	2.42
A-2	178.0	70.30	2.53

From Table 5.10, the wing box A-2 presents a maximum external torque T_{max} that is 116% greater than that of wing box A-1, in part due to the carbon fabric plies having a higher transverse tensile strength Y_t than the UD carbon plies. On the other hand, as the carbon fabric plies are also stiffer than the UD carbon plies, they provide wing box A-2 of a torsional stiffness K_θ^{FR} that is 106% greater than wing box A-1 torsional stiffness.

Therefore, the change of the spar webs' material from UD carbon plies to plain weave carbon fabric plies increases both the maximum external torque T_{max} and the torsional stiffness K_θ^{FR}, which in turn have the opposite effects of increasing and reducing $\theta_{FR}{}^{max}$, respectively. Then, as both effects cancel each other, the change in material only causes a slight 4.5% increase in $\theta_{FR}{}^{max}$.

On the other hand, the fact that the buckling-induced factor β of wing box A-2 is 267% greater than that of wing box A-1 (from Table 5.9) indicates that the buckling-induced reductions in the spar webs' effective shear stiffnesses are much greater when the spar webs are made from plain weave carbon fabric plies instead of UD carbon plies. Consequently, the buckling-induced reductions in torsional stiffness are much greater for wing box A-2 than for wing box A-1, which is illustrated in Figure 5.16 in terms of the evolution of the stiffness factor B with the non-dimensional torque $\overline{T}$.
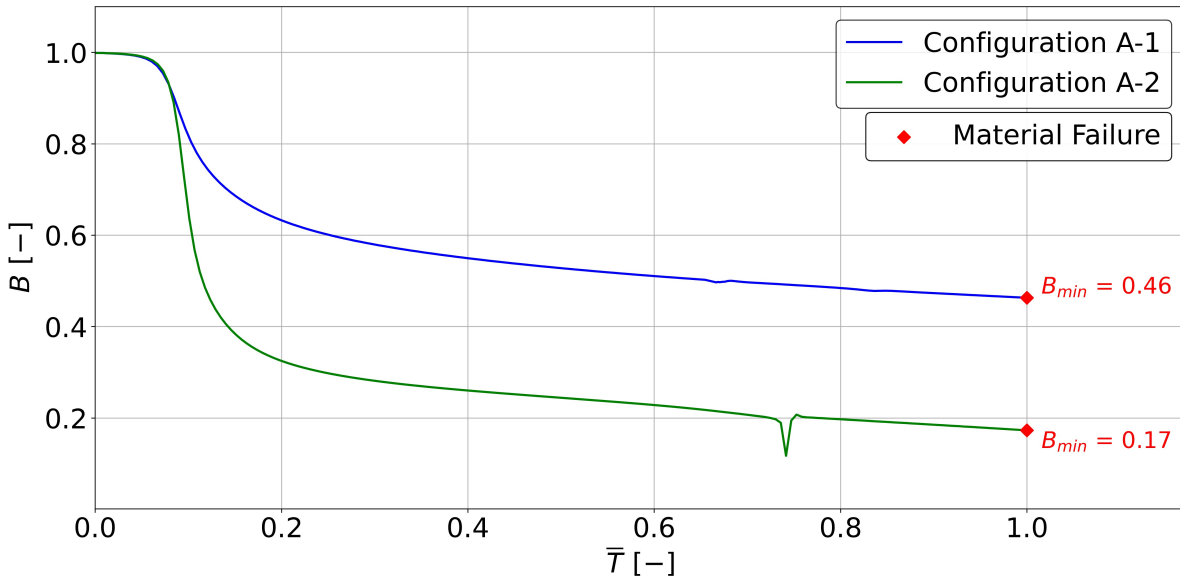
Figure 5.16: Evolution of the stiffness factor B with the non-dimensional torque $\overline{T}$ for wing box configurations A-1 and A-2.

From Figure 5.16, at the onset of buckling, the torsional stiffness of wing box A-2 (in the *no-restraint* condition) reduces almost a 30% more than that of wing box A-1, relative to their respective pre-buckling torsional stiffness values. This difference, measured in terms of the stiffness factor B, maintains practically constant as the spar webs progress further into their post-buckling regimes for higher torques. Ultimately, such difference in the evolution of the stiffness factor B is captured by the buckling-induced factor β, which Eq. (4.17) defines as:

$$\beta = \int_0^1 \frac{d\overline{T}}{B\left(\overline{T}\right)} - 1$$

registering for wing box A-2 a 267% greater buckling-induced factor β than for wing box A-1.

The reasons why the spar webs' buckling-induced reductions in effective shear stiffness are greater when made from plain weave carbon fabric plies HTS 12K PW/TC250 instead of UD carbon plies IM7/8552 can be attributed to the different elastic properties of the materials, most probably to the higher transverse Young's modulus E_{22} and/or the lower Poisson's ratio ν_{12} of the carbon fabric plies.

In conclusion, this material study has shed light on the fact that spar webs made from plain weave carbon fabric plies can lead to much higher buckling-induced twists than spar webs made from unidirectional carbon plies. On one hand, the original motivation for this study, of increasing the buckling-induced twists by increasing the maximum external torque T_{max}, did not lead to great increases in buckling-induced twist. The reason is that the pre-buckling torsional stiffness was found to also increase with the change of material, cancelling out most of the benefits associated to a higher T_{max}. However, the change of material still allowed for a great increase in the buckling-induced twist, as the spar webs were found to experiment much greater buckling-induced reductions in effective shear stiffness when made from plain weave carbon fabric plies instead of UD carbon plies.

5.3. Imperfection sensitivity

As explained in Section 4.1, a geometrical imperfection is introduced into the slender spar webs when calculating the wing box structural response to an external quasi-static torque in the *no-restraint* condition. This geometrical imperfection is introduced by superposing the shape functions of the first 3 buckling modes for a positive external torque, scaled to a maximum deflection of 10% the spar web thickness.

However, taking into account that the geometrical imperfection is an unknown that depends on manufacturing constraints, it is of interest to investigate if the buckling-induced twist θ_b is sensitive to the level of geometrical imperfection. Assuming that a maximum out-of-plane deflection as high as three times the spar web thickness may be created during manufacturing, the twisting response of the wing box configuration A-2 in the *no-restraint* condition is recalculated considering a geometrical imperfection with a maximum out-of-plane deflection of 0.81 mm (3 times the 0.27 mm thickness of the spar webs).

The wing box configuration A-2, introduced in Section 5.2, has a 60x60 mm cross-section and spar webs made from a single plain weave carbon fabric ply HTS 12K PW/TC250. Its twisting response in the *no-restraint* condition for a geometrical imperfection of 0.027 mm has already been addressed in Section 5.2. On the other hand, its twisting response for a geometrical imperfection of 0.81 mm is presented below.

The tip elastic twist and torsional stiffness of the wing box A-2 in the *no-restraint* condition and for a geometrical imperfection of 0.81 mm is presented in Figure 5.17, as a function of the external quasi-static torque.
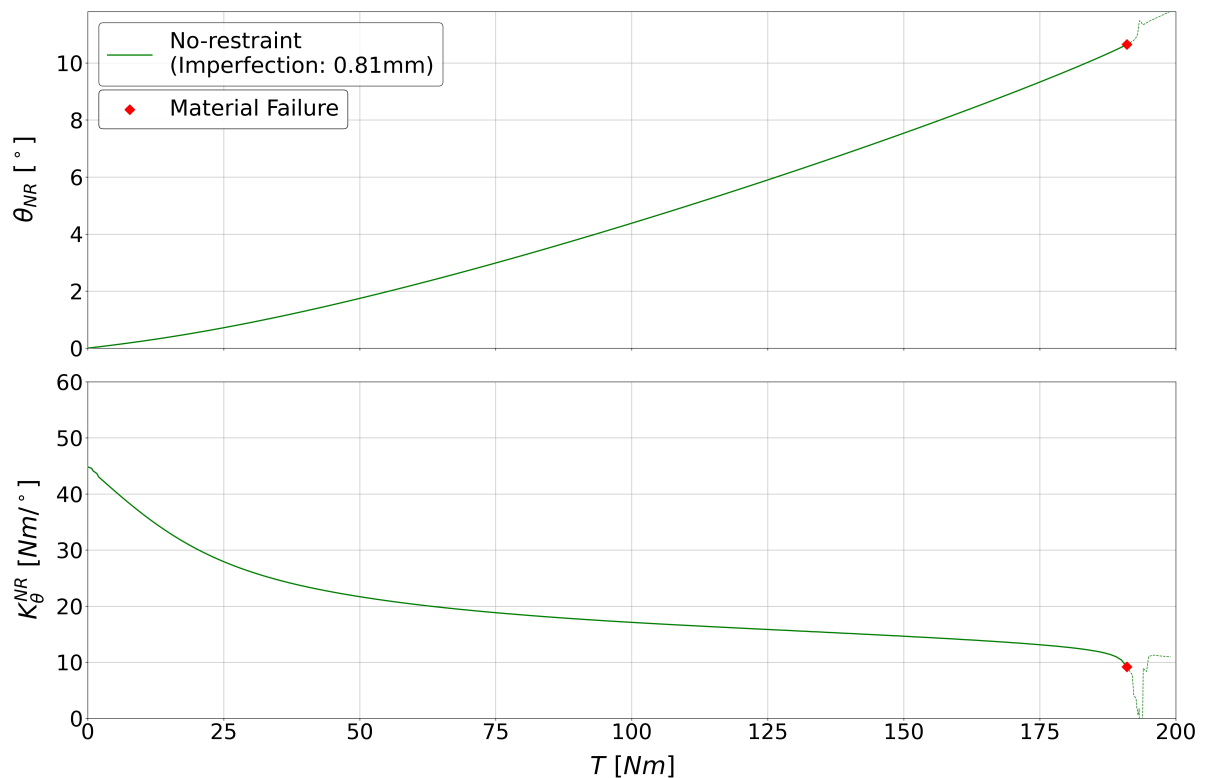
Figure 5.17: Configuration A-2 in the *no-restraint* condition for a geometrical imperfection of 0.81 mm — Evolution of the tip elastic twist and torsional stiffness with the external quasi-static torque.

Applying the Tsai-Hill failure criterion to assess the material failure of the composite spar webs, the front and rear spar webs fail for the same external torque of 191.0 Nm. For this external torque, the associated failure index I_{TH} surpasses a value of 1. In Figure 5.18, the envelope plots of the failure index I_{TH} across the middle station front and rear spar webs are displayed for the external torque of 191.0 Nm.[5]

---

[5]The spar webs of all stations have practically the same plot. The envelope plot is reduced to the middle station of the wing box to improve the clarity of the results.
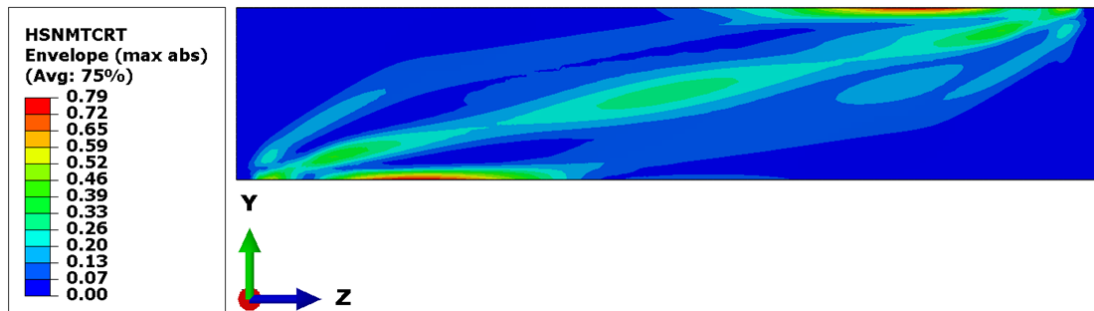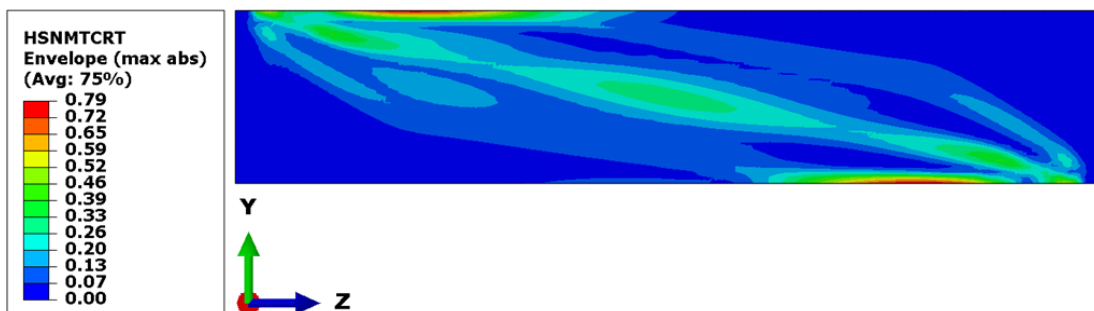
(a)

(b)
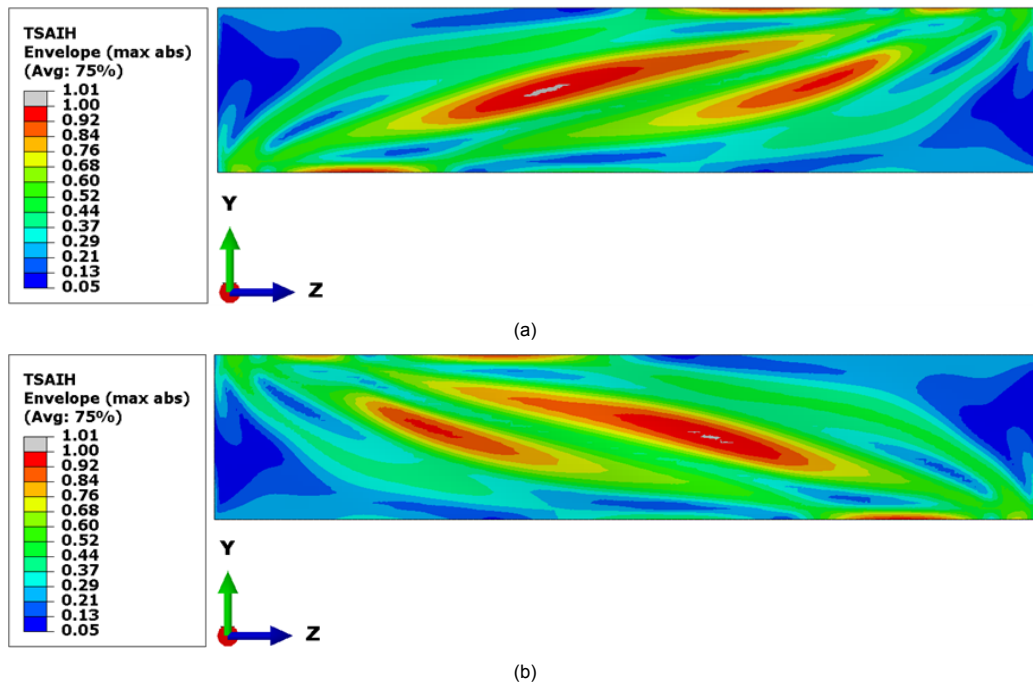
Figure 5.18: Configuration A-2 in the *no-restraint* condition for a geometrical imperfection of 0.81 mm and an external torque of 191.0 Nm — Envelope plot of failure index I_{TH} across the middle station (a) front spar web and (b) rear spar web.

To analyze the sensitivity of the twisting response to the level of geometrical imperfection, Figure 5.19 presents the tip twist and torsional stiffness of wing box A-2 in the *no-restraint* condition for the two investigated geometrical imperfections, of 0.027 mm and 0.81 mm. Furthermore, the evolution of the tip twist and torsional stiffness in the *full-restraint* condition is also presented in Figure 5.19.
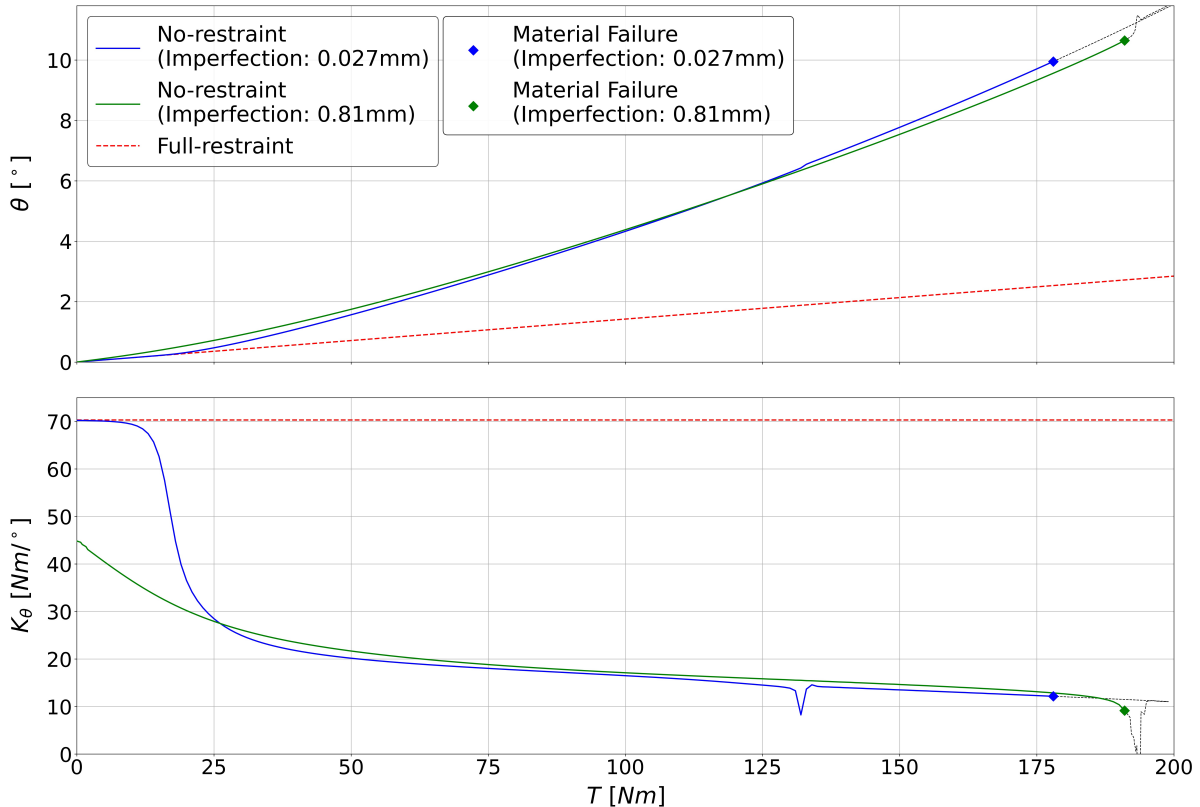
Figure 5.19: Configuration A-2 — Evolution of the tip elastic twist and torsional stiffness with the external quasi-static torque in the *full-restraint* and *no-restraint* conditions for different levels of geometrical imperfection.

From Figure 5.19, for the large geometrical imperfection of 0.81 mm, the spar webs are in a post-buckled state since the very beginning of the loading path, causing the initial torsional stiffness to be lower than that provided by spar webs with no geometrical imperfection (represented by the torsional stiffness in the *full-restraint* condition). Analyzing this phenomenon in terms of the stiffness factor B, defined by Eq. (4.15) as the ratio between the torsional stiffness provided by post-buckled spar webs in the *no-restraint* condition K_θ^{NR} and the torsional stiffness provided by non-buckling spar webs in the *full-restraint* condition K_θ^{FR}, the evolution of the stiffness factor B with the external quasi-static torque T is presented in Figure 5.20 for the two geometrical imperfections under consideration.
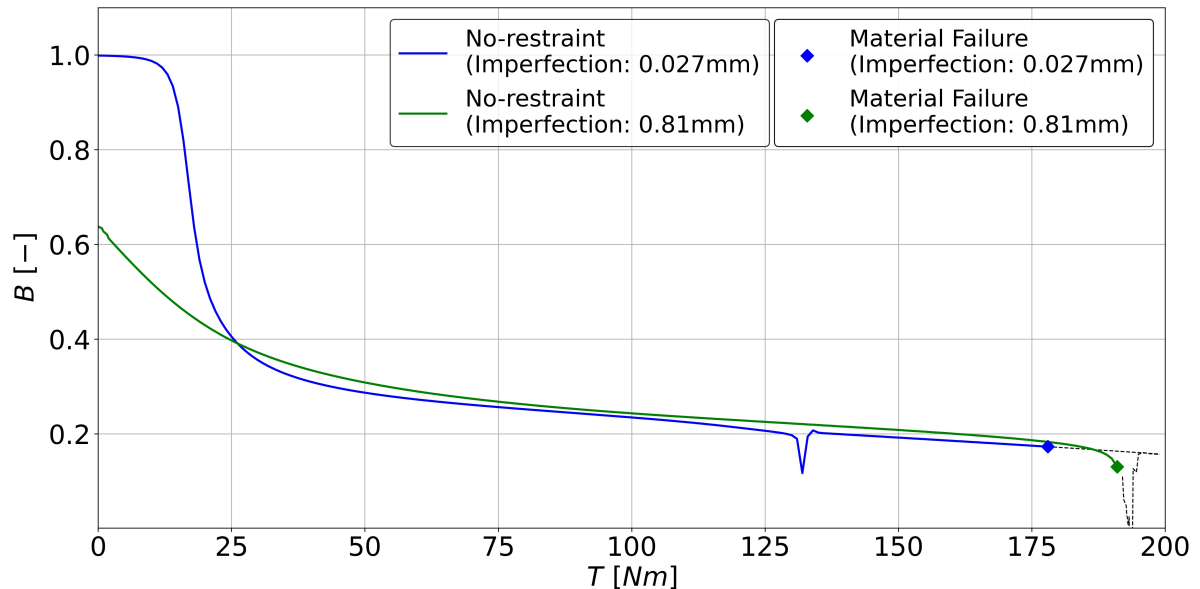
Figure 5.20: Configuration A-2 — Evolution of the stiffness factor B with the external quasi-static torque for different levels of geometrical imperfection.

From Figure 5.20, for the spar webs with a 0.027 mm geometrical imperfection, the wing box initial torsional stiffness coincides with that obtained for spar webs with no geometrical imperfection. On the other hand, for the large geometrical imperfection of 0.81 mm, the wing box initial torsional stiffness is a 36% smaller. Nevertheless, as the torque increases, both torsional stiffnesses become closer to each other, practically coalescing into the same response.

On the other hand, the critical torques at which snapping events occur, recognized in Figure 5.19 by sudden drops in torsional stiffness (and in Figure 5.20 by sudden drops in stiffness factor B), are sensitive to the level of geometrical imperfection. Thus, for the geometrical imperfection of 0.027 mm, a snapping event occurs for a critical torque of 133.0 Nm, while for the geometrical imperfection of 0.81 mm, the snapping event occurs for a higher critical torque, of 193.0 Nm (which is higher than the maximum external torque of 191.0 Nm). However, as the snapping events create local changes in torsional stiffness that rapidly settle around the original response (i.e., the response prior the snapping event), the torsional stiffness global evolution is not affected by snapping events occurring at different critical torques.

Finally, to analyze the sensitivity of the twist morphing capabilities to the level of geometrical imperfection, the *Active Regions* and buckling-induced twists θ_b predicted for the two different levels of geometrical imperfection are compared to each other in Figure 5.21 and Figure 5.22, respectively, as a function of the external quasi-static torque.

From Figure 5.22, at the beginning of the loading path, higher buckling-induced twists θ_b are obtained for the configuration with a 0.81 mm geometrical imperfection, as the wing box initial torsional stiffness is lower for spar webs with a 0.81 mm geometrical imperfection than for spar webs with a 0.027 mm geometrical imperfection. However, as the torque increases, the difference between both torsional stiffnesses reduces, and the rate at which the tip twist increases with the external torque becomes practically independent of the level of geometrical imperfection. This behaviour, together with the jumps in twist angle induced by snapping events, cause both configurations' buckling-induced twists θ_b to stay very close to each other along the loading path, as illustrated in Figure 5.22.
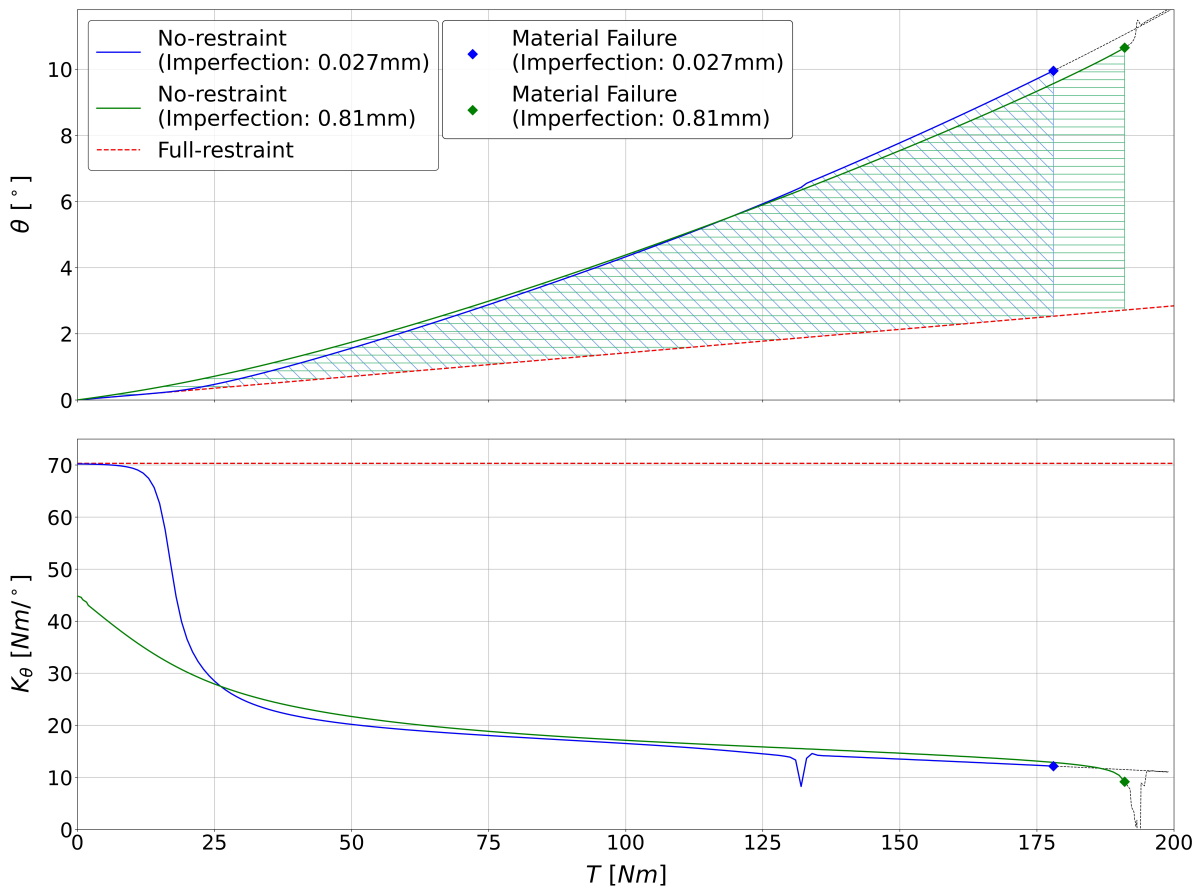
Figure 5.21: Configuration A-2 — Active regions for different levels of geometrical imperfection as a function of the external quasi-static torque T.
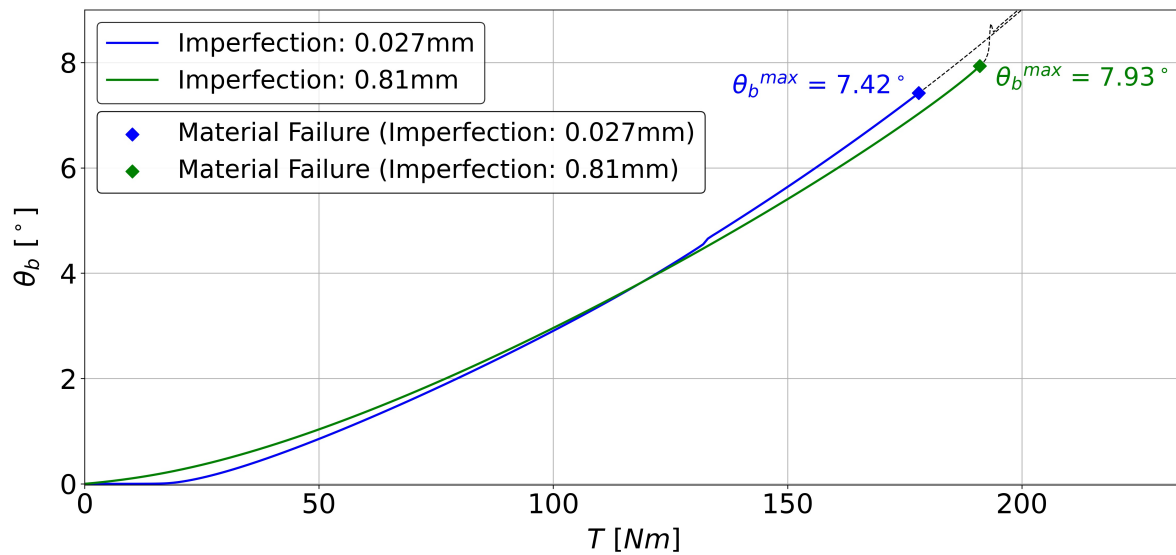
Figure 5.22: Configuration A-2 — Evolution of the buckling-induced twist θ_b with the external quasi-static torque T for different levels of geometrical imperfection.

In conclusion, the active twist created by an external quasi-static torque when adjusting the buckling constraints from the *full-restraint* condition to the *no-restraint* condition, i.e., the buckling-induced twist θ_b, is not sensitive to the level of geometrical imperfection. For the two extremes of the spectrum, defined by a minimum imperfection of 10% the spar web thickness, and a maximum imperfection of 300% the spar web thickness, the maximum buckling-induced twist $\theta_b{}^{max}$ differs only by 0.5°, as illustrated in Figure 5.22.

However, it should be highlighted that the twisting response in the *full-restraint* condition has only been predicted for spar webs with no geometrical imperfection, that are ideally prevented from buckling. Under these conditions, the wing box structural response to an external quasi-static torque can be determined by a linear static general analysis, which cannot capture the spar webs' non-linear buckling instabilities. However, a *full-restraint* condition for spar webs with an initial geometrical imperfection has not been yet defined, nor investigated.

According to the constraint-strategy that will be introduced in Chapter 6, the slender spar webs are bilaterally constrained in a *full-restraint* condition, restraining their out-of-plane buckling deformations to a maximum value that coincides with the initial maximum out-of-plane deflection introduced as geometrical imperfection. Under this type of buckling constraint, the spar webs operate in a post-buckled state under bilateral constraints, and hence the twisting response cannot be predicted without modeling the external devices required to implement such bilateral constraints. For this reason, the influence that the level of geometrical imperfection has on the twisting response in the *full-restraint* condition will be investigated in Chapter 7, where the structural finite element model is expanded to include both the wing box and the external constraining devices.

6

Wing box with adaptive constraints: Structural model

In this chapter, the final design for a wing box structure of promising twist morphing capabilities is presented. The structure comprises both the wing box and the external devices required to implement the adaptive constraints acting on the slender spar webs' out-of-plane buckling deformations. While the wing box design is determined from the exploration of the design space performed in Chapter 5, the design solution for the adaptive constraining devices is the result of an extensive design process. In the efforts of maximizing the morphing twists, the constraining devices' influence over the twisting response and their capability to restrain the spar webs' buckling deformations become the main concerns in the design of the adaptive constraining devices.

The assembly consisting of the wing box and the adaptive constraining devices is referred to as the *expanded wing box*. The investigated wing box is presented in Section 6.1, while the design for the adaptive constraining devices is introduced in Section 6.2. On the other hand, the expanded wing box FEM used to analyze the twist morphing capabilities is described in Section 6.3.

6.1. Wing box

For this study, the wing box configuration A-2 is investigated, as it showed the best morphing capabilities among the different configurations analyzed in Chapter 5. Presented in Section 5.2, this wing box configuration has a spanwise length of 900mm, a uniform cross-section of 60x60 mm, and comprises four panels: the front and rear spar webs and the top and bottom skins. Illustrated in Figure 6.1, the height of 60 mm is measured between the skins outer surfaces, while the width of 60 mm is measured between the spar webs' midlines. Furthermore, as illustrated in Figure 6.2, the wing box is divided into 3 stations of 300 mm by positioning 4 equally spaced ideal rigid ribs, with one rib located at the wing box tip and another at the root.
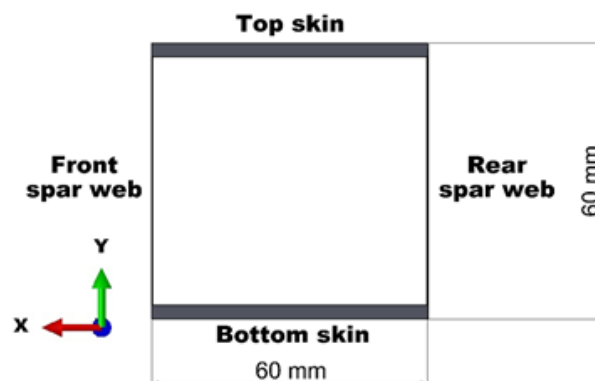
Figure 6.1: Cross-section of wing box configuration A-2 .
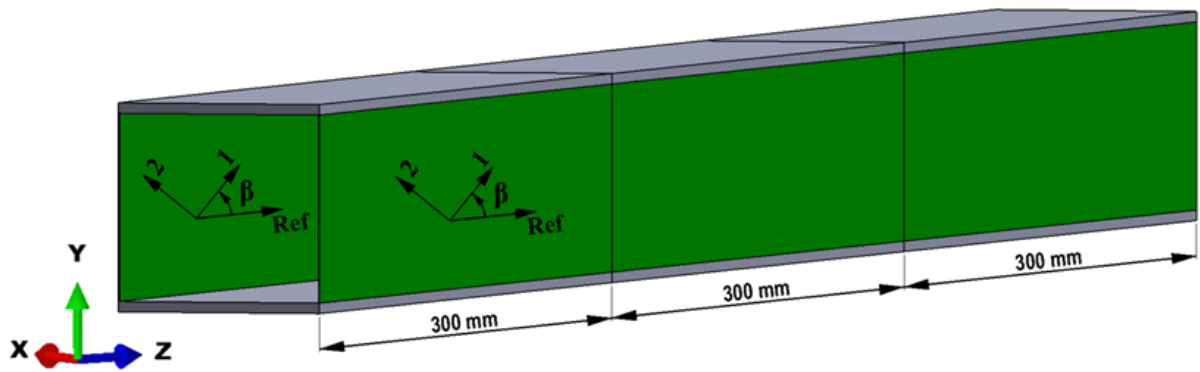
Figure 6.2: Principal axes orientation β of the front and rear spar webs' plies.

The top and bottom skins consist of 3mm thickness aluminum alloy panels, whose material properties are presented in Table 4.1. On the other hand, the front and rear spar webs are made of plain weave carbon fabric plies HTS 12K PW/TC250, whose material properties are presented in Table 5.5. Both composite spar webs are made of a single ply, oriented in opposite directions by assigning a $+45°$ orientation to the front spar web ply and a $-45°$ orientation to the rear spar web ply, both measured counter-clockwise relative to the spanwise axis when seen from the rear side of the wing box, as illustrated in Figure 6.2.

6.2. Adaptive constraining devices

To constrain the spar webs' out-of-plane buckling deformations, the spar webs are placed in-between walls. As illustrated in Figure 6.3, the walls constraining the buckling deformations to the inside of the wing box are referred to as internal walls, while the walls constraining the buckling deformation to the outside of the wing box are referred to as external walls.
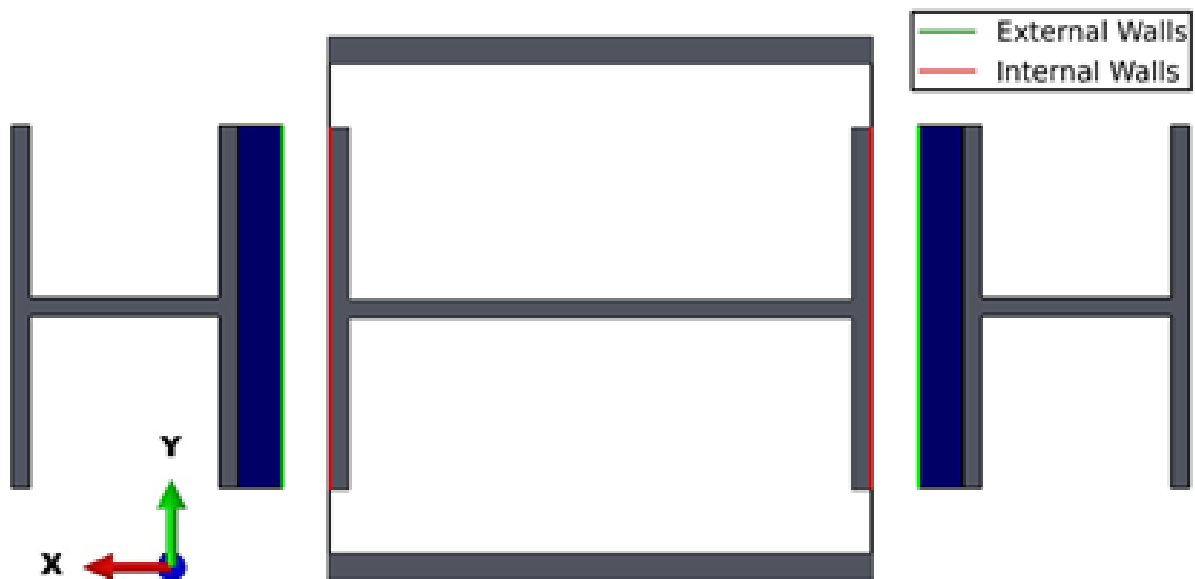
Figure 6.3: Illustration of the expanded wing box cross-section.

To successfully restrain the spar webs' out-of-plane buckling deformations, the walls require a high spanwise bending stiffness in the spar webs' perpendicular direction. For this purpose, the walls are integrated into I-section beam structures: the internal walls are integrated into a single I-section beam, referred to as the internal wall-beam, while the external walls are integrated into two different I-section beams, referred to as external wall-beams. Both the internal and external wall-beams have uniform cross-sections, defined in Table 6.1 and Figure 6.4, and are made of a representative aluminum alloy, whose material properties are presented in Table 4.1.

Table 6.1: Cross-sectional dimensions of the wall-beams.

Property	Symbol	Value
External wall beam - web width	$w_{w,E}$	25 mm
External wall beam - flanges width	$f_{w,E}$	40 mm
External wall beam - web & flanges thickness	$t_{w,E}$	2 mm
Internal wall beam - web width	$w_{w,I}$	59.73 mm
Internal wall beam - flanges width	$f_{w,I}$	40 mm
Internal wall beam - web & flanges thickness	$t_{w,I}$	2 mm

(a) External wall-beam.

(b) Internal wall-beam.
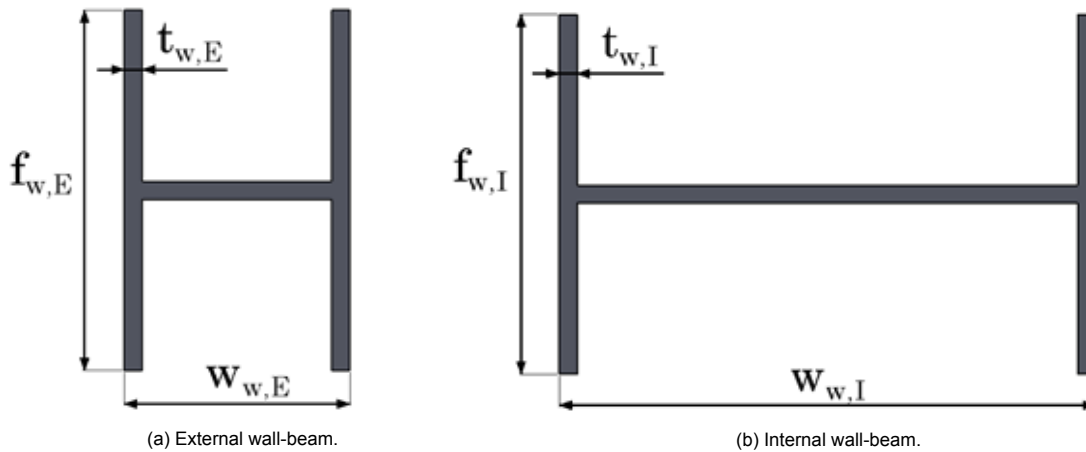
Figure 6.4: Cross-sectional dimensions of the wall-beams.

The wall-beams are attached to the ideal rigid ribs, forcing the wing box and wall-beams to have the same twist and deflections at the ribs' locations. This allows for the wall-beams to follow the wing box elastic deformations, ensuring the accurate positioning of the walls relative to the spar webs under the action of external loads. On the other hand, even though the attachment of the wall-beams to the ribs causes an increase in the torsional stiffness of the overall structure, this one is dominated by the wing box, as the thin-walled open section wall-beams are compliant in torsion.

The constraint-strategy to control the spar webs' out-of-plane buckling deformations consists in adjusting the gaps between the external walls and the front and rear spar webs. These gaps, referred to as G_F and G_R, respectively, are illustrated in Figure 6.5.
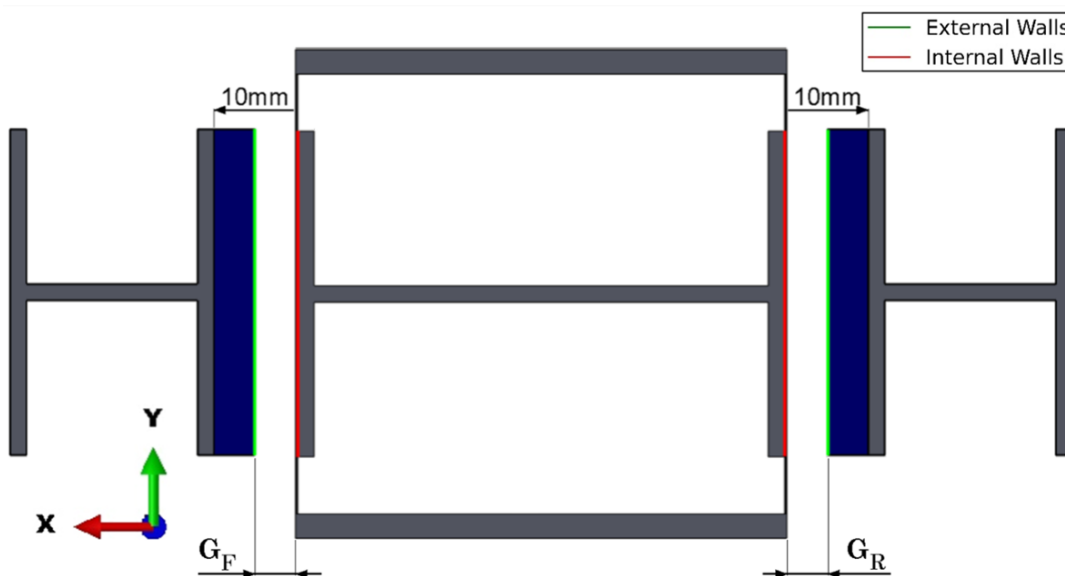
Figure 6.5: Illustration of the adjustable confining gaps G_F and G_R.

To adjust the gaps G_F and G_R, actuation systems attached to the external wall-beams move the external walls in the direction perpendicular to the spar webs. Nevertheless, as the design of such actuation systems is beyond the scope of this thesis, each external wall is modelled as a layer of material of adjustable thickness. This layer, referred to as *active wall*, has a uniform thickness t_{AW} that can be adjusted according to the following expression

$$t_{AW} = t_{AW,o} + s \quad \text{with} \quad 0\,\text{mm} < s < s_{max} \tag{6.1}$$

where $t_{AW,o}$ is the fully-retracted thickness of the active wall and s is the linear stroke provided by the actuation system, as illustrated in Figure 6.6. On the other hand, Table 6.2 presents the fully-retracted thickness $t_{AW,o}$ and the maximum linear stroke s_{max} of the investigated active walls.
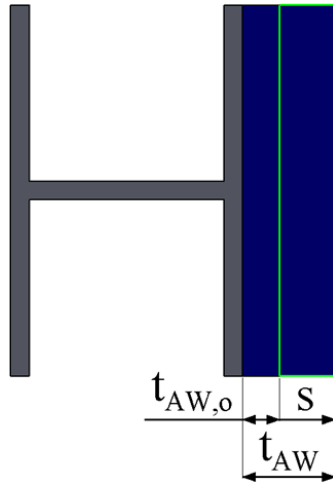
Figure 6.6: Active wall thickness adaptation.

Table 6.2: Active walls parameters.

Property	Symbol	Value
Fully-retracted thickness	$t_{AW,o}$	4 mm
Maximum linear stroke	s_{max}	6 mm

As illustrated in Figure 6.5, the interfaces between the external wall-beams and the active walls are placed 10 mm away from the spar webs. Consequently, the gaps G_F and G_R can be adjusted in the range of 0mm to 6mm, according to the following expressions:

$$G_F = 6\,\text{mm} - s_F \quad \text{with} \quad 0\,\text{mm} < s_F < 6\,\text{mm} \tag{6.2}$$

$$G_R = 6\,\text{mm} - s_R \quad \text{with} \quad 0\,\text{mm} < s_R < 6\,\text{mm} \tag{6.3}$$

where s_F and s_R are the linear strokes of the front and rear external walls, respectively.

The material assigned to the active walls has an isotropic elastic behaviour, defined by the Young's modulus E and Poisson's ratio ν presented in Table 6.3, which correspond with the material properties of a representative polylactic acid (PLA) material. On one hand, the Young's modulus is small enough for the expanded wing box torsional stiffness to be barely affected by the adjustment of the active walls' thicknesses, preventing such thicknesses' adaptations from influencing the twisting response. On the other hand, the Young's modulus is high enough for the active walls to experiment negligible elastic deformations under the contact loads transmitted by the buckling spar webs, preventing such elastic deformations from affecting the constraints acting over the spar webs' buckling deformations.

Table 6.3: Material properties of the active walls.

Property	Symbol	Value
Young's modulus	E	3.6 GPa
Poisson's ratio	ν	0.36

On the other hand, the investigated expanded wing box does not have the functionality of adjusting the gaps between the spar webs and the internal walls, reason why the internal wall-beam flanges act as the spar webs' internal walls, as illustrated in Figure 6.5. Furthermore, the internal walls are placed adjacent to the spar webs, fully restraining the spar webs' out-of-plane buckling deformations to the inside of the wing box.

6.3. Structural Finite Element Model

The structural response of the expanded wing box to an external quasi-static torque and under different buckling constraints is predicted by finite element analysis conducted with the commercial finite element software ABAQUS.

The modelling of the constraining devices imposes a much larger computational cost when compared to the simplified model analysed in Chapter 4, of a wing box without constraining devices. Therefore, to reduce computational times, only a single station of the expanded wing box is modeled, as all stations develop the same twisting response to an external torque that is constant throughout all stations (this was shown in Figure 4.7 for the simplified wing box under torsion analyzed in Chapter 4).

The expanded wing box station FEM is integrated by the wing box, the internal and external wall-beams and the active walls. Each of these components is modeled by linear shell elements S4R, uniformly distributed with a mesh seed size of 2mm across the wing box, and with a mesh seed size of 4mm across the wall-beams and active walls. Illustrated in Figure 6.7, the FEM is composed by 26,025 elements and 26,632 nodes.
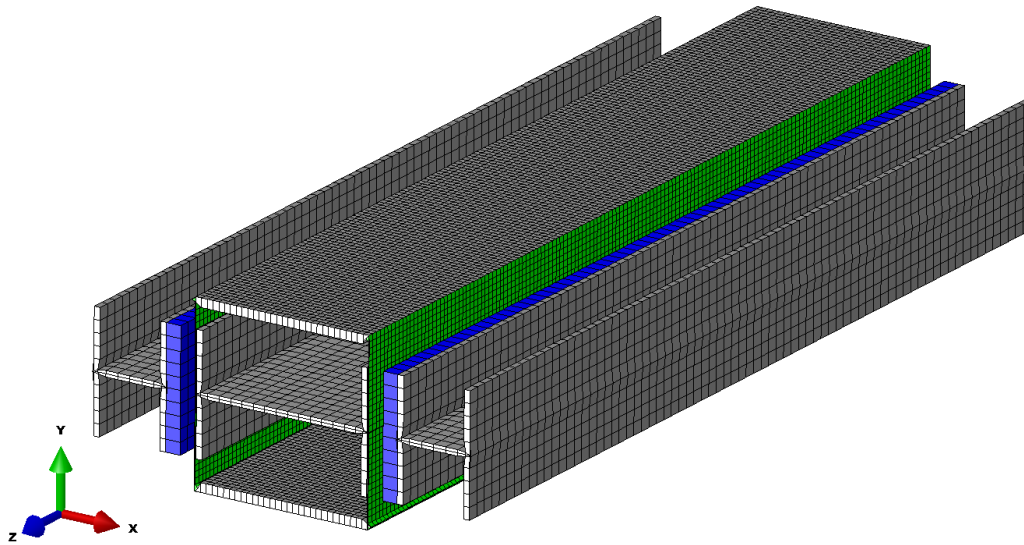
Figure 6.7: Expanded wing box FEM — Mesh.

The attachments of the active walls to the external wall-beams are modeled by surface-to-surface tie constraints, preventing any relative motion between the interfacing surfaces. As illustrated in Figure 6.8, the external wall-beams' flanges are selected as master surfaces, while the active walls are selected as slave surfaces. The tie constraints take into account the element thickness of the interfacing surfaces, as the active walls' reference surfaces are defined to be the surfaces closest to the spar webs.
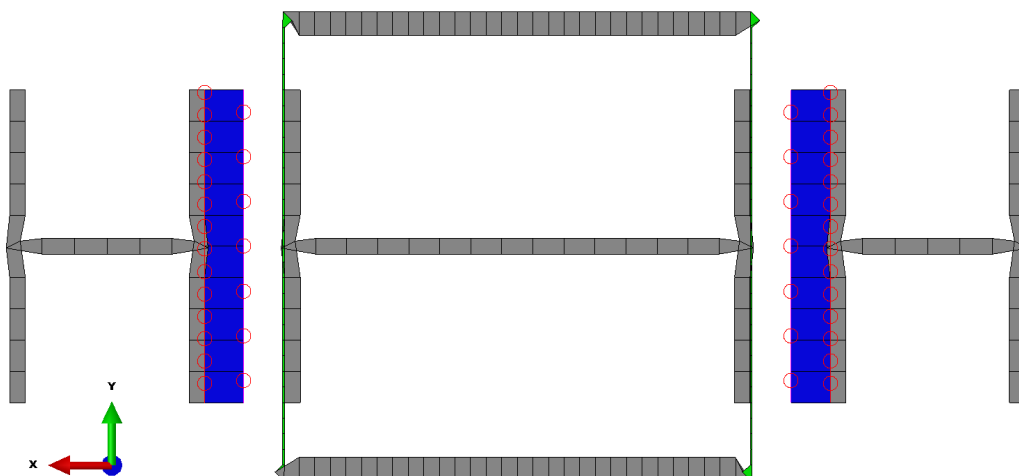
Figure 6.8: Expanded wing box FEM — Tie constraints modelling the attachment of the active walls to the external wall-beams.

The ideal rigid ribs are modelled by beam type Multi-Point Constraints (MPC), illustrated in Figure 6.9. At both extremes of the expanded wing box station, a beam type MPC constraint is defined, selecting the nodes along the wing box and wall-beams' cross-sections as slave nodes, and a reference point placed at the wing box cross-section's centroid as the control point. In this way, the nodes of the wing box and wall-beams are constrained to have equal displacements and rotations at the ribs' locations. It should be highlighted that the active walls are not included in these MPC constraints, as they are attached to the external wall-beams and not to the ribs. For clarity, Figure 6.10 illustrates the edges of the wing box and wall-beams' reference surfaces selected for the beam type MPC constraints.
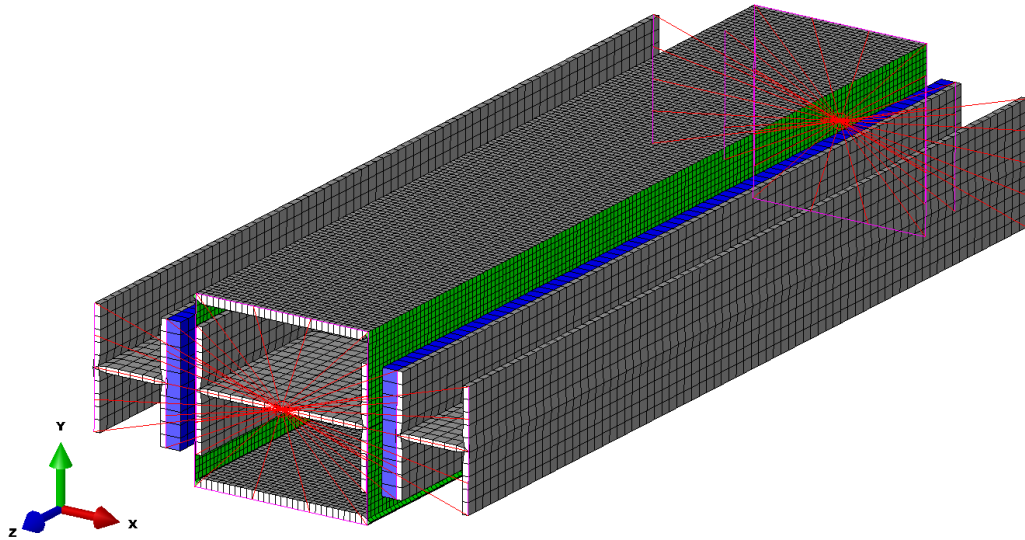
Figure 6.9: Expanded wing box FEM — Beam type Multi-Point Constraints simulating the ideal rigid ribs.
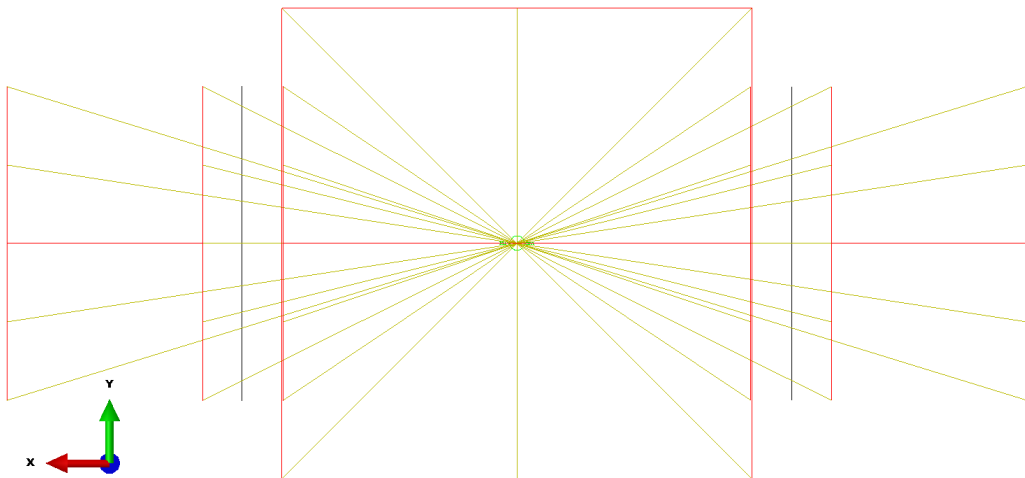
Figure 6.10: Expanded wing box FEM — Edges along the cross-sections of the wing box and wall-beams' reference surfaces selected for the beam type MPC constraints.

Contact interactions are defined for four contact pairs: (i) front external wall - front spar web external surface, (ii) front internal wall - front spar web internal surface, (iii) rear internal wall - rear spar web internal surface, and (iv) rear external wall - rear spar web external surface. For all contact pairs, the spar webs are selected as slave surfaces and the walls as master surfaces, as the spar webs have a finer mesh and experiment greater deformations than the walls. On the other hand, all contact interactions use a finite sliding, surface-to-surface formulation, with a frictionless tangential behaviour. Furthermore, the normal behaviour is defined by a "hard" contact pressure-overclosure relationship, allowing separation after contact and using the linear penalty method (default method) as contact constraint enforcement method.

The boundary and loading conditions are defined in Table 6.4, and their application to the FEM is illustrated in Figure 6.11. The expanded wing box station is fixed at one extreme, referred to as the station root, by imposing an encastre boundary condition to the control point of the MPC constraint simulating the rib present at this location. On the other hand, a positive concentrated torsional moment T is applied to the control point of the MPC constraint simulating the rib present at the opposite extreme of the station, referred to as the station tip. This positive torque corresponds to a clockwise moment when seen from the station root, also referred to as nose-up, which in turn creates a positive nose-up elastic twist.

Table 6.4: Boundary and loading conditions applied to the expanded wing box FEM.

Location	Boundary Condition	Loading Condition
Root ($Z = 0$)	$U_x = 0$, $U_y = 0$, $U_z = 0$, $UR_x = 0$, $UR_y = 0$, $UR_z = 0$	—
Tip ($Z = 300$mm)	—	Torque: CM3 = T
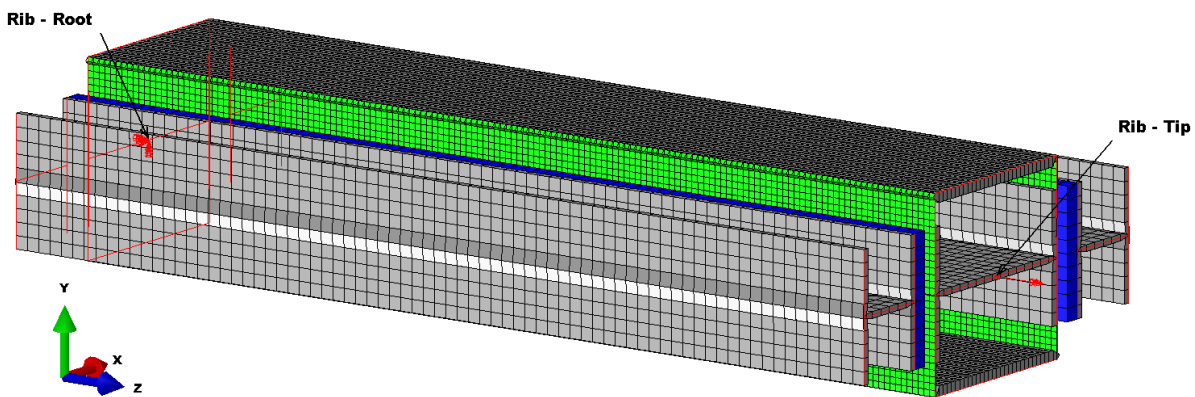
Figure 6.11: Expanded wing box FEM — Boundary and loading conditions.

The expanded wing box structural response to an external quasi-static torque is investigated under different buckling constraints. These buckling constraints are defined by setting different gap values between the external walls and the front and rear spar webs, and are implemented by adjusting the active walls' thicknesses in the FEM. On the other hand, the twisting response is calculated by a dynamic implicit analysis of quasi-static application, accounting for geometric nonlinearities. For this analysis, an initial geometrical imperfection is introduced into the slender spar webs by superposing the shape function of their first buckling mode.

Due to the relatively low Young's modulus of the active walls, the spar webs' first buckling modes are barely affected by the thickness of the active walls. Thus, for simplicity, the spar webs' first buckling modes are calculated considering the external walls at their fully-retracted positions, setting the gaps between the spar webs and the external walls to $G_F = G_R = 6\,mm$. Hence, when calculating the expanded wing box twisting response under any type of buckling constraint, it is considered that the spar webs have a geometrical imperfection with the shape of these buckling modes.

Calculated with the Lanczos eigensolver, the expanded wing box first buckling mode for a positive external torque corresponds with the spar webs' first buckling mode (due to being the slenderest components of the structure). Occurring for a buckling torque of 26.0 Nm, the buckling mode shape of the spar webs is represented in Figure 6.12. As the external torque creates shear flows of equal magnitude but opposite direction along the front and rear spar webs, both spar webs buckle with opposite buckling patterns and for the same external torque due to their opposite layups. On the other hand, the diagonal buckling patterns are due to the internal diagonal compressive stresses created by the shear flows acting on the spar webs.

The shape function of the expanded wing box first buckling mode is scaled to a maximum deflection of 0.027 mm, introducing in both the front and rear spar webs a maximum initial out-of-plane deflection of 0.027mm, which is a 10% of the 0.27 mm spar web thickness.

(a)

(b)
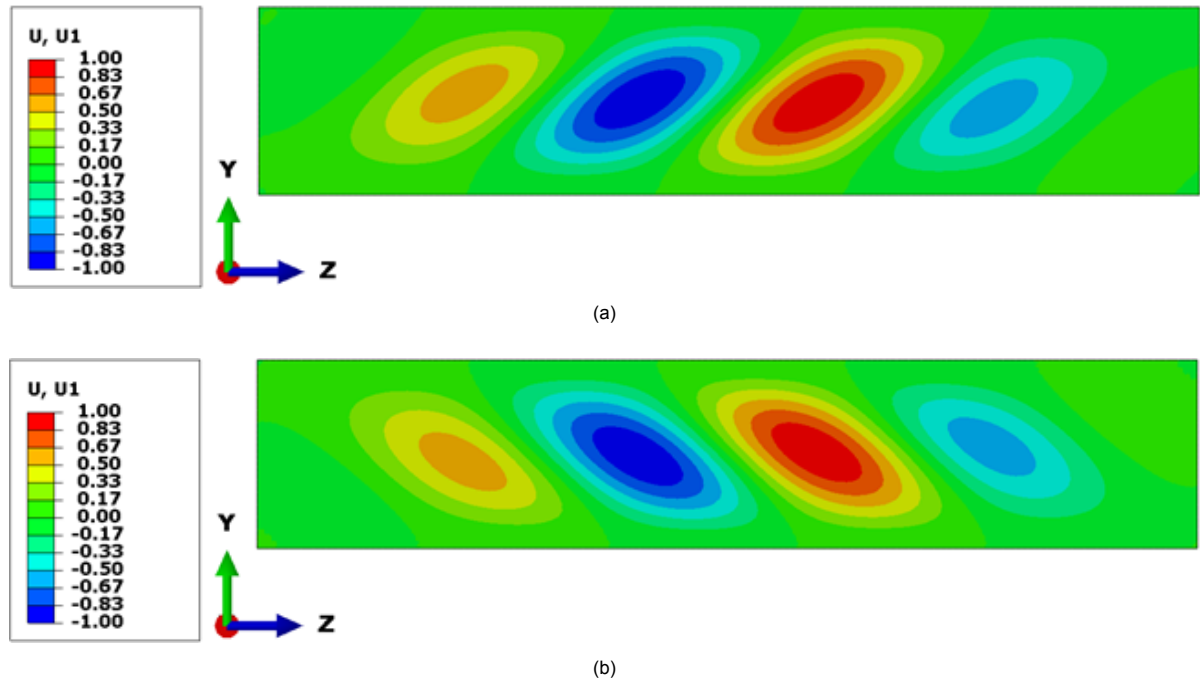
Figure 6.12: Expanded wing box — First buckling mode for a positive external torque. (a) Front spar web and (b) rear spar web.

As the contact interactions between the spar webs and the internal walls cannot be taken into account when performing a linear buckling analysis, the first buckling mode illustrated in Figure 6.12 presents half-waves protruding towards the inside (and outside) of the wing box. Consequently, when introducing the spar webs' geometrical imperfections into the FEM, the spar webs would penetrate the internal walls, causing an initial contact overclosure.

To overcome this issue, the width of the internal wall-beam web $w_{w,I}$ is reduced from 59.73 mm to 59.676 mm, which places the internal walls 0.027 mm away from the spar webs' zero-reference positions for the out-of-plane deflections. Then, as the spar webs have a maximum initial out-of-plane deflection of 0.027 mm, the initial contact overclosures between the spar webs' internal surfaces and the internal walls are prevented. On the other hand, reducing the width of the internal wall-beam web $w_{w,I}$ by 0.054 mm has a negligible effect on the twisting response.

6.3.1. Failure assessment

To assess the expanded wing box morphing capabilities, it is important to predict the maximum external torque that the expanded wing box can sustain previous the material failure of the buckling spar webs. To assess the material failure of the composite spar webs, the Tsai-Hill failure criterion (*Tsai* [63]) is applied.

<div align="right">7</div>

Wing box with adaptive constraints:
Twisting Response

In this chapter, the expanded wing box FEM presented in Chapter 6 is implemented to analyze the twist morphing capabilities, which are assessed based on the changes in the twisting response to an external quasi-static torque created by the adjustment of the adaptive constraints. Furthermore, the sensitivity of the twist morphing capabilities to the level of geometrical imperfection introduced into the slender spar webs is investigated. The final section is dedicated to a brief overview of the twist morphing capabilities under the action of a spanwise bending load.

7.1. *No-restraint & No-contact* conditions

The *no-restraint* buckling constraint is defined as the condition in which the spar webs' out-of-plane buckling deformations are unrestrained to the outside of the wing box. For this purpose, the external walls are placed in their fully-retracted positions, setting the gaps between the spar webs and the external walls to $G_F = G_R = 6 \, \text{mm}$. The expanded wing box FEM in the *no-restraint* condition is illustrated in Figure 7.1, for which the active walls' thicknesses have a value of $t_{AW} = t_{AW,o} = 4 \, \text{mm}$.
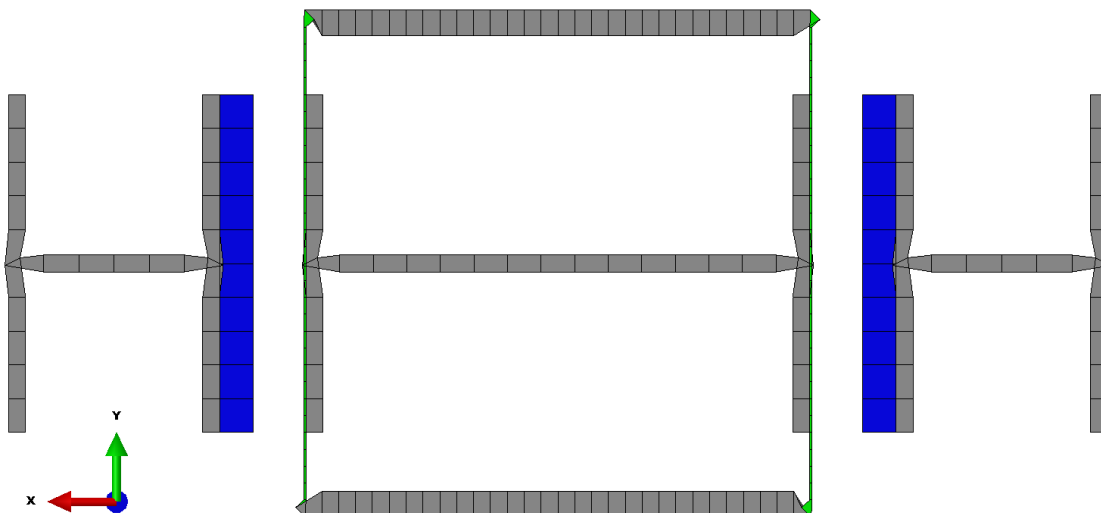
Figure 7.1: Expanded wing box FEM — *No-restraint* condition, with $G_F = G_R = 6 \, \text{mm}$.

From the FE analysis, the external torque creates a positive elastic twist that increases from a zero twist at the station's root to a maximum twist at the station's tip. For the elastic twist registered at the station's tip, defined as $\Delta\theta_{NR}$, Figure 7.2 presents its evolution with the external quasi-static torque T.

<div align="center">69</div>
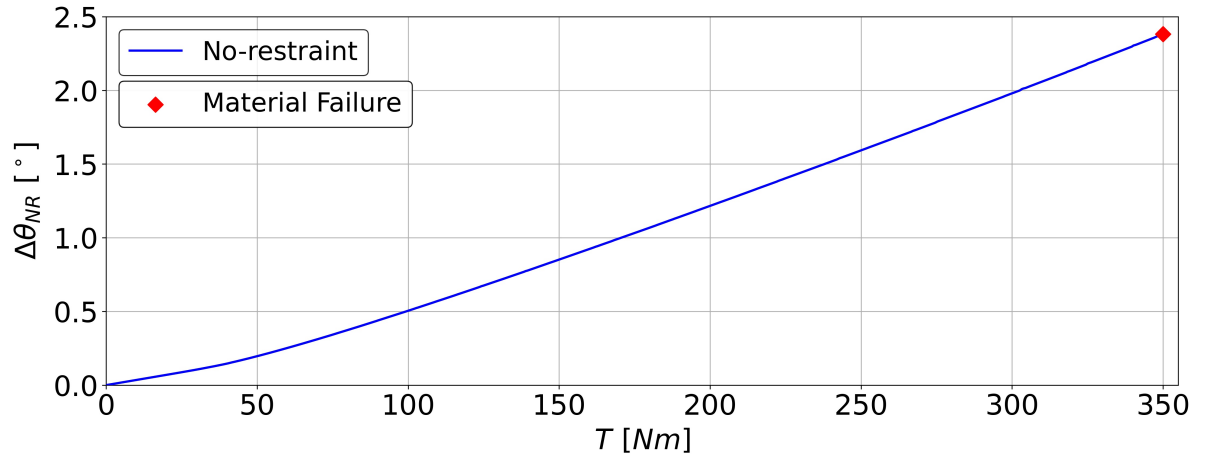
Figure 7.2: Expanded wing box in the *no-restraint* condition — Evolution of the twist increment per station $\Delta\theta_{NR}$ with the external quasi-static torque T.

Taking into account that the expanded wing box consists of three stations, the predictions for the twist increment per station $\Delta\theta_{NR}$ can be extrapolated to calculate the expanded wing box tip twist θ_{NR}, by adding the twist increment per station $\Delta\theta_{NR}$ three times; that is,

$$\theta_{NR} = 3 * \Delta\theta_{NR} \tag{7.1}$$

Thus, applying Eq. (7.1), the evolution of the expanded wing box tip twist θ_{NR} with the external quasi-static torque T is presented in Figure 7.3.

Taking into account that the expanded wing box torsional stiffness is the reciprocal of the rate of tip twist per unit torque, the torsional stiffness for each computed torque increment T_i can be approximated by Eq. (4.2), namely,

$$K_\theta^{NR}(T_i) \approx \frac{T_{i+1} - T_i}{\theta^{NR}(T_{i+1}) - \theta^{NR}(T_i)}$$

where K_θ^{NR} represents the expanded wing box torsional stiffness in the *no-restraint* condition. The reader can refer to Section 4.3 for more information regarding how Eq. (4.2) is obtained. Thus, by applying Eq. (4.2), the evolution of the torsional stiffness K_θ^{NR} with the external quasi-static torque is also represented in Figure 7.3.

Figure 7.3: Expanded wing box in the *no-restraint* condition — Evolution of the elastic tip twist θ_{NR} and torsional stiffness K_θ^{NR} with the external quasi-static torque T.

Due to the spar webs' geometrical imperfections, the buckling-induced reductions in torsional stiffness start manifesting for torques slightly lower than the linear buckling torque of 26.0 Nm (determined in Section 6.3). On the other hand, as predicted in Chapter 4 for the wing box without constraining devices, the highest reduction rates in torsional stiffness occur at the onset of buckling, rapidly flattening off for higher torques as the spar webs progress further into their post-buckling regimes.

As the spar webs progress into their post-buckling regimes, not only their out-of-plane deformations increase, but also their buckling shapes change, with buckling waves moving across the spar webs and new buckling waves forming. The buckling shapes progressively change as the external torque increases, but, at particular torque levels, changes also occur in a sudden manner. At each of these events, referred to as snapping events, the torsional stiffness experiences a sudden drop. However, as the new buckling shape stabilizes, the torsional stiffness increases again to return to its original response (i.e., the response prior the snapping event). In this readjustment process, the torsional stiffness experiences an overshoot, showing damped oscillations that rapidly settle around the original response.

The evolutions of the spar webs' buckling shapes with the external torque are investigated by analyzing the evolution of the out-of-plane buckling deformations. These out-of-plane deformations can be calculated from the ABAQUS output variable COPEN, which provides the contact opening (i.e., the gap) between two surfaces subjected to a contact interaction. For example, for the contact pair defined between the front spar web external surface and the front external wall, Figure 7.4 presents the COPEN variable measuring the gaps between the front spar web and the front external wall in the unloaded state, i.e., for $T = 0\,Nm$.
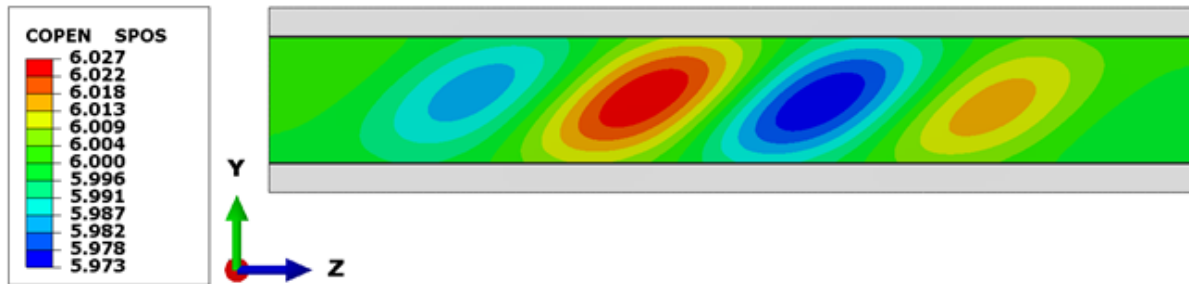
Figure 7.4: Expanded wing box station in the *no-restraint* condition for an external torque of 0 Nm — Output variable COPEN for the contact pair: front external wall - front spar web external surface.

Taking into account that the gaps between the spar webs and the external walls are set to $G_F = G_R = 6\,mm$ in the *no-restraint* condition, the front and rear spar webs' out-of-plane deformations in the unloaded state can be calculated in terms of these COPEN variables as:

$$OPD_F = -COPEN_F + 6\,mm \tag{7.2}$$

$$OPD_R = -COPEN_R + 6\,mm \tag{7.3}$$

where OPD_F and OPD_R are the out-of-plane deformations of the front and rear spar webs, respectively, defined positive to the outside of the wing box and negative to the interior of the wing box.

Applying Eq. (7.2), the out-of-plane deformations of the front spar web in the unloaded state are presented in Figure 7.5a. As expected, the out-of-plane deformations in the unloaded state coincide with the spar web's geometrical imperfection, which has the shape of the first buckling mode scaled to a maximum deflection of 0.027 mm.

Due to the attachment of the wall-beams to the ribs, the external (and internal) walls follow the global twisting deformations of the wing box. Consequently, even under the action of an external torque, the zero-reference positions for the spar webs' out-of-plane deformations, i.e., the positions for which OPD=0 mm, can be assumed to be located at a perpendicular distance of 6 mm from the external walls. Thus, under this assumption, Eq. (7.2) and Eq. (7.3) can also be applied to calculate the spar webs' out-of-plane deformations under the action of an external torque.

Therefore, the buckling shape evolution of the front spar web is illustrated in Figure 7.5 in terms of the out-of-plane deformations registered at four different torque levels. The rear spar web presents the same buckling shape evolution, but with the buckling patterns oriented in the opposite direction.

(a)

(b)

(c)

(d)

Figure 7.5: Expanded wing box station in the *no-restraint* condition — Front spar web out-of-plane deformations for four different torque levels: (a) T = 0 Nm, (b) T = 35.0 Nm, (c) T = 42.0 Nm, (d) T = 350.0 Nm.

The first torque level is the unloaded state, for which the out-of-plane deformations correspond to the four half-waves introduced as geometrical imperfection. As the torque increases, the out-of-plane deformations protruding towards the inside of the wing box are prevented from growing, due to the spar webs coming into contact with the internal walls. This phenomenon is illustrated for the second torque level, of 35.0 Nm, for which the out-of-plane deformations protruding towards the inside of the wing box remain below 0.03 mm.

For the third torque level, of 42.0 Nm, a new half-wave snaps, protruding towards the outside of the wing box. The oscillation in torsional stiffness created by this sudden change of buckling shape can be clearly identified in Figure 7.3. For the forth torque level, of 350.0 Nm, the spar webs experiment material failure. As the torque increases from 42.0 Nm to 350.0 Nm, the middle half-wave expands in the longitudinal direction, while its two adjacent half-waves shrink. These changes in buckling shape occur in a progressive manner, but, at particular torque levels, the half-waves also experiment snapping events, moving suddenly into new positions, and causing oscillations in the torsional stiffness (registered in Figure 7.3).

Applying the Tsai-Hill failure criterion to assess the material failure of the composite spar webs, the front and rear spar webs fail for the same external torque of 350.0 Nm. For this external torque, the associated failure index I_{TH} surpasses a value of 1. In Figure 7.6, the envelope plots of failure index I_{TH} across the front and rear spar webs are displayed for the external torque of 350.0 Nm.

(a)

(b)
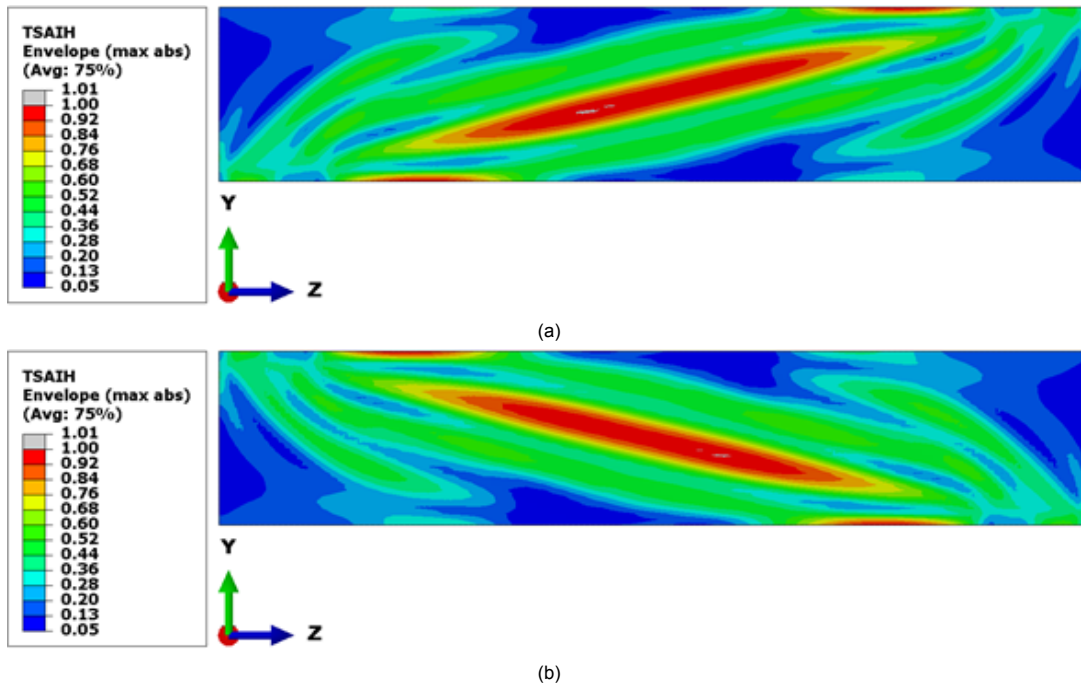
Figure 7.6: Expanded wing box station in the *no-restraint* condition for an external torque of 350.0 Nm — Envelope plot of failure index I_{TH} across the: (a) front spar web, (b) rear spar web.

For the maximum external torque of 350.0 Nm, the deformed shapes of the buckled spar webs are illustrated in Figure 7.7. On the one hand, Figure 7.7a provides a clear view of the three half-waves protruding towards the outside of the wing box. On the other hand, Figure 7.7b shows that the buckled spar webs do not come into contact with the external walls. From Figure 7.5d, the front spar web reaches a maximum out-of-plane deformation of 5.25 mm, leaving a 0.75 mm gap with external wall. The rear spar web reaches the same maximum out-of-plane deformation.

(a)

(b)

Figure 7.7: Expanded wing box station in the *no-restraint* condition for an external torque of 350.0 Nm — Deformed shapes with a deformation scale factor of 1 for: (a) wing box, (b) expanded wing box.

Taking into account that the internal walls constrain the spar webs' out-of-plane buckling deformations, it is of interest to investigate a condition in which the spar webs are unrestrained both to the inside and outside of the wing box. The expanded wing box twisting response under this type of buckling constraint, referred to as the *no-contact* condition, is investigated through the same FEM developed to study the *no-restraint* condition, illustrated in Figure 7.1, but cancelling the contact interactions between the spar webs and the internal walls. Thus, Figure 7.8 presents the tip twist θ_{NC} and torsional stiffness K_θ^{NC} of the expanded wing box in the *no-contact* condition, as a function of the external quasi-static torque T.
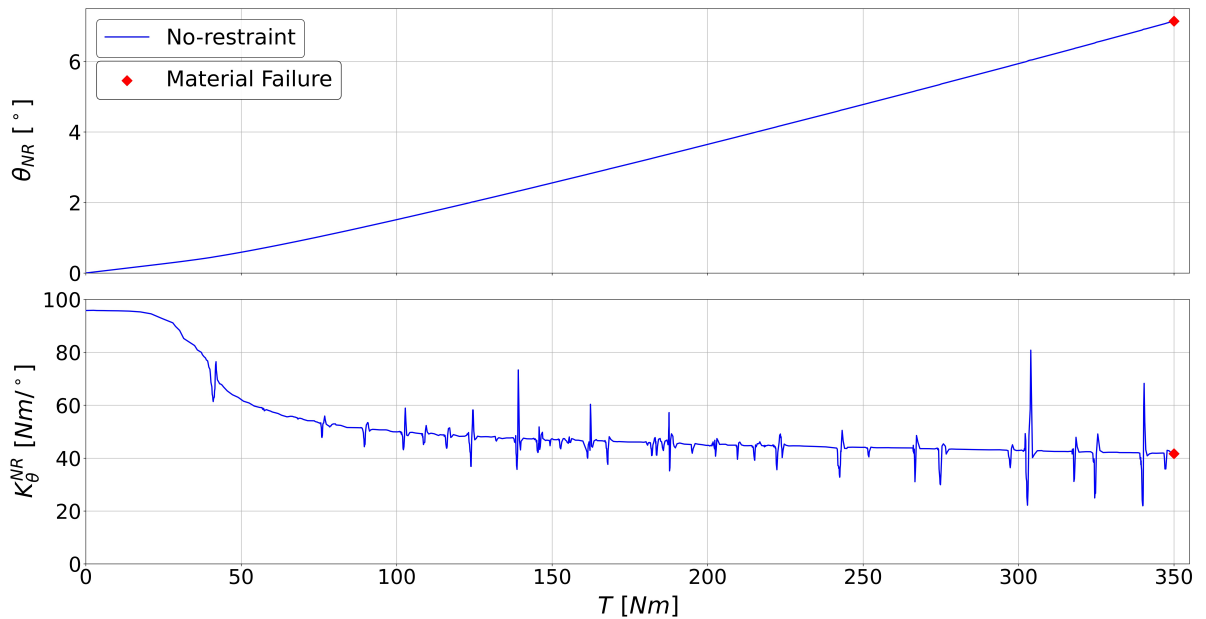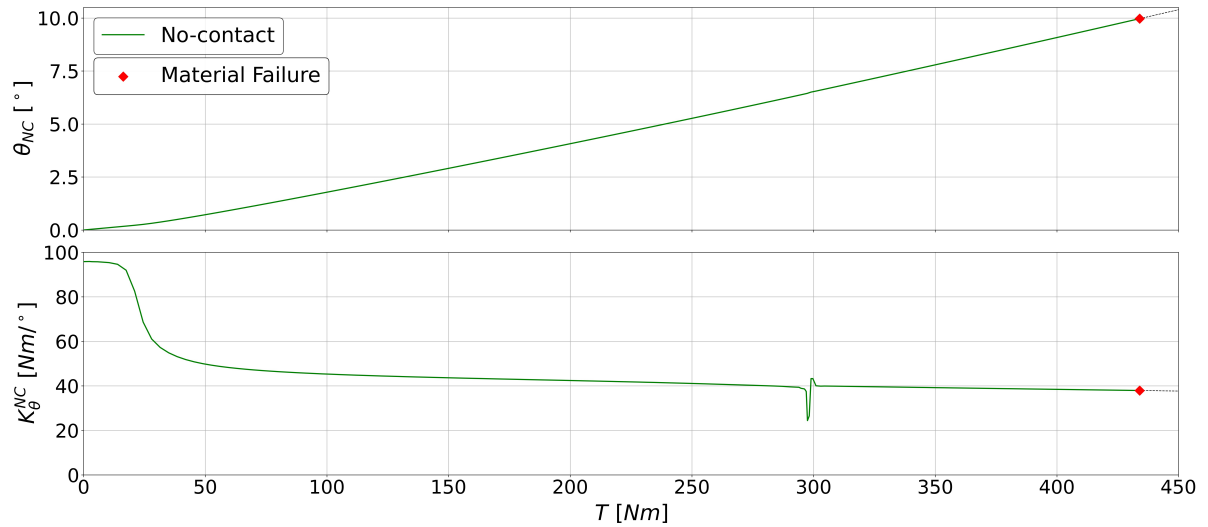

Figure 7.8: Expanded wing box in the *no-contact* condition — Evolution of the elastic tip twist θ_{NC} and torsional stiffness K_θ^{NC} with the external quasi-static torque T.

Applying the Tsai-Hill failure criterion to assess the material failure of the composite spar webs, the front and rear spar webs fail for the same external torque of 434.0 Nm. For this external torque, the associated failure index I_{TH} surpasses a value of 1. In Figure 7.9, the envelope plots of failure index I_{TH} across the front and rear spar webs are displayed for the external torque of 434.0 Nm.

(a)

(b)
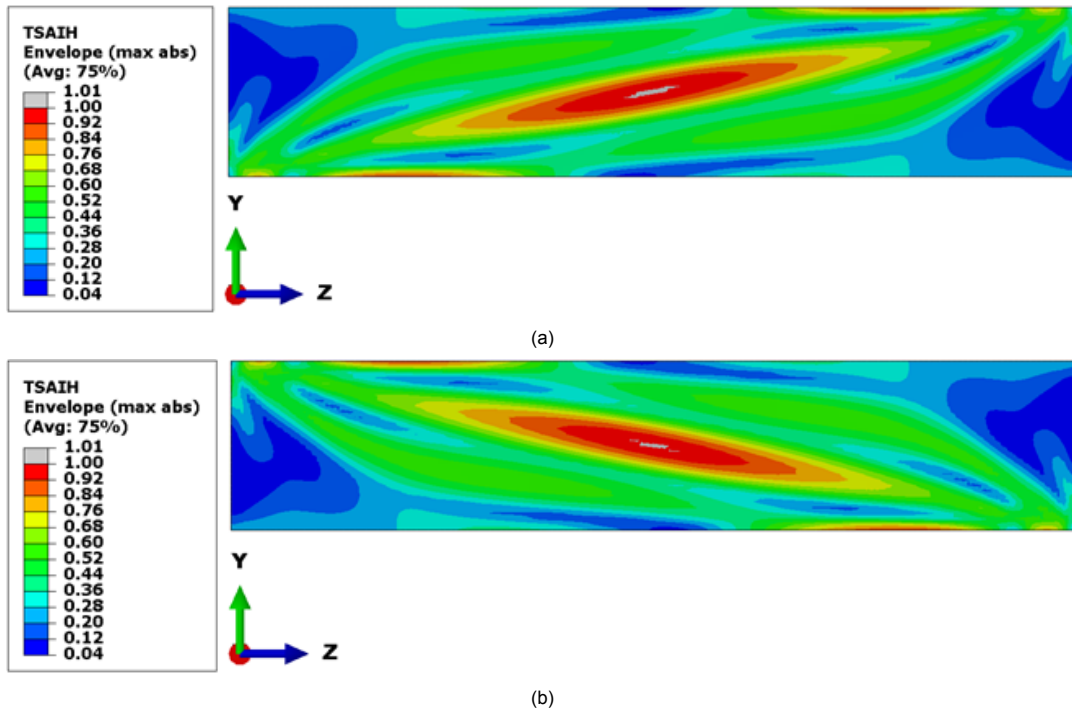
Figure 7.9: Expanded wing box station in the *no-contact* condition for an external torque of 434.0 Nm — Envelope plot of failure index I_{TH} across the: (a) front spar web, (b) rear spar web.

On the other hand, the buckling shape evolution of the front spar web is illustrated in Figure 7.10 in terms of the out-of-plane deformations registered at four torque levels. The rear spar web exhibits the same buckling shape evolution, but with the buckling patterns oriented in the opposite direction.

The first torque level is the unloaded state, for which the out-of-plane deformations correspond to the four half-waves introduced as geometrical imperfection. As the torque increases, the half-wave protruding towards the inside of the wing box and located adjacent to a rib reduces its size, while the other three half-waves expand in the longitudinal direction. This behaviour is illustrated for the second torque level, of 294.0 Nm, for which the shrinking half-wave has almost completely dissipated. To reach this buckling shape, the half-waves progressively move as the external torque increases from 0 Nm to 294.0 Nm, without experimenting any snapping events.

For the third torque level, of 301.0 Nm, the dissipating half-wave disappears, causing the three remaining half-waves to snap into new positions, filling up the space left by the dissipated half-wave. The oscillation in torsional stiffness created by this sudden change of buckling shape can be clearly identified in Figure 7.8. For the forth torque level, of 434.0 Nm, the spar webs experiment material failure. As the external torque increases from 301.0 Nm to 434.0 Nm, the out-of-plane displacements become larger, but the buckling shape does not change.
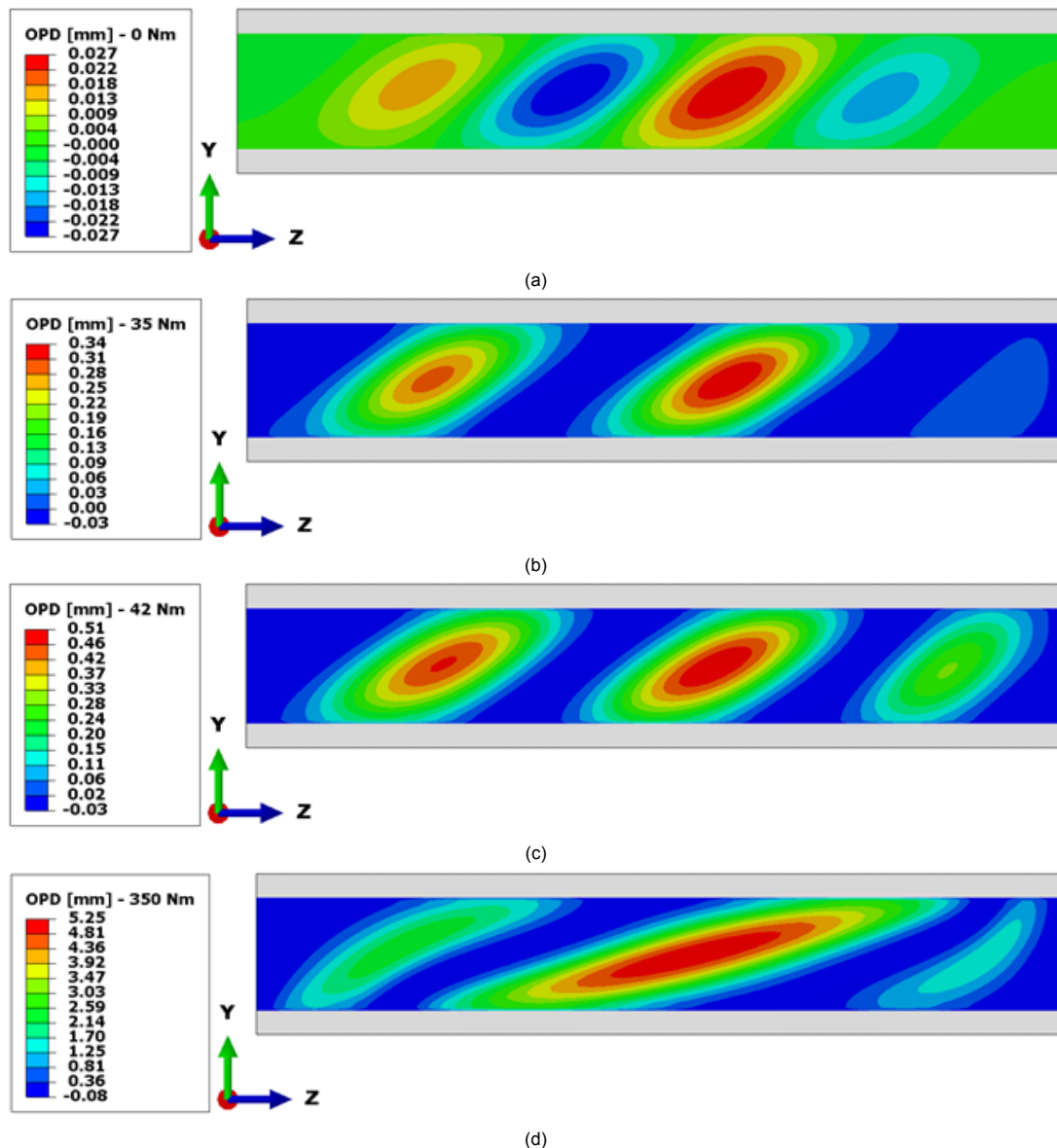

(a)

(b)

(c)

(d)
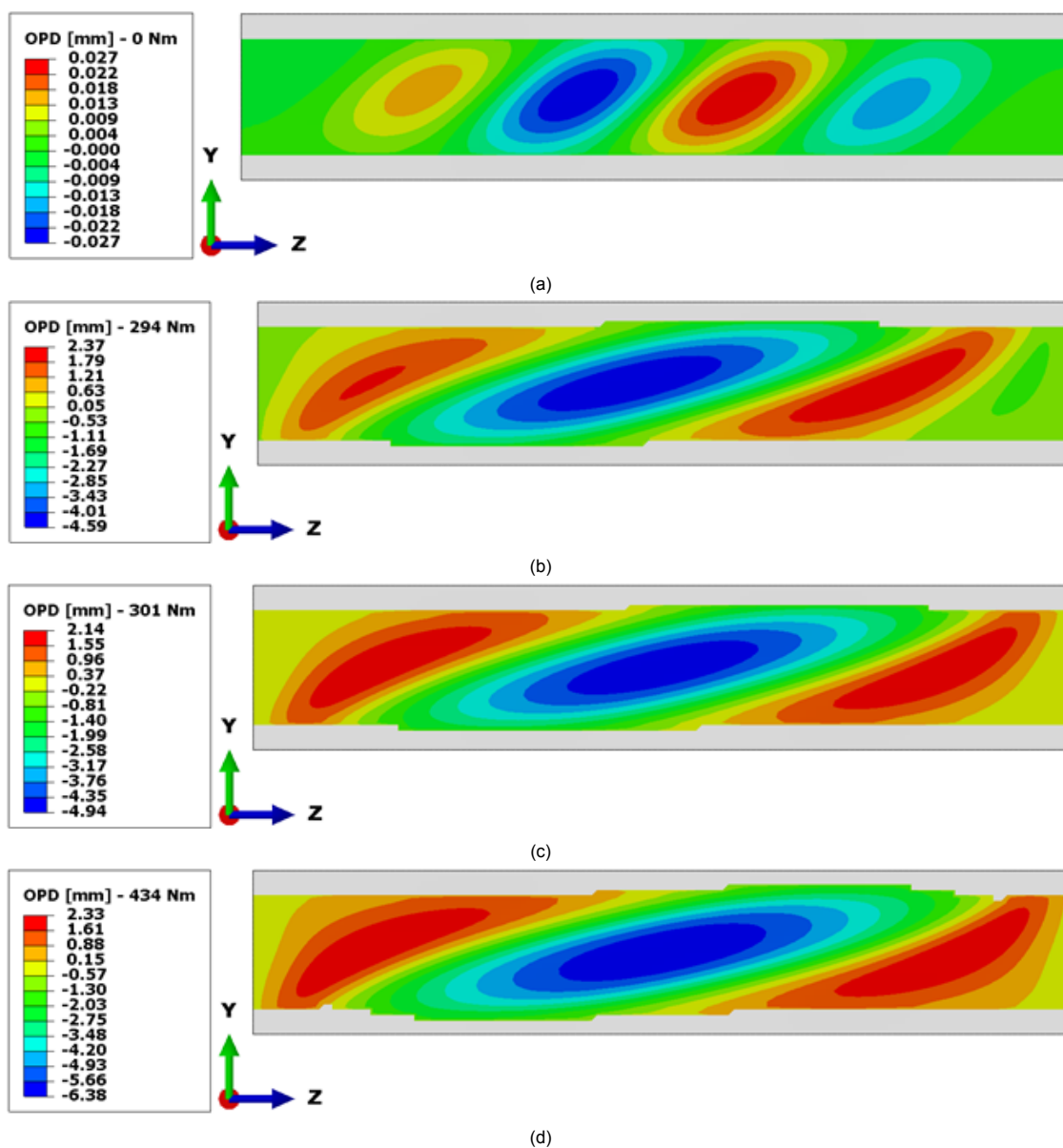
Figure 7.10: Expanded wing box station in the *no-contact* condition — Front spar web out-of-plane deformations for four different torque levels: (a) T = 0 Nm, (b) T = 294.0 Nm, (c) T = 301.0 Nm, (d) T = 434.0 Nm.

For the maximum external torque of 434.0 Nm, the deformed shapes of the buckled spar webs are illustrated in Figure 7.11, providing a clear view of the middle half-wave protruding towards the inside of the wing box. Furthermore, from Figure 7.10d, the front spar web reaches a maximum out-of-plane deformation of 2.3 mm towards the outside of the wing box, and of 6.4 mm towards the inside of the wing box. The rear spar web reaches the same maximum out-of-plane deformations.

Figure 7.11: Expanded wing box station in the *no-contact* condition for an external torque of 434.0 Nm — Deformed shape of the wing box. Deformation scale factor: 1.

To analyze the effects that the internal walls have on the twisting response, Figure 7.12 compares the tip twist and torsional stiffness in the *no-contact* condition with those predicted in the *no-restraint* condition.
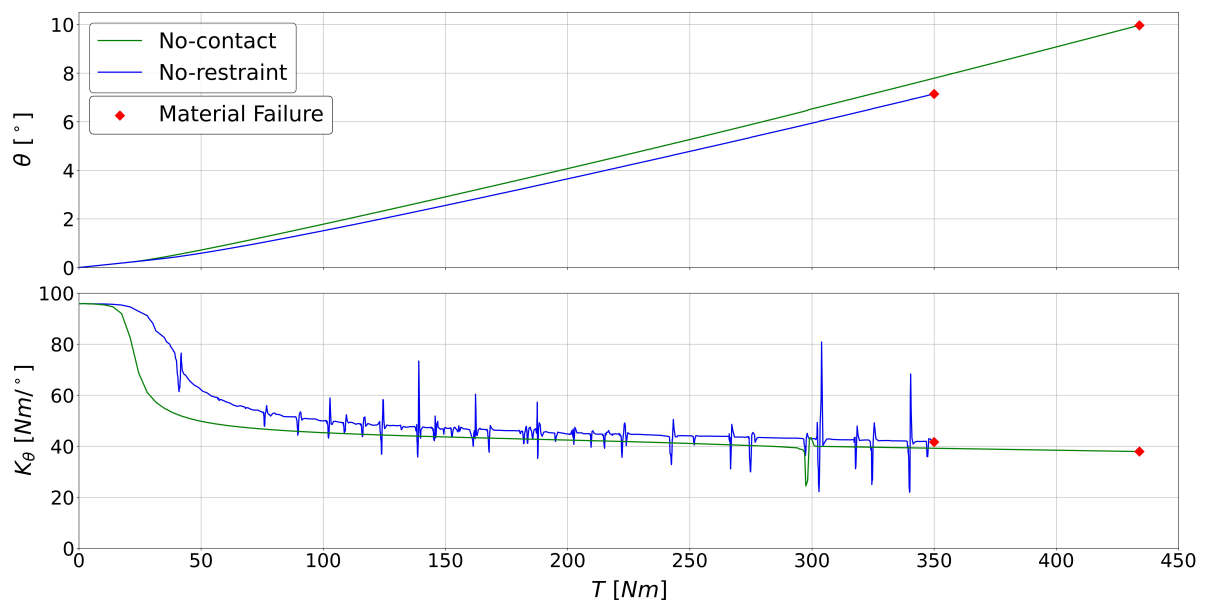
Figure 7.12: Expanded wing box in the *no-contact* and *no-restraint* conditions — Evolution of the elastic tip twist and torsional stiffness with the external quasi-static torque T.

From Figure 7.12, the reduction rates in torsional stiffness during the onset of buckling are lower in the *no-restraint* condition than in the *no-contact* condition, due to the unilateral constraints that the internal walls impose upon the spar webs' buckling deformations. Nevertheless, both torsional stiffnesses flatten out around the same value as the spar webs progress further into their post-buckling regimes, causing the differences in torsional stiffness between the *no-contact* and *no-restraint* conditions to gradually reduce for greater torques. Thus, for external torques greater than 150 Nm, the buckling-induced reductions in torsional stiffness in the *no-contact* condition are almost the same as those predicted in the *no-restraint* condition.

Another interesting observation is that in the *no-restraint* condition, the contacts between the spar webs and the internal walls cause the buckling half-waves to experiment frequent snapping events, creating oscillations in torsional stiffness that contrast with the smooth torsional stiffness evolution of the *no-contact* condition.

Finally, for an operational external torque T (i.e., before material failure), the tip twist in the *no-contact* condition is only slightly higher than the tip twist in the *no-restraint* condition. For example, for the external torque of 350.0 Nm, at which the spar webs fail in the *no-restraint* condition, the tip twist in the *no-contact* condition is only 0.65° higher than the tip twist in the *no-restraint* condition. However, as the spar webs' failure torque is 24 % greater in the *no-contact* condition than in the *no-restraint* condition, higher tip twists can be created in the *no-contact* condition for torques at which the spar webs have already failed in the *no-restraint* condition. Consequently, the maximum tip twist that can be achieved in the *no-contact* condition ends up being 2.8° higher than the maximum tip twist that can be created in the *no-restraint* condition.

7.2. *Full-restraint* condition

The *full-restraint* buckling constraint is defined as the condition in which the spar webs' out-of-plane buckling deformations are restrained both to the inside and outside of the wing box to a maximum value that coincides with the initial maximum out-of-plane deflection introduced as geometrical imperfection. As the front and rear spar webs have a maximum initial out-of-plane deflection of 0.027 mm, both to the inside and outside of the wing box, the gaps between the spar webs and the external walls are set to $G_F = G_R = 0.027$ mm, while the internal walls are already placed 0.027 mm away from their corresponding spar webs. The expanded wing box FEM in the *full-restraint* condition is illustrated in Figure 7.13, for which the external walls are moved 5.973 mm from their fully-retracted positions by increasing the thickness of the active walls up to a value of $t_{AW} = 9.973$ mm.
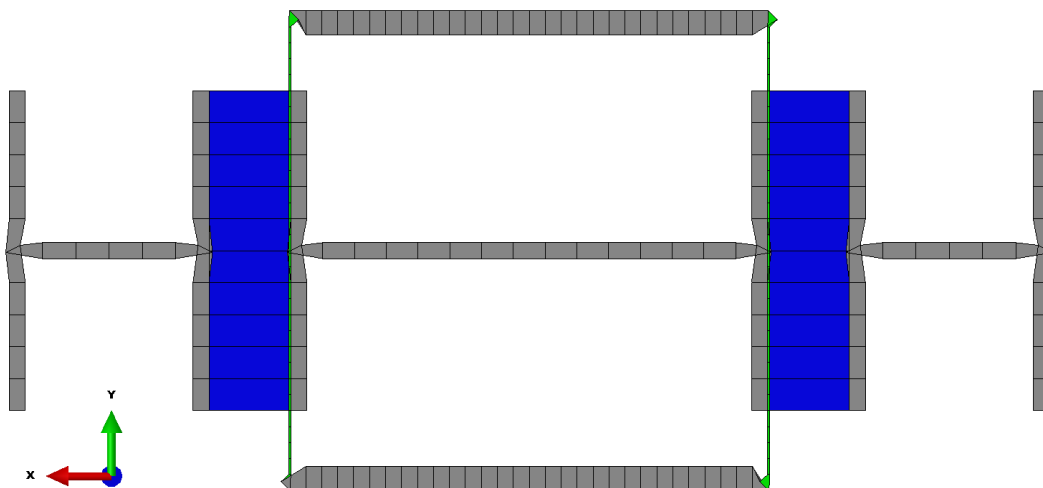
Figure 7.13: Expanded wing box FEM — *Full-restraint* condition, with $G_F = G_R = 0.027$ mm.

The predictions for the twisting response of a single station are extrapolated to calculate the twisting response of the expanded wing box, which consists of three stations. To do this, the same procedure described in Section 7.1 for the analysis of the *no-restraint* condition is applied. Thus, Figure 7.14 presents the tip twist θ_{FR} and torsional stiffness K_θ^{FR} of the expanded wing box in the *full-restraint* condition as a function of the external quasi-static torque T. The oscillations in torsional stiffness created by snapping events are filtered out of the response, although the original torsional stiffness response is also presented in grey dashed lines. To achieve a good fit between the filtered and the original response, the latter is divided into segments, and a low-pass Butterworth filter with a different cut-off frequency is applied to each segment.

As the external torque increases, the bilaterally constrained spar webs experiment consecutive snapping events, at which their buckling shapes snap into new configurations consisting of a higher number of buckling waves. Thus, from an initial buckling shape consisting of 4 half-waves, the number of half-waves successively increases with the external torque. To illustrate this, Figure 7.15 presents the spar webs' deformed shapes for a torque of 388.5 Nm, showing twenty-two half-waves across each spar web. In addition to the snapping of new half-waves, the existing half-waves also relocate across the spar webs through snapping events. Overall, these sudden changes of buckling shape lead to frequent oscillation in the torsional stiffness response.
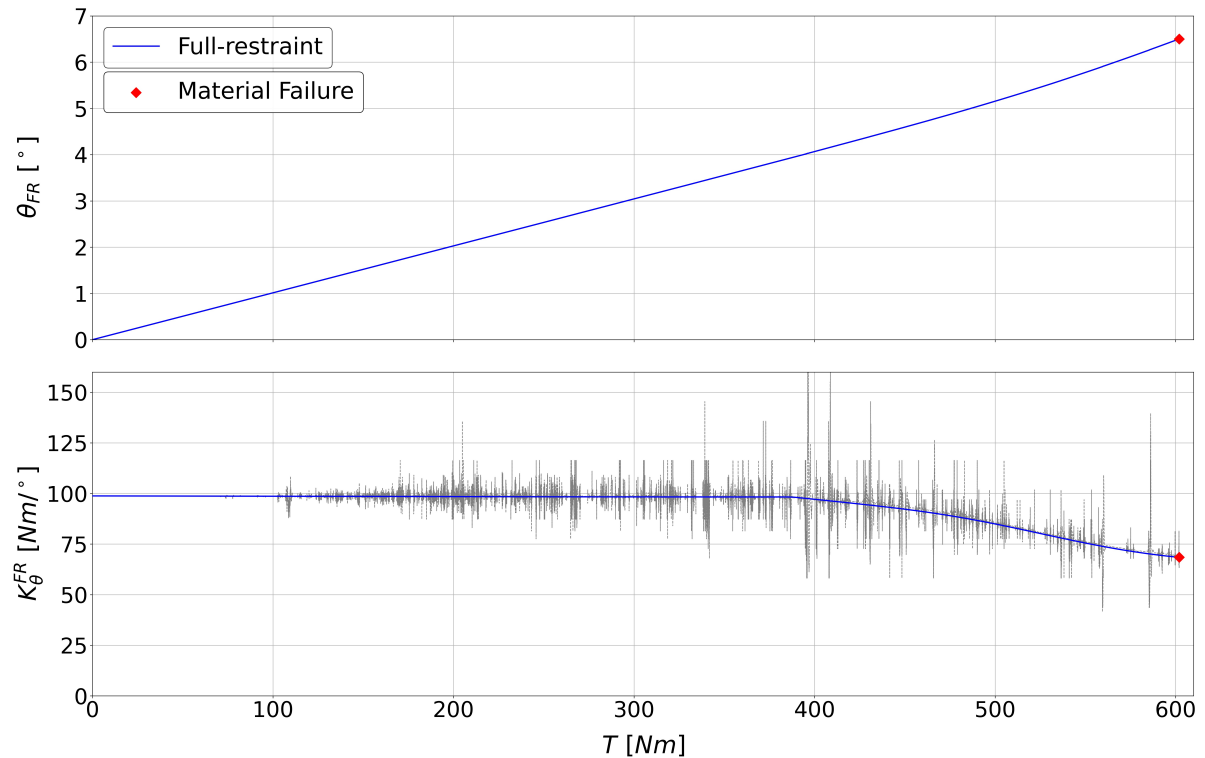
Figure 7.14: Expanded wing box in the *full-restraint* condition — Evolution of the elastic tip twist θ_{FR} and torsional stiffness K_θ^{FR} with the external quasi-static torque T.
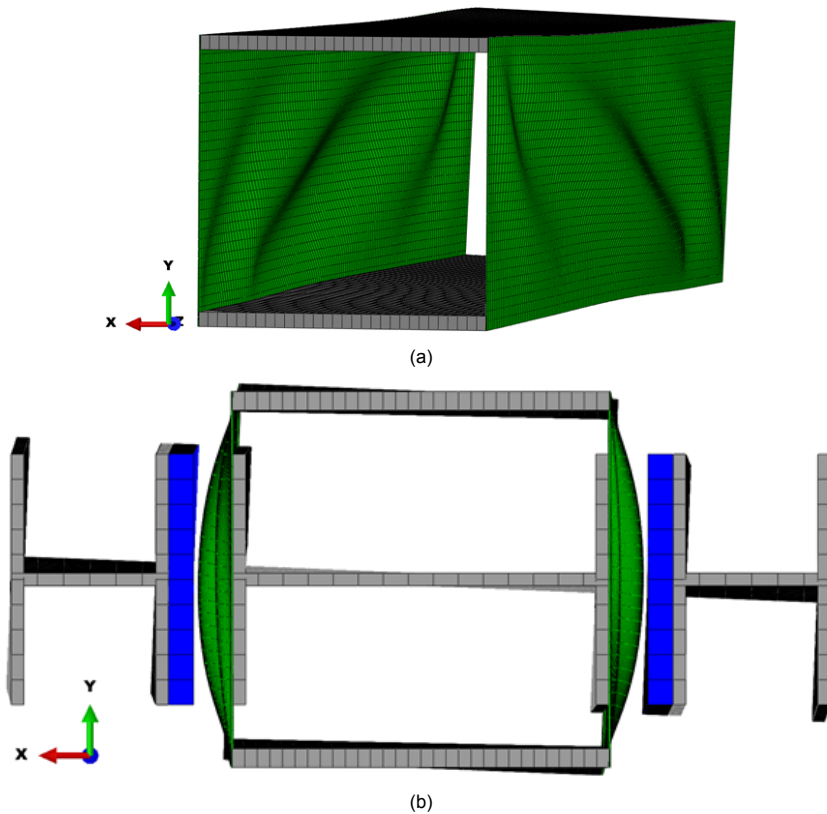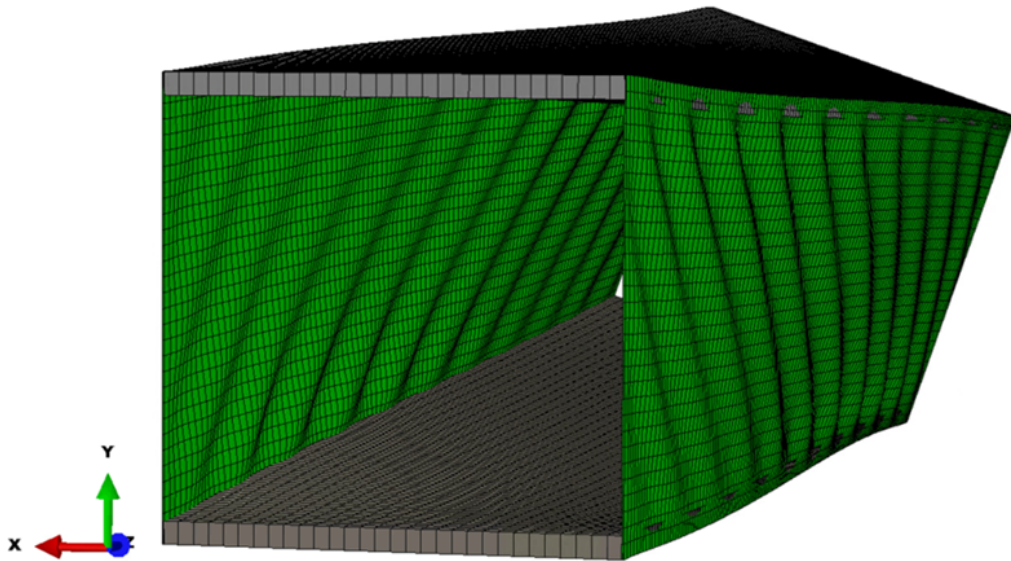

Figure 7.15: Expanded wing box station in the *full-restraint* condition for an external torque of 388.5 Nm — Deformed shape of the wing box. Deformation scale factor: 15.

To assess the walls' effectiveness in restraining the spar webs' buckling deformations, the *full-restraint* condition is compared to an *ideal full-restraint* condition, in which the spar webs have no geometrical imperfection and are ideally prevented from buckling.

The twisting response in the *ideal full-restraint* condition can be calculated by performing a linear static general analysis, as this one cannot capture the spar webs' non-linear buckling instabilities. Thus, Figure 7.16 compares the tip twist and torsional stiffness responses between the *full-restraint* and *ideal full-restraint* conditions. As the spar webs stay in a non-buckled state in the *ideal full-restraint* condition, the torsional stiffness remains constant throughout the loading path, causing the tip twist to increase linearly with the external torque.

Figure 7.16: Expanded wing box in the *full-restraint* and *ideal full-restraint* conditions — Evolution of the elastic tip twist and torsional stiffness with the external quasi-static torque T.

Up to the torque level of 388.5 Nm, referred to as the restraint-effectiveness threshold, the *full-restraint* condition exhibits practically the same tip twist response as the *ideal full-restraint* condition. Hence, the tip twist in the *full-restraint* condition evolves as if the torsional stiffness remained constant throughout the loading path, showing that the oscillations in torsional stiffness created by snapping events have a very small impact on the twisting response.

When neglecting these oscillations in torsional stiffness, Figure 7.16 shows that, up to the restraint-effectiveness threshold, the *full-restraint* condition exhibits the same torsional stiffness as the *ideal full-restraint* condition, being the reason why both conditions also exhibit the same tip twist response. However, for external torques greater than the restraint-effectiveness threshold, the constraining walls cannot longer prevent reductions in the spar webs' effective shear stiffnesses, leading to buckling-induced reductions in torsional stiffness.

It is found that these reductions in torsional stiffness are caused by two reasons that complement each other: (i) the constraining walls' widths being shorter than the spar webs' heights, in a ratio of 4:6, as illustrated in Figure 7.13, and (ii) the elastic deformations of the constraining walls due to the contact forces transmitted by the buckled spar webs.

At the restraint-effectiveness threshold, the spar webs' out-of-plane buckling deformations start slipping through the unrestrained regions left above the walls, increasing the contact forces at the walls' upper regions. Then, due to the low bending stiffness of the wall-beams' flanges, the walls bend, allowing greater out-of-plane buckling deformations. Ultimately, this has the effect of reducing the spar webs' effective shear stiffnesses, and, hence, of reducing the torsional stiffness.

To illustrate this, the spar webs' deformed shapes and the normal contact forces acting on the external walls are illustrated in Figure 7.17 at the restraint-effectiveness threshold, i.e. for a torque level of 388.5 Nm, and in Figure 7.18 for a slightly higher torque level, of 399 Nm. When comparing both conditions, it can be observed that some buckling waves dissipate in the vicinity to the bottom skin due to buckling deformations slipping through the unrestrained regions above the walls. On the other hand, the buckling waves slipping through the unrestrained regions above the walls cause the maximum contact force to increase by 55% (from 2.0 N to 3.1 N) compared to the maximum contact force registered at the restraint-effectiveness threshold.
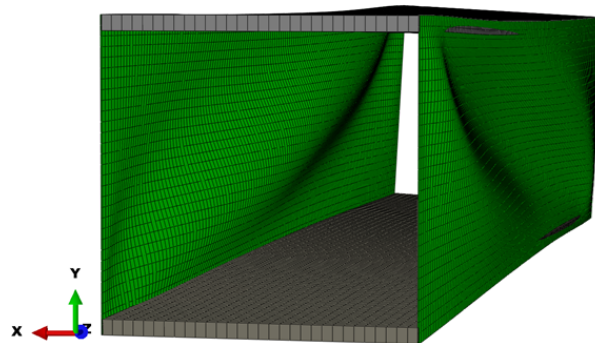
(a)

(b)
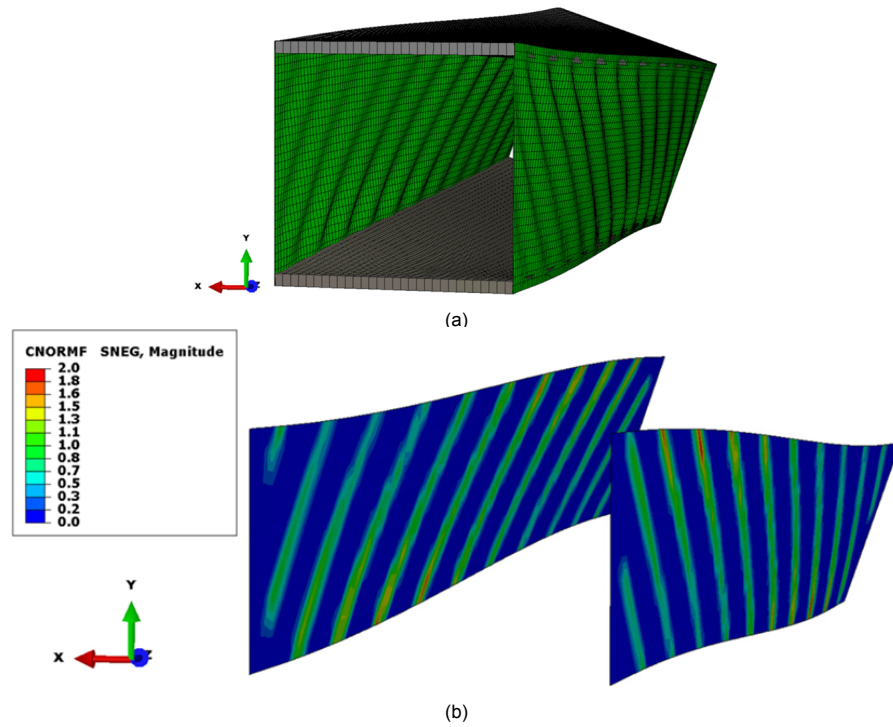
Figure 7.17: Expanded wing box station in the *full-restraint* condition for an external torque of 388.5 Nm — (a) Deformed shape of the wing box, (b) normal contact forces in Newtons across the external walls. Deformation scale factor: 15.

(a)

(b)
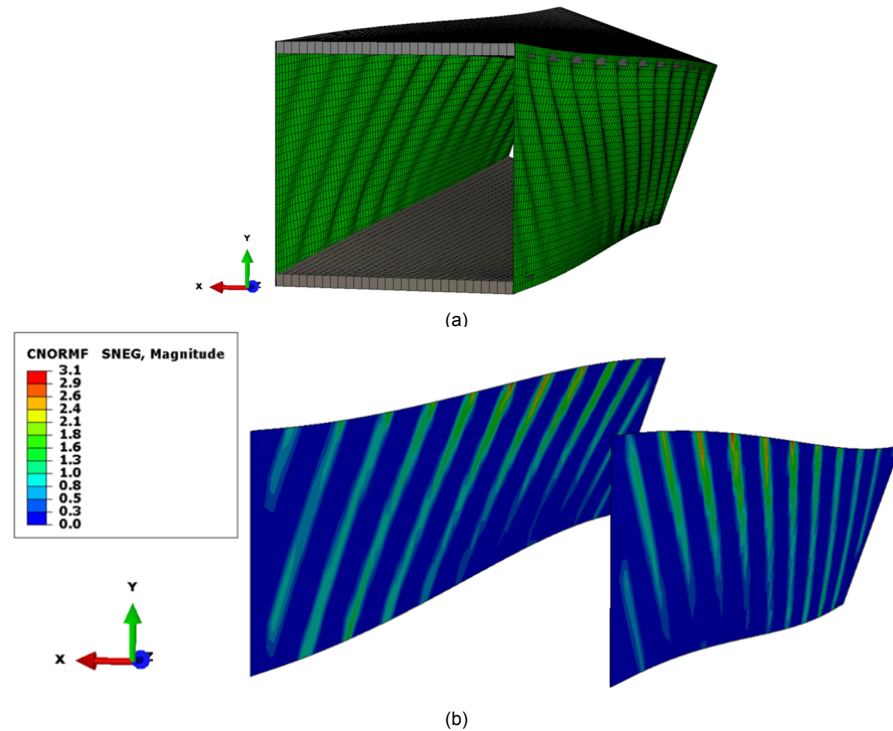
Figure 7.18: Expanded wing box station in the *full-restraint* condition for an external torque of 399.0 Nm — (a) Deformed shape of the wing box, (b) contact normal forces in Newtons across the external walls. Deformation scale factor: 15.

For the torque level of 602 Nm, at which the spar webs experiment material failure, Figure 7.19 presents the spar webs' deformed shapes and the normal contact forces acting on the external walls. On one hand, Figure 7.19a illustrates how the buckling deformations keep increasing through the unrestrained regions above the walls as the external torque is further increased past the restraint-effectiveness threshold. On the other hand, Figure 7.19b shows that the contact forces also increase with the external torque, registering a maximum contact force of 32.8 N, which is 16 times larger than the maximum contact force registered at the restraint-effectiveness threshold, of 2.0 N.

(a)

(b)
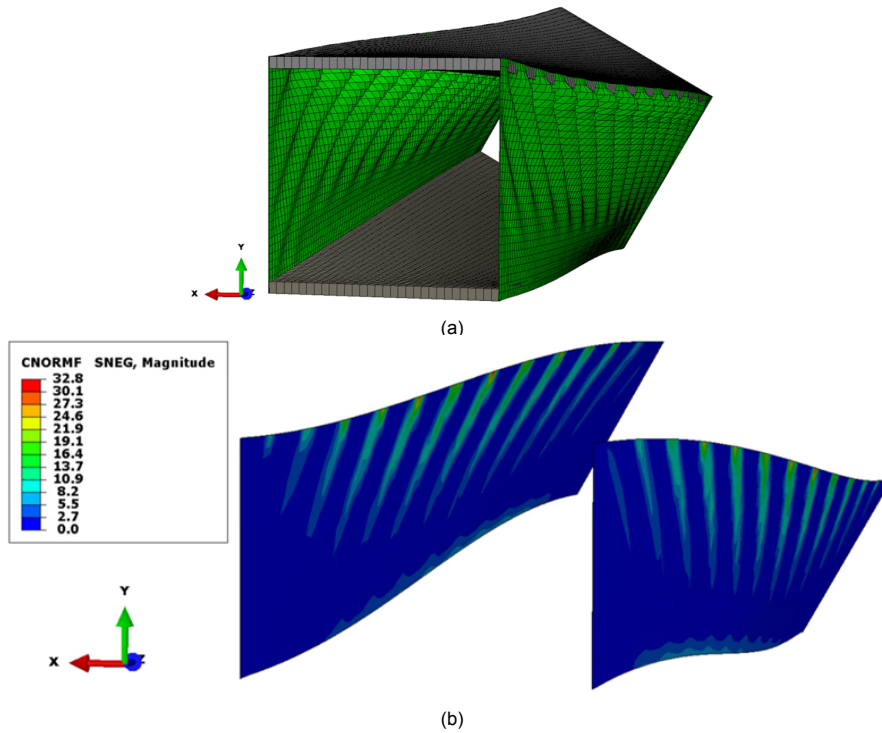
Figure 7.19: Expanded wing box station in the *full-restraint* condition for an external torque of 602 Nm — (a) Deformed shape of the wing box, (b) contact normal forces in Newtons across the external walls. Deformation scale factor: 15.

Ultimately, the walls' bending deformations increase with the contact forces, allowing the spar webs' out-of-plane buckling deformations to further increase, which in turn has the effect of reducing the spar webs effective shear stiffnesses, and, hence, of reducing the torsional stiffness.

As mentioned before, the expanded wing box can sustain a maximum external torque of 602.0 Nm previous the material failure of the spar webs. Predicted by the Tsai-Hill failure criterion, Figure 7.20 presents the envelope plots of the Tsai-Hill failure index I_{TH} across the front and rear spar webs for the external torque of 602.0 Nm.

(a)

(b)
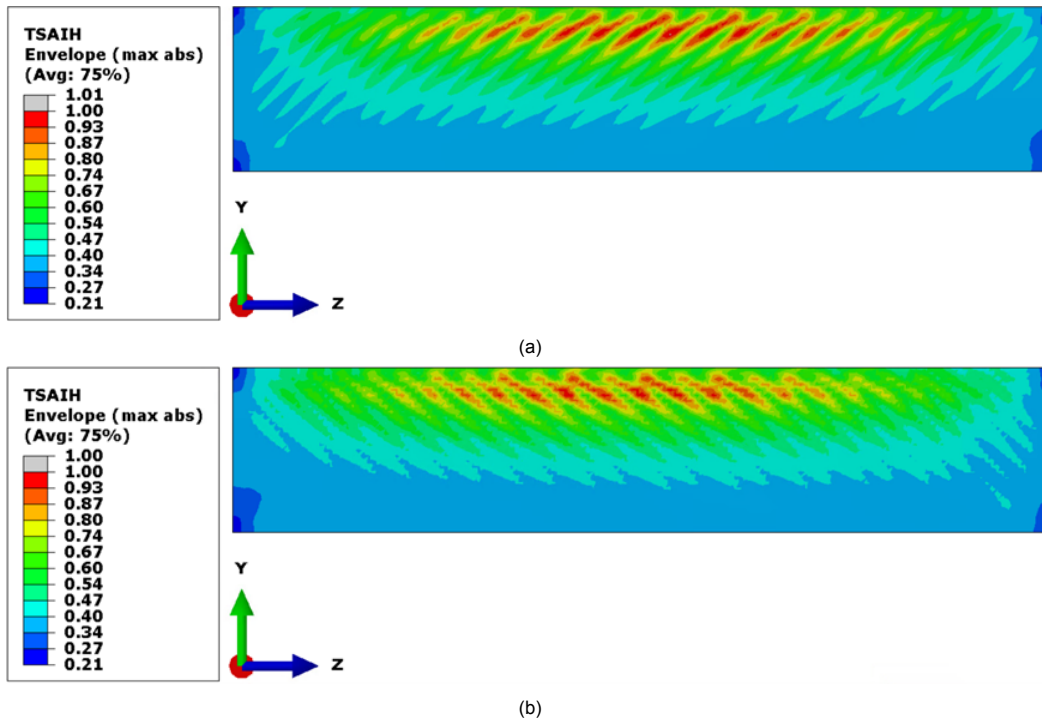
Figure 7.20: Expanded wing box station in the *full-restraint* condition for an external torque of 602.0 Nm — Envelope plot of failure index I_{TH} across the: (a) front spar web, (b) rear spar web.

From Figure 7.20, both spar webs fail for a torque of 602.0 Nm, as they both surpass a failure index value of 1. On the other hand, considering that failure initiates at the laminates' locations experimenting the greatest out-of-plane deformations, it is concluded that the increase of the buckling deformations through the unrestrained regions above the walls precipitates the spar webs' material failure.

Finally, based on the performance predicted for different wall-beams' designs, it is found that the restraint-effectiveness threshold is sensitive to the width of the wall-beams' webs and flanges. On one hand, the web width has great influence over a wall-beam spanwise bending stiffness, which needs to be high enough to prevent elastic bending deformations from hindering the buckling constraints. On the other hand, if the flanges' widths are reduced relative to the height of the spar webs, the spar webs' out-of-plane buckling deformations start slipping through the unrestrained regions located above or below the walls at lower torques, reducing the restraint-effectiveness threshold.

7.3. Active Region & Buckling-induced twist

The morphing capabilities of the expanded wing box can be assessed in terms of its *Active Region*, defined as the region delimited by the twist-torque responses in the *no-restraint* and *full-restraint* conditions. For this purpose, Figure 7.21 presents the tip twist of the expanded wing box as a function of the external quasi-static torque in the *no-restraint* and *full-restraint* conditions.
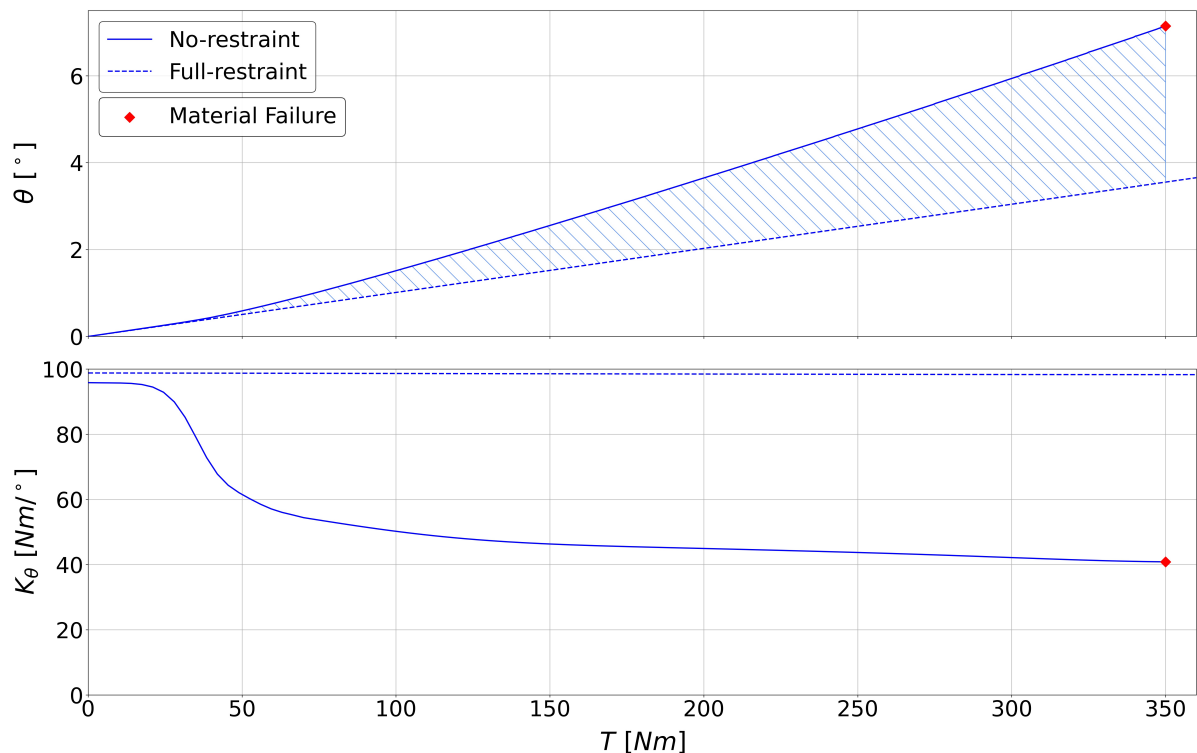
Figure 7.21: Expanded wing box in the *no-restraint* and *full-restraint* conditions — Evolution of the elastic tip twist and torsional stiffness with the external quasi-static torque T.

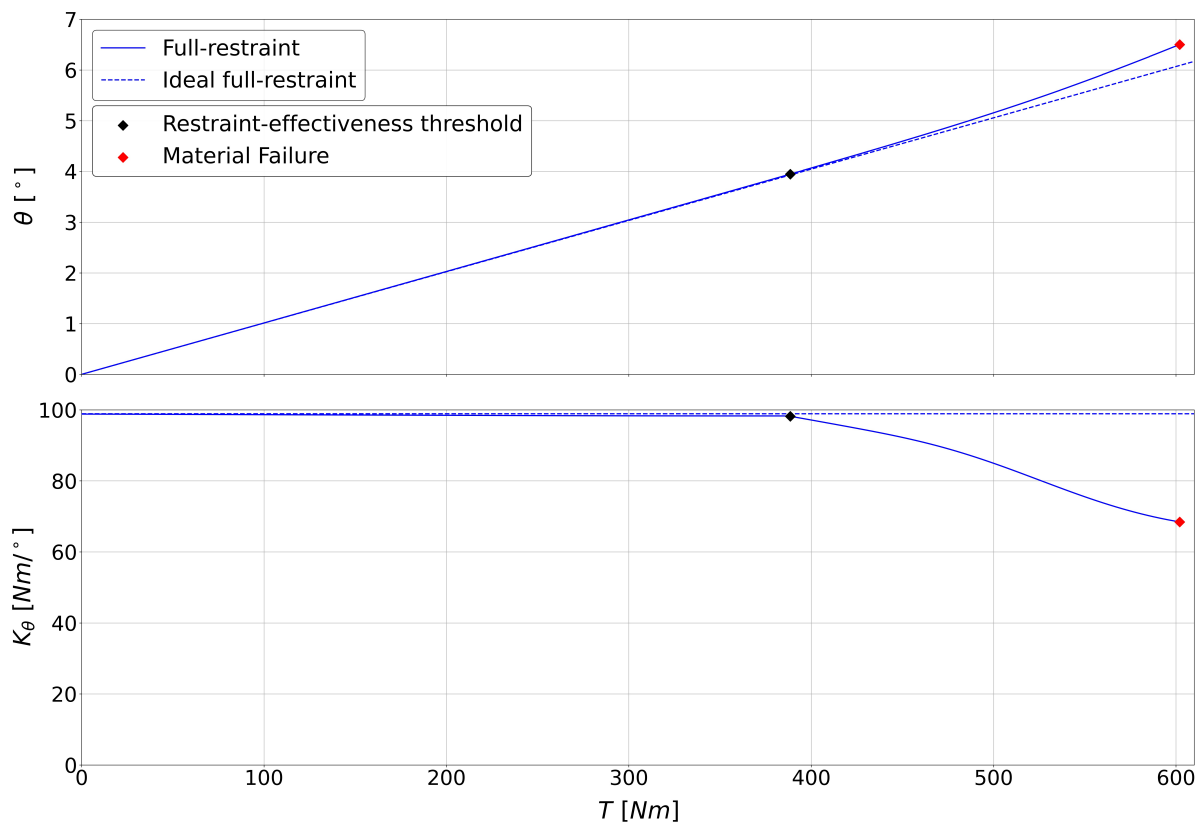The evolution of the torsional stiffness with the external quasi-static torque is also presented in Figure 7.21, filtering out the oscillations in torsional stiffness created by snapping events. The reader can observe that in the *full-restraint* condition, the torsional stiffness remains practically constant throughout the entire active loading path, which is limited by the maximum external torque of 350.0 Nm, at which the buckled spar webs fail in the *no-restraint* condition. Therefore, it is concluded that the constraining walls can successfully restrain the spar webs' buckling deformations across the entire *Active Region*.

On the other hand, as the active walls have a smaller thickness in the *no-restraint* condition than in the *full-restraint* condition, the initial torsional stiffness in the *no-restraint* condition, of 95.8 Nm/°, is slightly smaller than the initial torsional stiffness in the *full-restraint* condition, of 98.8,Nm/°. The adaptation of the active walls' thickness has such small effect on the torsional stiffness due to the relatively low Young's modulus selected for the active walls' material.

The *Active Region* encloses the different elastic tip twists that could be selected by actively adjusting the gaps between the external walls and the slender spar webs, i.e. G_F and G_R. In this way, the maximum active tip twist that could be introduced for a given external torque, referred to as the buckling-induced twist θ_b, is given by Eq. (4.4), namely,

$$\theta_b(T) = \theta_{NR}(T) - \theta_{FR}(T)$$

where θ_{NR} is the elastic tip twist in the *no-restraint* condition and θ_{FR} is the elastic tip twist in the *full-restraint* condition. Thus, the evolution of the buckling-induced twist θ_b with the external quasi-static torque T is presented in Figure 7.22, showing that a maximum buckling-induced twist of 3.6° can be created for the maximum external torque of 350.0 Nm.
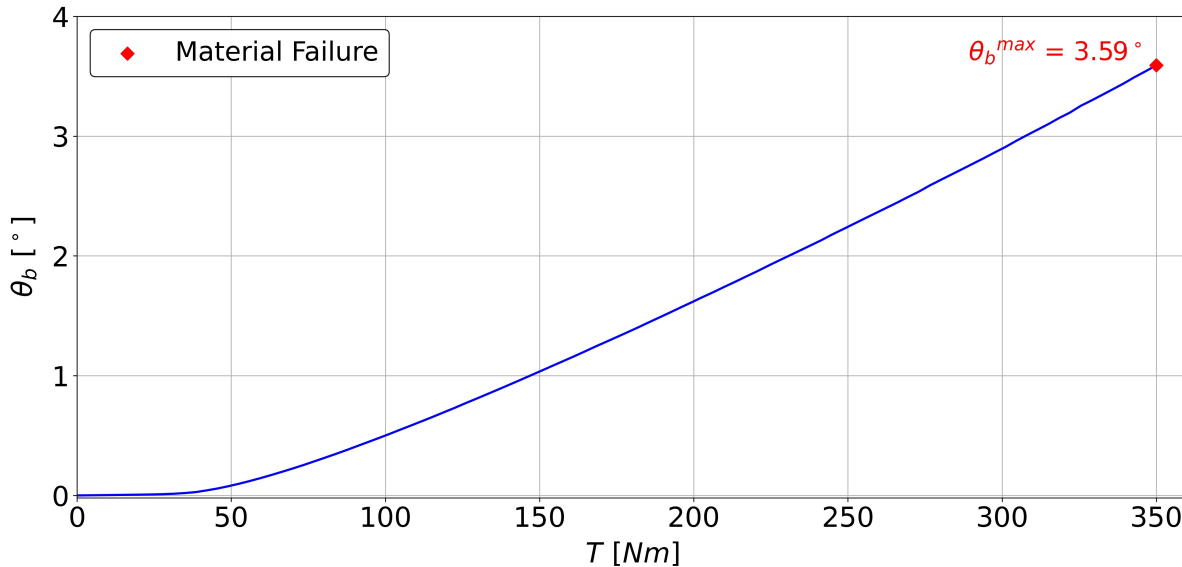
Figure 7.22: Expanded wing box — Evolution of the buckling-induced twist θ_b with the external quasi-static torque T.

On the other hand, it is of interest to also investigate the morphing capabilities of an expanded wing box endowed with the additional functionality of adjustable internal gaps (i.e., the gaps between the spar webs and their internal walls), which is referred to as the "special" expanded wing box. Adjustable internal gaps allow for the spar webs' buckling deformations to be left unrestrained both to the inside and outside of the wing box, which could contribute to achieving greater morphing twists. The twisting response under such buckling constraint, referred to as the *no-contact* condition, has already been investigated in Section 7.1, by cancelling the contact interactions between the spar webs and the internal walls.

Therefore, to analyze how the additional functionality of adjustable internal gaps affects the morphing capabilities, Figure 7.23 presents the tip twist and torsional stiffness of the expanded wing box in the *no-contact*, *no-restraint* and *full-restraint* conditions, as a function of the external quasi-static torque. On one hand, the *no-contact* and *full-restraint* responses delimit the *Active Region* of the "special" expanded wing box. On the other hand, the *no-restraint* and *full-restraint* responses delimit the *Active Region* of the "baseline" expanded wing box, with non-adjustable internal gaps. Furthermore, it should be highlighted that the oscillations in torsional stiffness created by snapping events are filtered out of the responses presented in Figure 7.23.

As mentioned before, the constraining walls can successfully restrain the spar webs' buckling deformations throughout the entire *Active Region* of the "baseline" expanded wing box, as the torsional stiffness in the *full-restraint* condition remains practically constant throughout the entire active loading path, which is limited by an external torque of 350.0 Nm. However, for external torques greater than 388.5 Nm (which represents the restraint-effectiveness threshold), the constraining walls cannot longer prevent buckling-induced reductions in torsional stiffness from occurring. Nevertheless, even though the constraining walls cannot effectively restrain the spar webs' buckling deformations throughout the entire *Active Region* of the "special" expanded wing box, its impact over the *Active Region* is very small.
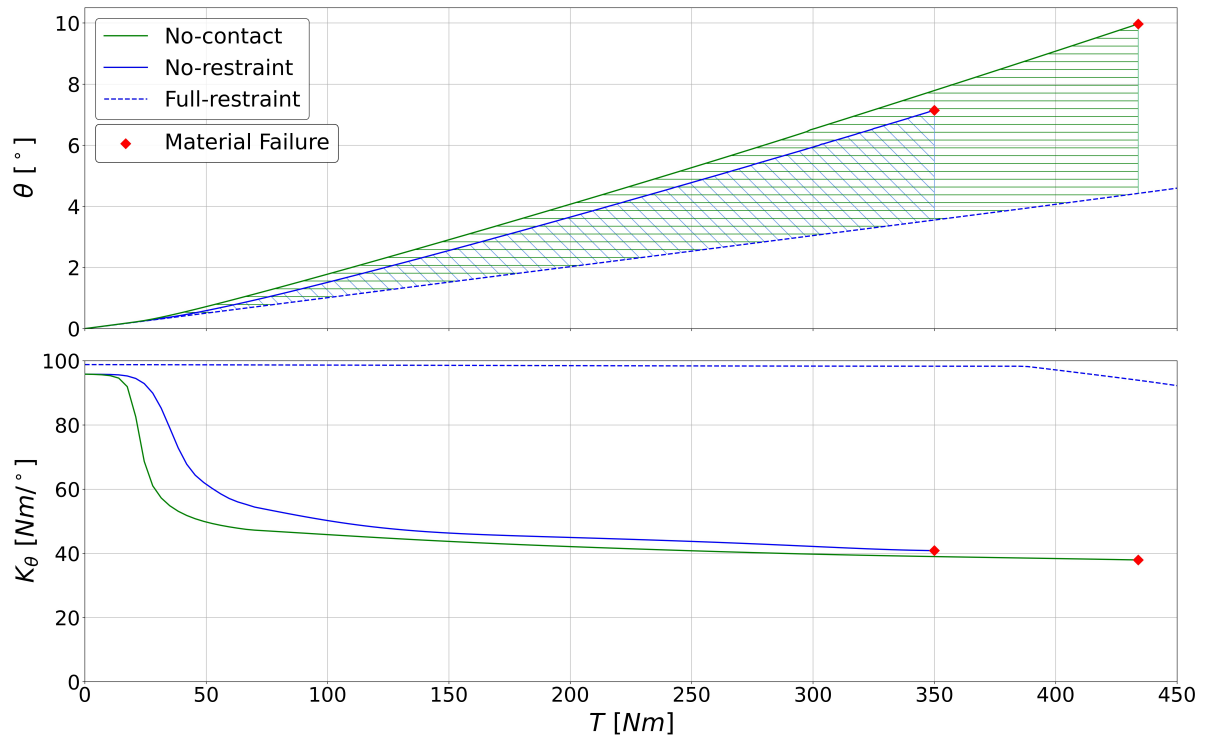
Figure 7.23: Expanded wing box — *Active Regions* and evolution of the torsional stiffness with the external quasi-static torque for the "baseline" and the "special" expanded wing boxes.

To compare the morphing capabilities between the "baseline" and "special" expanded wing boxes, their buckling-induced twists θ_b are presented in Figure 7.24 as a function of the external torque.
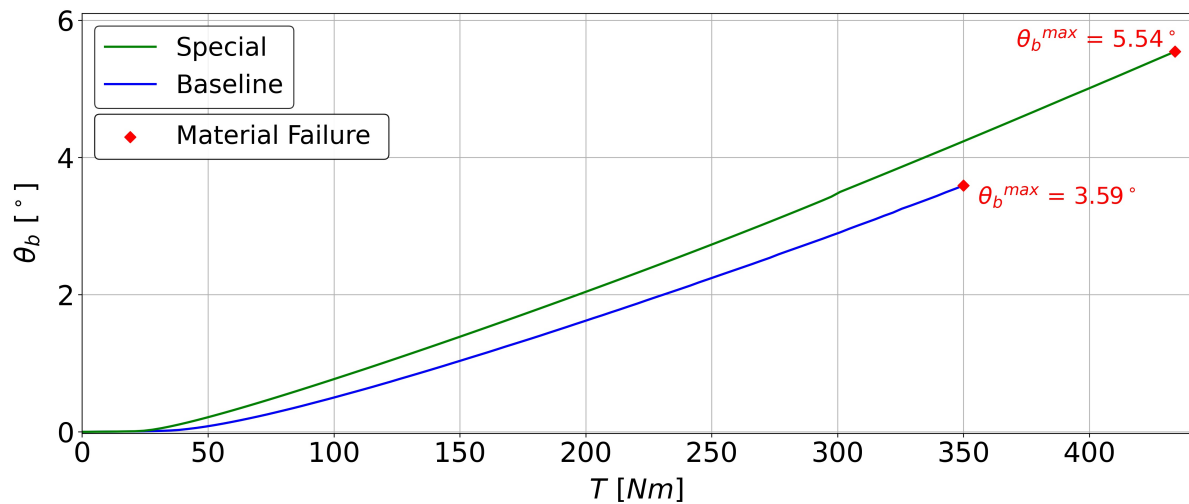
Figure 7.24: Evolution of the buckling-induced twist θ_b with the external quasi-static torque T for the "standard" and "special" expanded wing boxes.

Up to the external torque of 350.0 Nm, for which the spar webs fail in the *no-restraint* condition, the buckling-induced twists created by the "special" expanded wing box are slightly higher than those created by the "baseline" expanded wing box. For example, for a torque of 350.0 Nm, the "special" expanded wing box creates a buckling-induced twist that is only 0.65° higher than the one created by the "baseline" expanded wing box.

However, as the spar webs can sustain greater external torques in the *no-contact* condition than in the *no-restraint* condition, the "special" expanded wing box can create buckling-induced twists for torques at which the "baseline" expanded wing box cannot operate. Consequently, the maximum buckling-induced twist of the "special" expanded wing box ends up being 1.95° higher than the maximum buckling-induced twist of the "baseline" expanded wing box.

7.4. *Partial-restraint* conditions

Partial-restraint buckling constraints can be implemented by setting the gaps between the spar webs and the external walls to intermediate values between those defined for the *full-restraint* and *no-restraint* conditions. In particular, two *partial-restraint* conditions are investigated, setting the external gaps to $G_F = G_R = 0.75$ mm and $G_F = G_R = 2$ mm, respectively.

The expanded wing box FEM in the *partial-restraint* condition with $G_F = G_R = 0.75$ mm is illustrated in Figure 7.25, for which the external walls are moved 5.25 mm from their fully-retracted positions by increasing the thickness of the active walls up to a value of $t_{AW} = 9.25$ mm.

Figure 7.25: Expanded wing box FEM — *Partial-restraint* condition, with $G_F = G_R = 0.75$ mm.

The predictions for the twisting response of a single station are extrapolated to calculate the twisting response of the expanded wing box, which consists of three stations. Thus, Figure 7.26 presents the tip twist and torsional stiffness of the expanded wing box in the *partial-restraint* condition, as a function of the external quasi-static torque T. The oscillations in torsional stiffness created by snapping events are filtered out of the response, although the original torsional stiffness response is also presented in grey dashed lines.

Figure 7.26: Expanded wing box in a *partial-restraint* condition, with $G_F = G_R = 0.75$ mm — Evolution of the elastic tip twist and torsional stiffness with the external quasi-static torque.

As illustrated in Figure 7.26, the spar webs' buckling deformations come into contact with the external walls for an external torque of 49.0 Nm. Therefore, up to this torque, the expanded wing box presents practically the same twisting response as in the *no-restraint* condition (illustrated in Figure 7.3), for which the spar webs' out-of-plane buckling deformations are unrestrained to the outside of the wing box.

Once the spar webs come into contact with the external walls, the twisting response changes, as the spar webs' buckling deformations start being constrained both to the inside and outside of the wing box. From Figure 7.26, the torsional stiffness experiments a sudden increase at the onset of contact. However, as the torque increases, the torsional stiffness progressively reduces, leveling off close to the value registered at the onset of contact.[1]

On the other hand, the evolution of the spar webs' buckling shapes can be divided into two phases, separated by the contact torque of 49.0 Nm. Up to this torque, the buckling shapes evolve in the same way as in the *no-restraint* condition (whose buckling shape evolution was represented in Figure 7.5). Illustrating this, the front spar web's buckling shape evolution up to the external torque of 49.0 Nm is presented in Figure 7.27, based on the out-of-plane deformations registered at four torque levels.

(a)

(b)

(c)

(d)
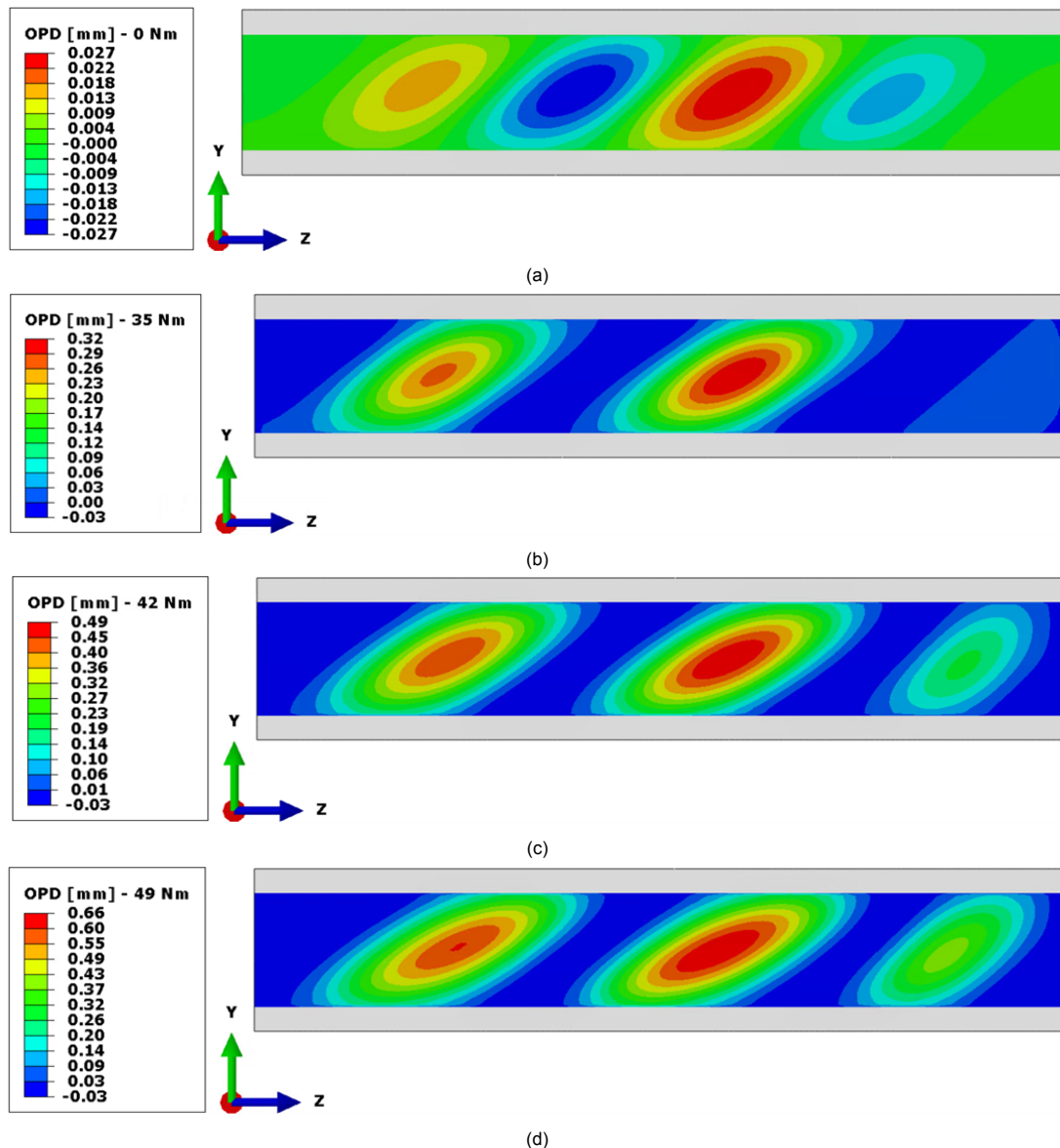
Figure 7.27: Expanded wing box station in the *no-restraint* condition — Front spar web out-of-plane deformations for four different torque levels: (a) T = 0 Nm, (b) T = 35.0 Nm, (c) T = 42.0 Nm, (d) T = 49.0 Nm.

---

[1] It should be clarified that the torsional stiffness response is only studied up to the maximum external torque of 616.0 Nm, for which the spar webs experiment material failure.

The first torque level is the unloaded state, for which the out-of-plane deformations correspond to the four half-waves introduced as geometrical imperfection. As the torque increases, the out-of-plane deformations protruding towards the inside of the wing box are prevented from growing, due to the spar webs coming into contact with the internal walls. This phenomenon is illustrated for the second torque level, of 35.0 Nm, for which the out-of-plane deformations protruding towards the inside of the wing box remain below 0.03 mm.

For the third torque level, of 42.0 Nm, a new half-wave snaps, protruding towards the outside of the wing box, and the oscillation in torsional stiffness created by this sudden change of buckling shape can be identified in Figure 7.26. Finally, the forth torque level corresponds to the contact torque, of 49.0 Nm. As the torque increases from 42.0 Nm to 49.0 Nm, the spar web does not experiment any considerable change in buckling shape.

However, once the torque increases past the contact torque of 49.0 Nm, the buckling shapes start evolving in the same way as in the *full-restraint* condition. Hence, as the external torque increases, the bilaterally constrained spar webs experiment consecutive snapping events, at which their buckling shapes snap into new configurations consisting of a higher number of buckling waves. Thus, starting from the buckling shape registered for the contact torque of 49.0 Nm (illustrated in Figure 7.27d), consisting of 3 half-waves, the number of half-waves successively increases with the external torque. In this way, for the torque of 616.5 Nm, at which the spar webs experiment material failure, twenty half-waves develop across each spar web, as illustrated in Figure 7.28. Furthermore, in addition to the snapping of new half-waves, existing half-waves also snap into new locations as the torque increases. Overall, all these sudden changes of buckling shape lead to the oscillations in torsional stiffness registered in Figure 7.26.

Figure 7.28: Expanded wing box station in the *partial-restraint* condition, with $G_F = G_R = 0.75$ mm, for an external torque of 616.5 Nm — Deformed shape of the wing box. Deformation scale factor: 2.

Applying the Tsai-Hill failure criterion to assess the material failure of the composite spar webs, the front and rear spar webs fail for the same external torque of 616.5 Nm. For this external torque, the associated failure index I_{TH} surpasses a value of 1. In Figure 7.29, the envelope plots of failure index I_{TH} across the front and rear spar webs are displayed for the external torque of 616.5 Nm. It can be observed that, unlike the *full-restraint* condition, the spar webs experiment material failure before the buckling deformations start slipping through the unrestrained regions located above the walls.

(a)

(b)
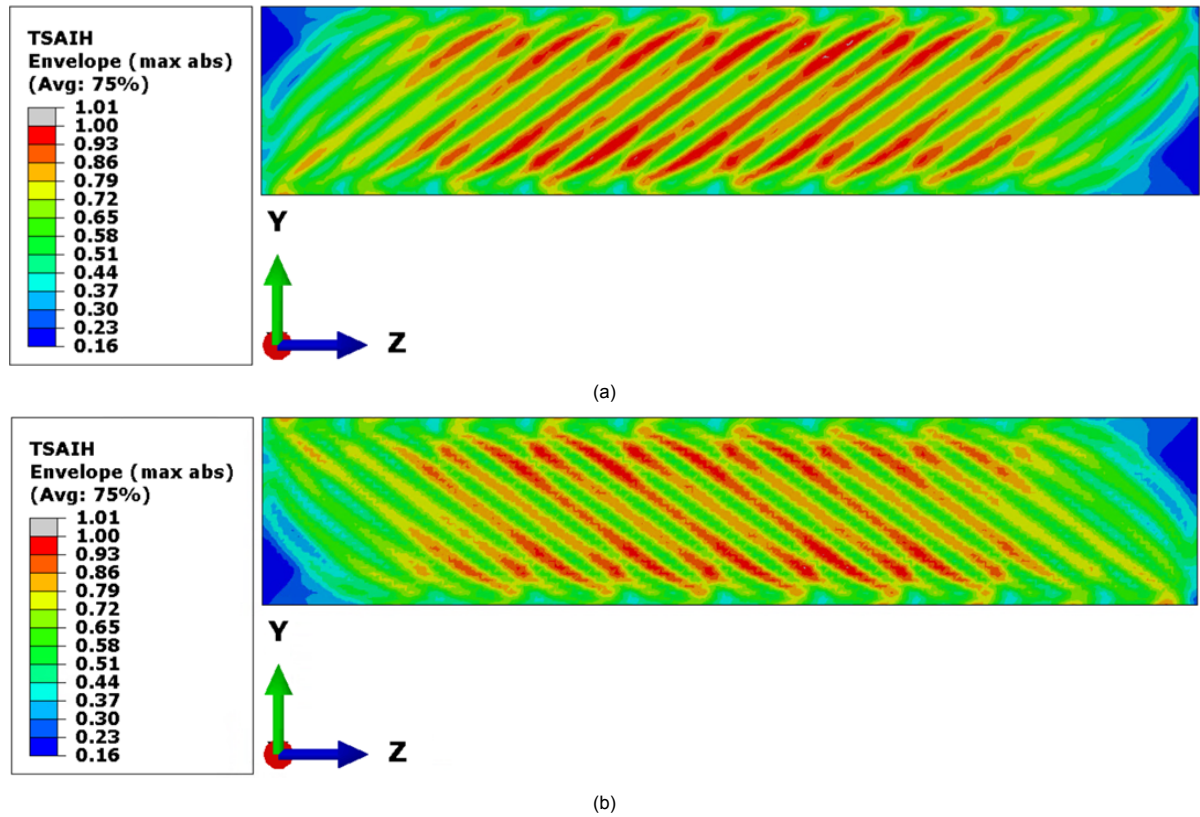
Figure 7.29: Expanded wing box station in a *partial-restraint* condition, with $G_F = G_R = 0.75$ mm, for an external torque of 616.5 Nm — Envelope plot of failure index I_{TH} across the: (a) front spar web, (b) rear spar web.

On the other hand, the expanded wing box FEM in the *partial-restraint* condition with $G_F = G_R = 2$ mm is illustrated in Figure 7.30, for which the external walls are moved 4 mm from their fully-retracted positions by increasing the thickness of the active walls up to a value of $t_{AW} = 8$ mm.
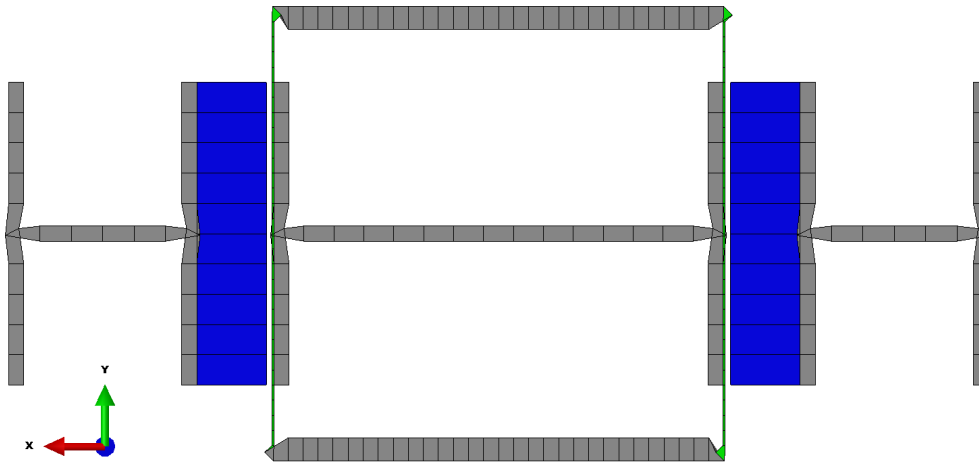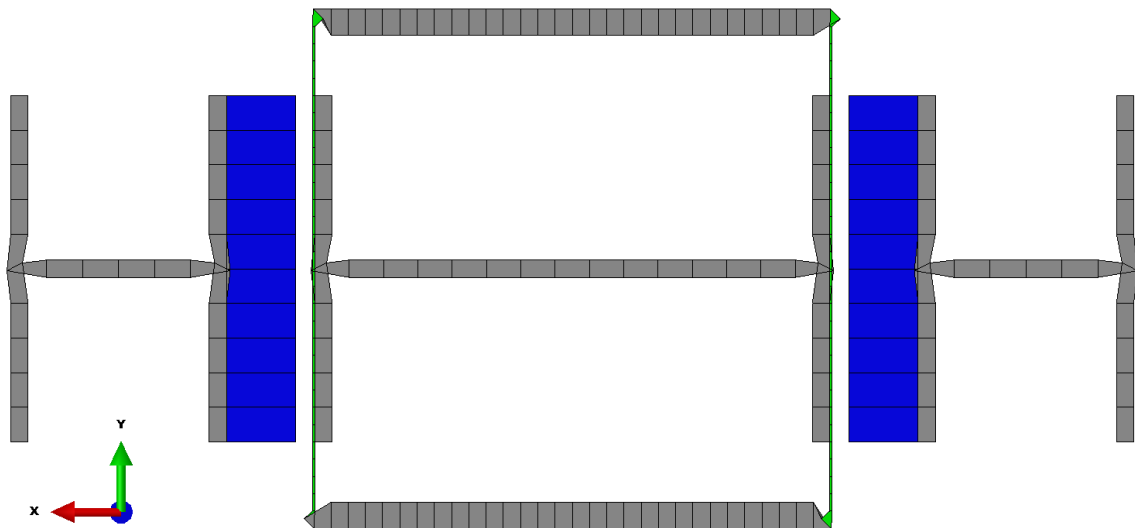

Figure 7.30: Expanded wing box FEM — *Partial-restraint* condition, with $G_F = G_R = 2$ mm.

The predictions for the twisting response of a single station are extrapolated to calculate the twisting response of the expanded wing box, which consists of three stations. Thus, Figure 7.31 presents the tip twist and torsional stiffness of the expanded wing box in this *partial-restraint* condition, with $G_F = G_R = 2$ mm, as a function of the external quasi-static torque T. The oscillations in torsional stiffness created by snapping events are filtered out of the response, although the original torsional stiffness response is also presented in grey dashed lines.
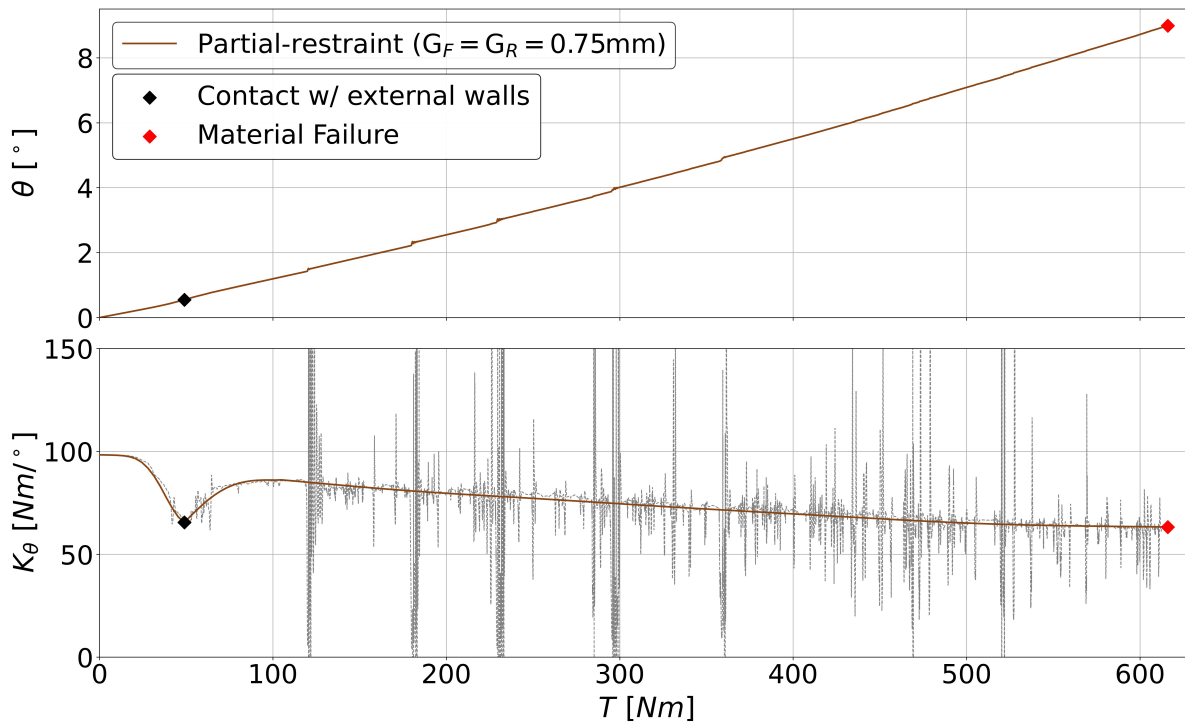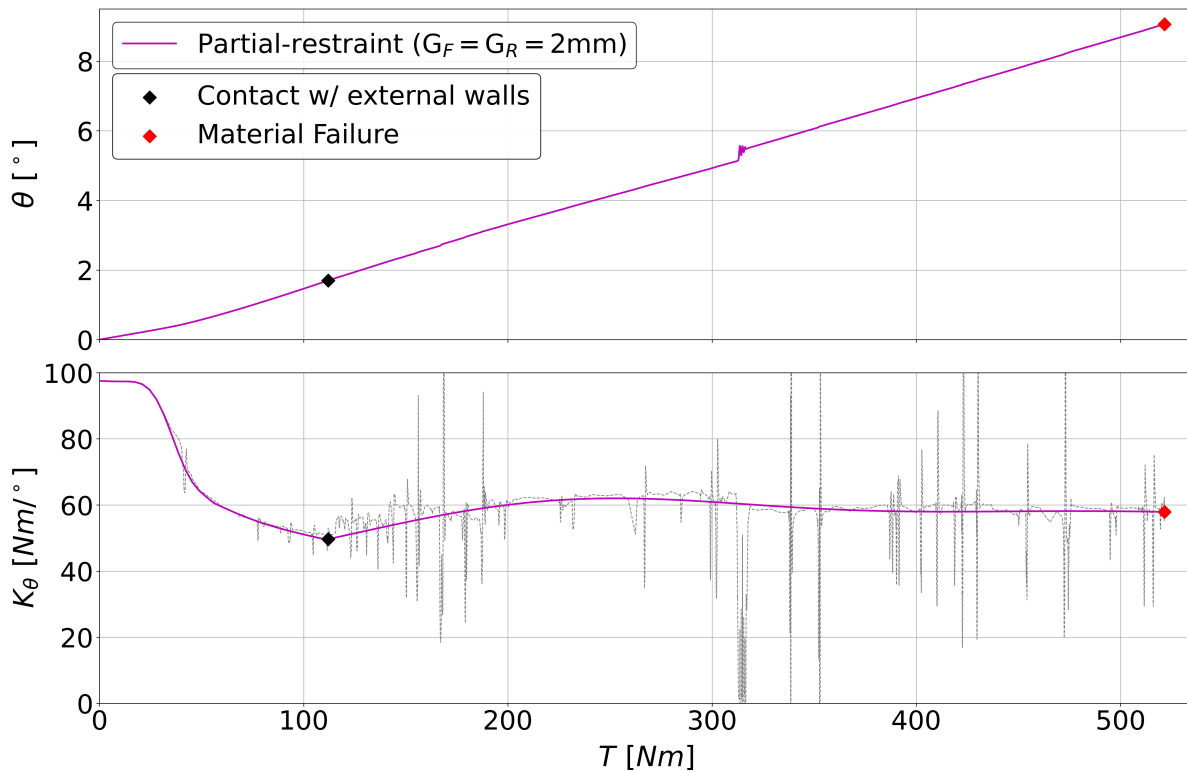
Figure 7.31: Expanded wing box in a *partial-restraint* condition, with $G_F = G_R = 0.75\,\text{mm}$ — Evolution of the elastic tip twist and torsional stiffness with the external quasi-static torque.

The twisting response is similar to that of the previously investigated *partial-restraint* condition, for which the external gaps were set to 0.75 mm. The main difference consists in a higher contact torque, of 112.0 Nm, as the greater external external gaps of 2 mm allow for higher out-of-plane buckling deformations before contact. Up to the contact torque, the twisting response and buckling shape evolution is practically the same as in the *no-restraint* condition. However, past the contact torque, the torsional stiffness first experiments an increase, but then it progressively reduces, levelling off close to the value registered at the onset of contact. On the other hand, as the external torque increases past the contact torque, the bilaterally constrained spar webs snap into new configurations of a higher number of half-waves. Ultimately, for the torque of 521.5 Nm, at which the spar webs experiment material failure, nine half-waves develop across each spar web, as illustrated in Figure 7.32.
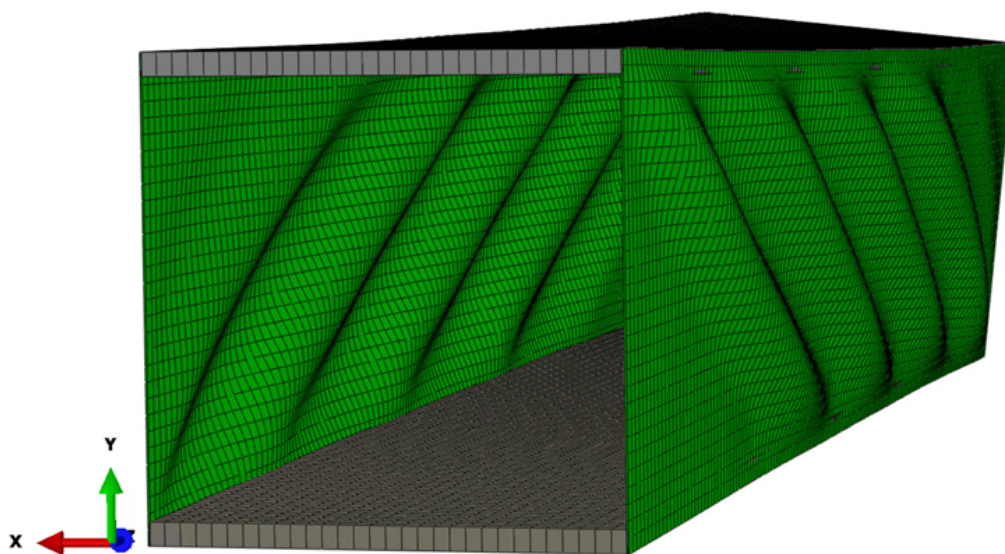
Figure 7.32: Expanded wing box station in the *partial-restraint* condition, with $G_F = G_R = 2\,\text{mm}$, for an external torque of 521.5 Nm — Deformed shape of the wing box. Deformation scale factor: 2.

Applying the Tsai-Hill failure criterion to assess the material failure of the composite spar webs, the front and rear spar webs fail for the same external torque of 521.5 Nm. For this external torque, the associated failure index I_{TH} surpasses a value of 1. In Figure 7.6, the envelope plots of failure index I_{TH} across the front and rear spar webs are displayed for the external torque of 521.5 Nm. Unlike the *full-restraint* condition, the spar webs experiment material failure before the buckling deformations start slipping through the unrestrained regions located above the walls.

(a)

(b)
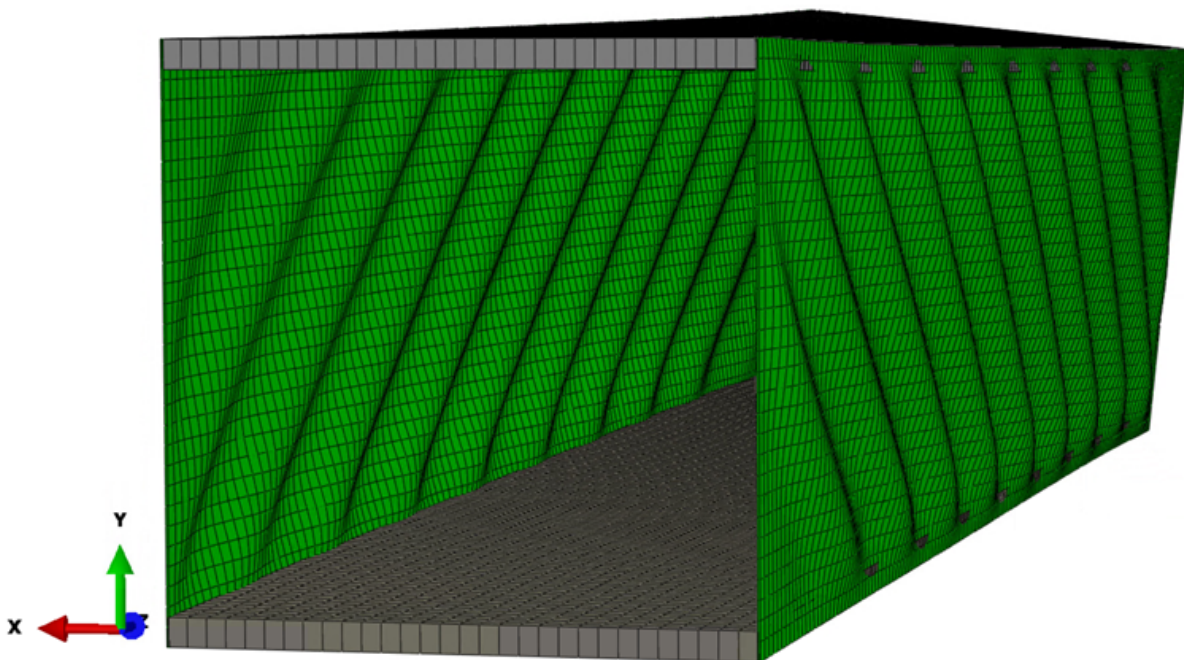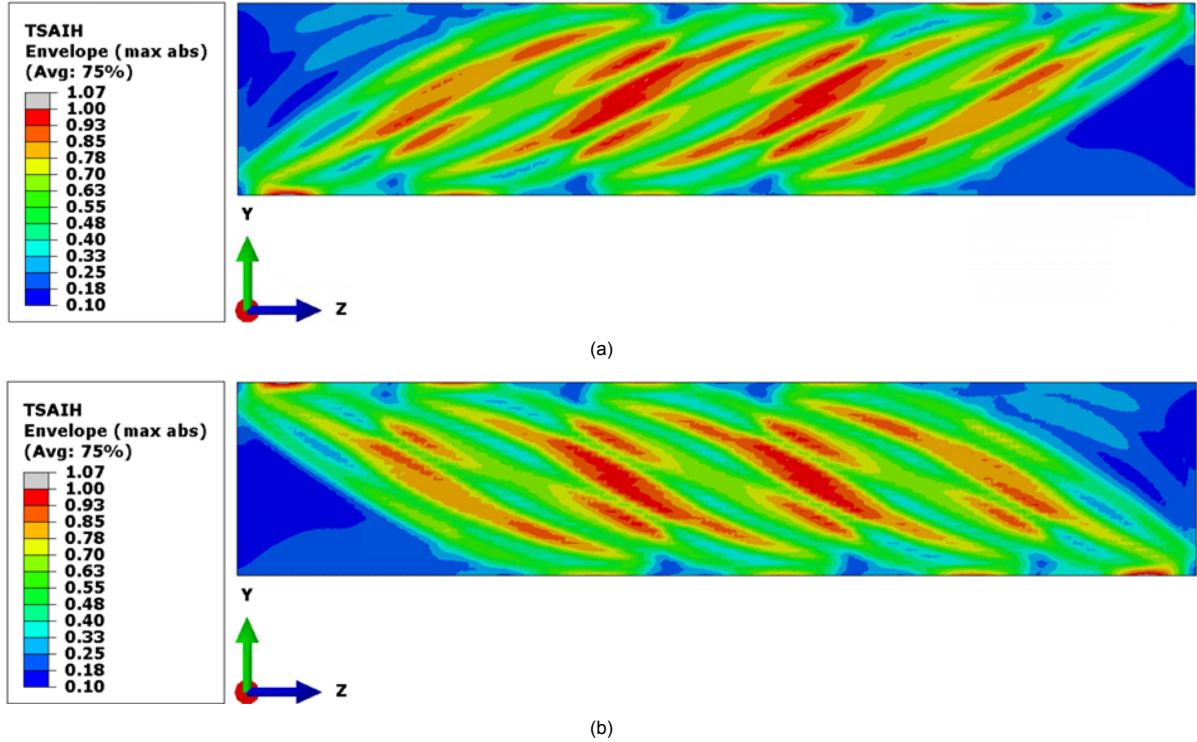
Figure 7.33: Expanded wing box station in a *partial-restraint* condition with $G_F = G_R = 2$ mm for an external torque of 521.5 Nm — Envelope plot of failure index I_{TH} across the: (a) front spar web, (b) rear spar web.

To investigate how the expanded wing box tip twist can be adjusted by controlling the gaps G_F and G_R, Figure 7.34 presents the twist-torque responses of the two investigated *partial-restraint* conditions, and their location within the *Active Region* delimited by the twist-torque responses in the *no-restraint* and *full-restraint* conditions.

So far, the buckling-induced twist θ_b has been defined as the morphing twist created by an external torque when adjusting the buckling constraints from the *full-restraint* to the *no-restraint* condition. However, as *partial-restraint* conditions are now being analyzed, the buckling-induced twist can be redefined as the morphing twist created by an external torque when adjusting the buckling constraints from the *full-restraint* to a different condition. Thus, under this new definition, the buckling-induced twist θ_b not only depends on the external torque T, but also on the external confining gaps G_F and G_R; that is,

$$\theta_b = f(T, G_F, G_R) \tag{7.4}$$

Therefore, for a given external torque T, different buckling-induced twists θ_b can be created, according to the values selected for the external confining gaps. The buckling-induced twists associated to a particular buckling constraint can then be described by the following expression:

$$\theta_b(T) = \theta(T) - \theta_{FR}(T) \tag{7.5}$$

where θ_{FR} is the elastic tip twist in the *full-restraint* condition, and θ is the elastic tip twist created under the buckling constraint being investigated. By applying Eq. (7.5), the buckling-induced twists associated to the investigated buckling constraints are also presented in Figure 7.34, for torque increments of 3.5 Nm.
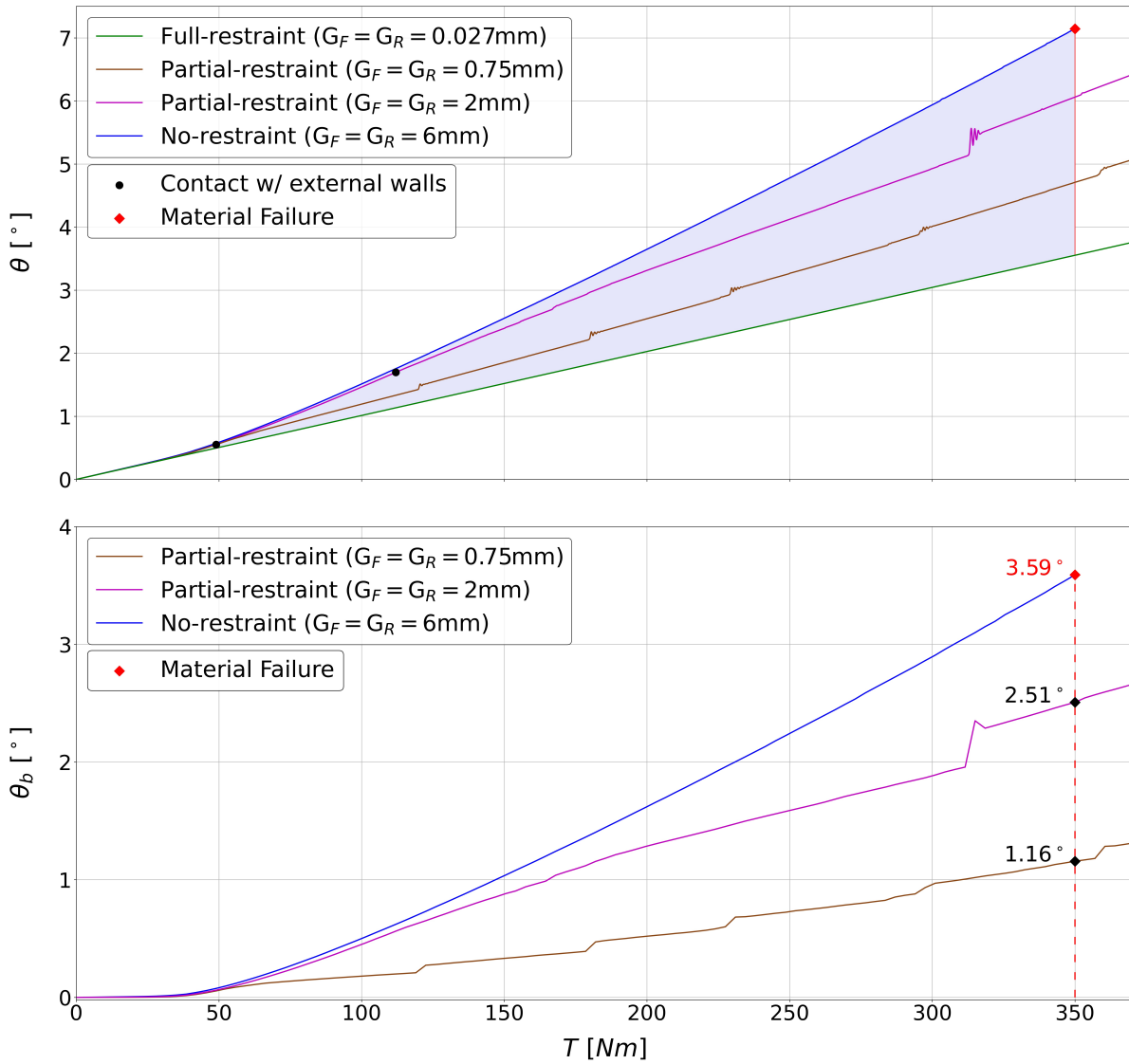
Figure 7.34: Expanded wing box in the *no-restraint*, *full-restraint* and *partial-restraint* conditions — Evolution of the elastic tip twist and buckling-induced twist with the external quasi-static torque.

From Figure 7.34, the buckling-induced twist increases with the external gaps G_F and G_R, but, with an increase rate that reduces as the gaps become larger. To analyze this behaviour, the buckling-induced twist is non-dimensionalized by the maximum buckling-induced twist, i.e., the buckling-induced twist in the *no-restraint* condition. This new variable, referred to as the non-dimensional buckling-induced twist $\overline{\theta_b}$, is then defined as

$$\overline{\theta_b}(T) = \theta_b(T)/\theta_b^{NR}(T) \tag{7.6}$$

where θ_b^{NR} is the buckling-induced twist in the *no-restraint* condition. For the external torque of 350.0 Nm, at which the spar webs fail in the *no-restraint* condition, Figure 7.35 presents the non-dimensional buckling-induced twist $\overline{\theta_b}$ as a function of the external gaps, for which the gap variables G_F and G_R are unified as one single variable G, as both the front and rear gaps have the same value in all investigated buckling constraints.

The three data points presented in Figure 7.35 show how the rate at which the buckling-induced twist increases with the external gap G reduces as the external gap increases. Adjusting the external gaps in the range of 0 mm to 2 mm, which represents only a 33.33% of the available actuation range, allows controlling the buckling-induced twist up to 70% of the maximum achievable buckling-induced twist, while controlling the external gaps in the range of 2 mm to 6 mm only provides control over the remaining 30%.
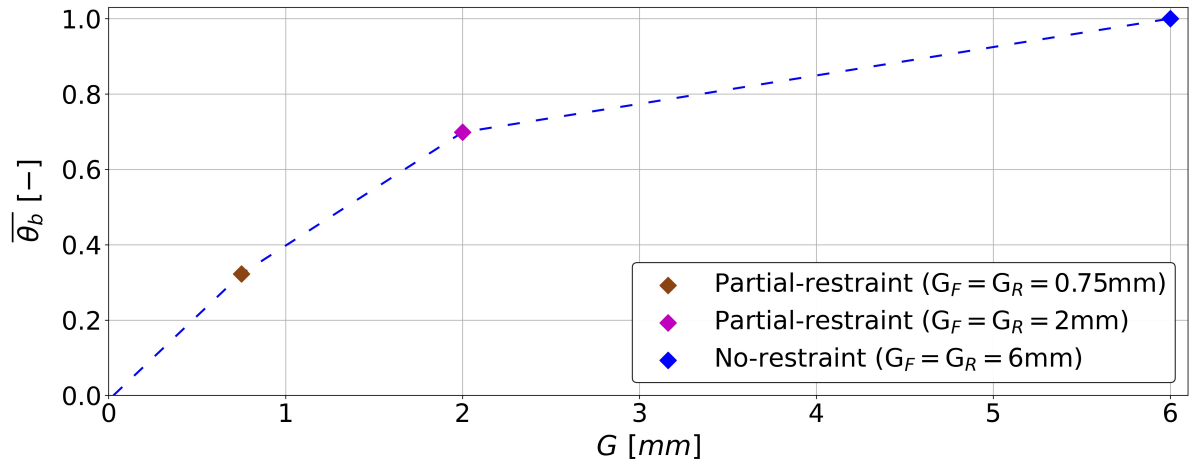
Figure 7.35: Expanded wing box station for an external torque of 521.5 Nm — Evolution of the non-dimensional buckling-induced twist $\overline{\theta_b}$ with the external gap G.

The reasons for this behaviour are based on how the spar webs' effective shear stiffnesses change with the buckling constraints, which in turn ends up affecting the expanded wing box torsional stiffness and twisting response. Thus, Figure 7.36 presents the tip twist and torsional stiffness of the expanded wing box as a function of the external torque, for all investigated buckling constraints. The oscillations in torsional stiffness created by snapping events are filtered out of the responses.
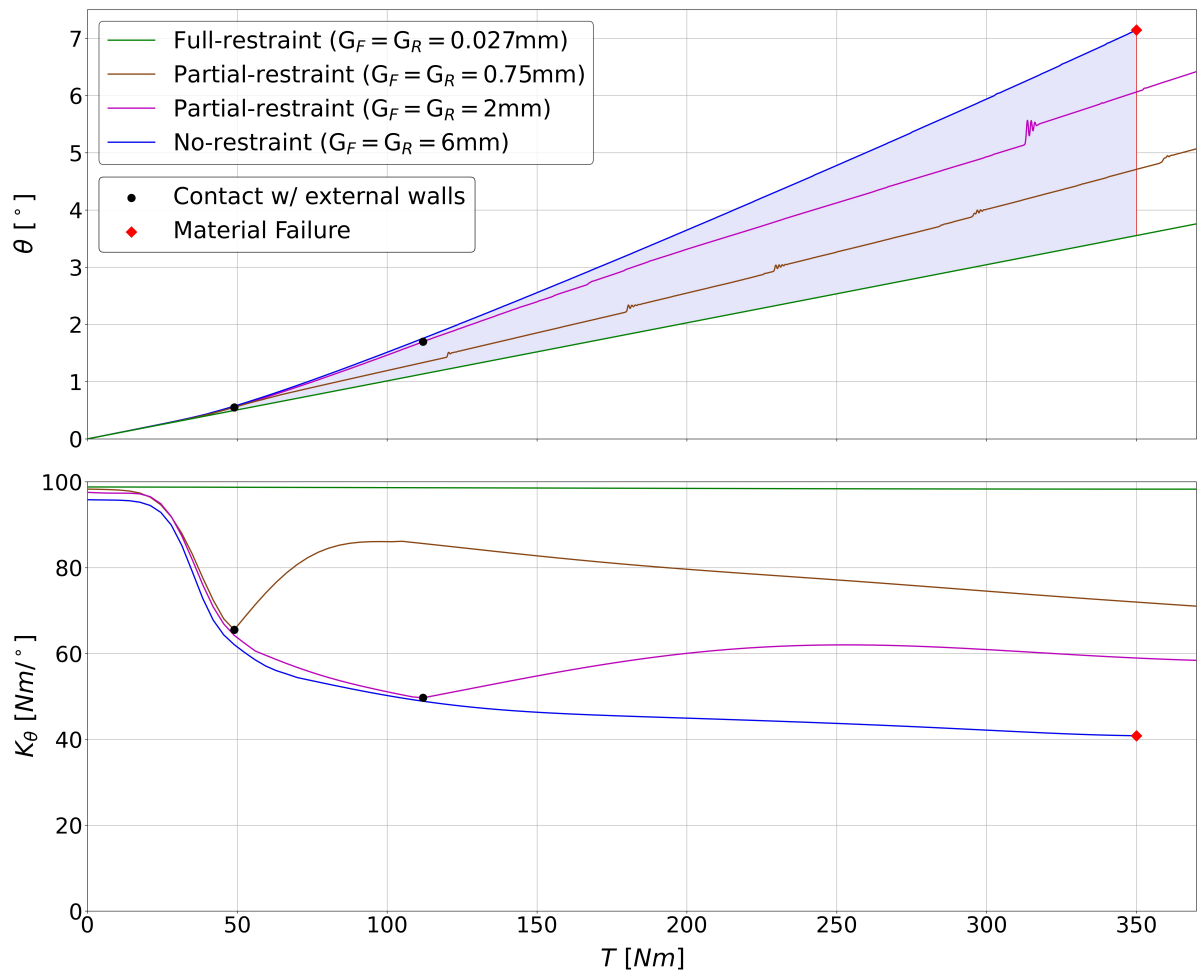
Figure 7.36: Expanded wing box in the *no-restraint*, *full-restraint* and *partial-restraint* conditions — Evolution of the elastic tip twist and torsional stiffness with the external quasi-static torque.

Up to the contact torques, for which the buckled spar webs come into contact with the external walls, the torsional stiffnesses evolve as in the *no-restraint* condition, with only small differences caused by the different active walls' thicknesses between conditions (that lead to slightly different initial torsional stiffnesses). Therefore, as in the *no-restraint* condition, the *partial-restraint* conditions show the highest torsional stiffness reduction rates at the onset of buckling, rapidly flattening off as the torque increases.

On the other hand, once the spar webs come into contact with the external walls, the torsional stiffness stops reducing and levels off close to the value registered at the onset of contact. Thus, considering that the contact torque increases with the external gaps, greater external gaps allow reaching lower torsional stiffnesses. Consequently, higher buckling-induced twists are obtained for greater external gaps, as it increases the difference in torsional stiffness with the *full-restraint* condition. Nevertheless, if the torsional stiffness reduction rate has already flatten off for the torque at which contact occurs, increasing or reducing the contact torque by adjusting the external gaps will have a small influence on the torsional stiffness, leading to small changes in buckling-induced twist. For example, for the *partial-restraint* condition with $G_F = G_R = 2$ mm, Figure 7.36 shows how the torsional stiffness reduction rate has already flatten off for the torque at which contact with the external walls occurs, and, hence, Figure 7.35 shows how increasing the external gaps beyond 2 mm provides a small increase in buckling-induced twist, relative to the values achieved up to 2 mm. In conclusion, this is the reason why the rate at which the buckling-induced twist increases with the external gaps reduces as the gaps become larger.

7.5. Imperfection sensitivity

As explained in Section 6.3, a geometrical imperfection is introduced into the slender spar webs when calculating the twisting response of the expanded wing box. This geometrical imperfection is introduced by superposing the shape function of the expanded wing box first buckling mode for a positive external torque, scaled to a maximum deflection of 0.027 mm. In this way, a maximum initial out-of-plane deflection of 0.027mm is introduced into the front and rear spar webs, which represents a 10% of the 0.27 mm thickness of the spar webs.

However, taking into account that the geometrical imperfection is an unknown that depends on manufacturing constraints, it is of interest to investigate if the morphing capabilities are sensitive to the level of geometrical imperfection. Thus, assuming that a maximum out-of-plane deflection as high as three times the spar web thickness may be created during manufacturing, the twisting responses of the expanded wing box in the *no-restraint* and *full-restraint* conditions are recalculated, introducing a maximum initial out-of-plane deflection of 0.81 mm into the spar webs (which is 3 times the 0.27 mm thickness of the spar webs).

As explained in Section 6.3, the buckling shape introduced as geometrical imperfection presents out-of-plane deflections both to the inside and outside of the wing box. Therefore, to prevent initial contact overclosures between the spar webs' internal surfaces and the internal walls, the width of the internal wall-beam web $w_{w,I}$ is reduced from 59.73 mm to 58.11 mm, placing the internal walls 0.81 mm away from the spar webs' zero-reference positions.

The sensitivity of the twisting response to the level of geometrical imperfection is investigated in Section 7.5.1 for the *no-restraint* condition, and in Section 7.5.2 for the *full-restraint* condition. Finally, the sensitivity of the morphing capabilities to the level of geometrical imperfection is investigated in Section 7.5.3, by analyzing how the level of geometrical imperfection affects the *Active Region* and the buckling-induced twists.

7.5.1. *No-restraint* condition

The expanded wing box FEM in the *no-restraint* condition is illustrated in Figure 7.37, for which the external walls are placed in their fully-retracted positions, setting the gaps between the spar webs and the external walls to $G_F = G_R = 6$ mm. Therefore, except for the larger geometrical imperfections and the slightly shorter web of the internal wall-beam, the FEM is the same as that used to study the twisting response in the *no-restraint* condition for a geometrical imperfection of 0.027 mm in Section 7.1 .

Figure 7.37: Expanded wing box FEM for a geometrical imperfection of 0.81 mm — *No-restraint* condition, with $G_F = G_R = 6\,\text{mm}$.

The predictions for the twisting response of a single station are extrapolated to calculate the twisting response of the expanded wing box, which consists of three stations. Thus, Figure 7.38 presents the tip twist and torsional stiffness of the expanded wing box in the *no-restraint* condition, as a function of the external quasi-static torque T. The oscillations in torsional stiffness created by snapping events are filtered out of the response, although the original torsional stiffness response is also presented in grey dashed lines.

Figure 7.38: Expanded wing box in the *no-restraint* condition for a geometrical imperfection of 0.81 mm — Evolution of the elastic tip twist θ_{NR} and torsional stiffness K_θ^{NR} with the external quasi-static torque T.

Applying the Tsai-Hill failure criterion to assess the material failure of the composite spar webs, the front and rear spar webs fail for the same external torque of 406.0 Nm. For this external torque, the associated failure index I_{TH} surpasses a value of 1. In Figure 7.39, the envelope plots of failure index I_{TH} across the front and rear spar webs are displayed for the external torque of 406.0 Nm.

(a)

(b)

Figure 7.39: Expanded wing box station with a geometrical imperfection of 0.81 mm in the *no-restraint* condition for an external torque of 406.0 Nm — Envelope plot of failure index I_{TH} across the: (a) front spar web, (b) rear spar web.

For the maximum external torque of 406.0 Nm, the spar webs' out-of-plane deformations are presented in Figure 7.40, showing that each spar web reaches a maximum out-of-plane deformation of 4.74 mm, leaving 1.26 mm gaps with the external walls. These gaps are illustrated in Figure 7.41, where the expanded wing box station deformed shape is displayed.

(a)

(b)

Figure 7.40: Expanded wing box station with a geometrical imperfection of 0.81 mm in the *no-restraint* condition — Out-of-plane deformations for an external torque of 406.0 Nm across the: (a) front spar web, (b) rear spar web.

Figure 7.41: Expanded wing box station with a geometrical imperfection of 0.81 mm in the *no-restraint* condition — Deformed shape, with a deformation scale factor of 1, for an external torque of 406.0 Nm.

To analyze the sensitivity of the expanded wing box twisting response in the *no-restraint* condition to the level of geometrical imperfection, Figure 7.42 presents the evolution of the tip twist and torsional stiffness with the external quasi-static torque for the two investigated levels of geometrical imperfection, of 0.027 mm and 0.81 mm. It should be highlighted that the oscillations in torsional stiffness created by snapping events are filtered out of the responses presented in Figure 7.42.

Figure 7.42: Expanded wing box in the *no-restraint* condition for different levels of geometrical imperfection — Evolution of the tip elastic twist and torsional stiffness with the external quasi-static torque T.

From Figure 7.42, for the large geometrical imperfection of 0.81 mm, the spar webs are in a post-buckled state since the very beginning of the loading path, causing the initial torsional stiffness to be 25% lower than that computed for the spar webs with a small geometrical imperfection of 0.027 mm. However, as the torque increases, both torsional stiffnesses become closer to each other, practically coalescing into the same response.

On the other hand, it can also be observed that the maximum external torque T_{max}, at which the spar webs experiment material failure, is sensitive to the level of geometrical imperfection. For the large geometrical imperfection of 0.81 mm, the T_{max} has a value of 406.0 Nm, which is 16% higher than the T_{max} predicted for the small geometrical imperfection of 0.027 mm, of 350.0 Nm. Consequently, the maximum tip twist that can be achieved for the geometrical imperfection of 0.81 mm ends up being 1.5° higher than the maximum tip twist predicted for the geometrical imperfection of 0.027 mm.

7.5.2. *Full-restraint* condition

The *full-restraint* buckling constraint is defined as the condition in which the spar webs' out-of-plane buckling deformations are restrained both to the inside and outside of the wing box to a maximum value that coincides with the initial maximum out-of-plane deflection introduced as geometrical imperfection. As the front and rear spar webs have a maximum initial out-of-plane deflection of 0.81 mm, both to the inside and outside of the wing box, the gaps between the spar webs and the external walls are set to $G_F = G_R = 0.81$ mm, while the internal walls are already placed 0.81 mm away from their corresponding spar webs. The expanded wing box FEM in the *full-restraint* condition is illustrated in Figure 7.43, for which the external walls are moved 5.19 mm from their fully-retracted positions by increasing the thickness of the active walls up to a value of $t_{AW} = 9.19$ mm.
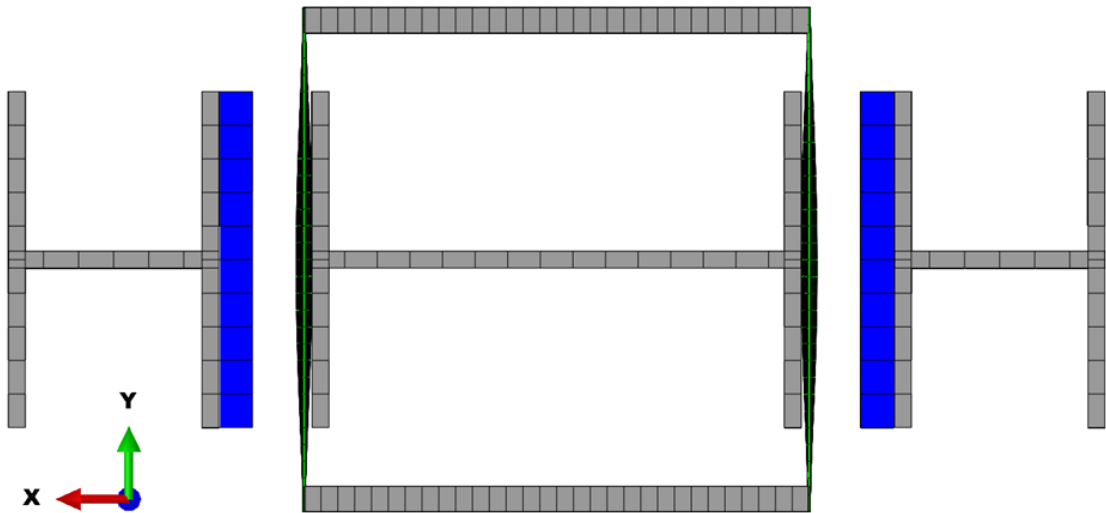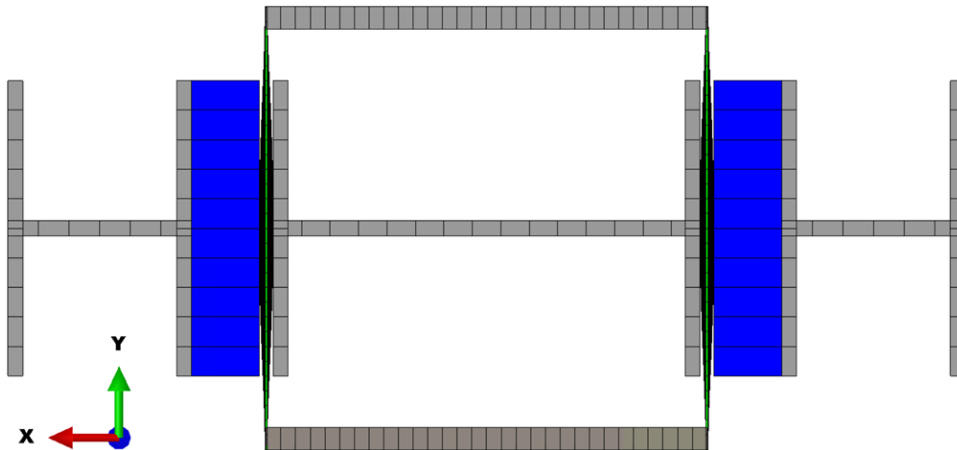

Figure 7.43: Expanded wing box FEM for a geometrical imperfection of 0.81 mm — *Full-restraint* condition, with $G_F = G_R = 0.81$ mm.

The predictions for the twisting response of a single station are extrapolated to calculate the twisting response of the expanded wing box, which consists of three stations. Thus, Figure 7.44 presents the tip twist and torsional stiffness of the expanded wing box in the *full-restraint* condition, as a function of the external quasi-static torque T. The oscillations in torsional stiffness created by snapping events are filtered out of the response, although the original torsional stiffness response is also presented in grey dashed lines.
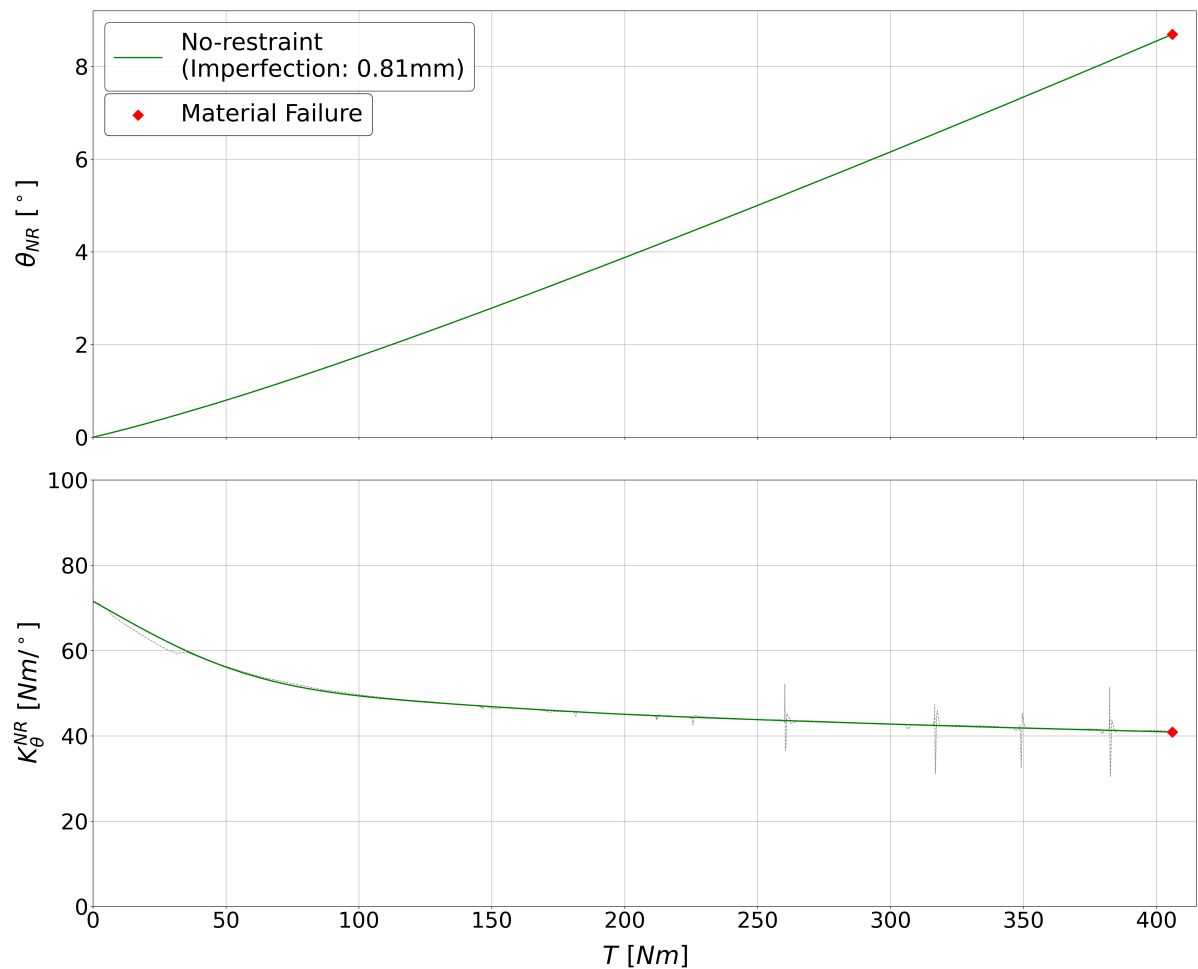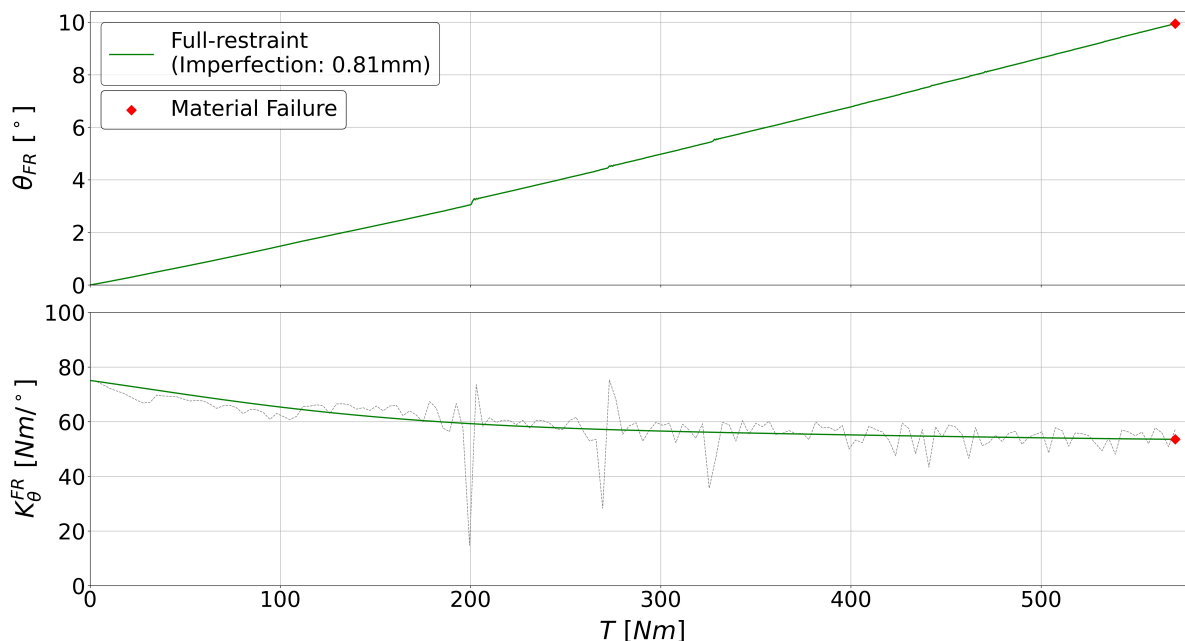

Figure 7.44: Expanded wing box in the *full-restraint* condition for a geometrical imperfection of 0.81 mm — Evolution of the elastic tip twist θ_{FR} and torsional stiffness K_θ^{FR} with the external quasi-static torque T.

As the external torque increases, the bilaterally constrained spar webs experiment consecutive snapping events, at which their buckling shapes snap into new configurations consisting of a higher number of buckling waves. Thus, from an initial buckling shape consisting of 4 half-waves, the number of half-waves successively increases with the external torque. To illustrate this, Figure 7.45 presents the spar webs' deformed shapes for the maximum external torque of 570.5 Nm, showing thirteen half-waves across each spar web.
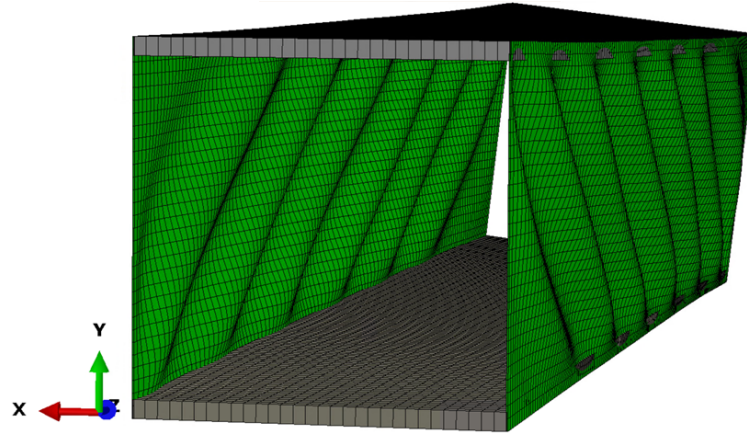
Figure 7.45: Expanded wing box station in the *full-restraint* condition for an external torque of 570.5 Nm — Deformed shape of the wing box. Deformation scale factor: 2.

Applying the Tsai-Hill failure criterion to assess the material failure of the composite spar webs, the front spar web fails first for an external torque of 570.5 Nm. For this external torque, the associated failure index I_{TH} surpasses a value of 1. In Figure 7.46, the envelope plots of failure index I_{TH} across the front and rear spar webs are displayed for the external torque of 570.5 Nm.
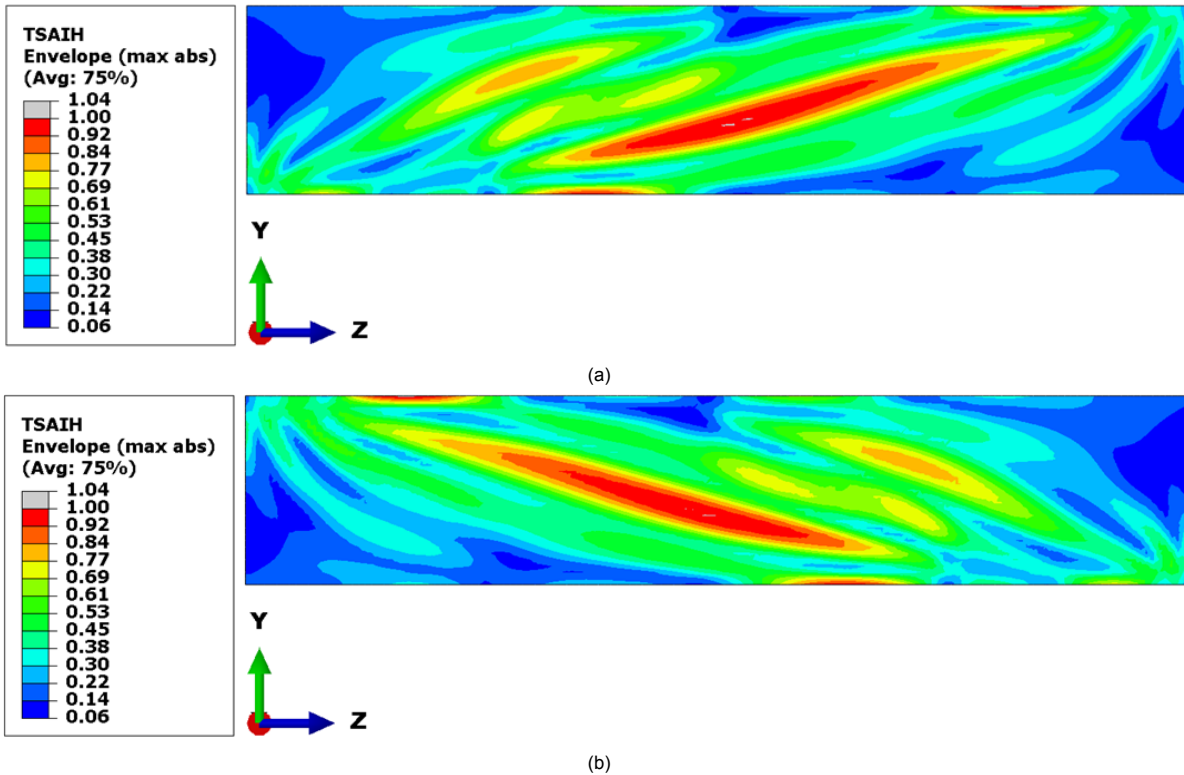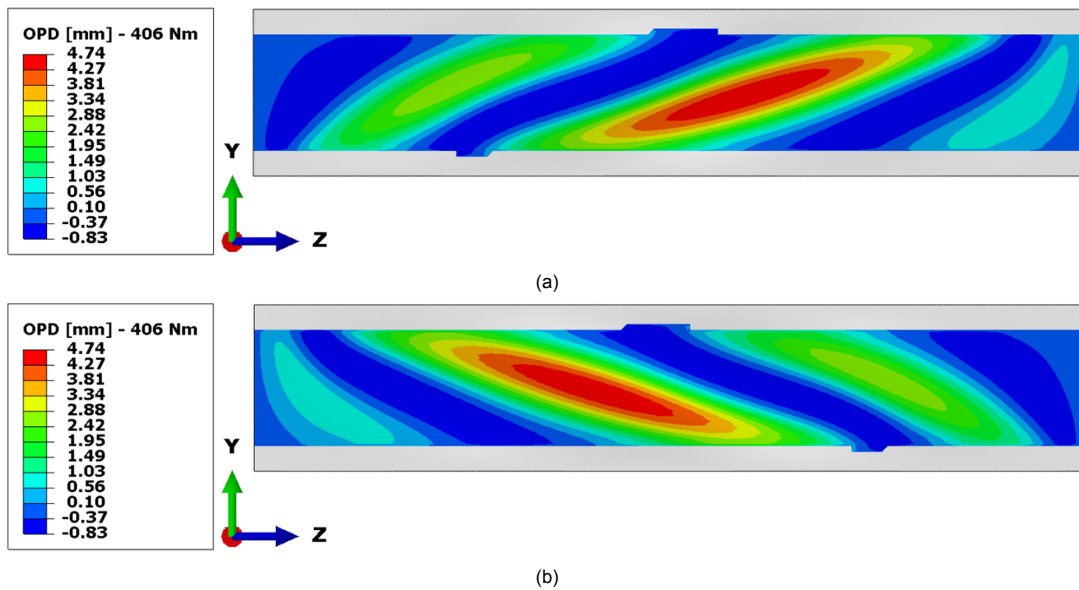

(a)

(b)
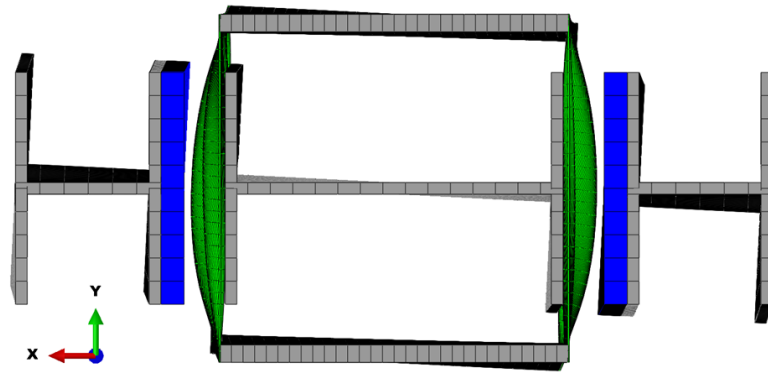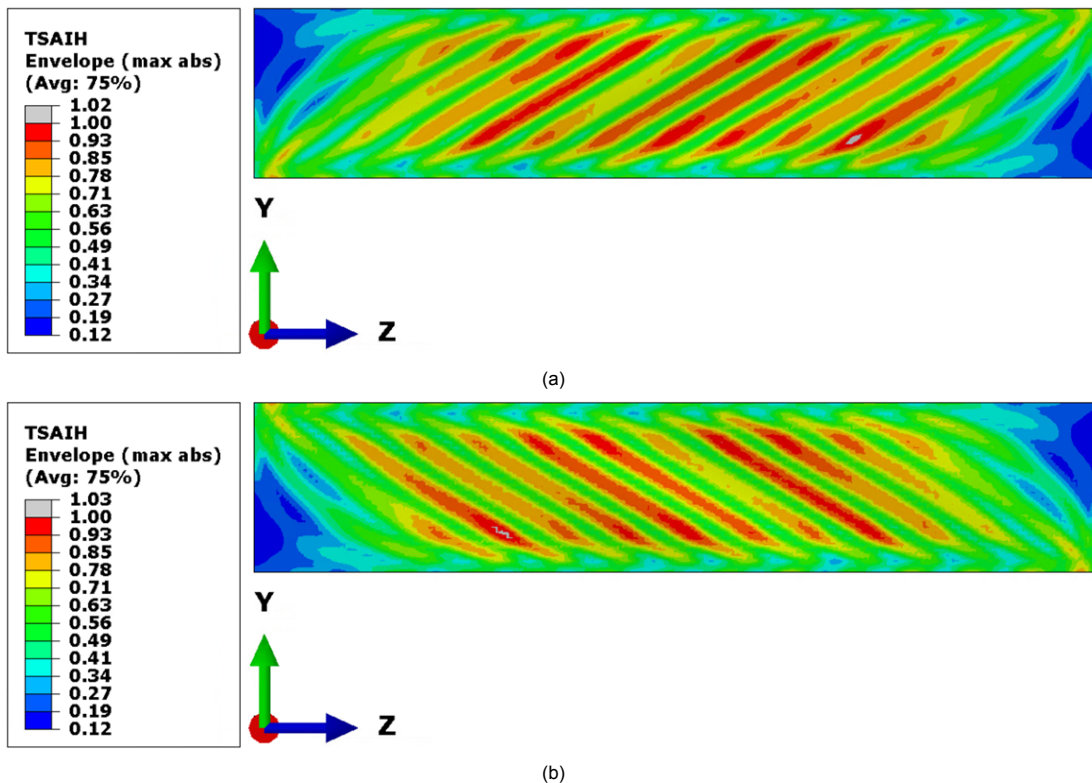
Figure 7.46: Expanded wing box station with a geometrical imperfection of 0.81 mm in the *full-restraint* condition for an external torque of 570.5 Nm — Envelope plot of failure index I_{TH} across the: (a) front spar web, (b) rear spar web.

To analyze the sensitivity of the expanded wing box twisting response in the *full-restraint* condition to the level of geometrical imperfection, Figure 7.47 presents the evolution of the tip twist and torsional stiffness with the external quasi-static torque for the two investigated levels of geometrical imperfection, of 0.027 mm and 0.81 mm. The oscillations in torsional stiffness created by snapping events are filtered out of the responses, and, to assess the constraining walls' effectiveness in restraining the buckling deformations, the twisting response in the *ideal full-restraint* condition, i.e., for spar webs with no geometrical imperfection and ideally prevented from buckling, is also presented in Figure 7.47.
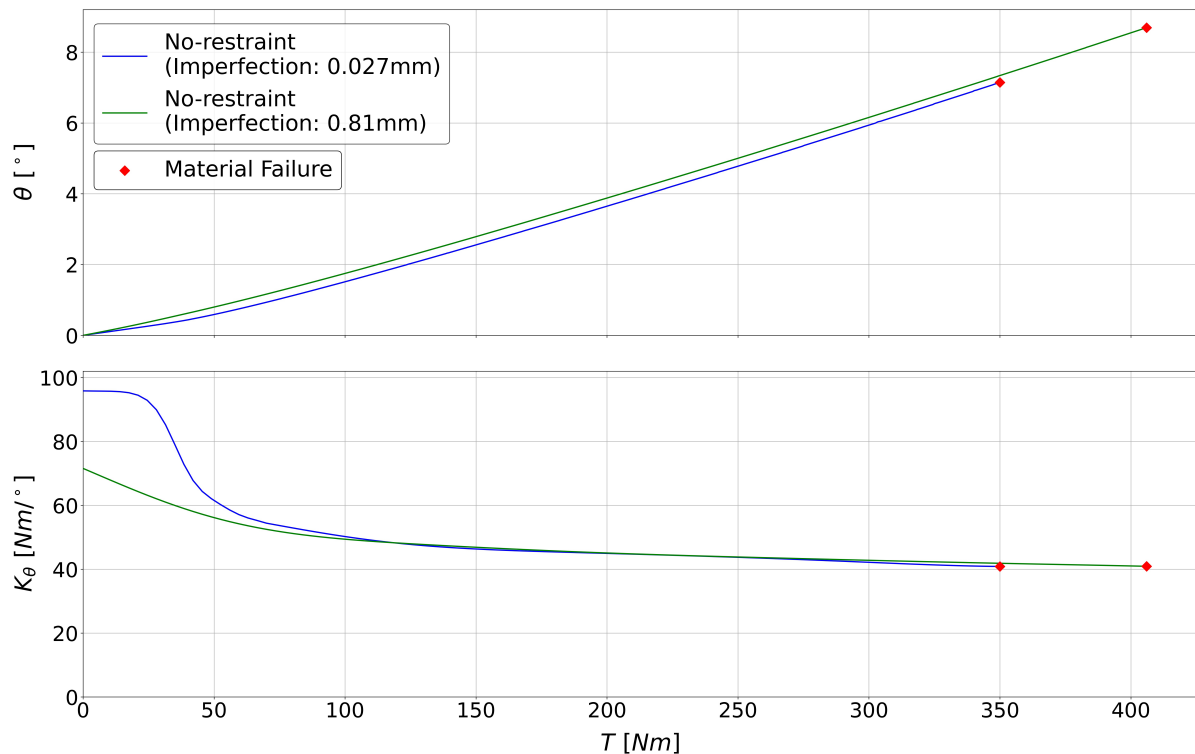

Figure 7.47: Expanded wing box in the *full-restraint* condition for different levels of geometrical imperfection — Evolution of the tip elastic twist and torsional stiffness with the external quasi-static torque T.

The constraining walls' effectiveness in restraining the buckling deformations in the *full-restraint* condition can be assessed in terms of their capability to prevent buckling-induced reductions in torsional stiffness from occurring. Ideally, for spar webs whose out-of-plane deformations are fully restrained (i.e., fixed to zero), the torsional stiffness remains constant throughout the loading path, as shown in Figure 7.47 for the *ideal full-restraint* condition. However, when considering spar webs with geometrical imperfections, the spar webs' initial out-of-plane deflections prevent the out-of-plane deformations from being fully restrained. Instead, the out-of-plane deformations are left unrestrained both to the inside and outside of the wing box up to the value of the initial maximum out-of-plane deflection.

For the small geometrical imperfection of 0.027 mm, the out-of-plane buckling deformations are constrained to a maximum value of 0.027 mm, both to the inside and outside of the wing box. From Figure 7.47, the small out-of-plane deflections introduced as geometrical imperfection have no effect on the initial torsional stiffness, which coincides with the torsional stiffness computed for spar webs with no geometrical imperfection in the *ideal full-restraint* condition. On the other hand, as the external torque increases, the torsional stiffness remains practically constant up to the restraint-effectiveness threshold of 388.5 Nm, showing that the spar webs' bilaterally constrained post-buckling deformations have no effect on the effective shear stiffness of the spar webs.[2]

---

[2]The reasons why buckling-induced reductions in torsional stiffness occur for torques higher than 388.5 Nm have already been discussed in Section 7.2.

For the large geometrical imperfection of 0.81 mm, the out-of-plane buckling deformations are constrained to a maximum value of 0.81 mm, both to the inside and outside of the wing box. From Figure 7.47, the large out-of-plane deflections introduced as geometrical imperfection cause the initial torsional stiffness to be 24% lower than that computed for spar webs with no geometrical imperfection in the *ideal full-restraint* condition. The reason for this is that since the beginning of the loading path, the shear loads acting on the spar webs are supported by tension fields perpendicular to the diagonal half-waves introduced as geometrical imperfection, which has the effect of reducing the effective shear stiffness of the spar webs. On the other hand, as the external torque increases, Figure 7.47 shows that the torsional stiffness reduces, presenting the highest reduction rates at the beginning of the loading path, and progressively flattening off for higher torques.

Therefore, buckling-induced reductions in torsional stiffness occur since the very beginning of the loading path when the out-of-plane buckling deformations are allowed to increase unconstrained up to 0.81 mm. The reason for this behaviour is related to the fact that new half-waves snap throughout the spar webs as the external torque increases. With the snapping of new half-waves, the diagonal tension fields (perpendicular to the diagonal half-waves) expand throughout the spar webs, ultimately reducing the effective shear stiffness of the spar webs.

It should be highlighted that even though new half-waves also snap throughout the spar webs when the out-of-plane buckling deformations are constrained to the maximum value of 0.027 mm, the fact that the out-of-plane deformations are only allowed to increase unconstrained up to 0.027 mm prevents the diagonal tension fields from developing. Consequently, such post-buckling deformations have no effect on the effective shear stiffness of the spar webs, and hence neither on the expanded wing box torsional stiffness.

7.5.3. Active Region & Buckling-induced twist

Finally, to analyze the sensitivity of the morphing capabilities to the level of geometrical imperfection, the *Active Regions* predicted for the two investigated levels of geometrical imperfection, of 0.027 mm and 0.81 mm, are compared to each other. For this purpose, Figure 7.48 presents the elastic tip twist and torsional stiffness of the expanded wing box in the *no-restraint* and *full-restraint* conditions as a function of the external quasi-static torque, filtering out the oscillations in torsional stiffness created by snapping events.
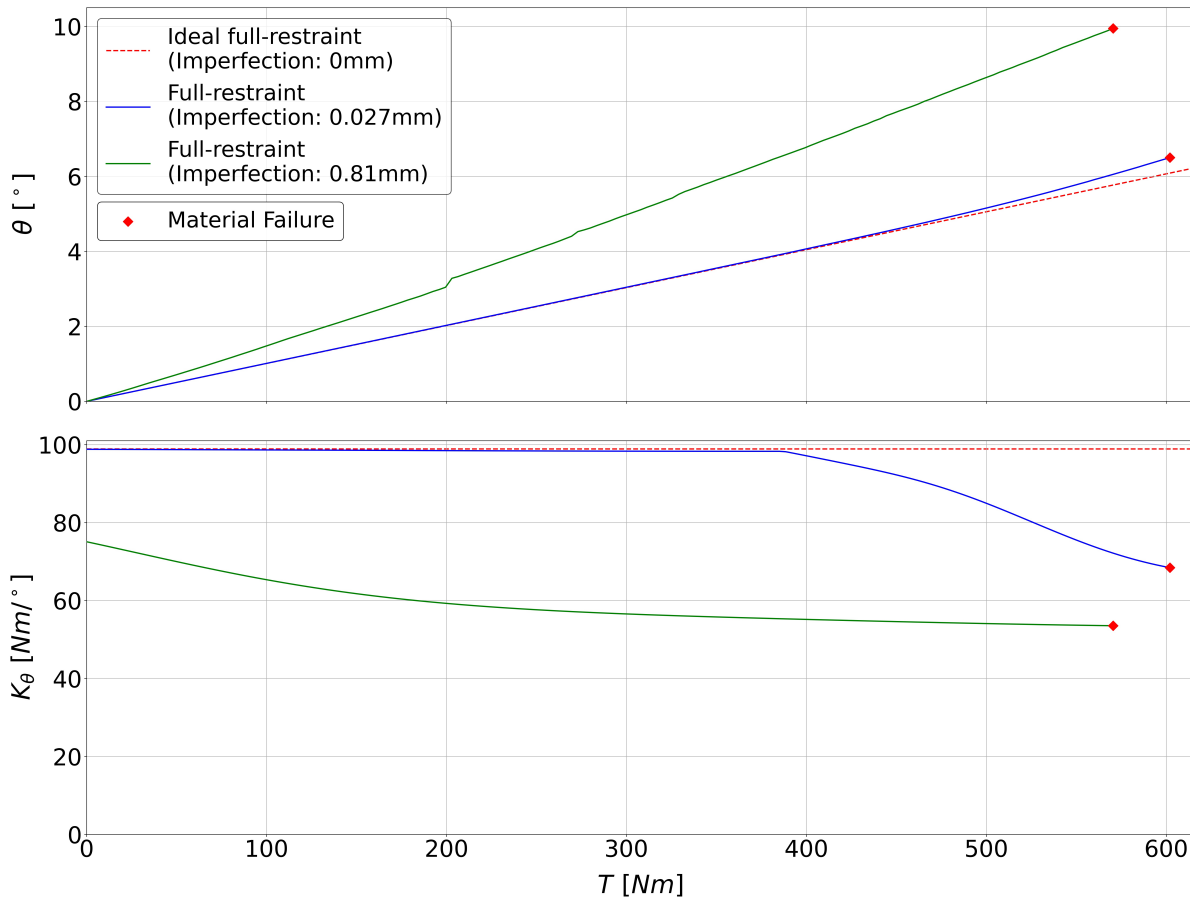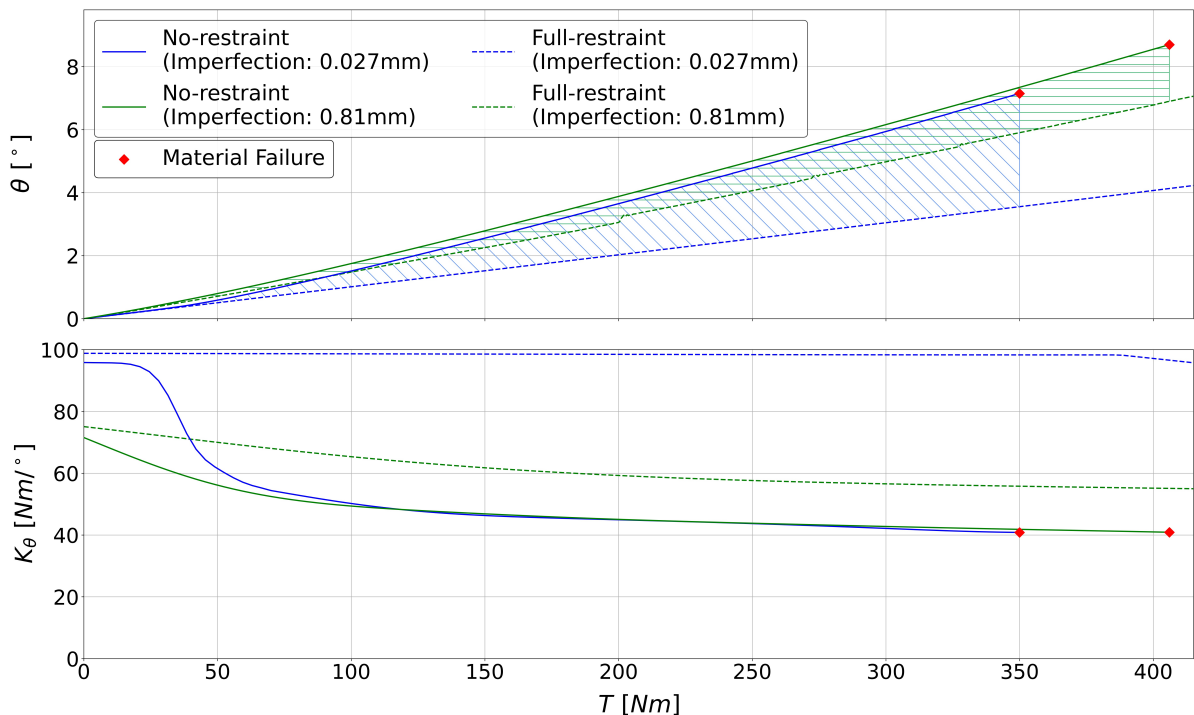

Figure 7.48: Expanded wing box in the *no-restraint* and *full-restraint* conditions for different levels of geometrical imperfection — Evolution of the elastic tip twist and torsional stiffness with the external quasi-static torque T.

From Figure 7.48, the *Active Region* for the geometrical imperfection of 0.81 mm is considerably smaller than the *Active Region* for the geometrical imperfection of 0.027 mm. Taking into account that the *Active Regions* enclose the different elastic tip twists that could be selected by actively adjusting the external confining gaps G_F and G_R under the action of an external torque, a smaller *Active Region* is associated to lower morphing capabilities.

Lower morphing capabilities are predicted for the geometrical imperfection of 0.81 mm due to the lower effectiveness with which buckling-induced reductions in torsional stiffness are prevented from occurring in the *full-restraint* condition for the geometrical imperfection of 0.81 mm. As illustrated in Figure 7.48, for the small geometrical imperfection of 0.027 mm, the torsional stiffness in the *full-restraint* condition does not experiment any buckling-induced reduction up to the maximum external torque of 350.0 Nm. However, for the large geometrical imperfection of 0.81 mm, the torsional stiffness in the *full-restraint* condition experiments great buckling-induced reductions, reaching values more than 40% lower than those obtained for the geometrical imperfection of 0.027 mm. Consequently, the range within which the torsional stiffness can be selectively controlled by adjusting the external confining gaps G_F and G_R reduces, which in turn has the effect of reducing the morphing twists that can be achieved.

The morphing capabilities can be measured in terms of the greatest morphing twist that could be created for a given external torque, which corresponds with the buckling-induced twist created by adjusting the buckling constraints from the *full-restraint* condition to the *no-restraint* condition. Hence, by applying Eq. (4.4), Figure 7.49 presents the evolution of such buckling-induced twist with the external torque for the two investigated levels of geometrical imperfection, of 0.027 mm and 0.81 mm.
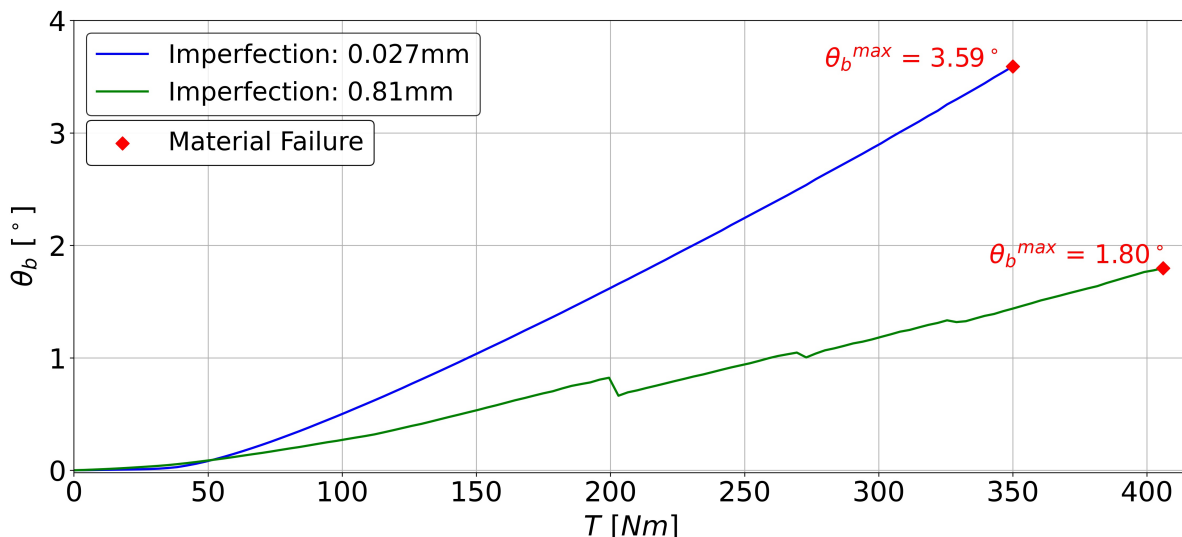
Figure 7.49: Expanded wing box for different levels of geometrical imperfection — Evolution of the buckling-induced twist in the *no-restraint* condition θ_b with the external quasi-static torque T.

From Figure 7.49, greater morphing twists can be created for the small geometrical imperfection of 0.027 mm than for the large geometrical imperfection of 0.81 mm. Thus, for the geometrical imperfection of 0.81 mm, a maximum buckling-induced twist of 1.8° can be created, which is only half of the maximum buckling-induced twist created for the 0.027 mm geometrical imperfection, of 3.6°. Another interesting observation is that the difference between both morphing twists increases with the external torque, until reaching the maximum difference value of 2.1° for the external torque of 350.0 Nm, at which the spar webs with a 0.027 mm geometrical imperfection experiment material failure.

In conclusion, the morphing capabilities are very sensitive to the level of geometrical imperfection introduced into the spar webs. It is found that for a given external torque, the morphing twists that can be created by adjusting the external confining gaps G_F and G_R reduce with the level of geometrical imperfection. The main reason for this behaviour is that the effectiveness with which buckling-induced reductions in torsional stiffness are prevented from occurring in the *full-restraint* condition reduces with the level of geometrical imperfection. In particular, for geometrical imperfections ranging from a minimum imperfection level of 0.027 mm (10% of the spar web thickness) to a maximum imperfection level of 0.81 mm (3 times the spar web thickness), the morphing twists can differ by up to 2.1°, depending on the level of geometrical imperfection and the level of external torque applied.

7.6. Twist morphing capabilities under bending

Throughout this thesis, the twist morphing capabilities under the application of an external quasi-static torque have been reported. However, large efforts have also been devoted to investigating the influence of the structural design on the twist morphing capabilities under the application of a spanwise bending load. In particular, the spar webs' buckling-induced reductions in effective shear stiffness can be exploited to adjust the cross-sectional location of the shear centre, affecting the twisting response to the bending load.

Without taking into account the adaptive constraining devices, it has been found that the twist morphing capabilities for a bending load applied at the tip of the wing box are severely limited by the buckling of the skin panels at the root of the wing box. In particular, the level of limitation depends greatly on the span of the wing box, as the bending moment increases towards the root. Nevertheless, in the efforts to maximize the morphing twists, a wing box configuration with a slender rear spar web and a thick front spar web with a cutout showed promising results. As the cutout reduces the front spar web shear stiffness, the proportion of the bending load supported by the slender spar web increases, allowing the slender spar web to operate far in its post-buckling regime before the buckling of the skin panels.

However, when considering the adaptive constraining devices' influence over the twisting response, the twist morphing capabilities undergo another severe reduction. Due to the attachment of the I-section wall-beams to the ribs, most of the bending load is now supported by the wall-beams' flanges, whose shear stiffness is much higher than that of the slender composite spar webs. Consequently, the slender spar webs' bending buckling load increases up to a level for which the skin panels closest to the root may have already buckled, especially for a long span wing box.

In the efforts to maximize the morphing twists, it has been found that reducing the width of the wall-beams' flanges contributes to increasing the proportion of the bending load supported by the slender spar webs, allowing for greater morphing twists before the buckling of the skin panels. However, as reported in Section 7.2, if the flanges' widths are reduced relative to the height of the spar webs, the effectiveness with which the constraining walls restrain the buckling deformations reduces. Overall, as some of the benefits of reducing the width of the wall-beams' flanges cancel out due to the lower effectiveness in restraining the buckling deformations, the morphing twists that can be created under an external bending load end up being very small when compared to those that can be achieved under the action of an external torque.

For the expanded wing box design presented in Chapter 6, the twisting response to a bending load applied at the tip of the wing box cannot be controlled, as the skin panels close to the wing box root buckle before the slender spar webs. Nevertheless, if the wing box is subjected to both an external torque and a bending load, the slender spar webs could operate in a post-buckled state due to the external torque, and a buckling-induced relocation of the shear centre could be exploited to affect the bending-twisting coupling. This functionality may be investigated in future work.

8
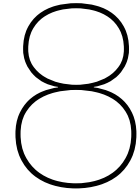
Conclusions and Recommendations

A two-level design process of increased complexity has been developed for the design of a morphing wing box embedded with slender spar webs. In the first level, the objective is to maximize the wing box twist morphing capabilities without taking into account the design of the external constraining devices required to control the spar webs' out-of-plane buckling deformations. For this purpose, a methodology has been developed for evaluating the twist morphing capabilities based on the wing box twisting response to an external quasi-static torque under two different conditions: the *no-restraint* condition, in which the spar webs are free to buckle, and the *full-restraint* condition, in which the spar webs have no geometrical imperfection and are ideally prevented from buckling. In particular, the morphing capabilities are evaluated in terms of the morphing twists created by an external quasi-static torque when the buckling deformations are actively adjusted from the *full-restraint* condition to the *no-restraint* condition. As the twisting response in the *full-restraint* condition can be determined without applying any external constraint to the slender spar webs, neither the adaptive constraining devices nor the constraint-strategy with which the buckling deformations are to be controlled need to defined at this level.

Implementing this methodology to evaluate the twist morphing capabilities, the wing box design space has been explored in terms of the wing box cross-sectional dimensions and the materials of the slender spar webs. On the one hand, it has been found that greater morphing twists can be achieved for smaller wing box cross-sections, due to their lower pre-buckling torsional stiffness and greater buckling-induced reductions in torsional stiffness. On the other hand, it has been found that slender spar webs made from plain-weave carbon fabric plies can lead to much higher buckling-induced twists than spar webs made from unidirectional carbon plies, as they experiment greater buckling-induced reductions in effective shear stiffness. Ultimately, among all investigated wing box configurations, a wing box with slender spar webs made from plain weave carbon fabric plies showed the best morphing capabilities, reaching morphing twists at the tip of the wing box as high as 7.4° before the spar webs' material failure.

This wing box configuration of promising morphing capabilities was then input into a second level of design, in which the adaptive constraining devices required to control the slender spar webs' out-of-plane buckling deformations are designed. With the objective of maximizing the twist morphing capabilities under an external quasi-static torque, different designs for the adaptive constraining devices have been considered in an extensive design process, until finding the design solution proposed in this thesis. For this design solution, each slender spar web is placed in-between two walls. One wall is located inside the wing box, fixed in a position adjacent to the spar web, while the other wall is located outside the wing box, placed away from the spar web at a distance referred to as the external confining gap that can be actively adjusted to control the out-of-plane buckling deformations. These walls are integrated into I-section beam structures attached to the ribs of the wing box, referred to as wall-beams, fulfilling three different purposes: (i) provide the walls of sufficient spanwise bending stiffness to effectively restrain the spar webs' buckling deformations, (ii) provide the walls of a supporting structure that follows the global twisting deformations of the wing box, and (iii) provide a supporting structure for the attachment of the actuation system required to actively adjust the position of the walls.

A structural finite element model has been developed to study the twisting response of the resultant morphing structure, referred to as the expanded wing box, that consists of the wing box and the adaptive constraining devices. The expanded wing box twisting response has been investigated under different buckling constraints, i.e., for different external confining gaps, determining the evolution of the tip twist, torsional stiffness and spar webs' buckling shape with an external quasi-static torque, taking into account the material failure of the spar webs.

For slender spar webs with a geometrical imperfection of 10% of the spar web thickness, it is predicted that a maximum morphing twist of 3.6° can be created at the tip of the expanded wing box. However, if the morphing structure is endowed with the additional functionality of adjustable internal gaps, the maximum operational torque increases, leading to a higher maximum tip morphing twist of 5.5°. Nevertheless, the benefits in providing actuation to the internal walls only become considerable if the morphing structure is expected to operate at sufficiently high external torques. For torque levels below the maximum operational torque of the "baseline" configuration (i.e., with fixed internal walls), adjustable internal gaps only provide a relatively small increase in morphing twist. Comparing to the maximum tip morphing twist of 7.4° predicted at the first level, the integration of the adaptive constraining devices into the morphing structure causes the maximum tip morphing twist to reduce by a 51%, although this percentage reduces to a 26% if the morphing structure is endowed with the additional functionality of adjustable internal gaps.

On the other hand, even though the post-buckled spar webs reach maximum out-of-plane buckling deformations of 5.25 mm when left unrestrained to the outside of the wing box, it has been found that adjusting the external confining gaps up to maximum value of 2 mm already provides control over 70% of the range of possible morphing twists. The reason for this is that constraining out-of-plane buckling deformations that occur far in the post-buckling regime has a small effect on a spar web effective shear stiffness, as the greatest buckling-induced reductions in effective shear stiffness occur at the onset of buckling.

Furthermore, it has been found that the twist morphing capabilities reduce with the level of geometrical imperfection introduced into the slender spar webs. Under the assumption that in the *full-restraint* condition the constraining walls are placed at a distance from the spar webs equal to the initial maximum out-of-plane deflection introduced as geometrical imperfection, the twisting response in the *full-restraint* condition becomes very sensitive to the level of geometrical imperfection. In particular, the constraining walls need to be placed further from the spar webs for higher levels of geometrical imperfection, causing the bilaterally constrained post-buckled spar webs to experiment greater buckling-induced reductions in effective shear stiffness. Ultimately, this has the effect of reducing the range within which the torsional stiffness can be selectively controlled by adjusting the buckling constraints, which in turn reduces the twist morphing capabilities. These negative effects that the spar webs' geometrical imperfections have on the morphing capabilities cannot be captured at the first level of design, as only a *full-restraint* condition in which the spar webs have no geometrical imperfection can be evaluated without taking into account the adaptive constraining devices.

8.1. Recommendations

Overall, this thesis has contributed to developing a wing box structure that exploits the buckling instabilities of slender spar webs to adjust its twisting response to an external torque. However, much research still needs to be done to implement such twist morphing concept into a real wing. Therefore, some recommendations for future work are presented below.

First, the numerical predictions for the twisting response of the wing box with adaptive constraining devices need experimental validation. Therefore, an experimental demonstrator should be designed, manufactured and tested. For this purpose, the different structural components constituting the morphing structure are to be manufactured and assembled, but also the actuation system required to adjust the location of the constraining walls needs to be designed. However, if the experimental testing objectives are restricted to the validation of the numerical predictions of this thesis, the constraining walls could be manually adjusted to new positions between different test runs, as the twisting response of the morphing wing box to an external quasi-static torque has only been investigated considering buckling constraints that do not change throughout the loading path.

Even though the design of the actuation system may not be strictly required for the experimental validation of the numerical predictions of this thesis, it represents an important research gap for the

development of the twist morphing concept. On one hand, taking into account that the twist morphing concept is envisioned to be implemented as a wing shape morphing solution, the actuation system will need to be lightweight to prevent the weight-penalty of the morphing concept from canceling the aerodynamic benefits associated to a twist morphing wing. On the other hand, the actuation system would also need to fulfill the actuation requirements of loading, stroke and actuation bandwidth required to control the spar webs' effective shear stiffness.

On the other hand, the morphing twists investigated throughout this thesis correspond to those created by an external torque when the wing box torsional stiffness is selectively reduced by partially or fully releasing buckling deformations that were being restrained by the constraining walls. Even though it has been envisioned that these morphing twists could be reversed by reducing the gaps between the walls and the spar webs, as the consequent reductions in the out-of-plane buckling deformations could potentially increase the post-buckled spar webs' effective shear stiffnesses, this functionality needs to be further investigated. For this purpose, structural models that consider the movement of the constraining walls under the action of the external torque need to be developed. If the buckling-induced reductions in the spar webs' effective shear stiffnesses prove to be reversible, pressing the constraining walls on the spar webs to remove their initial geometrical imperfections may be a way to prevent the twisting response in the *full-restraint* condition from being affected by the level of geometrical imperfection, helping to reduce the negative effects that the spar webs' geometrical imperfections have on the morphing capabilities.

Finally, the morphing wing box structure will have to be integrated into a twist morphing wing. For this purpose, the rest of the wing structure will need to be designed ensuring that the torsional stiffness continues being dominated by the wing box, as it was also considered in this thesis for the design of the adaptive constraining devices. Furthermore, as an active aeroelastic adaptive concept that will extract the mechanical work to twist the wing from the aerodynamic forces, a structural model of the morphing wing would have to be coupled to an aerodynamic model to predict the aeroelastic active twists that could be created at different flight conditions, and verify that aeroelastic instabilities, like divergence and flutter, do not occur at operating velocities.

Bibliography

[1] S. Barbarino, O. Bilgen, R.M. Ajaj, M.I. Friswell, and D.J. Inman. "A Review of morphing aircraft". In: *Journal of Intelligent Material Systems and Structures* 22 (2011), pp. 823–877.

[2] R.M. Ajaj, M.I. Friswell, W.G. Dettmer, A.T. Isikveren, and G. Allegri. "Roll control of a MALE UAV using the adaptive torsion wing". In: *The Aeronautical Journal* 117 (2013), pp. 299–314.

[3] J.E. Cooper. "Adaptive stiffness structures for air vehicle drag reduction". In: *Multifunctional Structures / Integration of Sensors and Antennas*. 2006.

[4] P.C Chen, D. Sarhaddi, R. Jha, D.D. Liu, K. Griffin, and R. Yurkovich. "Variable stiffness spar approach for aircraft maneuver enhancement using astros". In: *Journal of Aircraft* 37.5 (2000), pp. 865–871.

[5] J. Florance, J. Heeg, C. Spain, T. Ivanco, C. Wieseman, and P. Lively. "Variable stiffness spar wind-tunnel model development and testing". In: *45th AIAA/ASME/ASCE/AHS/ASC Structures, Structural Dynamics Materials Conference*. 2004.

[6] W. Raither, A. Bergamini, and P. Ermanni. "Profile beams with adaptive bending–twist coupling by adjustable shear centre location". In: *Journal of Intelligent Material Systems and Structures* 24.3 (2012), pp. 334–346.

[7] W. Raither, M. Heymanns, A. Bergamini, and P. Ermanni. "Morphing wing structure with controllable twist based on adaptive bending–twist coupling". In: *Smart Materials and Structures* 22.6 (2013).

[8] F. Runkel, A. Reber, G. Molinari, A.F. Arrieta, and P. Ermanni. "Passive twisting of composite beam structures by elastic instabilities". In: *Composite Structures* 147 (2016), pp. 274–285.

[9] F. Runkel. "Shape Adaptability by Elastic Instability: Exploiting Buckling-Induced Selective Stiffness in Structures and Metastructures." PhD thesis. ETH Zurich, 2018.

[10] F. Runkel, U. Fasel, G. Molinari, A.F. Arrieta, and P. Ermanni. "Wing twisting by elastic instability: A purely passive approach". In: *Composite Structures* 206.15 (2018), pp. 750–761.

[11] J. Zhang and C. Bisagni. "Buckling-driven mechanisms for twisting control in adaptive composite wings". In: *Aerospace Science and Technology* 118 (2021), p. 107006.

[12] J.B. Samuel and D. Pines. "Design and testing of a pneumatic telescopic wing for unmanned aerial vehicles". In: *Journal of Aircraft* 44.4 (2007), pp. 1088–1099.

[13] J.E. Cooper. "Aeroelastic adaptive structures". In: *Adaptive Structures: Engineering Applications.* Ed. by D. Wagg, I. Bond, P. Weaver, and M.I. Friswell. Wiley, 2007, pp. 137–162.

[14] E.W Pendleton, D. Bessette, P.B. Field, G.D. Miller, and K.E. Griffin. "Active aeroelastic wing flight research program: Technical program and model analytical development". In: *Journal of Aircraft* 37.4 (2000), pp. 554–561.

[15] C. Nam, A. Chattopadhyay, and Y. Kim. "Application of shape memory alloy (SMA) spars for aircraft maneuver enhancement". In: *SPIE's 9th annual international symposium on smart structures and materials*. 2002.

[16] P.B. Leal, H. Stroud, E. Sheahan, M. Cabral, and D.J. Hartl. "Skin-based camber morphing utilizing shape memory alloy composite actuators in a wind tunnel environment". In: *2018 AIAA/AHS Adaptive Structures Conference*. 2018.

[17] P.L. Bishay, R. Finden, S. Recinos, C. Alas, E. Lopez, D. Aslanpour, D. Flores, and E. Gonzalez. "Development of an SMA-based camber morphing UAV tail core design". In: *Smart Materials and Structures* 28.7 (2019).

[18] G. Molinari, M. Quack, A. F. Arrieta, M. Morari, and P Ermanni. "Design, realization and structural testing of a compliant adaptable wing". In: *Smart Materials and Structures* 24 (2015).

[19]   R. Vos, R. Barrett, R. De Breuker, and P. Tiso. "Post-buckled precompressed elements: A new class of control actuators for morphing wing UAVs". In: *Smart Materials and Structures* 16.3 (2007), pp. 919–926.

[20]   O. Bilgen, K.B. Kochersberger, D.J. Inman, and O.J. Ohanian. "Novel, bidirectional, variable-camber airfoil via macro-fiber composite actuators". In: *Journal of Aircraft* 47.1 (2010), pp. 303–314.

[21]   I.K. Kuder, A.F. Arrieta, M. Rist, and P. Ermanni. "Aeroelastic response of a selectively compliant morphing aerofoil featuring integrated variable stiffness bi-stable laminates". In: *Journal of Intelligent Material Systems and Structures* 27.14 (2016), pp. 1949–1966.

[22]   B.K. Woods and M.I. Friswell. "Preliminary investigation of a fishbone active camber concept". In: *ASME 2012 conference on smart materials, adaptive structures and intelligent systems.* 2012.

[23]   B.K. Woods, O. Bilgen, and M.I. Friswell. "Wind tunnel testing of the fish bone active camber morphing concept". In: *Journal of Intelligent Material Systems and Structures* 25.7 (2014), pp. 772–785.

[24]   A. Rivero, S. Fournier, P. Weaver, and J.E. Cooper. "Manufacturing and characterization of a composite FishBAC morphing wind tunnel model". In: *29th International Conference on Adaptive Structures and Technologies*. 2018.

[25]   A.E. Rivero, P.M. Weaver, J.E. Cooper, and B.K. Woods. "Structural modeling of compliance-based camber morphing structures under transverse shear loading". In: *AIAA Journal* 58 (2020).

[26]   A. Rivero, P. Weaver, J.E. Cooper, and B.K. Woods. "Progress on the design of a composite Fish-BAC morphing device for spanwise lift control". In: *22nd International Conference on Composite Materials*. 2019.

[27]   N. Nguyen. "Elastically shaped future air vehicle concept". NASA Technical Report, ARC-E-DAA-TN3743. 2010.

[28]   J. Urnes and N. Nguyen. "A mission adaptive variable camber flap control system to optimize high lift and cruise lift to drag ratios of future N+3 transport aircraft". In: *51st AIAA Aerospace Sciences Meeting including the New Horizons Forum and Aerospace Exposition*. 2013.

[29]   S. Lebofsky, E. Ting, D. Chaparro, J. Urnes, N. Nguyen, and U. Kaul. "Development of variable camber continuous trailing edge flap for performance adaptive aeroelastic wing". In: *SAE 2015 AeroTech Congress Exhibition*. 2015.

[30]   T. Mkhoyan, N.R. Thakrar, R. De Breuker, and J. Sodja. "Design of a smart morphing wing using integrated and distributed trailing edge camber morphing". In: *ASME 2020 Conference on Smart Materials, Adaptive Structures and Intelligent Systems*. 2020.

[31]   T. Mkhoyan, N.R. Thakrar, R. De Breuker, and J. Sodja. "Design and development of a seamless smart morphing wing using distributed trailing edge camber morphing for active control". In: *AIAA Scitech 2021 Forum*. 2021.

[32]   N. Werter, J. Sodja, G. Spirlet, and R. De Breuker. "Design and experiments of a warp induced camber and twist morphing leading and trailing edge device". In: *24th AIAA/AHS Adaptive Structures Conference*. 2016.

[33]   S. Pantelakis, M. Kintscher, M. Wiedemann, H.P. Monner, O. Heintze, and T. Kühn. "Design of a smart leading edge device for low speed wind tunnel tests in the European project SADE". In: *International Journal of Structural Integrity* 2.4 (2011), pp. 383–405.

[34]   M. Kintscher, J. Kirn, S. Storm, and F. Peter. "Assessment of the SARISTU Enhanced Adaptive Droop Nose". In: *Smart Intelligent Aircraft Structures (SARISTU)*. Ed. by Piet Christof Wölcken and Michael Papadopoulos. Springer International Publishing, 2016, pp. 113–140.

[35]   S. Vasista, A. De Gaspari, S. Ricci, J. Riemenschneider, H.P. Monner, and B. Van de Kamp. "Compliant structures-based wing and wingtip morphing devices". In: *Aircraft Engineering and Aerospace Technology* 88.2 (2016), pp. 311–330.

[36]   A. Rudenko, A. Hannig, H.P. Monner, and P. Horst. "Extremely deformable morphing leading edge: Optimization, design and structural testing". In: *Journal of Intelligent Material Systems and Structures* 29.5 (2017), pp. 764–773.

[37] S. Vasista, H.P. Monner, F. Nolte, P. Horst, and M. Burnazzi. "Three-dimensional design of a large-displacement morphing wing droop nose device". In: *Journal of Intelligent Material Systems and Structures* 29.16 (2018), pp. 3222–3241.

[38] S. Vasista, J. Riemenschneider, R. Keimer, H.P. Monner, F. Nolte, and P. Horst. "Morphing wing droop nose with large deformation: Ground tests and lessons learned". In: *Aerospace* 6.10 (2019), p. 111.

[39] S. Vasista, J. Riemenschneider, and H.P. Monner. "Design and testing of a compliant mechanism-based demonstrator for a droop-nose morphing device". In: *23rd AIAA/AHS Adaptive Structures Conference*. 2015.

[40] A. De Gaspari, S. Ricci, and L. Riccobene. "Design, manufacturing and wind tunnel test of a morphing wing based on compliant structures". In: *24th AIAA/AHS Adaptive Structures Conference*. 2016.

[41] A. De Gaspari and S. Ricci. "Knowledge-based shape optimization of morphing wing for more efficient aircraft". In: *International Journal of Aerospace Engineering* 2015 (2015).

[42] A. De Gaspari and S. Ricci. "A two-level approach for the optimal design of morphing wings based on compliant structures". In: *Journal of Intelligent Material Systems and Structures* 22.10 (2011), pp. 1091–1111.

[43] J. Sodja, M.J. Martinez, J.C. Simpson, and R. De Breuker. "Experimental evaluation of a morphing leading edge concept". In: *Journal of Intelligent Material Systems and Structures* 30.18-19 (2019), pp. 2953–2969.

[44] A. De Gaspari. "Multiobjective optimization for the aero-structural design of adaptive compliant wing devices". In: *Applied Sciences* 10.18 (2020).

[45] I.K. Kuder, A.F. Arrieta, W.E. Raither, and P. Ermanni. "Variable stiffness material and structural concepts for morphing applications". In: *Progress in Aerospace Sciences* 63 (2013), pp. 33–55.

[46] J. Zhang. "Numerical investigation of buckling-driven mechanisms for shape morphing of composite wings". M.Sc. thesis. Delft University of Technology, 2020.

[47] B. Roman and A. Pocheau. "Postbuckling of bilaterally constrained rectangular thin plates". In: *Journal of the Mechanics and Physics of Solids* 50.11 (2002), pp. 2379–2401.

[48] H. Chai. "On the post-buckling behavior of bilaterally constrained plates". In: *International Journal of Solids and Structures* 39.11 (2002), pp. 2911–2926.

[49] P. Jiao, W. Borchani, H. Hasni, and N. Lajnef. "Static and dynamic post-buckling analyses of irregularly constrained beams under the small and large deformation assumptions". In: *International Journal of Mechanical Sciences* 124-125 (2017), pp. 203–215.

[50] P. Jiao, W. Borchani, H. Hasni, and N. Lajnef. "Enhancement of quasi-static strain energy harvesters using non-uniform cross-section post-buckled beams". In: *Smart Materials and Structures* 26.8 (2017), p. 085045.

[51] N. Lajnef, R. Burgueño, W. Borchani, and Y. Sun. "A concept for energy harvesting from quasi-static structural deformations through axially loaded bilaterally constrained columns with multiple bifurcation points". In: *Smart Materials and Structures* 23.5 (2014), p. 055005.

[52] S. Katz and S. Givli. "The post-buckling behavior of a beam constrained by springy walls". In: *Journal of the Mechanics and Physics of Solids* 78 (2015), pp. 443–466.

[53] H. Chai. "The post-buckling response of a bi-laterally constrained column". In: *Journal of the Mechanics and Physics of Solids* 46.7 (1998), pp. 1155–1181.

[54] P. Jiao, W. Borchani, A.H. Alavi, H. Hasni, and N. Lajnef. "An energy harvesting and damage sensing solution based on postbuckling response of nonuniform cross-section beams". In: *Structural Control and Health Monitoring* 25.1 (2018).

[55] P. Jiao, H. Hasni, N. Lajnef, and A.H. Alavi. "Mechanical metamaterial piezoelectric nanogenerator (MM-PENG): Design principle, modeling and performance". In: *Materials Design* 187 (2020).

[56] W. Borchani, N. Lajnef, P. Jiao, and R. Burgueno. "Control of postbuckling mode transitions using assemblies of axially loaded bilaterally constrained beams". In: *Journal of Engineering Mechanics* 143.10 (2017).

[57]   P. Jiao, W. Borchani, H. Hasni, A.H. Alavi, and N. Lajnef. "Post-buckling response of non-uniform cross-section bilaterally constrained beams". In: *Mechanics Research Communications* 78.Part A (2016), pp. 42–50.

[58]   P. Jiao, A.H. Alavib, W. Borchanic, and N. Lajnefc. "Micro-composite films constrained by irregularly bilateral walls: A size-dependent post-buckling analysis". In: *Composite Structures* 195 (2018), pp. 219–231.

[59]   P. Jiao, W. Borchani, and N. Lajnef. "Large deformation solutions to post-buckled beams confined by movable and flexible constraints: A static and dynamic analysis". In: *International Journal of Solids and Structures* 128 (2017), pp. 85–98.

[60]   Hexcel. In: *HexPly* ® *8552 Epoxy matrix (180°C/356°F curing matrix) Product Data Sheet* (2020).

[61]   U.O. Iñigo. "Experimental determination of fracture toughness for delamination analysis in structural components". M.Sc. thesis. Delft University of Technology, 2020.

[62]   Hashin, Z. "Failure criteria for unidirectional fiber composites". In: *Journal of Applied Mechanics* 47 (1980), pp. 329–334.

[63]   Tsai, S.W. "Strength characteristics of composite materials". In: *NASA CR-224* 47 (1965), pp. 329–334.

[64]   T.H.G. Megson. *Aircraft structures for engineering students*. Sixth Edition. Butterworth Heinemann, 2016, pp. 569–572.

[65]   T.H.G. Megson. *Aircraft structures for engineering students*. Sixth Edition. Butterworth Heinemann, 2016, pp. 56–57.

[66]   Toray Advanced Composites. In: *Toray TC250 Product Data Sheet* (2020).

.